UNIVERSITÀ
DEGLI STUDI
DI PADOVA

Sede Amministrativa: Università degli Studi di Padova

Dipartimento di *Ingegneria Industriale DII*

SCUOLA DI DOTTORATO DI RICERCA IN INGEGNERIA INDUSTRIALE
INDIRIZZO ENERGETICA
CICLO XXV

SIMULATION, DESIGN AND TESTS OF A DIAGNOSTIC CALORIMETER FOR THE SPIDER EXPERIMENT

Direttore della Scuola : Ch.mo Prof. Paolo Colombo
Coordinatore d'indirizzo: Ch.ma Prof.ssa Luisa Rossetto
Supervisore : Ch.mo Prof. Piergiorgio Sonato
Co-tutor: Dott. Gianluigi Serianni

Dottorando : Michela De Muri

TABLE OF CONTENTS

ACKNOWLEDGMENTS **5**
SUMMARY **7**
SOMMARIO **9**
INTRODUCTION **11**
1 NEUTRAL BEAM INJECTOR SYSTEMS **19**
1.1 PRIMA **21**
1.2 RF Source concept **23**
1.3 MITICA **27**
1.4 SPIDER **30**
2 THE DIAGNOSTIC CALORIMETER FOR SPIDER **37**
2.1 Physical phenomena due to beam-plasma and beam-surface interaction **37**
2.1.1 Interaction between beam and background gas 37
2.1.2 Interaction between beam and surfaces 38
2.2 Conceptual design of STRIKE **40**
2.3 Starting point of the PhD work **41**
2.4 Requirements and Interfaces **42**
2.5 Alternative design **52**
3 STRIKE DESIGN **59**
3.1 Final Design **59**
3.2 Diagnostic systems dedicated to STRIKE **71**
3.3 Simulations dedicated to the design **76**
3.3.1 Thermal simulations 76
3.3.2 Electrostatic simulations 82
4 CFC CHARACTERISATION **89**
4.1 Carbon Fibre Carbon Composite **89**
4.2 Fibre and voids **90**
4.3 Profilometry **93**
4.4 X-ray Diffraction (XRD) **96**
4.5 Optical analyses **98**
5 TESTS ON CFC PROTOTYPES BY POWER LASER PULSES **106**
5.1 Layout for laser test **106**
5.2 Thermal analysis **107**
5.3 Comparison between experimental data and simulation data **108**
6 VALIDATION OF THE DESIGN **121**
6.1 Risk analysis **121**
6.2 FMEA **124**
6.3 Control Plan **126**
6.4 Design Review **128**
6.5 Mock-up of thermocouple fixing system **128**
6.5.1 Preliminary test on thermocouples 129
6.5.2 Studies for connection of thermocouples to stainless steel pipes 130
6.5.3 Set up of the tests on thermocouple mock-up 132
6.5.4 Results of the tests on thermocouple mock-up 135
6.6 Thermal camera discretisation **140**
6.7 "SPIDER like" data analysis **142**
7 TESTS IN PARTICLE BEAMS **149**
7.1 Test at IPP-BATMAN **149**
7.1.1 Design of CFC tile support 150
7.1.2 In-house tests on mock-up 159
7.1.3 Simulations 165
7.1.4 Measurements and data analysis 166
7.2 Tests at IPP-GLADIS **185**
7.2.1 Design of CFC tile support 188

7.2.2 Comparison between simulations and experimental data 190
7.2.3 Measurement campaigns 193
7.2.4 Preliminary remarks on CFC tiles exposed to GLADIS beam 197
7.3 NIO1 202
7.3.1 Description of NIO1 experiment 203
7.3.2 Simulations of expected signals 203
8 CONCLUSIONS 209
REFERENCES 213
APPENDIX 219
PARTICIPATION TO NATIONAL AND INTERNATIONAL CONFERENCES 221
PUBLICATIONS IN INTERNATIONAL JOURNALS 221
TECHNICAL NOTES OF CONSORZIO RFX 222

Acknowledgments

My PhD work would not have been possible without the collaboration of several people. I would like to thank everybody who helped and encouraged me during these three years.

Summary

One of the most critical issues for fusion reactors, to be studied in ITER (the prototype that has to prove the feasibility of production of electric energy by fusion), is the generation of sufficient energy to the sustainment of fusion reactions as well as to the injection on the electric transmission network. As ohmic heating, produced by the current flowing in the plasma, is not sufficient for the operation in fusion conditions, it is necessary to use additional heating systems. One of these methods, to be evaluated during ITER operations, is the additional heating of the plasma by means of neutral particle beams injected into the core plasma.

At Consorzio RFX, in the research area of the C.N.R. of Padua, the design of the project PRIMA-MITICA-SPIDER (PMS) is ongoing and construction of the building has already started. The PMS project includes two experiments: MITICA is the full-size prototype of ITER injector and SPIDER, whose operations will start before MITICA, is realized with the aim of optimising the production of the negative ions composing the beam. To this scope a detailed knowledge of the parameters of the plasma inside the source and of the beam features is fundamental, obtained with diagnostic systems foreseen on SPIDER; one of them is the diagnostic calorimeter STRIKE, developed in the present PhD work.

During the thesis the requirements of the calorimeter have been defined and the design has been concluded. Verifications of some design solutions have been performed by designing and realizing dedicated prototypes. CFC, a unidirectional carbon fibre composite with a carbon matrix, is the main component of the calorimeter. Several samples of 1D CFC have been purchased from different suppliers, to characterise their thermal properties by a power laser and by high-energy particle beam tests. A prototype of the whole system has been realized, including the thermal camera, and was used in the BATMAN ion source at IPP-Garching (Germany) with the aim of evaluating the diagnostic capabilities in conditions similar to those expected in SPIDER. Non linear transient finite element thermal analyses and electrostatic simulations have been developed for the design phase as well as the test phase. Moreover, the planning of the activities for the calorimeter together with the preparation and writing of the whole documentation have been supervised.

The small and flexible NIO1 source, under development as a collaboration between Consorzio RFX and INFN-LNL, will soon be ready to study the negative ion source behaviour. Preliminary studies for the use of CFC prototypes to characterise the NIO1 beam, carried out during the PhD, are also presented.

The conclusion of this work is that STRIKE should prove a very valuable diagnostic of the SPIDER beam characteristics and should allow to assess the compliance of the SPIDER beam with the ITER requirements.

Sommario

Uno degli aspetti più critici dei reattori a fusione, che verrà studiato in ITER (prototipo che dovrà provare la fattibilità di questa tecnica di produzione dell'energia elettrica), è la generazione di energia sufficiente sia all'autosostentamento della reazione di fusione sia all'immissione nella rete elettrica di trasmissione. Non essendo sufficiente per il funzionamento in condizioni di fusione il riscaldamento ohmico, prodotto dalla corrente che fluisce nel plasma, è necessario utilizzare delle tecniche di riscaldamento addizionali. Una delle vie che saranno valutate in ITER è l'ulteriore riscaldamento del plasma ottenuto tramite l'iniezione di un fascio di particelle neutre nel plasma centrale.

Al Consorzio RFX, nell'area di ricerca del C.N.R. di Padova, si sta procedendo con l'ultimazione della progettazione e l'avvio dei lavori di costruzione del progetto PRIMA-MITICA-SPIDER, che comprende due esperimenti: MITICA è il prototipo in scala reale dell'iniettore di ITER mentre SPIDER, che sarà in esercizio prima di MITICA, è realizzato con l'obiettivo di ottimizzare il funzionamento della sorgente di ioni negativi che costituiscono il fascio. Allo scopo, è fondamentale una conoscenza accurata dei parametri del plasma internamente alla sorgente e del fascio, ottenuta tramite i vari sistemi diagnostici previsti in SPIDER, tra i quali il calorimetro diagnostico STRIKE, argomento del presente lavoro di dottorato.

Durante la tesi si sono definiti i requisiti del calorimetro e se ne è concluso il progetto. Si sono verificate, progettando e realizzando appositi prototipi, alcune soluzioni costruttive. Si sono acquistati da produttori diversi alcuni prototipi di CFC 1D, elemento principale che costituisce il calorimetro, un materiale in fibra di carbonio unidirezionale su matrice di carbonio, per caratterizzarne le proprietà termiche mediante riscaldamento con laser di potenza e nell'esperimento GLADIS presso l'IPP di Garching (Germania), con fascio di particelle di alta intensità. Si è anche realizzato un prototipo del sistema completo, inclusa la telecamera termica, che è stato utilizzato nell'esperimento BATMAN presso l'IPP di Garching (Germania), con lo scopo di valutarne il funzionamento in condizioni simili a quelle di SPIDER. Sia la fase di progettazione che quella di test sono state accompagnate da simulazioni numeriche agli elementi finiti, di tipo elettrostatico e termico transitorio non lineare. Inoltre, si è seguita anche la parte di pianificazione e documentazione relativa al progetto del calorimetro.

Nella collaborazione tra Consorzio RFX and INFN-LNL, si sta sviluppando un'ulteriore sorgente di ioni negativi: NIO1, che a breve entrerà in operazione. La particolarità di questa sorgente è di essere piccola e flessibile. In questa tesi saranno inoltre presentati i risultati preliminari sulla valutazione dell'utilizzo di campioni di CFC per la caratterizzazione anche del fascio di NIO1.

Il lavoro di tesi si conclude pronunciandosi positivamente sulla validità dell'utilizzo di STRIKE per studiare approfonditamente le caratteristiche del fascio di SPIDER e valutarne la corrispondenza ai requisiti richiesti da ITER.

Introduction

Nuclear fusion is one of the environmentally acceptable, safe and sustainable energy technologies researchers from all over the world are working on for the development of the human kind.

Nuclear fusion is the process (Figure 0.1) that powers the sun and other stars, providing heat and light to sustain life on Earth. While gravity confines the hot plasma in the stars, on Earth strong magnetic fields can be used to hold the plasma inside a chamber in a quasi-stable condition; this is the magnetic confinement approach (also inertial confinement is studied) [1].

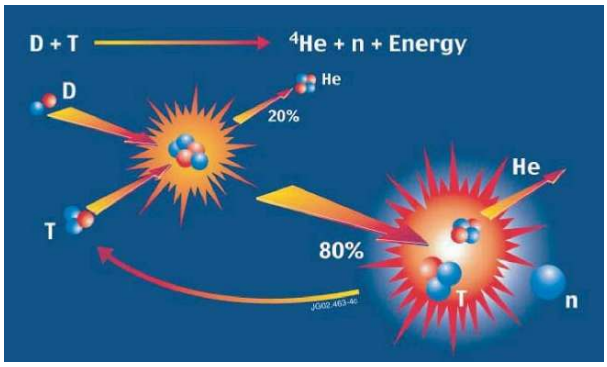

Figure 0.1: The nuclear fusion reaction.

To harness fusion power, light nuclei are forced together, undergoing reactions that produce a net energy gain. In order to make fusion happen, the fuel in plasma state has to be heated up to very high temperatures (in the order of 100 million degrees).

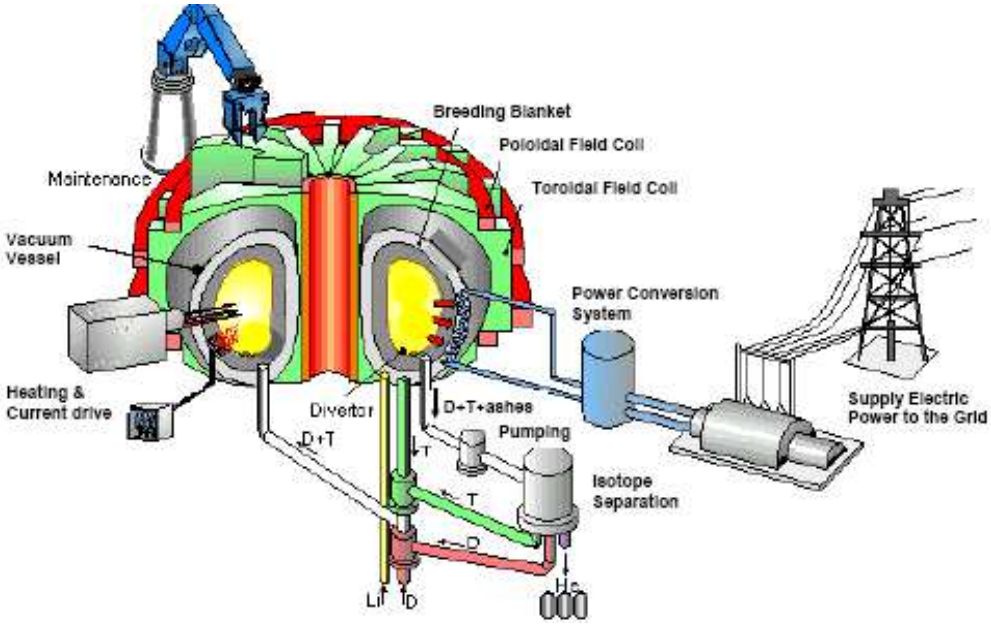

Figure 0.2: Schematic of a future fusion power plant.

The “tokamak” has been the most successful concept for confining fusion plasmas up to now: current flows into the plasma along the toroidal direction, with a consequent production of a poloidal magnetic field. A much stronger toroidal magnetic field is produced by external coils in order to stabilize the configuration [2]. Alternative concepts, like the Reversed Field Pinch and the Stellarator, are also developed to prepare for fusion power plants.

The primary fuels for nuclear fusion are deuterium and lithium. Deuterium can be extracted from sea water and lithium is abundant in the Earth’s upper crust. In a power plant lithium is used to breed the tritium which fuses together with deuterium. Only 150 kg deuterium and 2÷3 tonnes of lithium are needed for a full year of electricity supply for one million persons.

Fusion power plants will be particularly suited for base load energy generation to serve the needs of densely populated areas and industrial zones (see Figure 0.2).

In Figure 0.3 a cutaway of ITER is shown.

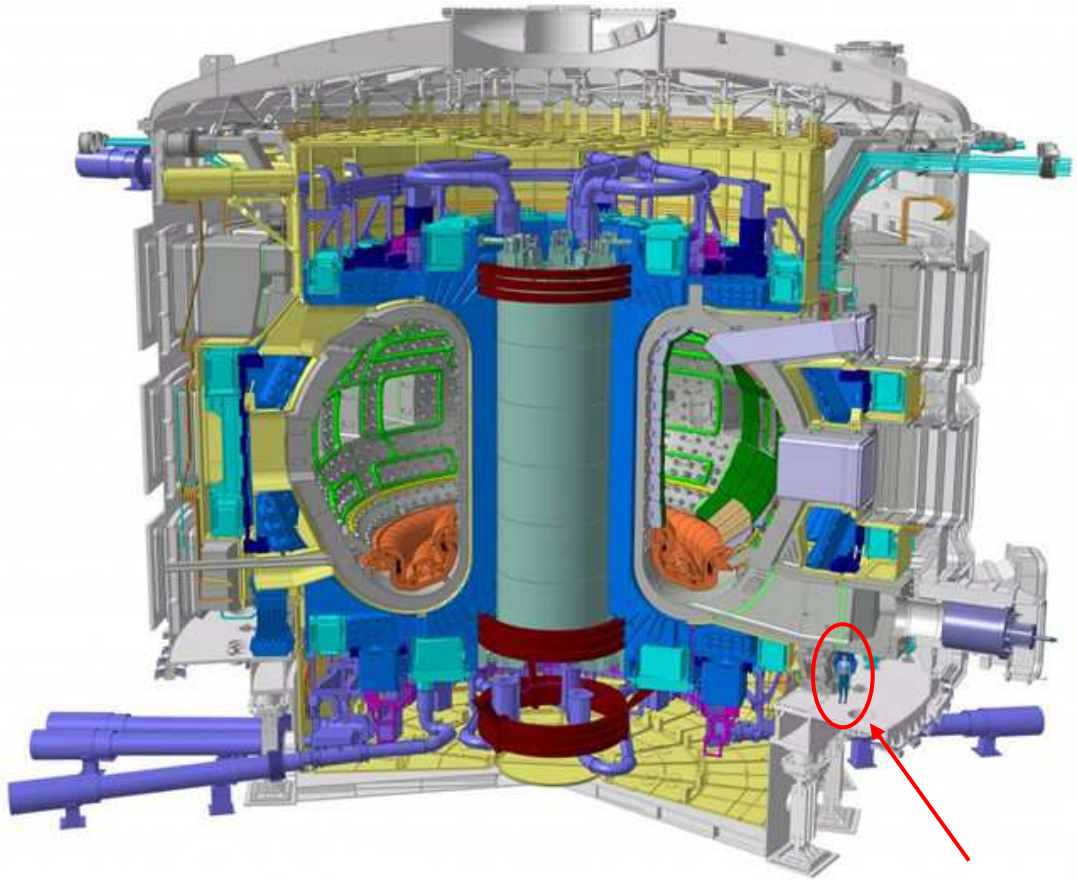

Figure 0.3: Technical cutaway of the ITER Tokamak Torus encasing. Note the human figure for size comparison.

ITER is the next milestone towards the development of a reactor based on the controlled thermonuclear fusion reactions [3]. ITER is an international tokamak research project which is intended to be an experimental step between today's studies of plasma physics and future fusion power plants. It will be built upon research conducted with devices such as DIII-D [4], TFTR [5], JET [6] and JT-60 [7] [8] and will be considerably larger than any of them.

On November 21, 2006, European Union, United States of America, Russian Federation, Japan, Republic of Korea, People's Republic of China and India formally agreed to fund the project. The program was anticipated to last for 30 years (10 years for construction, and 20 years of operation) and costs approximately 15 billion Euros, which makes it one of the most expensive modern techno-scientific megaprojects. It will be based in Cadarache, France. It was foreseen to be technically ready to start construction and the first plasma operation was expected in the early years of the next decade.

In the years the planning has been updated and the first plasma is now foreseen in 2019. The cost of ITER has also been revised and it has been increased of a factor 1.7.

The ITER experiment has the aim of demonstrating the feasibility of the fusion power plant; that means:

- demonstrating the feasibility of creating and maintaining a confined fusion plasma for one hour, in order to extract a continuous flux of energy;
- demonstrating the technical and technological feasibility of the reactor;
- studying the behaviour of the materials, especially the first wall components which directly face the plasma;
- testing all the needed auxiliary plants, including heating and injection components;
- verifying the processes for the recovery and treatment of the nuclear reactor activated materials;
- obtaining a net production of energy: thermal energy obtained from the fusion reaction $\geq$ 5-10 times the energy given to the plasma by the auxiliary systems;
- testing the fuel injection and heating systems;
- testing the breeding blanket modules;
- demonstrating the safety of this kind of reactors.

So ITER has to demonstrate the operation in steady state regime and with high Q (ratio between energy produced by nuclear fusion reactions and energy injected into the plasma): Q=10 during pulsed operation and Q=5 in steady state).

The main goal of ITER is to produce approximately 500 MW of fusion power sustained for at least 300 seconds (compared to JET's peak of 16 MW for less than a second) by the fusion of about 0.5 g of deuterium/tritium mixture in its approximately 840 m^3 reactor chamber. This configuration requires a really considerable quantity of energy in order to create the toroidal magnetic field. In addition, the pure ohmic heating is not enough to reach the state where the fusion power produced is larger than the power used to sustain the reaction. For this reason the tokamak needs additional heating systems. These systems can also regulate the plasma density profile and drive the current to suppress the instabilities so as to operate in a steady state mode (Figure 0.4).

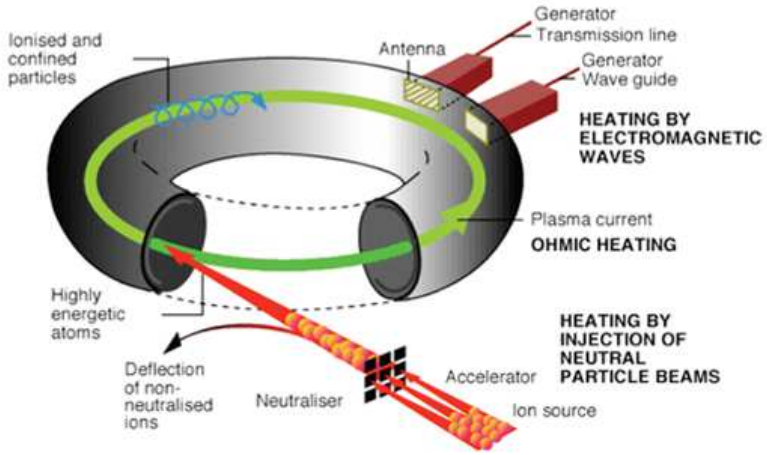

Figure 0.4: Additional heating concept.

The main ITER parameters are reported in the next table.

Total fusion power	500 MW
Q = Exhausted Fusion Power/Plasma Heating Power	5-10
Specific Power from 14 MeV neutrons on the first wall	>0.5 MW/m^2
Discharge duration	>300 s
Major radius of the torus	6.2 m
Mean minor radius of the torus	2 m
Plasma current	15 MA
Toroidal magnetic field strength	5.3 T
Plasma volume	837 m^3
Plasma surface	678 m^2

Table 0.1: ITER nominal parameters.

Within the tokamak, the changing magnetic fields that are used to control the plasma produce a heating effect. The varying magnetic fields create a high-intensity electrical current through induction, and as this current travels through the plasma, electrons and ions become energized and collide. Collisions exchange momentum among particles, create macroscopic 'resistance' which results in plasma heating, but, unlike most solid conductors at room temperature, as the temperature of the plasma rises, this resistance - and therefore the heating effect - decreases. Heat produced by high-intensity current is limited to a level defined by the balance between energy injection by ohmic heating and energy loss via radiation and particle loss, which are more effective as the particle energy increases. For this reason the ITER tokamak needs additional heating systems that are also used for regulating the plasma density profile, and for suppressing some of the plasma instabilities, aiming at reaching and sustaining the high performance regime (H-mode) [9], [10].

The Heating and Current Drive (H&CD) systems for ITER are an appropriate combination of Neutral Beam Injectors (NBI) and Radio Frequency (RF) H&CD antennas operating at the electron cyclotron (EC), ion cyclotron (IC) and lower hybrid (LH) frequencies (Figure 0.5) [11].

They contribute, together, at providing an active control on all the key phases of the operating scenarios, acting on:

- the plasma temperature,
- the achievement of a steady burn,
- the suppression of instabilities, and
- the achievement of a soft termination.

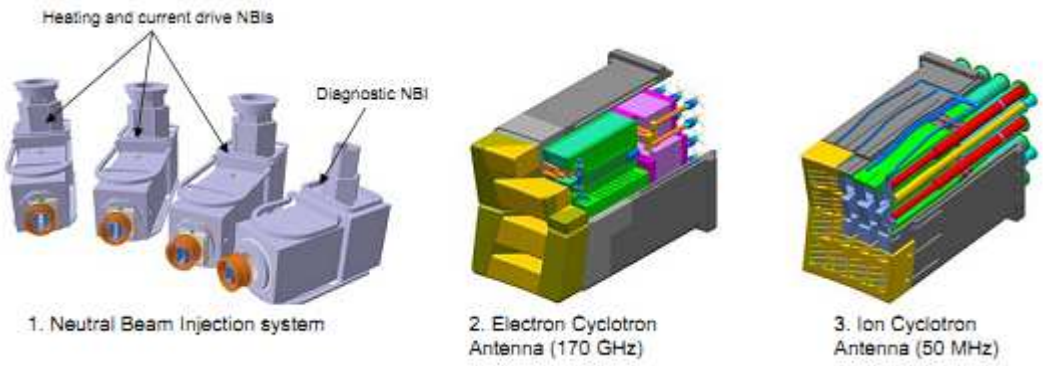

Figure 0.5: Overview of the Heating & Current Drive systems.

The neutral beam system design for ITER consists, at present, of two heating and current drive (H&CD) injectors and one diagnostic neutral beam (DNB) injector. Each H&CD injector will deliver a deuterium beam of 16.5 MW (total 33 MW), with energy of 1MeV, and will be able to operate for long pulses (up to 3600 s for steady state operation). A third H&CD NBI is

foreseen to be added in a second stage, in order to increase to 50MW the heating power to the ITER plasma [12], [13].

In order to obtain an effective and reliable Neutral Beam Injector (NBI) for ITER, a large amount of research & development (R&D) is required, both on the physics and the engineering side. For this reason, a neutral beam test facility is being built in Padova [14]. The facility is named PRIMA (Padova Research on Injector Megavolt Accelerated); it will host both SPIDER (Source for Production of Ion of Deuterium Extracted form Rf-plasma) and MITICA (Megavolt ITER Injector Concept Advanced) test-beds that have the goal to address and solve the main physics and engineering issues related to this system.

This thesis aims at solving important engineering issues and proposing design solutions of one component of the ITER NBI test-bed, the diagnostic calorimeter for SPIDER.

In Chapter 1 the basic concepts of ITER NBIs are described. The PRIMA test facility, and the two experiments MITICA and SPIDER, under development at Consorzio RFX in Padua with the purpose to study the physical and engineering problems of neutral beam injection, are then presented. In the final section of the first chapter the physics of negative ion formation and the effect of caesium seeding in negative ion sources are described.

In Chapter 2 the conceptual design of the calorimeter is introduced together with its requirements, part of which coming from the physical phenomena occurring inside SPIDER; moreover, the previous design has been described.

In Chapter 3 the final design of the calorimeter and of its diagnostics is discussed, considering all design solutions and the simulation results performed to verify and to develop the design.

Chapter 4 describes the production process of the CFC 1D, the main and most delicate component of the calorimeter as well as the analyses made on the purchased CFC prototypes.

Chapter 5 focuses on a particular study made on CFC prototypes, the laser tests, together with the data analysis to characterise the thermal behaviour of the prototypes by comparing the experimental findings with the simulation results carried out to reconstruct the experimental data.

Chapter 6 presents the verifications of the project, including the documentation produced and the assessment of some design solutions by means of mock-up tests.

Finally, in Chapter 7 the tests of the CFC prototypes under irradiation by particle beams are shown, in particular, experiments have been made to test the diagnostic capability of the calorimeter project and to assess the thermo-mechanical behaviour of the CFC, due to its

importance in the design. The most important conclusions of the thesis work are summarised; some open issues to be addressed in the next activities are also described.

1 Neutral Beam Injector systems

The concept of the neutral beam injection is to introduce high-energy neutral particles into the plasma: these energetic particles, by way of collisions, will heat the plasma by transferring their energy to the plasma particles; the momentum of the energetic particles is also transferred to the plasma particles, resulting in the injection of current in the plasma. Particles are accelerated by electrostatic fields and are neutralised before being injected into the vessel to avoid that the high magnetic field produced to confine the plasma deflects beam particles before they reach the core plasma, where they are expected to deposit their energy. All these steps, from the production of negative ions up to the injection into the discharge chamber, happen inside the vessel of the injector and the duct connecting it to the machine vessel.

The beam power deposition in the plasma principally depends on the beam energy and the plasma density and it is necessary to deposit the beam power inside the so-called H-mode barrier, this means some meters for ITER (see the P_d trend in Figure 1.2) so, as shown in Figure 1.2, the beam produced should have deuterium particles with en energy of about 1MeV.

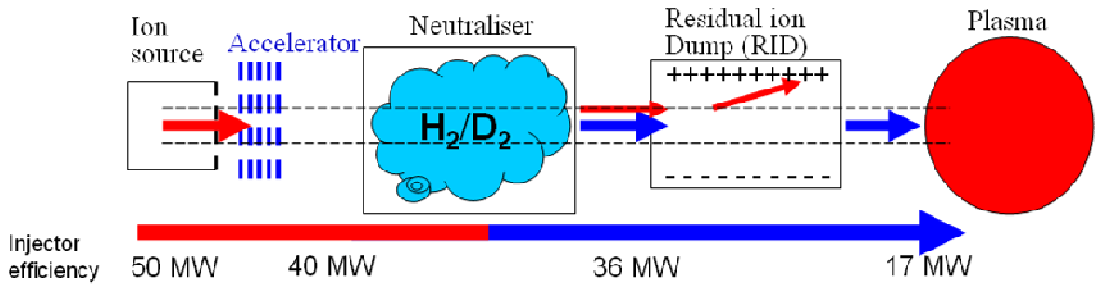

Figure 1.1: Beam production and neutral beam injection.

At this high energy level, it is necessary to use injection based on negative ions. Currently, most of the operating injectors are based on the acceleration of positive ions: having then a beam source producing positive charges. The drawback of having a positive ion beam is that the neautralisation is more and more difficult as the particle energy increases (good neutralisation efficiency is obtained up to particle energies of 100keV) [15]. The neutralization efficiency measured in negative-ion based NBI for the Japanese tokamak JT-60U is shown as a function of the beam energy in Figure 1.2 [16].

A beam of negative ions can thus fulfill the ITER requirement on beam energy to penetrate deep enough into the plasma and in this way to sustain the plasma current and to maximize the power per injector, permitting a neutralization efficiency of 60%. So it was decided to use

negatively charged ions, which are easier to neutralize at 1MeV. On the other hand they are more difficult to create and to handle than positive ones.

Each ITER NBI delivers a deuterium beam of 16.5MW with particles energy of 1MeV which will be injected as fast neutrals into the plasma.

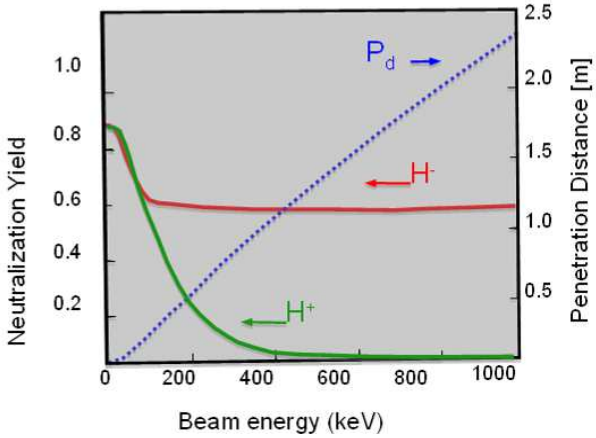

Figure 1.2: Hydrogen ions neutralisation efficiency as a function of energy.

Initially ITER will use two heating neutral beams (HNB) that are designed to inject 33MW of either 1MeV deuterium (D^0) or 870keV Hydrogen (H^0) into the ITER plasma, depending on the discharge gas used in the specific operational phase. A third heating beam may be added later, bringing the total D^0 power that may be injected into ITER up to 50 MW. Another different Neutral Beam injector will be used for diagnostic purposes (DNB). They can be seen in Figure 1.3.

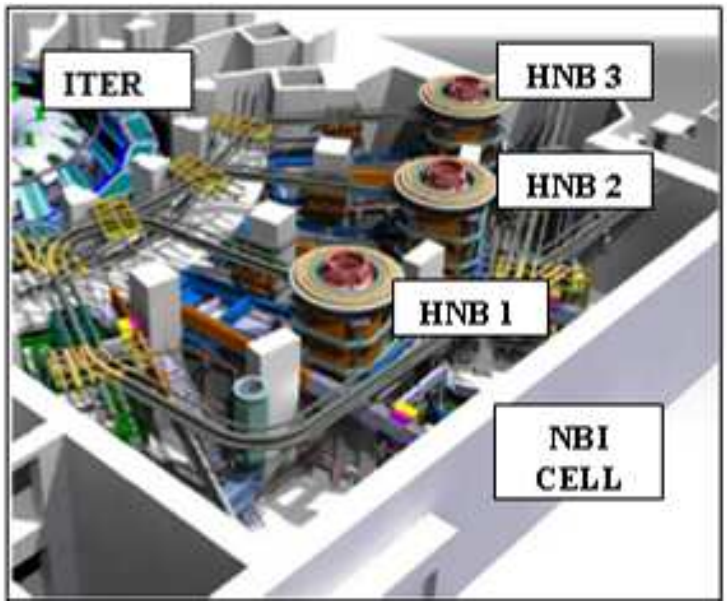

Figure 1.3: ITER and the NBI cell with DNB and 3 HNB.

The neutral beam injector technology for the required energy and power is well beyond the present performance reached by similar systems and therefore it is necessary to create a new experimental facility addressing all the current issues and to fill up all the residual technical and scientific gaps.
The realization of this laboratory, with the financial support of ITER, European Union and Italy, has been committed to Consorzio RFX in Padova. The experimental devices hosted in the facility will be realised with the contribution of important European research institutes (from France, Germany and United Kingdom) and the contribution of international ITER partners, Japan and India.
Some of these contributions are limited to the design phase, others will extend to the supply, installation and commissioning of components and services. At the end this facility will be available to all ITER parties for the exploitation and the development of the high energy neutral beam injectors for plasma heating and current drive based on negative ions.

1.1 PRIMA

In order to finalize the development of the ion sources required for ITER neutral beam injectors, to test all the essential aspects of the diagnostic accelerator, and so to achieve the full performances, a full-size test facility will be realized. It will allow the acquisition of an adequate operational experience before the manufacturing and operation of ITER injectors.

Padova **R**esearch on **I**TER **M**egavolt **A**ccelerated (PRIMA) [17] identifies all the R&D facilities that will be realised and hosted at Consorzio RFX in Padova in the framework of international agreements with all the different actors: ITER Organization, Europe and the Host, Consorzio RFX, with contributions from the other ITER Parties, Japan and India, directly involved in the neutral beam systems procurements. The PRIMA activities include the design, construction, installation and exploitation of two experimental devices in a new building whose construction is ongoing.

The laboratory that will host the prototype experimental injector, for the technical and scientific development of the injectors to be installed in ITER, is located in the site of the National Research Council (C.N.R.) of Padova in Corso Stati Uniti, 4. The facility is being built in the Southern side of the research C.N.R. area, next to the 400kV power station that supplies energy to the existing RFX-mod device and that will also supply energy to the experimental plants of PRIMA.

The facility will host two experimental devices: MITICA (described in Section 1.3) and SPIDER (described in Section 1.4), all the experimental service plants and the control rooms necessary for the operation of the two devices. The buildings will be built on a surface of

approximately 17500m^2, whereas the area covered by buildings is of approximately 7000m^2. The tallest building will reach 26m in height. A cutaway view can be seen in Figure 1.4.

Figure 1.4: PRIMA experimental hall cutaway view.

Figure 1.5 shows the building layout. The main building is subdivided in two bodies having different height, but the same length of 110m. The main single-span building (1) will host the mechanical parts of the two devices; it will cover a surface of 3000m^2 and is 26m high. A single crane having a total capacity of 50tons and covering the whole building area will allow manoeuvring and placing of all components to be installed in the experimental devices. The second body (2) is adjacent to the first one and has a surface of 2100m^2; it is partially divided into rooms that are distributed in two floors. The whole height of the building is 18m. The body is divided in two spans to host on the roof some of the experimental apparatuses. In particular some components of the cooling and of the cryogenic plants will be installed here. To move the components inside the buildings, two cranes (10tons total capacity) have been foreseen for each span in the single floor rooms. A second body of buildings is composed of two rooms; the first one (3) with a surface of about 800m^2 and a height of 26m will host a -1MV shielded deck, containing power supply systems and other devices operating at -1MV voltage to ground. The second room (4) having a surface of 400m^2 and 17m height has two floors; it will host other power supply systems and utility devices. A final building (5), connecting the previous ones, will host two experiment control rooms; computers, network devices and data storage systems. In the external area, other systems and components necessary for the experimental plant operation can be seen: the MITICA acceleration grid power supply, including five secondary 200kV transformers series-connected in order to reach the voltage value of -1MV (6), the underground -1MV transmission line (7) and two underground water basins which serve as heat capacity of the cooling system (8).

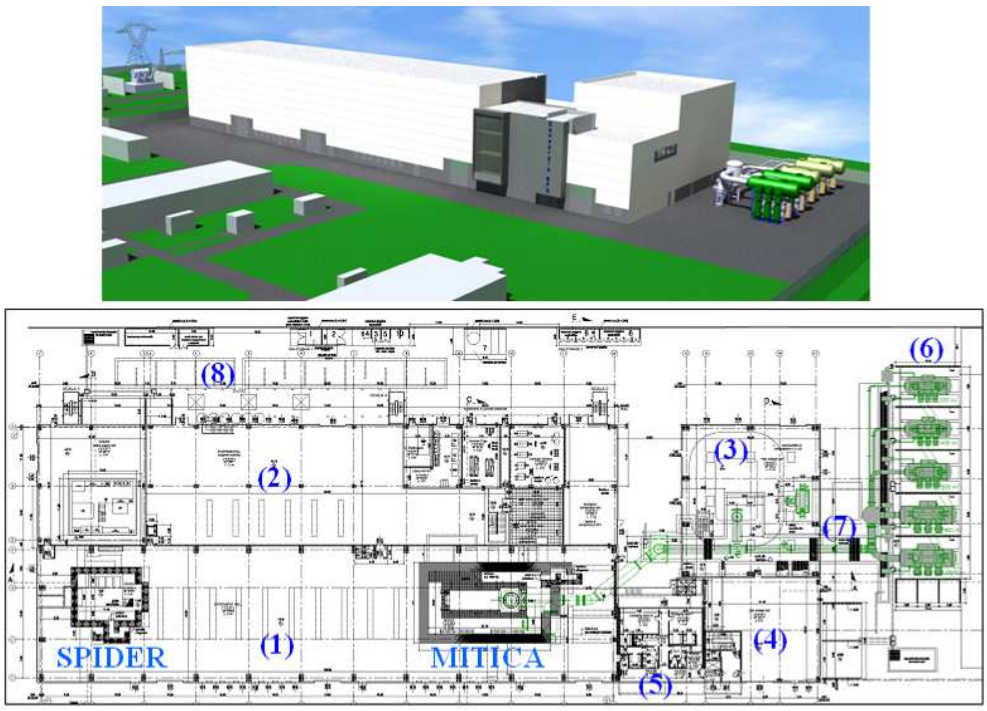

Figure 1.5: PRIMA buildings, layout and side views.

1.2 RF Source concept

The Radio Frequency (RF) source, whose conceptual scheme is shown in Figure 1.6 consists of three parts [18]:

the **driver**, that is mounted on the back of the source body, where the RF is coupled to the plasma;

the **expansion region**, where the plasma expands into the actual source body;

the **extraction region**, where negative particles are extracted from the plasma;

and the **acceleration region**, where negative ions are accelerated.

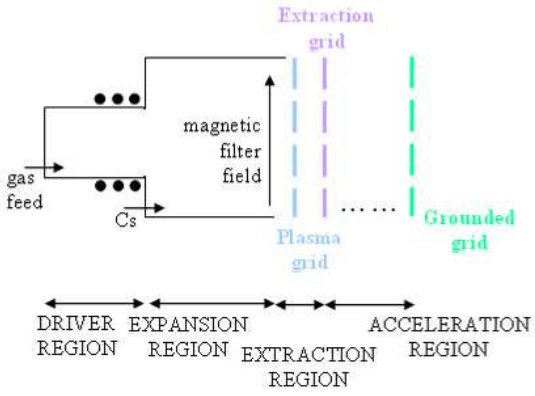

Figure 1.6: RF source scheme.

The extraction of the ion current is affected by space charge forces [19]: if electrical charges of the same signs accumulate, they repel each other limiting the extracted current. The negative ion current at the exit of the accelerator planar grid is given by the Child-Langumuir law:

$$I_{CL} = \frac{4}{9}\pi\varepsilon_0\sqrt{\frac{2e\zeta}{m}}S^2U^{3/2}$$

- ε_0 = vacuum permittivity;
- e = electronic unit charge;
- ζ = ion charge state;
- m = ion mass;
- S is the aspect ratio r/d between the radius of the grid holes at the plasma grid and d the distance between plasma grid and extraction grid.

So, the extraction current is proportional to $U^{3/2}$ and the proportionality constant P is the perveance:

$$P_0 = \frac{4}{9}\pi\varepsilon_0\sqrt{\frac{2e\xi}{m}}S^2$$

The perveance of an ion beam is:

$$P = \frac{I}{U^{3/2}}$$

The perveance is related to the optic of the beam: in a condition of perveance match the beam is parallel.

The driver is mounted on the back of the source body and consists of a cylinder with a winded RF coil connected to a 1MHz oscillator. An internal Faraday screen protects the cylinder from the plasma. Due to the Faraday screen that allows only inductive coupling, a so-called starter filament is necessary in order to ignite the plasma together with a gas puff of a few 100ms length. The starter filament is switched off some 100ms after the plasma ignition.

At the end of the expansion region (Figure 1.6) a magnetic field is present, parallel to the plasma grid, which extends into the extraction region: the so called filter field. This field is necessary in order to keep the ‘hot’ electrons, which are generated by the RF and have energies larger than 2eV, away from the extraction region, as these electrons efficiently destroy negative hydrogen ions by collisions [18] and [20]. At 2eV the rate coefficient for electron collisions equals the one from mutual neutralization. Electron temperatures below 2eV are necessary for minimizing the destruction rate of the negative hydrogen ions by electron collisions.

The extraction grid is biased positively with respect to the plasma grid: the resulting electric field extracts the negative particles from the source plasma through the plasma grid apertures.

The cool-down from the expansion region is further assisted by magnets embedded in the extraction grid which are primarily there to deflect the co-extracted electrons. The filter field also helps to reduce the co-extracted electron current.

The plasma grid (Figure 1.6) can be biased positive against the source body. This is found to enhance the negative ion yield and to suppress the co-extracted electrons. This biasing requires the addition of a so-called bias plate, electrically connected with the source body to enhance the surface area at source potential in the neighbourhood of the extraction apertures.

A fraction of the ions passing the plasma grid is stripped in the extractor/accelerator, consequently, the source has to deliver more negative ions than the amount exiting the accelerator at full energy. Some of the negative ions exiting the accelerator exhibit bad optical properties; they are extracted from the source at the edges of the plasma grid apertures or they are generated on the downstream side of the plasma grid [21].

The production of negative hydrogen-like ions is explained according to two important formation processes, the surface and the volume production [22].

Volume production: the production of negative ions occurs in the volume of plasmas generated in molecular gases (hydrogen, deuterium). The main formation process of negative hydrogen ions in pure hydrogen plasma is dissociative attachment of low energy electrons to highly rovibrationally excited molecules:

$H_2 + e(\leq 1\ eV) \rightarrow H^- + H$

Three *volume destruction processes* are the most important ones: mutual neutralization in collision with positive ions:

$H^- + H^+(H^+_2, H^+_3) \rightarrow H + e + \cdot\ldots$

electron detachment in collision with electrons:

$H^- + e \rightarrow H + 2e$

and associative detachment in collision with atoms:

$H^- + H \rightarrow H_2 + e$

Among the H^- ion destruction processes the most important one is mutual neutralisation.

The electron detachment can be reduced by lowering the density of energetic electrons. Since low energy electrons (<1 eV) are required for H^- production by electron attachment, an ion source denoted as tandem or magnetically filtered ion source is proposed, in which the plasma

production region (containing a group of energetic electrons, with an energy of several tens of electronvolts) is separated from the negative ion production region, which contains a cold plasma, by a transverse magnetic field, called magnetic filter.

The H^- ion density exhibits a dependence on the pressure. Several studies [22] have shown that there is an optimum pressure for the H^- ion density: this density increases with hydrogen pressure up to a maximum and then decreases.

Surface production: caesium adsorption lowers the surface work function and this increases the probability of sputtered particles escaping in the form of negative ions. After seeding a certain amount of caesium it was observed that the negative ion current increased with the plasma grid temperature, up to a surface temperature of 250–300°C.

The survival length for negative ions [18] is in the range of a few cm due to the various destruction mechanisms (mutual neutralization with H^+ ions and/or electron collisions, the latter being dominant above 2 eV). As a consequence, the formation of negative ions close to the extraction system must be maximized. This is done by the 'surface process', for instance the interaction of atoms or ions with materials having low work function:

H^+_x + surface $e^- \rightarrow H^-$.

Currently evaporation of caesium is used to cover the plasma grid of the extraction system with a thin layer of caesium; the work function is reduced to a value that depends on the thickness of the caesium layer. The negative ions produced at the plasma grid can then enter the plasma and are bent back to the extraction system by collisions, charge exchange or magnetic fields. As experiments show, the current densities are much higher in a caesiated source compared with caesium-free operation. This has been observed in filamented arc sources as well as in radiofrequency sources.

Caesium accumulates in areas where there is little contact between the plasma and the source wall. This has the effect that any modification in the confinement magnet arrangement will also redistribute the caesium in the source.

As explained above, the filter field seems to solve the problem of H^- ion destruction by fast electrons [22], since the magnetic filter prevents the energetic electrons in the driver from entering the region where the extracted H^- ions are supposed to be formed. Both positive and negative ions together with cold electrons can diffuse across the filter field into the extraction region. In the latter low temperature plasma is present, which is favourable for dissociative attachment (volume process).

1.3 MITICA

The **M**egavolt **ITE**R **I**njector & **C**oncept **A**dvancement (MITICA) is the first of the two experiments which will be hosted on the premises of the new laboratory. MITICA is the prototype of the injectors which will be realised and installed in ITER. Figure 1.7 shows the injector with its main dimensions in the experimental hall. The 1.8m thick concrete bio-shield has been partially removed to show the injector.

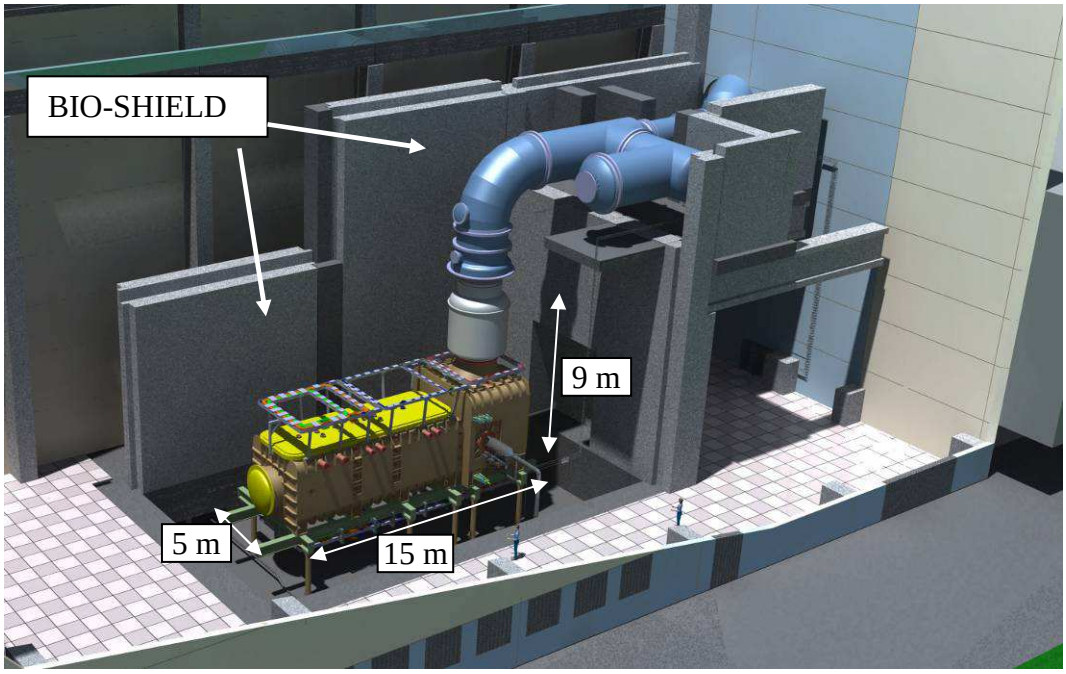

Figure 1.7: External view of the MITICA experiment.

The injector is being designed in order to be able to produce a beam of neutral particles of deuterium, electrostatically accelerated up to the energy of 1MeV. The beam shall be able to transfer a power of 16.5MW to the plasma for 3600s, continuously. The process for the production of deuterium neutral particles originates from a deuterium (D) plasma produced by means of 8 inductive radiofrequency generators (1MHz) in a chamber 1.8m high, 0.6m wide and 0.2m deep. The chamber (plasma source) faces a surface (plasma grid) having 1280 holes, each with a diameter of 14mm, previously covered with a caesium layer [23]. As mentioned earlier, deuterium – caesium surface interactions and reactions within the plasma can generate deuterium ions having an additional electron, i.e. negative deuterium ions (D^-). There are many processes that lead to the destruction of D^-, which exacerbates the difficulties of producing high extracted current densities. The choice for ITER of 1MeV is a compromise between the foreseen difficulties of developing higher energy, high power, power supplies and accelerators and the difficulty in making and accelerating high D^- currents [15]. A cutaway view of MITICA is shown in Figure 1.8 and a brief description of its main components is given hereafter.

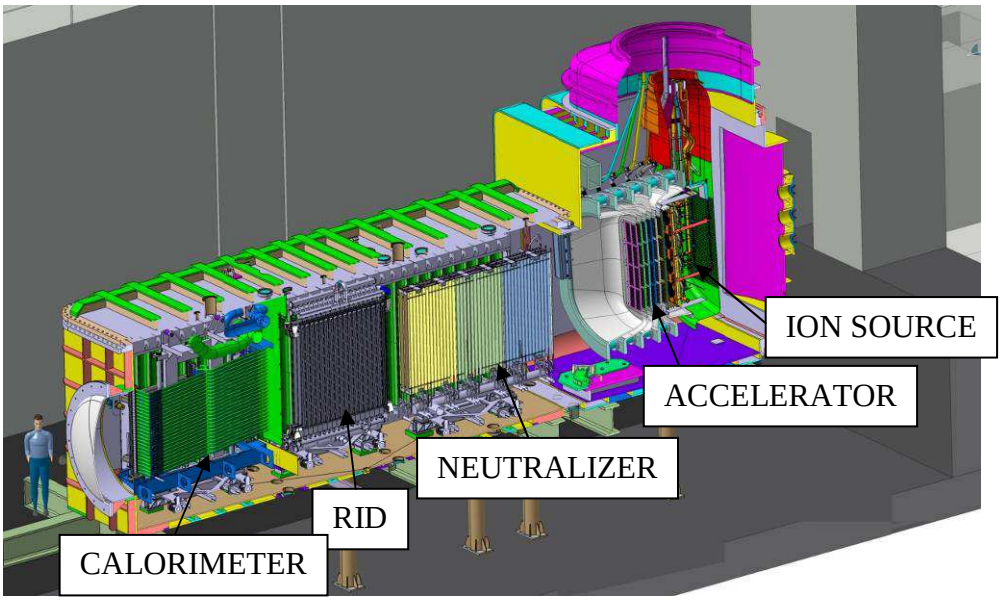

Figure 1.8: Cutaway view of the MITICA components.

The ion source is held at −1MV and the D^- ions are accelerated up to ground potential by a system of 5 grids (accelerator) set at different potentials, by steps of 200kV (Figure 1.9), applied to each pair of grids.

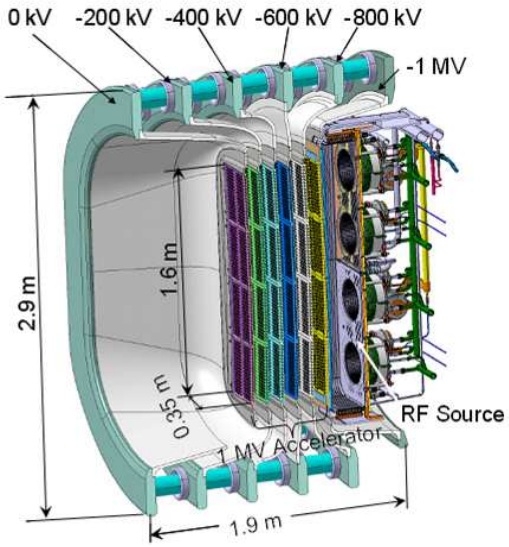

Figure 1.9: MITICA acceleration steps.

At the end of the accelerating grid system, a beam of negative deuterium ions accelerated to an energy of 1MeV will be obtained and a current of 40A is required. The composition of the ion source and the accelerator is called Beam Source. The beam will then pass through a cloud of deuterium gas where the negative ions get partially neutralised by a charge exchange process

(neutraliser), in order to generate a neutral beam. During the passage through the neutralizer, collisions of the D^- with the D_2 injected into the neutralizer leads to formation of D^0 by simple stripping of the outer electron from the D^-, and double stripping creates D^+. D^+ is also created by re-ionization of the D^0 resulting from D^-.

At the exit of the neutralizer, the beam, approximately composed by 60% D^0, 20% D^-, 20% D^+, will pass through an electrostatic field (Residual Ion Dump, RID). The electric field deflects the charged particles of the beam onto a set of plates, leaving the neutral beam to impinge onto the Calorimeter located just downstream of the residual ion dump. The two panels making up the calorimeter form a V with the open end of the V facing the RID. In this configuration the injector can be commissioned and the neutral power dumped onto the calorimeter can be measured. In the ITER NBI, the V calorimeter will be opened and the neutralized deuterium beam of 16.5MW power will flow along the duct until the ITER plasma is reached.

Large cryopumps are placed on either side of the beam path and the beamline components (neutralizer, RID and calorimeter) inside the injector to reduce the pressure downstream of the accelerator and downstream of the neutralizer exit to the required values. The pressure downstream of the accelerator must be low in order to minimize losses in the accelerator due to stripping. The pressure downstream of the neutralizer must be low in order to minimize re-ionization of D^0 by collision with the background D_2. The nominal parameters of the MITICA injector [24] are reported in Table 1.1.

MITICA	Unit	H	D
Neutral beam power	MW	16.5	16.5
Beam energy	keV	870	1000
Acceleration current	A	49	40
Maximum Beam Source pressure	Pa	<0.3	<0.3
Beamlet divergence	mrad	≤7	≤7
Beam-ON time	s	3600	3600
Co-extracted electron fraction (e^-/H^- or e^-/D^-)		<0.5	<1

Table 1.1 Nominal MITICA parameters.

1.4 SPIDER

The **S**ource for **P**roduction of **I**on of **D**euterium **E**xtracted from **R**f plasma (SPIDER) is the second experiment that will be hosted in the premises of the new laboratory [25]. SPIDER is an experiment which will allow to develop the knowledge on negative ions and to optimize the uniformity of negative ion production, up to the ITER requirement, before MITICA enters into operation (indicatively 2.5 years later than SPIDER) and then in parallel to MITICA operation. SPIDER will be equipped with a source for negative ion production that, once optimized, will be duplicated for MITICA. The beam is composed of 1280 beamlets, corresponding to the holes of the acceleration grids (Figure 1.10), spanning an area of 1520x560 mm^2. The grids are subdivided in 4x4 sectors named beamlet groups and each beamlet group is composed of 5x16 beamlet. Figure 1.11 shows the SPIDER experiment in the experimental hall. The 1.2m thick concrete bio-shield has been partially removed to show the device. The high voltage deck (in yellow colour) and the square-cross-section transmission line can be seen.

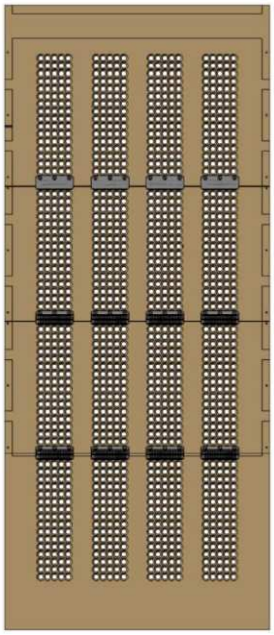

Figure 1.10: Example of SPIDER grid: the plasma grid.

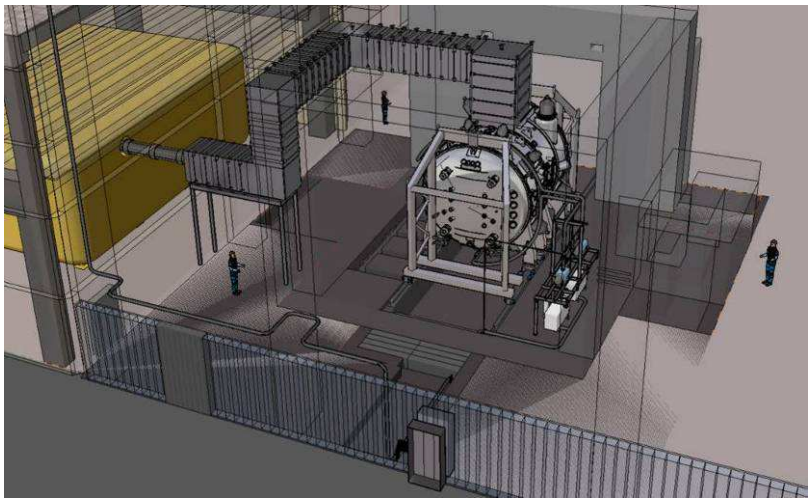

Figure 1.11: External view of the SPIDER experiment.

The SPIDER beam source will be characterised by a lower acceleration voltage (100kV) than MITICA (1MV). This is due to the fact that SPIDER will focus on the optimization of the negative ion beam creation process. The full acceleration and neutralization processes will be the scope of MITICA injector that will be the prototype of the ITER neutral beam injector. Thus, the mission of the SPIDER experiment is developing the ion source to guarantee on a large extraction surface of 1.52x0.56 m^2 the following parameters:

- the necessary ion current density;
- the lowest possible source pressure;
- the required uniformity;
- the lowest percentage of co-extracted electrons.

The SPIDER nominal parameters [24] are reported in Table 1.2 and an overall picture of the whole experiment can be seen in Figure 1.12.

SPIDER	Unit	H	D
Beam energy	keV	100	100
Maximum Beam Source pressure	Pa	<0.3	<0.3
Uniformity	%	90	90
Extracted current density	A/m^2	>350	>290
Beam-ON time	s	3600	3600
Co-extracted electron fraction (e^-/H^- or e^-/D^-)		<0.5	<1

Table 1.2 Nominal SPIDER parameters.

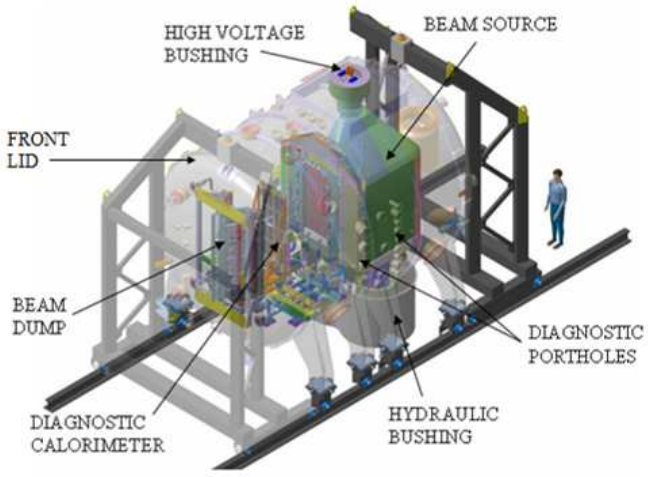

Figure 1.12: SPIDER device with transparent vessel.

The most important component of the SPIDER device is the beam source (Figure 1.13); nevertheless, the experiment would be useless without dedicated diagnostic systems [26] which

are able to measure the beam parameters (Figure 1.12). Visible tomography estimates the 2D beam intensity profile with sufficient spatial resolution and its evolution during the entire pulse duration. It measures the line of sight (LOS) integrated H_α or D_α radiation (656nm) generated after the collisions between fast beam particles and neutral background molecules; a sufficient number of well arranged LOSs allows a tomographic reconstruction of the 2D beam emission profile, which is proportional to the beam density. Tomography complements four other diagnostics. The instrumented calorimeter STRIKE measures with IR cameras the thermal pattern on the back surface of a set of 1D carbon fibre composite tiles, used as beam dump. It provides the best spatial resolution (about 2mm) at 50Hz frame rate, but it is incompatible with the heat load of long pulses (>10s). Installed only on SPIDER, it serves as a benchmark for other beam profile diagnostics to be used more confidently on MITICA. Beam emission spectroscopy (BES) measures the LOS integrated, spectrally dispersed H_α line. The two corresponding line components are spectrally resolved by the Doppler effect when the beam is observed at an angle different from 90°. Line intensity is proportional to the average beam particle density along the LOS: BES can be used to evaluate the beam uniformity, by comparison of LOS intensities, but with low spatial resolution, because of the limited number of LOSs. Its main role is to estimate the beam divergence from the width of the high energy line component. Beam intensity profile is also measured on the beam dump panels: thermocouples measure cooling water and bulk material temperature, providing respectively an estimate of the vertical power load profile (30 points) and a 2D temperature map (60 points) of the dump panels front surface; a neutron imaging diagnostic measures the neutron 2D profile generated by reaction of beam deuterons with those implanted in the dump surface.

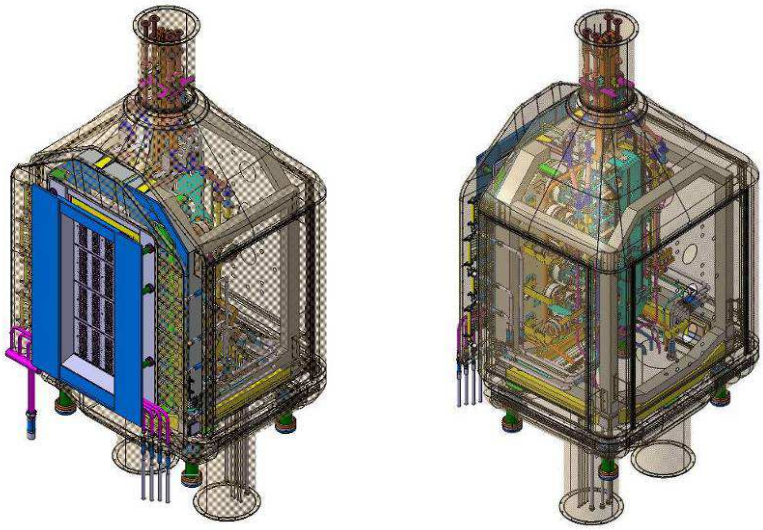

Figure 1.13: SPIDER Beam Source: frontal view (left) and rear view (right).

MITICA and SPIDER share the same Plasma Source and also the Bias Plate, the Plasma Grid and the Extraction Grid are coincident, that is they share the same ion source [23].

In Figure 1.14 the SPIDER plasma source can be seen [23]. The plasma source is mainly a box (chamber) open on the front side, having 1.8m high, 0.9m long and 0.2m wide prism shape. Eight inductive radiofrequency sources, called drivers, are placed on the rear edge of the chamber. Each driver is composed of a ceramic cylinder, made of alumina, around which electric coils, where a Radio Frequency current at 1MHz flows, are wound. The driver is the component where the plasma is produced by the radiofrequency electromagnetic fields. Thus, in order to protect the ceramic from the plasma, the inner part of the driver is constituted by an actively cooled copper shield; permanent magnet systems for plasma confinement are installed too. On the rear of the source three caesium ovens are connected; their aim is to feed the caesium into the source chamber in order to enhance the negative ion production. On the rear of the source also the load matching capacitors for the RF circuit are installed. Also all hydraulic connections for the source component coolant, coming from the hydraulic bushing, are routed there. The source lateral walls and the back of the plasma chamber (the Plasma Driver Plate), are actively cooled as well and the former also houses other permanent magnet systems for magnetic plasma confinement of the main chamber. Finally, the plasma source chamber is open on the front, where the plasma grid is located.

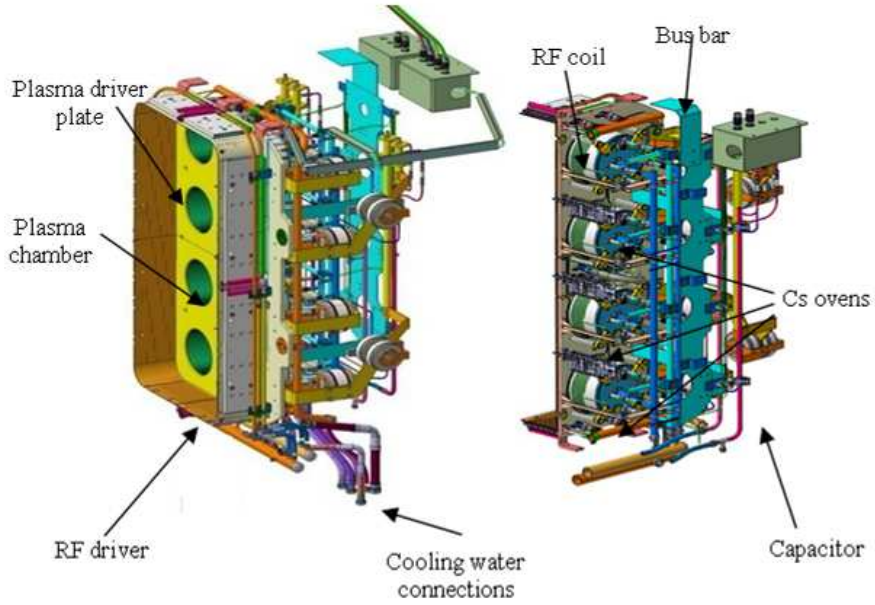

Figure 1.14: SPIDER plasma source views.

What differs between MITICA and SPIDER sources is essentially the presence of demountable hydraulic connections in SPIDER, not used in MITICA, to allow a higher flexibility to modifications, and the presence of a different accelerating grid system of the

extracted beam. In fact, as the aim of SPIDER is the production of an ion beam satisfying the ITER NBI requirements, the ion beam extracted is accelerated up to a lower energy (only 100keV instead of 1MeV) through just one accelerating grid placed at zero potential [23].

The SPIDER grid system is composed as follows:

- Bias Plate (for controlling the potential close to the PG apertures);
- Plasma Grid (for negative ion production);
- Extraction Grid (for negative ion extraction and dumping of co-extracted electrons);
- Grounded Grid (for negative ion acceleration).

As the last accelerating grid (grounded grid) is placed at zero potential, the accelerating voltage is 100kV and another 12kV is needed for the ion extraction between the extraction grid and the plasma grid, the SPIDER source is at -112kV potential with respect to the zero potential reference. This potential configuration leads to a specific isolating system design and to a specific design of the source electric and hydraulic service feedthroughs. An exploded view of the SPIDER beam source is given in Figure 1.15.

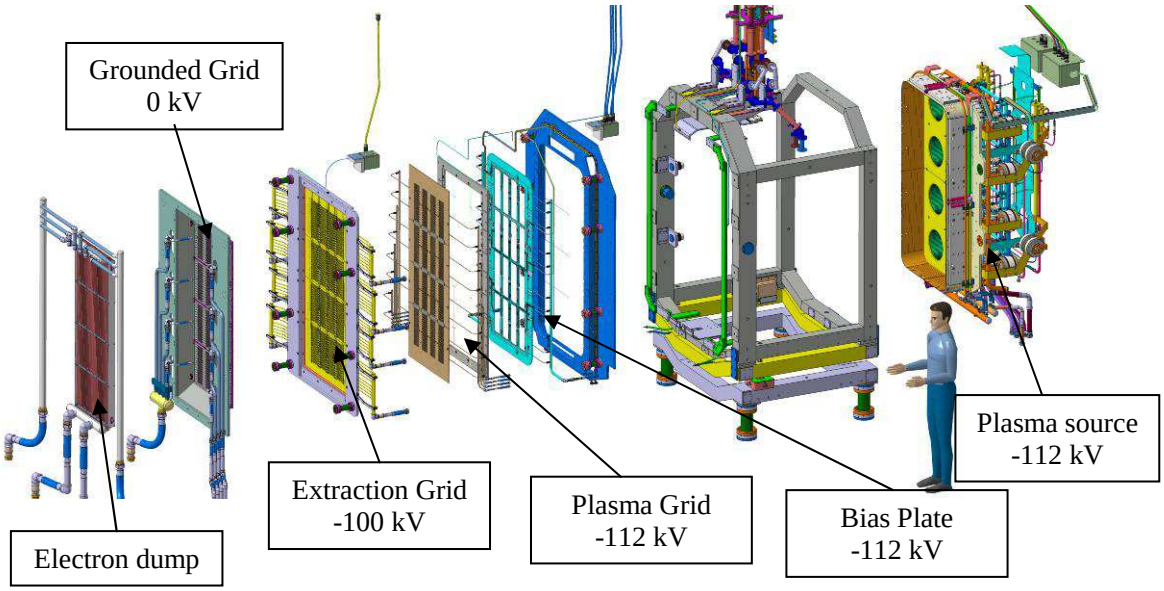

Figure 1.15 SPIDER Beam Source: exploded view.

Once they are extracted from the plasma source and accelerated out of the accelerator, electrons can be dangerous because, they are easily steered by magnetic fields (much more than ions because of the mass difference) so focusing and hitting other components depositing large power and huge energy flux. This happens because electrons are negatively charged and thus they feel the electric field in the same way as negative ions. Consequently, their extraction is

unavoidable (the electron to deuterium ion extraction ratio is required to be kept <1) and co-extracted electrons are one of the major sources of heat loads on the Extraction Grid; suitable magnets are in fact embedded in the Extraction Grid itself with the specific purpose of deflecting and collecting the co-extracted electrons. The other main source of thermal loads on the grids is given by impinging electrons created by stripping. The electrons that exit from the Grounded Grid are collected on the Electron Dump to prevent them from hitting downstream components or the vacuum vessel.

Since the grids are loaded by very high and localized heating power, they feature many cooling channels inside the grids themselves. This guarantees the proper cooling of the components that otherwise could not survive in a steady state regime, as that required for the ITER NBIs. Magnets to steer the electrons, before they are fully accelerated, are also embedded in dedicated grooves into the grids. A detailed view of the grids and of their features is given in Figure 1.16.

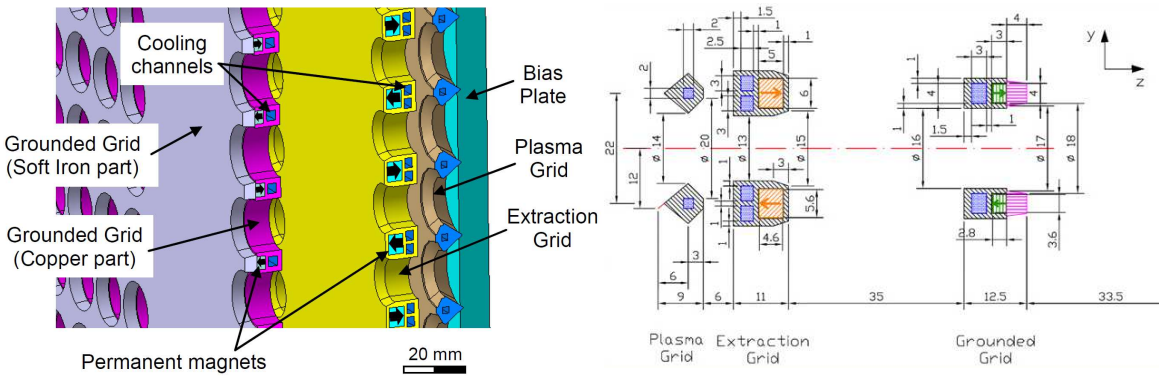

Figure 1.16 SPIDER grid system.

2 The Diagnostic Calorimeter for SPIDER

The primary scope of the diagnostic calorimeter is to verify whether the SPIDER beam meets the ITER requirement about the maximum allowed beam non-uniformity (below ±10%). STRIKE is made of 16 tiles to reproduce the source geometry (Figure 1.10). It is observed on the rear side by thermal cameras. When STRIKE panels are opened, SPIDER can operate with long beam pulses; if the panels are closed, STRIKE can perform measurements and SPIDER operates with short beam pulses. If STRIKE is in use, it can be in the backward position (nearer the beam source) or in the forward position (farther from the beam source): the comparison of the thermal patterns in these two positions allows the assessment of the beam divergence, a complementary measurement. Another complementary measurement is the estimation of the beam current, which requires biasing of STRIKE tiles, and can provide, by comparison with the 2D thermal pattern, an estimation of the stripping losses inside SPIDER.

The operation of the calorimeter will take place in a particular environment in which several interactions with the beam can occur. The results of these interactions are very important to define some design characteristics of the diagnostic calorimeter, which has to perform measurements notwithstanding the disturbances encountered in SPIDER due to the presence of a particle beam.

2.1 Physical phenomena due to beam-plasma and beam-surface interaction

The present section describes some physical phenomena which must be considered while interpreting the measurements performed by STRIKE. A distinction is made between the phenomena taking place because of the interaction of the beam with the background gas and the phenomena due to the interaction of the beam with material surfaces. These phenomena can affect the measurements performed by STRIKE.

2.1.1 Interaction between beam and background gas

In the following a brief description is given concerning some physical phenomena occurring during the interaction between the beam and the background gas, with the consequent generation of secondary particles.

2.1.1.1 Plasma formation and emission of line radiation

Ionisation of the background gas creates positive ions and electrons, which are in the field of the beam space charge. In the case of negative ion beams, positive ions are trapped inside the beam, whereas electrons are expelled.

Positive and negative ions result in the formation of plasma, all along the beam path. Consequently, any electrode, biased with respect to ground and exposed to this plasma, will draw a current. Furthermore a contribution is also to be expected by the aforementioned electrons.

The interaction of the beam with the background gas is also responsible for the emission of line radiation, particularly by hydrogen (H_α) [27] and by other species. Such radiation is partially in the red wavelength range, so that it may affect the observation of hot surfaces by thermal cameras.

2.1.1.2 Space charge compensation

Space charge compensation proceeds via the ionisation of the background gas. In the drift region, where the electric field of the electrodes is negligible, the production of secondary particles through the ionisation of the background gas results in the accumulation of space charge and in the consequent creation of a plasma shielding the self induced potential of the beam [28].

This phenomenon, known as space charge compensation (SCC) is a typical issue in accelerator physics, and it allows the transport of the beam for long distances with an acceptable divergence as it leads to the reduction of space charge repulsion inside the beamlets.

2.1.2 Interaction between beam and surfaces

In the following a brief description is given of the main physical phenomena occurring when a high power particle beam impinges on a material surface. These phenomena take place as impinging particles transfer momentum to the lattice particles and deposit heat on the material surface.

2.1.2.1 Transfer of momentum (current measurement, particle backscattering, secondary electron emission, sputtering)

Since the SPIDER beam is mainly composed of charged particles, their collection corresponds to the measurement of a current. Such current measurement is affected by the presence of free charges, like the plasma particles in front of STRIKE generated by ionisation of the background gas. The contribution of this current must be subtracted from the total current to obtain the beam current.

As particles hit a material surface they can be backscattered or produce secondary electron emission. In the energy range of particles produced by the SPIDER accelerator (100keV), the particle reflection coefficient for hydrogen is below 1‰ [29] (with a small dependence on the solid material), so that this phenomenon is not expected to affect STRIKE current measurements, though most of the reflected particles would be ions. Backscattered particles

provide also a negligible contribution to the energy deposited on STRIKE surfaces, since the energy reflection coefficient is well below 1‰ in the same conditions [29]. Impact of ions and neutrals on material surfaces induces the emission of secondary electrons [30]; particularly, when the impinging energy is high, kinetic emission occurs, which corresponds to momentum transfer between the impinging particles and the lattice electrons. The coefficient of secondary emission depends on the projectile-target pair; e.g. for 100keV hydrogen impinging on graphite it is 2.55. Such electrons have an energy distribution function which is peaked around 2-4eV [31]. As the secondary electron emission coefficient can be so high, it affects the results when measuring the beam current; consequently its contribution must be considered or suitable expedients to reduce the impact of secondary electrons on the current measurements must be adopted. Physical sputtering is the transfer of projectile momentum to the target atoms, leading to atom displacements and possibly also to ejection of surface atoms if a sufficient kinetic energy has been overcome [32]. Hence physical sputtering yields erosion of the STRIKE panels and must be taken into account (1μm/year) in the choice of the material for STRIKE panels. Furthermore, chemical sputtering can occur if the implanted atom can react with the lattice atoms; for instance in the case of hydrogen impinging over graphite, hydrocarbons can be emitted (corresponding to 47μm/year of eroded thickness) [33].

2.1.2.2 Thermal power deposition (heating, sublimation, radiation enhanced sublimation)

The particles impinging on STRIKE panels will produce heating of the surface. Since the energy flux can locally reach 20 MW/m^2 such heating produces quite rapidly a high temperature. Though detection of the thermal pattern of the beam is the basic working principle of STRIKE, the STRIKE panel material must be capable of supporting some seconds of exposure to the beam, so that the latter can be studied after reaching steady-state conditions. Moreover, heating is expected to be localised at the beamlets, so that thermo-mechanical stresses can occur in the bulk of the material [34].

At high surface temperature, STRIKE panels will lose mass by sublimation [35]. Moreover, when the temperature passes a threshold, it is found that the sputtering coefficient rises and radiation enhanced sublimation sets in [36]; altogether this results in an increase of the loss of mass from STRIKE panels. However, all these aspects are relevant if STRIKE will be exposed to the beam for a long time. It must also be considered that when the particle flux is high, the radiation enhanced sublimation coefficient seems to decrease [37].

Particles eroded from STRIKE panels via these processes and by sputtering can deposit over any surface inside the SPIDER vacuum vessel, modifying the superficial properties, e.g. in

terms of optical reflectivity and electrical conductivity. So in the choice of the material for the STRIKE panels also this aspect must be considered.

When the beam impinges on the STRIKE panels the resulting thermal pattern is tightly related to the local deposition of energy. If materials are chosen in such a way that the thermal pattern is preserved until it is measured, beam properties can be investigated on the beamlet space scale. Exploiting the emission of radiation in the infrared range, thermal cameras can provide a conversion of the recorded data of emitted radiation into a temperature map, provided that the proper coefficient of emissivity is used; the thermal image provides information about the beam features.

2.2 Conceptual design of STRIKE

From the phenomena discussed in the previous sections, some prescriptions can be derived for the design of the diagnostic calorimeter STRIKE.

Due to the radiating layer originated in front of the calorimeter, the observation of the calorimeter by thermal cameras will be performed on the rear side. This in turn requires the use of a material with very anisotropic thermal properties (thermal conductivity), so that heat is quickly transferred from the front to the rear side, while the thermal pattern is not too distorted due to conduction of heat parallel to the tile surface.

STRIKE is made of 16 CFC tiles, to reproduce the beam source geometry. The overall size of STRIKE is to be designed so as to collect also the stray particles.

Due to the anisotropic properties of the material, thermalisation of the tiles requires a long time; moreover, both the front and the rear sides of the tiles must not be hampered by the presence of objects (either obstructing the beam or the observation of the tile). This has two consequences: active cooling of the tiles cannot be provided and cooling takes place in between the beam discharges, by radiation and conduction of heat towards the supporting structures; a material must be used having a very high operating temperature: graphite or carbon-fibre-carbon composites are acceptable candidates.

Tile biasing is foreseen to avoid or at least to reduce the effect of secondary electrons on the measurement of current uniformity of the beam. Hence the tiles will be electrically insulated.

Two measurement positions, along the axial direction, are required for the assessment of the beam divergence. Another position, the open position, is foreseen for the calorimeter to permit the long operation of SPIDER. No active cooling is foreseen for STRIKE.

2.3 Starting point of the PhD work

During my graduate thesis, the feasibility study of STRIKE was investigated and a preliminary design was completed .The design of the calorimeter STRIKE at the end of 2009 consisted in two panels forming a V-shape to decrease the power density at the calorimeter surface (Figure 2.1). The panels can be closed, to perform measurements on the beam, and opened, to move them off the beam to permit the long source operation. No cooling system was adopted so a proper material was selected for the calorimeter tiles that are the sensitive elements of this diagnostic.

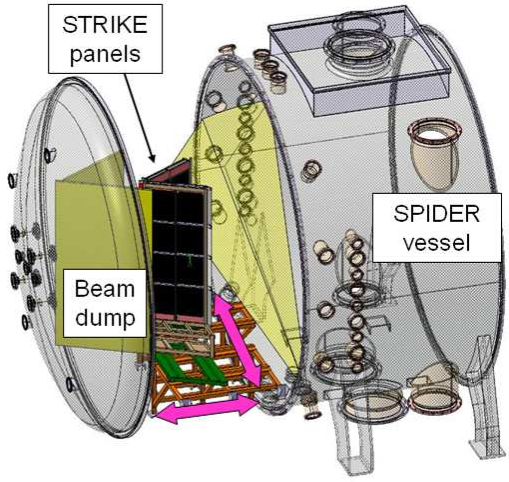

Figure 2.1: 2009 STRIKE design.

Transient non-linear thermal analyses (including radiation in some cases) were performed to investigate the behaviour of materials and the thermal response of the stainless steel frame. Electrostatic analyses allowed to choose a polarization value to avoid the effect of secondary electrons. From simulation results the requirements about the calorimeter were deduced: one-dimensional CFC (Carbon Fibre Carbon composite) as the reference material, angled position, observation at the rear side, no active cooling, two axial distances, two positions (open/closed), electrically insulated tiles, 10 s pulse duration and 1200 s in between the pulses.

Figure 2.2: CFC: the fibres are arranged along the thickness.

2.4 Requirements and Interfaces

The SPIDER beam is composed by 1280 beamlets. Beamlets are assumed to exhibit a Gauss curve profile in two dimensions (eq. 2.1) with a width given by a 3 mm intrinsic width (that is at the end of the accelerator) and a contribution due to a specified divergence δ = 3 mrad (see eq. 2.2); so, in a generic position in the plane (x,y) perpendicular to the beam, the amplitude, G_g, of the energy flux associated to each beamlet is represented as follows:

$$G_g(x,y) = A_g\left(-\frac{(x-x_{0g})^2}{2\sigma^2_{xg}} - \frac{(y-y_{0g})^2}{2\sigma_{yg}^2}\right) \qquad \text{eq. 2.1}$$

where σ_{xg} and σ_{yg} are respectively the beamlet half-widths in the x and y directions and A_g is the amplitude of the beamlet energy flux at the maximum position (x_{0g},y_{0g}). One of the scopes of STRIKE is the measurement of the beamlet divergence. Given the previous representation of the energy flux associated to the beamlets, in each direction, the beamlet width can be written as the superposition of an intrinsic width, σ_{0g} (which is assumed = 3 mm in the computations) and the increase of the beamlet width due to the angular aperture of the beamlet as a function of the distance along z from the end of the accelerator (divergence), as indicated in eq. 2:

$$\sigma_g = \sigma_{0g} + \delta z \qquad \text{eq. 2.2}$$

A deflection angle can also be defined with respect to the required beamlet direction. A sketch of the beamlet parameters is given in Figure 2.3.

The scope of STRIKE is to characterise the beam features, in particular to verify that the beam uniformity is better than 90% as prescribed by ITER; so STRIKE shall directly intercept the whole beam. The heat flux and the current associated to the whole beam shall be measured; the uniformity of the current of the beam will be assessed on the scale of the beamlet groups. The heat flux will be measured by thermal cameras, providing a finer spatial resolution for the beam uniformity measurement; possibly the divergence of the beam and of the beamlets will be measured. Not to perturb the thermal pattern, it is important that the calorimeter is aligned with the SPIDER beam source: STRIKE positioning systems will permit to control the axial (z axis) and vertical (y axis) positions and the beam incidence angle of the panels. Considering the expected temperatures the beam pulse duration will be shorter than 10s in order to limit the maximum tile temperature. In long beam pulses, STRIKE can not operate.

Due to plasma formed between the GG and STRIKE that acts as a conducting path, transient suppressors will be installed to protect STRIKE insulations against electrical breakdown events occurring inside the accelerator.

To study the beamlet divergence, STRIKE will be positioned at two different distances: about 1m and 0.5m from the GG.

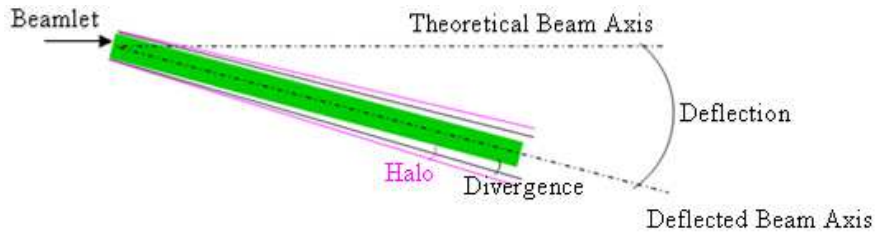

Figure 2.3: Beamlet description.

The presence of STRIKE represents a physical obstacle, which might block the lines-of-sight of optical diagnostics like BES, Tomography and inspection of in-vessel components. So when STRIKE is not in use the panels must be opened.

A detailed list of STRIKE requirements, subdivided into categories, is given in the following [38].

Diagnostic requirements

1. STRIKE shall directly intercept the whole beam (Figure 1.10 and Figure 2.3), in order to characterise its features and shall withstand the whole heat flux associated to the beam, for a pulse duration up to several seconds at maximum beam power.

2. ITER prescribes that the heat flux uniformity of the beam shall be within 10%; for the purpose of the present work, uniformity is defined as in [39]; STRIKE shall be able to assess whether the beam uniformity lies within the prescribed range.

3. STRIKE shall measure the current associated to the whole beam as well as the uniformity of the current of the beam on the scale of the beamlet groups.

4. Consequently STRIKE shall be subdivided into 4x4=16 tiles, corresponding to the distribution of the beamlets into beamlet groups. The tiles shall be electrically insulated from each other and from the supporting structure.

5. The tiles and the kerbs (section 3.1) shall be equipped with transient suppressors, to provide a low-impedance path to the current in the case of breakdowns in the accelerator; the voltage rating of the suppressors is 500V.

6. STRIKE shall measure the divergence of the beam and beamlets.

Mechanical requirements

7. The system composed of tiles and kerbs shall have a sufficient size so as to collect the whole beam.

8. STRIKE shall operate inside the SPIDER vessel so it has be vacuum compatible.

9. The calorimeter shall operate in two different configurations: “open”, where the beam shall not be intercepted by STRIKE; “closed”, where the entire beam power shall be intercepted by STRIKE.

10. Two axial positions shall be designed for beam divergence measurement; the ratio between the axial distances of STRIKE from the GG shall be greater than 2 (1m and 0.5m are first tentative values). Axial positioning accuracy: ±5 mm, to limit the variation of the beamlet pattern below ±5‰.

11. Exposure angle accuracy: the beam facing surfaces of the tiles of each panel shall lie within two parallel vertical planes spaced by 10mm.

12. The tile thickness shall be 20±0.1mm.

13. The maximum expected temperature of panel elements is 2800K in front (beam facing surface) and 1900K on the back side, in the case of CFC [40].

14. Handling and maintenance of STRIKE shall be carried out with the Vessel front lid in open position, (considering 1m distance between the closed front lid and the bio-shield wall.

15. Number of moving cycles: 1000 aperture/closure cycles and 1000 forward/backward cycles in vacuum; during operation the latter will be more frequent than the former.

16. Expected number and characteristics of beam pulses: pulse duration 10s, time between pulses 1200s, beam power 5MW, Gaussian shaped heat flux with peak value of 20MW/m^2 [41].

Requirements of the diagnostic dedicated to STRIKE

Several diagnostic systems are dedicated to STRIKE to characterise the SPIDER beam.

Hereafter the Requirements of the STRIKE Diagnostic systems are given:

17. IR cameras shall measure the 2D temperature map of the entire beam cross section, with a spatial resolution ≤2 mm[I] and a frame rate ≥25 frames/s [II]. IR cameras shall have an operating

[I] See section 6.6.
[II] To follow possible variations of the beam features compatibly with the global memory occupation and the characteristics of present-day thermal cameras.

range of 20-2000°C, with an absolute accuracy ≤2% above 100°C. Signals from IR cameras shall be suitable to be integrated in the SPIDER central control and data acquisition system.

18. The tiles shall be instrumented with 2 thermocouples each, arranged so as to measure the extreme values of the temperature profile for IR camera calibration. Two tiles per panel can be instrumented with 10 thermocouples each, arranged so as to reconstruct the temperature profile [42]. Each kerb (see section 3.1) element shall be equipped with one thermocouple, to monitor its temperature during the operation and to help in assessing the halo contribution, particularly in the case of large beam deflection. Each strip (see section 3.1) shall be equipped with one thermocouple, to monitor its temperature during the operation and to help in assessing the halo contribution, particularly in the case of large beam deflection.

19. The current flowing into each tile shall be measured to assess that non-uniformity is within 10%. The current meters shall be able to measure a current up to 5A, with 1kHz bandwidth, 12 bit resolution; the current meter shall be insulated at least up to 500V with respect to the tiles. The current flowing through each kerb element shall be measured, to help in assessing the halo contribution, particularly in the case of large beam deflection. The current meters shall be able to measure a current up to 0.5A, with 1kHz bandwidth, 12 bit resolution and shall be insulated at least up to 500V with respect to the tiles. The total current flowing through the strips of each panel shall be measured, to help in assessing the halo contribution, particularly in the case of large beam deflection. The current meters shall be able to measure a current up to 8A, with 1kHz bandwidth, 12 bit resolution; the current meter shall be insulated at least up to 500V with respect to the tiles.

20. To characterise the plasma in front of STRIKE, 2 electrostatic probes shall be installed in each panel.

Requirements of the power supplies dedicated to STRIKE

In order to prevent secondary electrons from escaping the tile surface, a voltage is applied to the tiles with respect to the vacuum vessel. Such biasing is provided by 2 suitable power supplies, whose ratings are:

21. output voltage: 500V.

22. total output current: 80A.

STRIKE interface requirements

The interfaces between STRIKE and the surrounding environment are described herein; the requirements of such interfaces are also presented.

STRIKE interfaces

Figure 2.4 gives an overview of the components having an interface relationship with STRIKE.

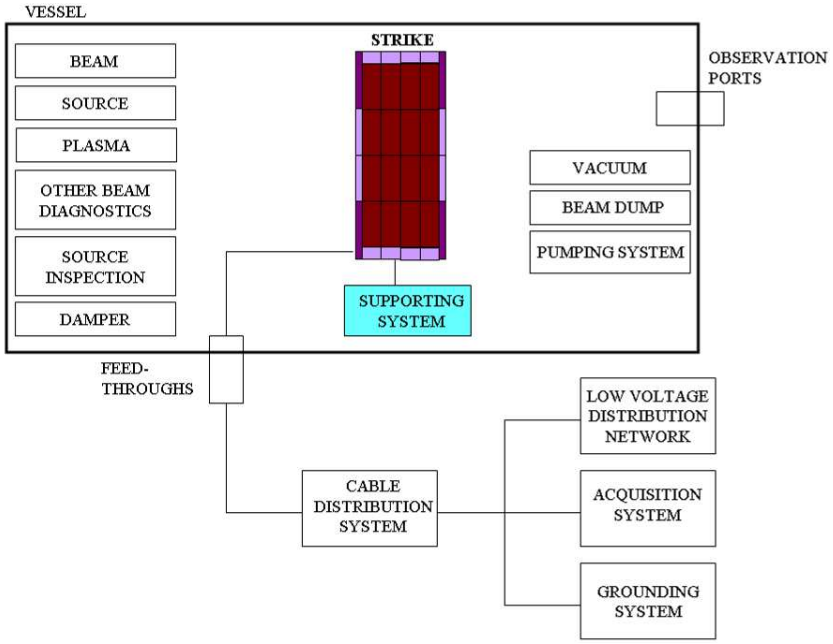

Figure 2.4: Schematic of the SPIDER components, which are interfaced with STRIKE.

Definition of interfaces

STRIKE has the following types of interfaces (Table 2.1):

- Mechanical (M), consisting in a physical connection between STRIKE and another component and/or the necessity of respecting the overall dimensions of STRIKE and of another component;
- Electrical (E), consisting in prescriptions concerning voltages and/or currents;
- Optical (O), consisting in blocking lines-of-sight;
- Particles (P), consisting in interactions with or mediated by ionised and neutral particles;
- Radiation (R), consisting in interactions due to neutrons, X-rays and infra-red radiation.

INTERFACE	M	E	O	P	R
COMPONENTS	beam dump	vessel	other beam diagnostics	beam	source
	vessel	cable distribution system	source	plasma	beam dump
	cable distribution system	grounding system	beam dump	vacuum	pumping system
	grounding system	acquisition system	vessel		vessel
		low voltage distribution network			dampers

Table 2.1: SPIDER components sorted as functions of the type of interfaces with STRIKE.

Interface with the beam:

Interface with the Beam is a Particles type interface: STRIKE is directly hit by the beam particles (negative and positive ions, neutrals, electrons) when it is in the closed position; this way the beam properties are measured, which is the aim of STRIKE; the beam particles produce the emission of secondary electrons from the STRIKE surface.

23. A suitable bias (<500V) with respect to the vessel shall be applied to STRIKE tiles to attract the secondary electrons back to the tile surface.

24. In the open position, STRIKE shall not intercept any fraction of the beam.

Interface with the plasma:

Interface with the Plasma corresponds to Particles type interface. Between the GG and STRIKE a plasma is formed by the interaction of the beam particles with the background gas. Such a plasma electrically connects the GG to the STRIKE tiles; this can modify the tile potential in correspondence to the electrical breakdown events occurring inside the accelerator, when the GG potential reaches some tens of kV with respect to ground (the vessel).

25. Suitable devices shall be adopted to preserve STRIKE insulations, power supplies, and signal front-ends.

Interface with beam diagnostic:

Interfaces with Beam Diagnostics is an Optical type interface: the presence of STRIKE represents a physical obstacle, which might block the lines-of-sight of optical diagnostics, both in the closed and open positions of STRIKE:

26. STRIKE shall preserve a suitable volume for beam Tomography, except when STRIKE is in its closed position at ~0.5m from the beam source; such respect volume is bounded by two sets of fans of lines-of-sight (magenta lines in Figure 2.5) tilted by 90° and 75° with respect to

the beam, starting from the portholes located on the tomography section placed close to the beam origin and ending where the lines-of-sight exit the beam. The reason is to allow the lines-of-sight to run unintercepted across the whole beam in order to characterise it.

27. No hot STRIKE surface (specifically, with surface temperature greater than 900K) shall intercept the lines-of-sight of Tomography: thermal radiation from surfaces at temperature greater than 900K affects the wavelength range relevant for the tomographic diagnostic (CCD detectors for H_α or D_α radiation).

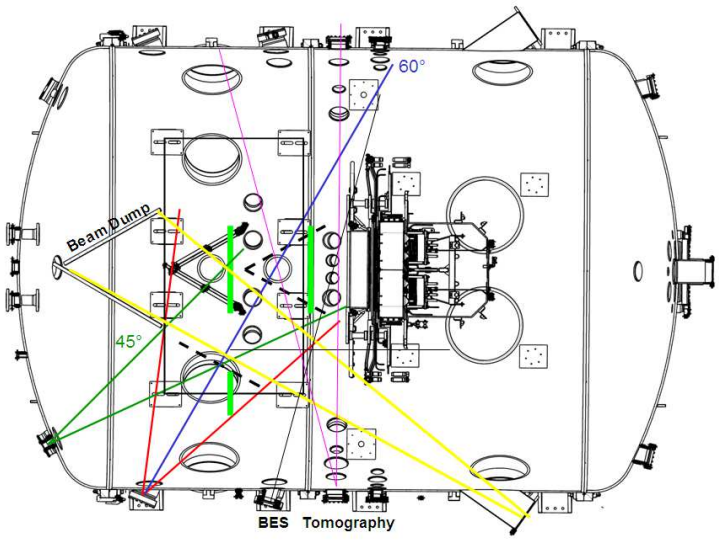

Figure 2.5: Top view of SPIDER vessel highlighting the port-holes dedicated to some diagnostics: the red lines define the view cone for STRIKE observation (in the case STRIKE is exposed to 60°); the green lines bound the cone of view for BES and for source inspection; the yellow lines delimit the view cone for beam dump inspection; the black line indicates the direction of the lines-of-sight of BES; the magenta lines bound the area reserved for beam tomography.

28. STRIKE shall not intercept the lines-of-sight of Beam Emission Spectroscopy (BES, see Figure 2.5, Figure 2.6 and Figure 2.7) from their starting point at the port hole until they have crossed the whole beam; this constraint shall be satisfied in all experimental conditions, except, but still, if possible, when the calorimeter is in the closed position at ~0.5m from the beam source. The reason is to allow the lines-of-sight to run through the whole beam in order to characterise it.

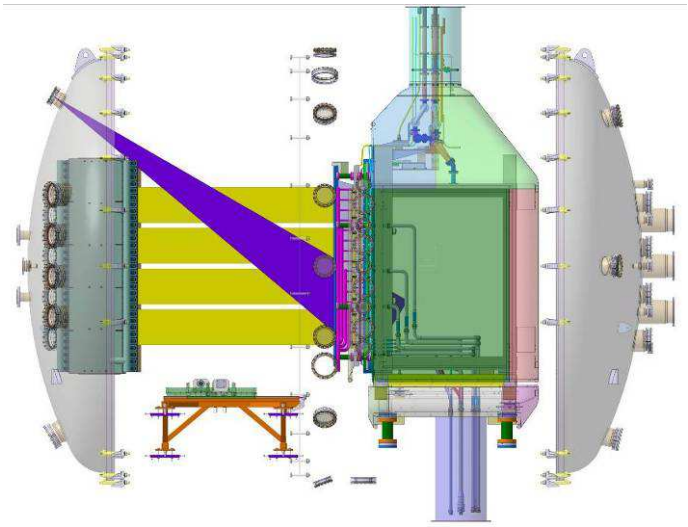

Figure 2.6: Lateral view of SPIDER vessel highlighting some of the port-holes dedicated to BES and to the observation of STRIKE with the IR cameras.

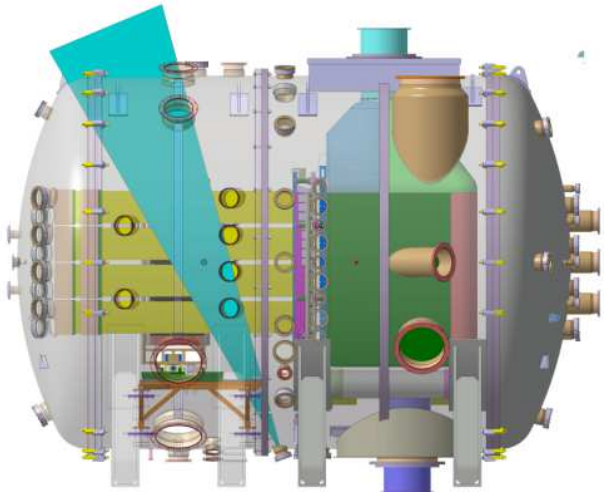

Figure 2.7: Lateral view of SPIDER vessel highlighting some of the port-holes dedicated to BES.

Interface with the Beam Source:

Interface with the Source is a Mechanical type of interface: in both measurement positions, the STRIKE tile surface shall be aligned with respect to the GG surface:

29. The minimum and the maximum distance from the GG of each of the two parallel vertical planes referenced in requirement 15 shall not differ by more than 10mm.

Interface with the Source; type Radiation: during short operation, STRIKE reaches high temperature (2800K) and radiated flux is not negligible in this case. STRIKE radiates toward the source.

Interface with the Source Inspection System

This is an Optical type interface: the presence of STRIKE represents a physical obstacle, which might block the lines-of-sight of the cameras dedicated to the observation of the GG, both in the closed and open positions of STRIKE:

30. STRIKE in the open position shall not obscure the viewing ports for source inspection (Figure 2.8) to permit the check of the GG and ED.

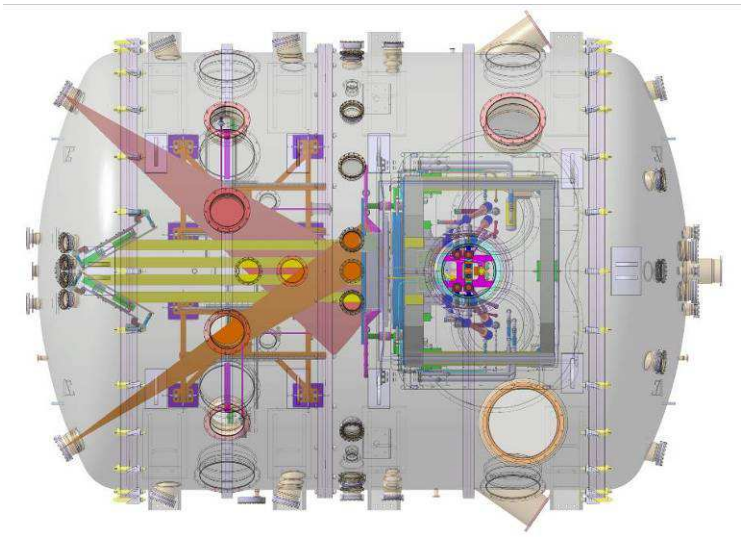

Figure 2.8: View of SPIDER vessel highlighting the port-holes dedicated to GG and ED inspection and to BES.

Interface with the Beam Dump:

Interface with the Beam Dump, Radiation type interface: STRIKE radiates toward the Beam Dump.

Interface with the Beam Dump; Mechanical and Optical types of interfaces: when STRIKE is in the close position (STRIKE is operating), the observation of the beam dump by means of the dedicated camera is blocked and the beam dump does not intercept the beam. In the open position, STRIKE shall not intercept any part of the beam, preventing it from reaching the beam dump with the risk of overheating of the exposed STRIKE tiles; STRIKE shall also not obstruct the observation of part of the beam dump panels. STRIKE and its supporting structure might have an impact on the beam dump and its overall dimensions and vice versa.

31. STRIKE in the closed position shall accommodate the whole beam so that the Beam Dump is not directly hit by any fraction of the beam.

32. STRIKE in the open position shall not obscure the lines-of-sight for beam dump inspection (yellow line in Figure 2.5) to permit the check of the beam dump.

Interface with the Dampers:

Interface with the Dampers and the instrumentation installed on them is a Radiation type of interface: STRIKE radiates toward the Dampers dedicated to mitigate the effect of the breakdowns inside the accelerator.

Interface with the Vacuum:

Interface with the SPIDER Vacuum, Particles type interface:

33. STRIKE components shall be high-vacuum compliant. STRIKE tile outgassing might raise the pressure inside the vessel, thus changing the SPIDER operating conditions and emitting impurities. Moreover impurities will increase the radiation in front of STRIKE tiles.

Interface with the SPIDER Pumping System:

Interface with the SPIDER Pumping System; STRIKE radiates toward the cryo-pumps.

Interface with SPIDER Vessel:

Interface with the Vessel; type Radiation: STRIKE radiates toward the Vessel. Since the vessel external surface is surrounded by air, such heat load should not create any danger to the vessel.

Interface with SPIDER Vessel; types Mechanical, Electrical and Optical:

34. STRIKE shall fit inside SPIDER vessel, in any axial position and both open and closed.

35. SPIDER vessel shall support the STRIKE supporting and moving structure.

36. SPIDER vessel shall be provided with suitable brackets, which must allow sufficient alignment and positioning accuracies.

37. SPIDER vessel shall be provided with dedicated feed-throughs, located in dedicated flanges, for the extraction of several types of cables (for thermocouples, tile biasing, electrostatic sensors). The feed-through shall be insulated at 500V from the vessel and from each other.

38. SPIDER vessel shall be provided with dedicated portholes for the thermal cameras dedicated to the observation of STRIKE tiles.

Interface with the Cable Distribution System:

Types Mechanical and Electrical. Outside of SPIDER vessel and bioshield, STRIKE cables reach the electrical cabinet where data conditioning and acquisition is performed.

39. The cable runs must accommodate all STRIKE cables; the path and features of the cable runs must be suitable for preserving the signal integrity.

Interface with the Grounding System; types Mechanical and Electrical. The environment of SPIDER signals is prone to be affected by noise (e.g. due to the RF applied to the source; breakdown events in the accelerator …). Signal integrity must be preserved up to the acquisition modules.

40. The layout and the features of the PRIMA Grounding System must be suitable for preserving the integrity of STRIKE signals, both along the cables and in the cabinets.

Interface with the Acquisition System; type Electrical.

41. The acquisition system must be suitable for sampling and storing all STRIKE signals, including the storage of the panel positions.

Interface with the Low Voltage Distribution Network; type Electrical.

42. The low voltage distribution network must supply the necessary power for tile biasing signal conditioning, data acquisition, panel movement and dedicated services.

2.5 Alternative design

After an economic evaluation of the 2009 design, alternative solutions were considered to reduce the costs of the diagnostic. An attempt consisted in the use of different carbon fibre materials but this solution was not feasible due to larger complexity in the design and not so high cost reduction.

Another way considered a different geometry: the strong anisotropy of thermal conductivity, much higher in one direction, is a key characteristic for the STRIKE material to ensure the correct transfer of the thermal pattern from the front side to the rear of the calorimeter; an alternative design involves tiles made of graphite and the one-directional property, intrinsic for the 1D CFC, is guaranteed by a particular geometry of the tiles, made of several elements, and by the arrangement of these elements. The graphite elements will be placed side by side to form a 2D pattern of columns and with the slots all along the same direction, as shown in Figure 2.9.

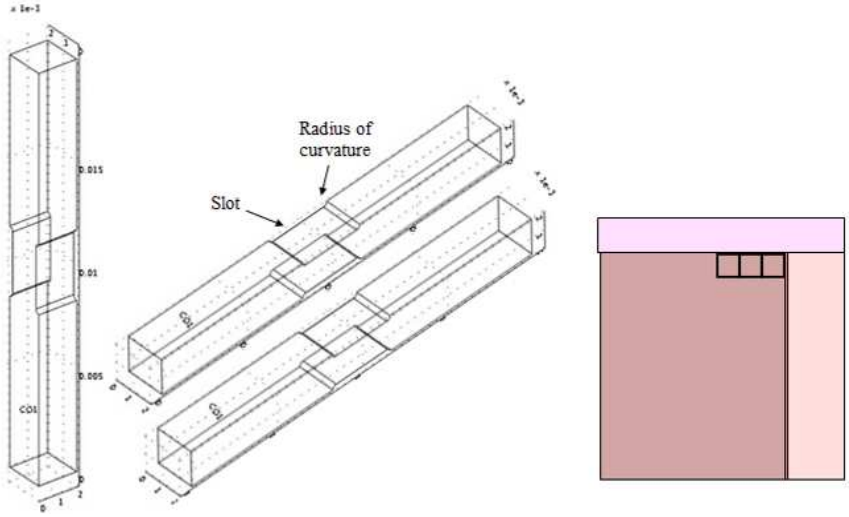

Figure 2.9: Single graphite elements (left hand side); example of assembly (central); arrangement of elements in the tile (right hand side).

Machining the central region of the elements allows to insert a bar to prevent the elements from moving along the beam direction. Such bar should be made of a material having thermal characteristics very different from graphite, like alumina. The lateral surfaces should be machined to realise an inefficient thermal contact between the neighbouring elements to avoid the heat dispersion in the direction transverse with respect to the beam direction.

This particular geometry introduces a structural discretisation of the thermal pattern of the beam at the tile. This effect has been investigated to evaluate the proper element size to guarantee the right reconstruction of the thermal pattern corresponding to a single beamlets spatial scale. The study has been performed by dividing the surface hit by the beam into squares and by computing the average of the energy flux over the single squares. Figure 2.10 shows an example of the heat load in a central area of the beamlet group, highlighting the rows of 5 beamlets, together with the discretisation in the 2D map introduced by $3\times3mm^2$ and $2\times2mm^2$ graphite elements.

The profile of the power density is shown along a line passing through the centre of the beamlets, compared with its spatial sampling with the $2\times2\ mm^2$ (Figure 2.11) and $3\times3\ mm^2$ (Figure 2.12) resolution and with the sampling along contiguous rows; the same indicated in Figure 2.10.

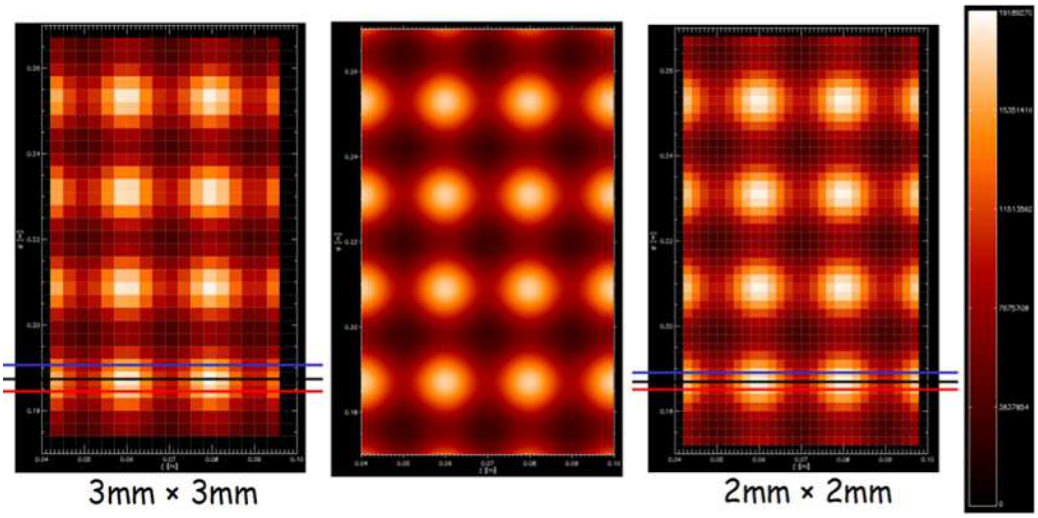

Figure 2.10: Beam energy flux impinging on a tile (central), compared with its spatial sampling with 3×3mm^2 resolution (left) and 2×2mm^2 resolution (right).

The agreement between the continuous line and the discretization results is good in both resampling conditions, but the less refined spatial resolution of the 3×3mm^2 leads to results differing more from the theoretical results and exhibiting larger asymmetry around the maximum, so a cross-section of 2×2mm^2 is preferable. Similar results have been obtained considering the vertical profiles.

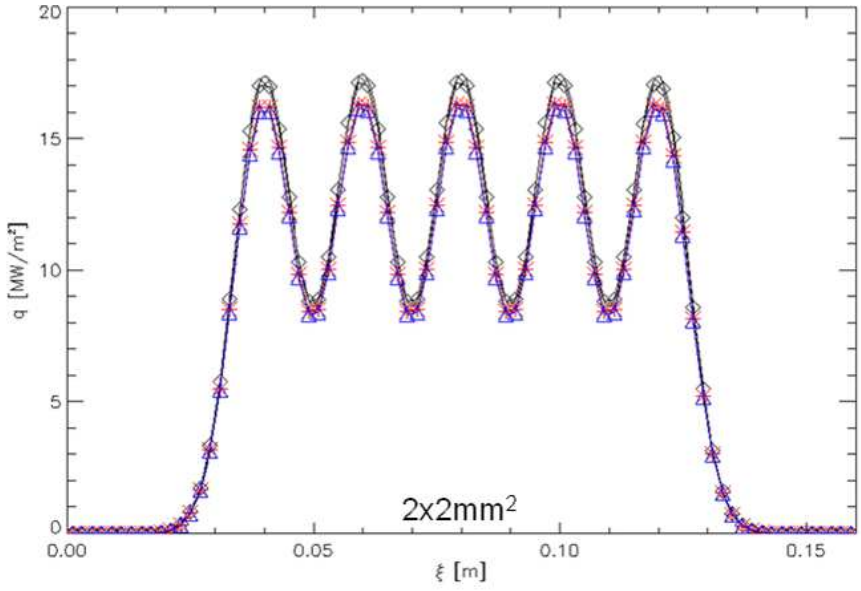

Figure 2.11: Power density profile along horizontal lines, 2×2 mm^2 discretisation.

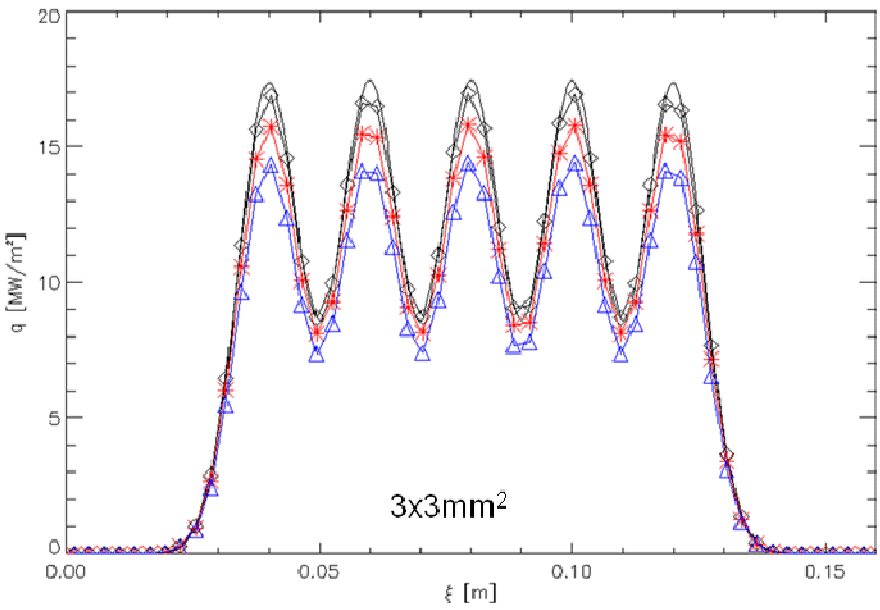

Figure 2.12: Power density profile along horizontal lines, 3×3 mm^2 discretisation.

A series of experiments has been carried out to test the thermal behaviour of the graphite elements assembly. Two custom made peek supports, one for 2x2 elements and the other one for the 3x3 elements, has been realised. The peek supports have the characteristics that they do not conduct heat towards other parts and minimize the contact between the elements and the same support. The tests have been carried out with different arrangement of the graphite elements: in some cases a spacer was inserted between the elements to investigate different thermal contact between the elements together with a different compression provided by the end element of the peek support, as shown in Figure 2.13. A shutter was used to deposit heat only over a single graphite element, to observe the thermal transfer from one element to the surrounding ones.

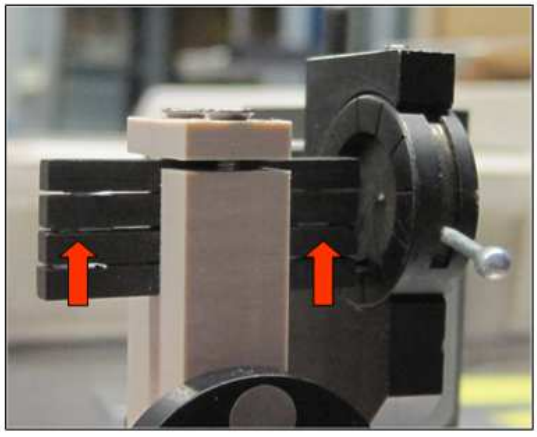

Figure 2.13: Set up using spacer between the elements and no compression.

The heat load consisted in a CO_2 laser (10.58µm wavelength) with 5.7W output power and duration of 5s, 10s or 15s. The laser beam is about 3mm diameter but after the shutter just before the graphite target it was reduced to 1.5mm and the laser power has been reduced to about 0.9W on the element. Figure 2.14 shows an example of the temperature profile at 10s laser application for 2x2 elements.

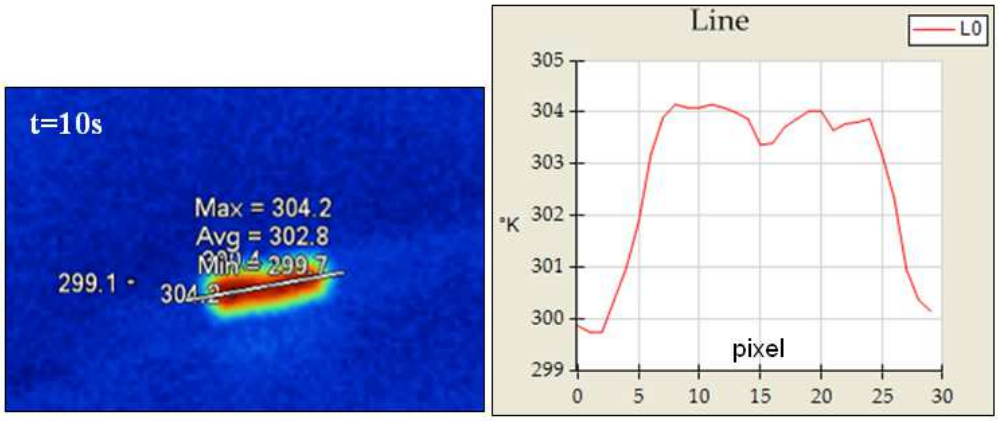

Figure 2.14: Temperature profile along the elements.

After the study of several combinations of the set-up, some results have been obtained:

- No appreciable difference is found in terms of heat transfer towards the surrounding elements.
- The smaller samples would provide a better spatial resolution on the final images.
- Heat transfer towards the neighbouring elements is only slightly affected by the compression of the graphite elements: only for short times a better thermal insulation is obtained in the absence of compression.
- By interposing paper pieces in between the graphite elements, thermal insulation improves: as long as the laser is on, the illuminated element exhibits a higher temperature. Heat is flowing towards the neighbouring elements, so that after 10s during the illumination the temperature profile is less peaked, the nearest neighbours display half the temperature increase of the illuminated element and this temperature ratio remains constant as long as the laser is on. The temperature, 10s after turning the laser off, shows a broad peak encompassing all four elements.

Some simulations were carried out to study the thermal behaviour of the element, to be compared to experimental results performed by heating by a laser. The study was carried out by varying the geometric parameters of the elements, for instance radius of curvature (see Figure 2.9) or the height of the slots (see Figure 2.9), and the load conditions. The heat flux is computed by dividing the power by the cross-section, so that the load is supposed to be

uniformly applied over the cross-section. The model is thermally insulated: no radiation and no convection are considered, only conduction through the sample. The starting temperature is 300K.

The numerical results of the case corresponding to the same heat flux of Figure 2.14 is shown in Figure 2.15: at the end of 5s pulse the maximum temperature on the front surface is 313K, and the minimum temperature on the rear surface is 308K. The steady state temperature at 500 seconds after heat load ends is 309K. This model considers only conduction inside the material.

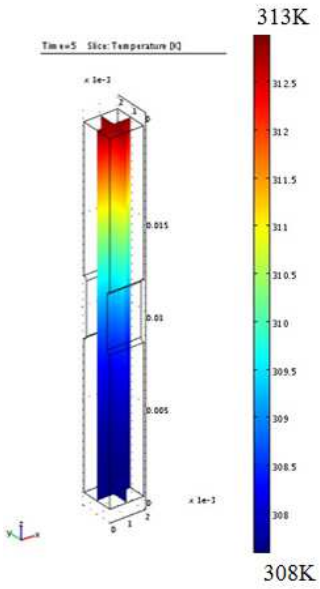

Figure 2.15: Temperature distribution inside a 2x2mm^2 element.

The realisation and assembly of such a system would be very complicated and would require huge manpower. Moreover a tile composed of thousands of independent graphite elements does not have the mechanical properties of a CFC tile. Finally, the discretization of the thermal pattern introduced also by the thermal camera has to be superimposed.

Consequently, the solution using one-dimensional CFC was preferred.

3 STRIKE Design

The design of the calorimeter has been developed with the support of thermal and electrostatic numerical simulations. In the following the results of this work, the final design, is described along with the solutions adopted for the integration of the diagnostics of the calorimeter. Moreover, the simulation results to evaluate the diagnostic capability of the system are also presented.

3.1 Final Design

In front of the calorimeter a radiative sheet, due to the interaction between the beam and the background gas, disturbs the frontal view by the thermal camera. Hence, the observation is performed at the rear side of the diagnostic and the tile material must maintain at the rear side a beamlet footprint as similar to the front one as possible. The STRIKE tile outgassing rate must be compatible with the SPIDER base vacuum (10^{-5} mbar [25]).

The material studied and adopted is a graphite composite: one-dimensional CFC (Carbon Fibre Composite). The 1-D property refers to the thermal conductivity: 1D-CFC has a high ratio between the thermal conductivity in the direction parallel to the beam and the thermal conductivities in the direction orthogonal to the beam (in-plane) [43]. Other important feature of the material is the maximum allowable superficial temperature. The calorimeter is directly exposed to the beam and it can withstand about 10s at SPIDER full power (about 5W). In these conditions STRIKE will operate without a cooling system.

The possible positions of STRIKE are represented simultaneously on the left hand side of Figure 3.1, far and near to the beam source intercepting the beam and in the open position to allow SPIDER long pulses. On the right hand side of Figure 3.1 STRIKE system can be seen together with the principal components.

STRIKE consists of two separated panels to permit a simple removal from the beam path when it is not in use. The front and rear sides of the panels are shown in Figure 3.2.

STRIKE is made of 16 CFC tiles, to reproduce the beam source geometry. Each tile is expected to receive one of the beamlet groups of the SPIDER beam (Figure 1.10).

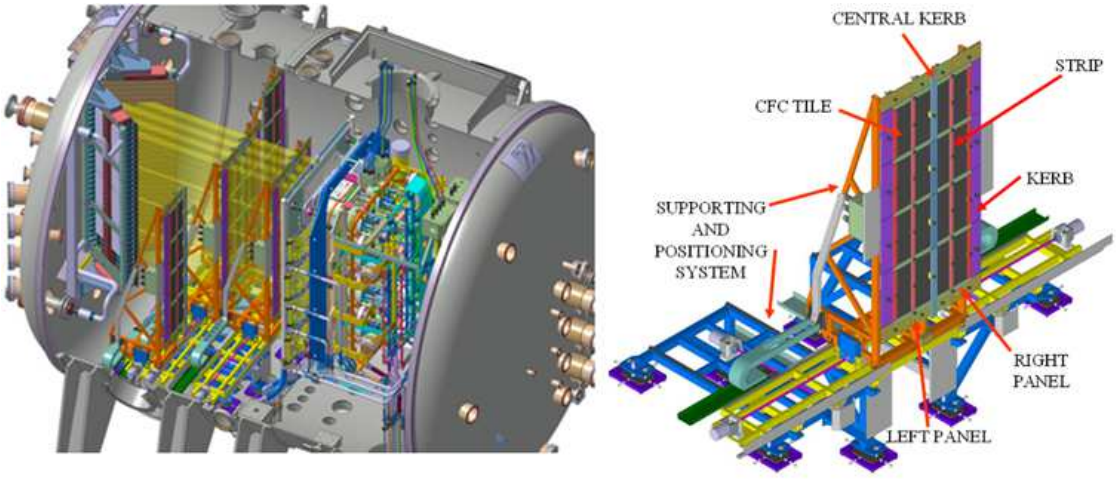

Figure 3.1: Positions of the STRIKE inside SPIDER; STRIKE system.

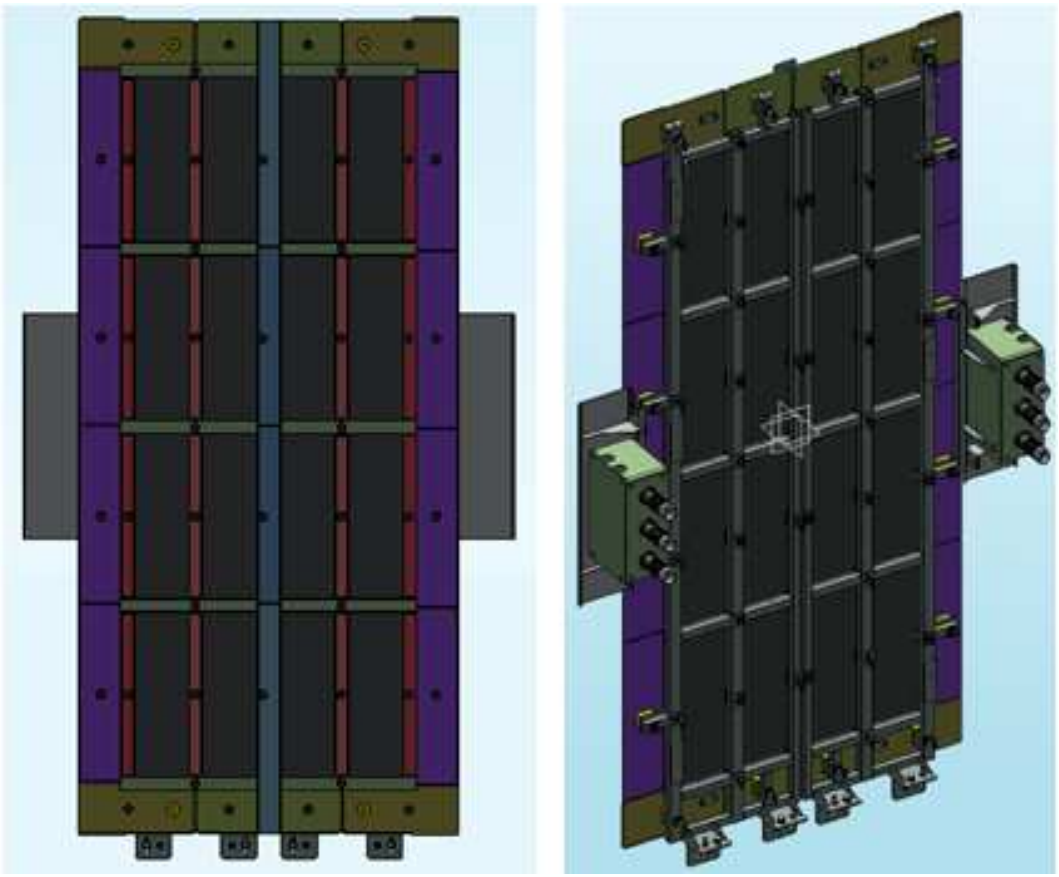

Figure 3.2: Front side and rear side of the calorimeter.

The exposure of the calorimeter is orthogonal with respect to the beam direction (Figure 3.1). Each of the tiles has dimensions of 160 x 398 mm^2. The overall size of STRIKE is about 1800 x 840 mm^2 so as to collect also the stray particles.

The main elements of the panels are the CFC tiles. They are surrounded by kerbs to collect the halo particles. In between the tiles, strips are used to occlude the gaps foreseen to permit the thermal expansion of the tiles and to protect the supporting frame, as shown in Figure 3.2.

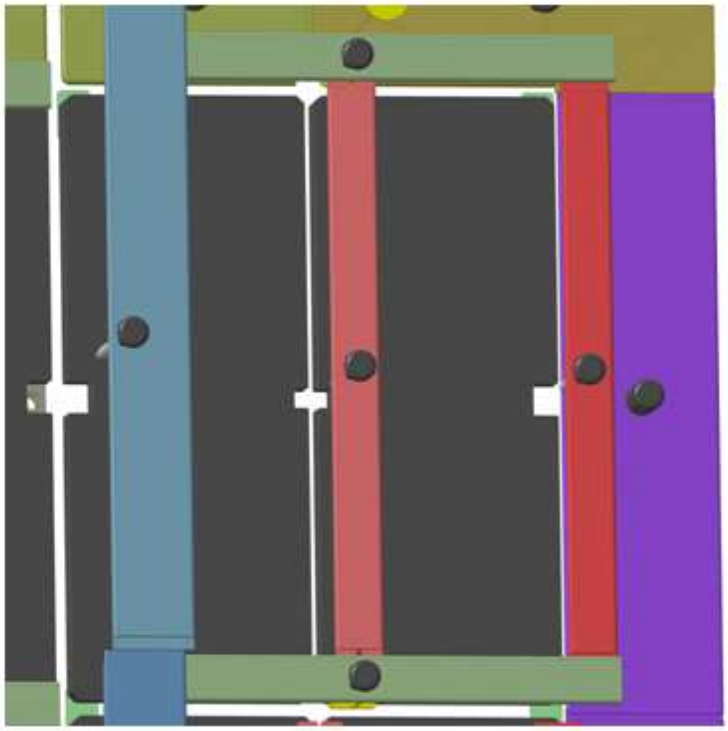

Figure 3.3: Gap in between the tiles; zoom.

To measure the current, the tiles (Figure 3.4) and the kerbs (Figure 3.6, right) are insulated with respect to the frame to avoid the direct contact of the AISI 304 L (frame material) with the CFC and graphite (tiles and kerbs material respectively). This insulation will be realised with Macor elements (in yellow in the following pictures) in order to prevent carbon migration to steel and chemical changes at the frames. Furthermore, the installation of Macor elements will electrically insulate each tile with respect to the frame, the strips, the kerbs and the other tiles (Figure 3.5 and Figure 3.6, left). Macor shape allows to realize a notch coupling with kerbs and strips so as to fix all elements guaranteeing electrical insulation at the same time.

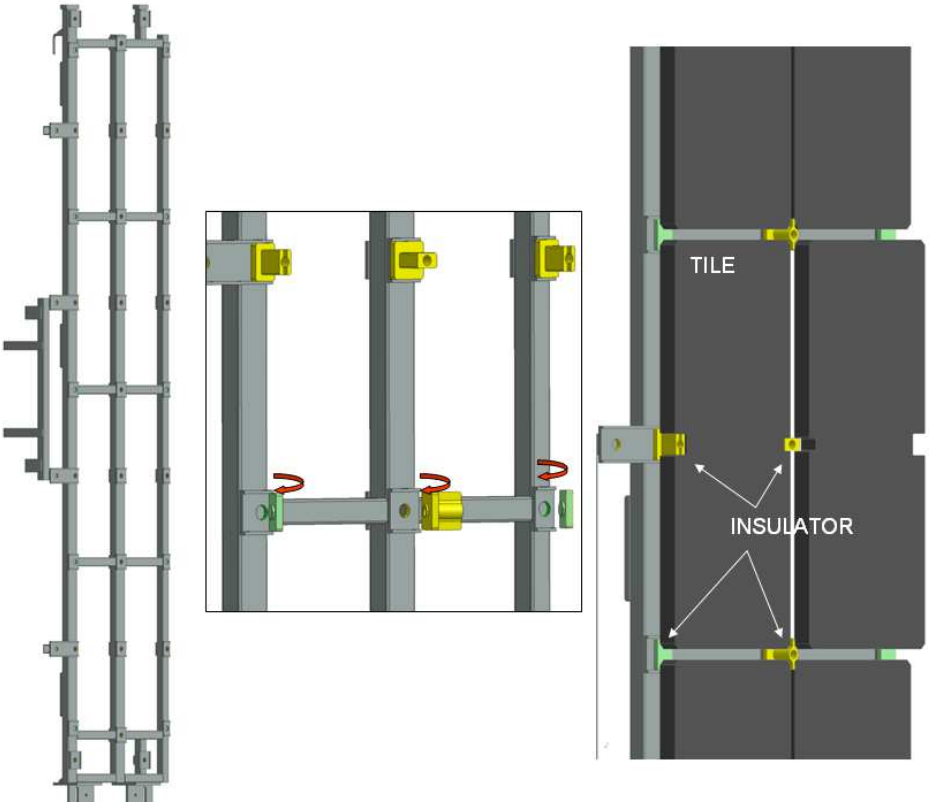

Figure 3.4: Frame (left), Macor elements (centre), tile assembly (right).

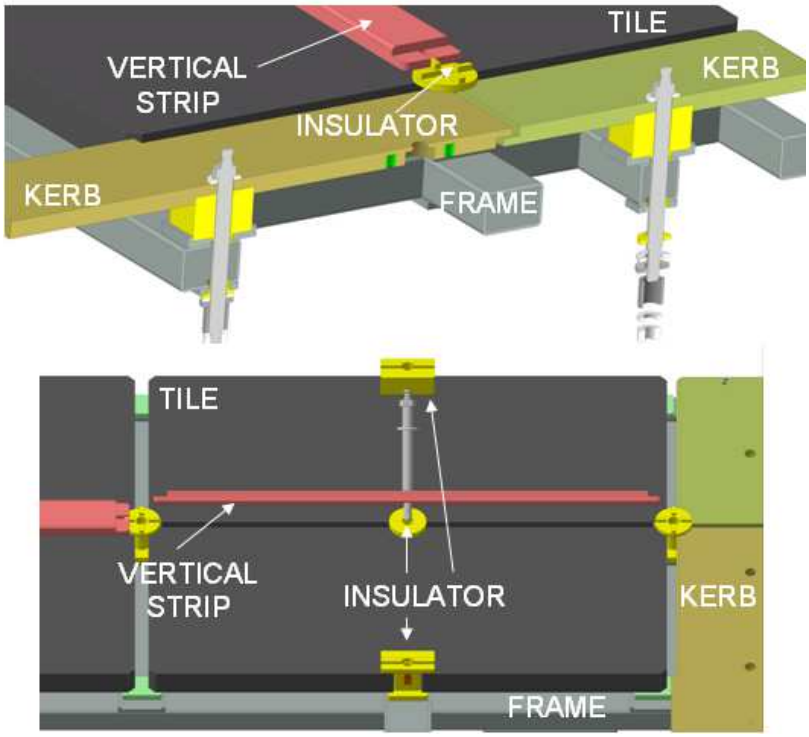

Figure 3.5: Vertical strips assembly.

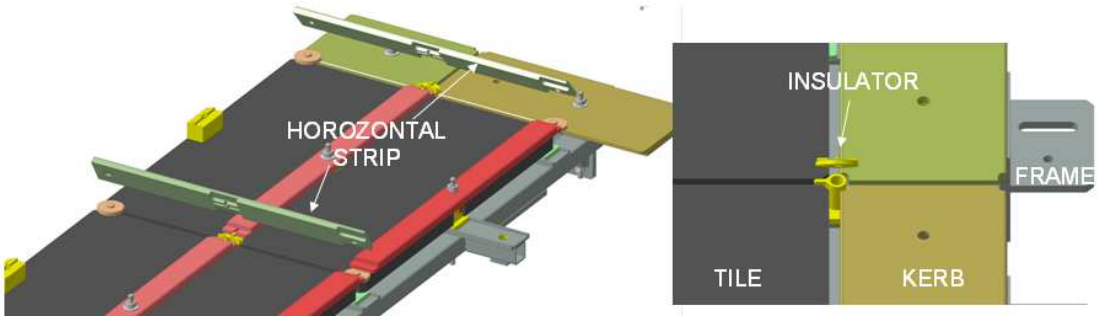

Figure 3.6: Horizontal (left) and kerb (right) assembly.

An example of the fixing system to the frame is shown in Figure 3.7.

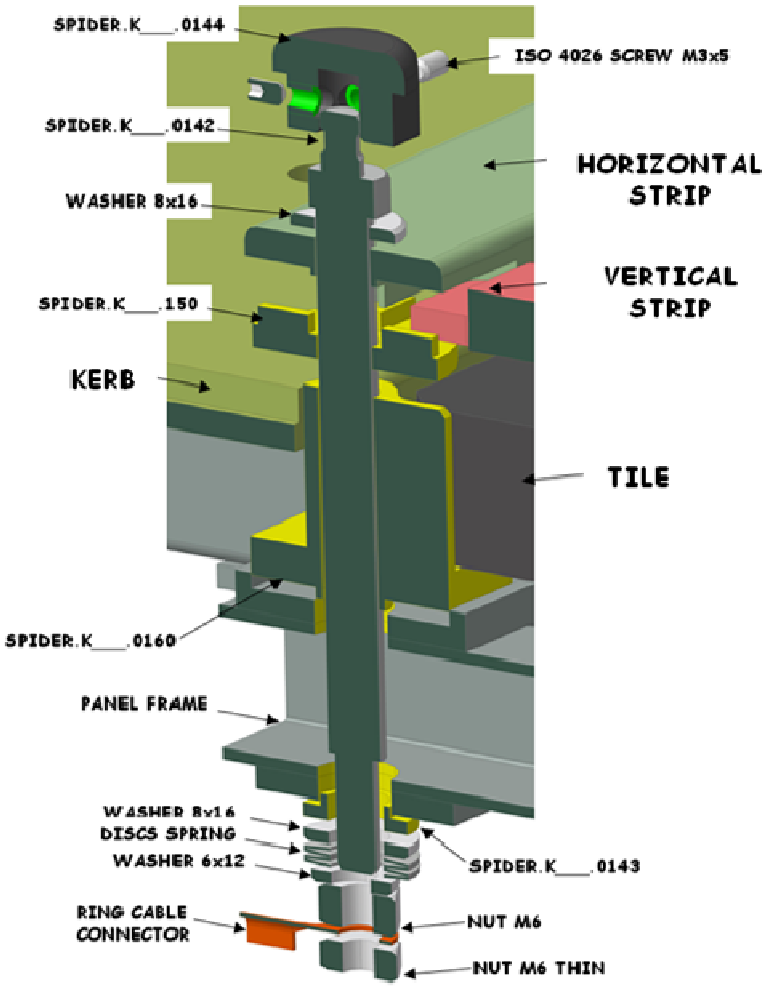

Figure 3.7: Kerb, strips and tile fixing system to the frame.

The fixing point is on the side of the tile, at half height, to reduce the risk of cracking due to thermal expansion (Figure 3.9, left hand side). Besides, this solution avoids drilling holes in the tiles. The tile fixing system includes insulating elements (the yellow part in Figure 3.8),

Belleville washers (to give a specific pre-load), and an electrical contact to bias the tile. Details of tile and strip fixing system can be seen in Figure 3.9, right hand side.

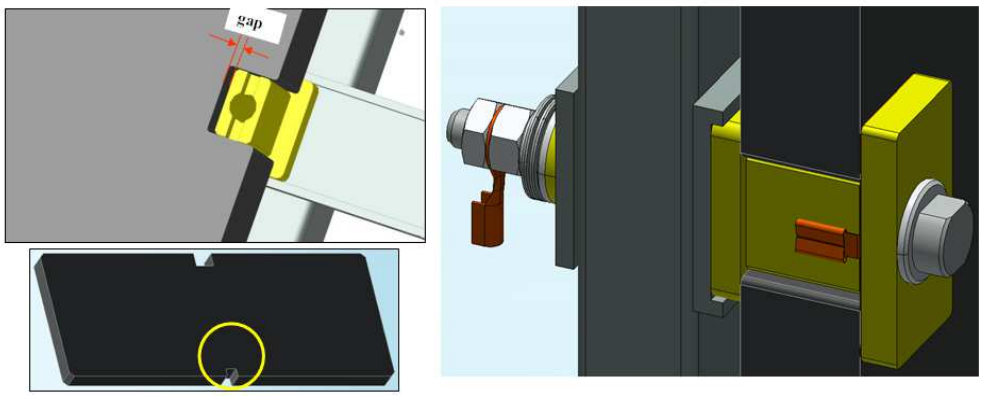

Figure 3.8: Tile fixing system.

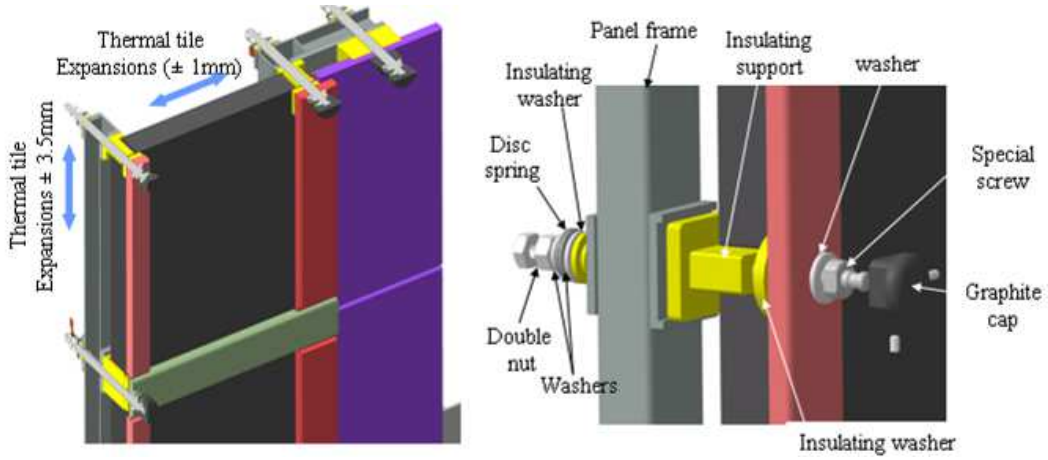

Figure 3.9: Tile thermal expansions; fixing system to the frame.

The calorimeter will operate in two different configurations (Figure 3.1, left hand side): “open”, where the beam will not be intercepted by STRIKE; “closed”, where the entire beam power shall be intercepted by STRIKE. In the latter case, two axial positions shall be designed for beam divergence measurement, one close to the beam source and the other one farther away. Measurements can be performed also in intermediate positions. In all measurement positions, the STRIKE tile surfaces will be parallel to the GG surface.

The mechanical structure that supports the panels is composed of three main parts: the basement frame, the trolley and the panel support structure (Figure 3.10) and is also dedicated to move STRIKE between the measurement positions. Moreover it allows parking STRIKE

outside of the beam path during long pulses. Each panel constituting STRIKE is supported by a dedicated structure interfaced with the SPIDER vacuum vessel.

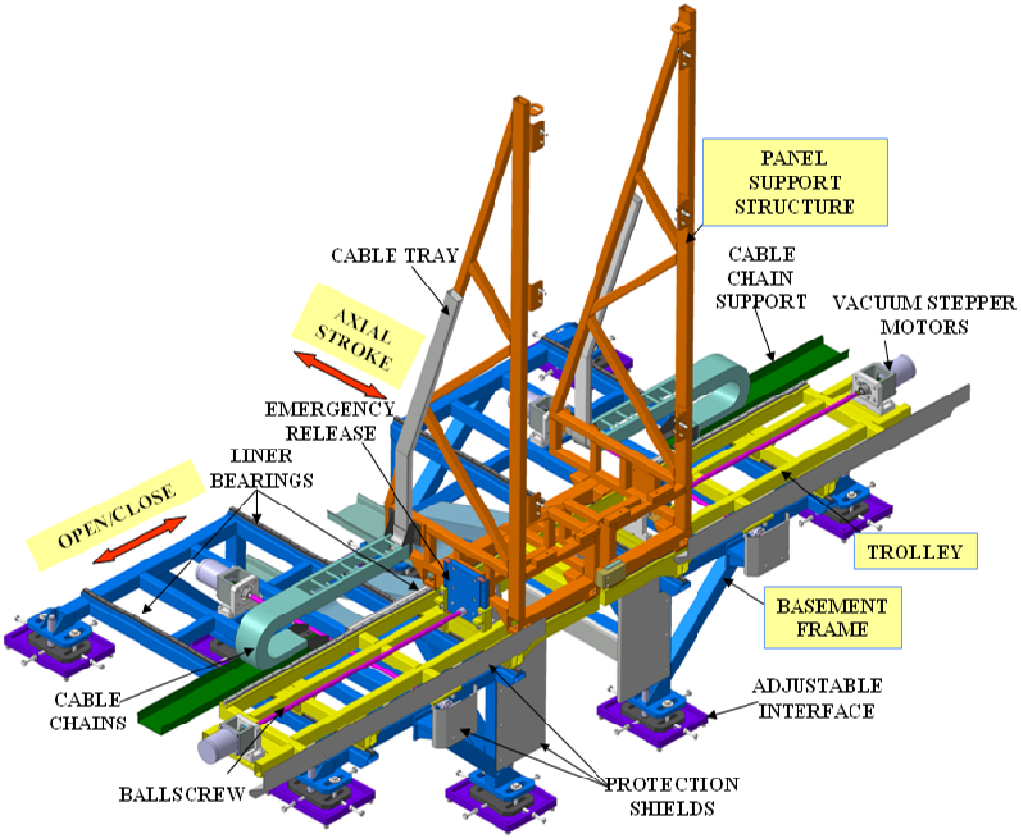

Figure 3.10: Supporting and positioning system.

It is estimated that the system will undergo the following number of moving cycles: 1000 aperture/closure and 1000 forward/backward in vacuum; during operation the latter will be more frequent than the former.

The axial translation, which permits the forward/backward (along (x axis) beam axis) movement of the panels, is realised by means of a trolley mounted on linear bearings on the basement frame (Figure 3.11). The two panels move along the x direction without interferences.

The linear bearings with needles are properly preloaded in order to avoid backlashes and assure a precise alignment and high stiffness also in case of thermal elongation of the frames. The displacement of the trolley is realised by means of a motor for vacuum and radiation environments. This motor drives directly a ball screw with 2mm lead. This lead combined with a 200 steps motor can give a high resolution of 0.01mm per step. The ball screw has steel and ceramic spheres in alternate configuration. The steel idler balls, smaller in diameter, preclude friction and wear because there is no ceramic-to-ceramic contact. Thus the load is supported by the ceramic spheres and there is no risk of vacuum sticking between the steel spheres and the

nut. All the sliding elements are dimensioned for a nominal load that is more than twice the real one, because they operate in vacuum without lubrication. The minimum stroke is 800mm.

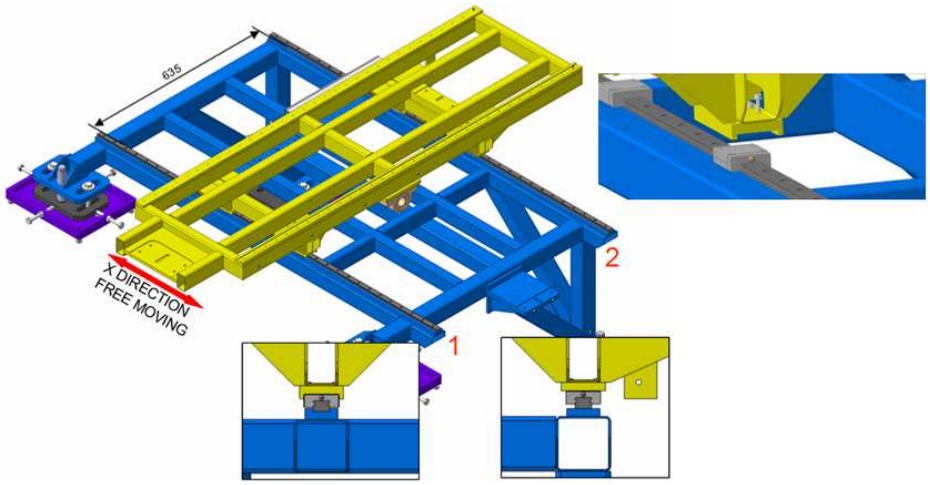

Figure 3.11: Basement frame with linear guides and trolley for forward/backward displacement.

The particular of the ball screw together with the system for the positioning along x axis are shown in Figure 3.12: a ball screw is supported by ball bearings mounted on supports and fixed to the basement frame.

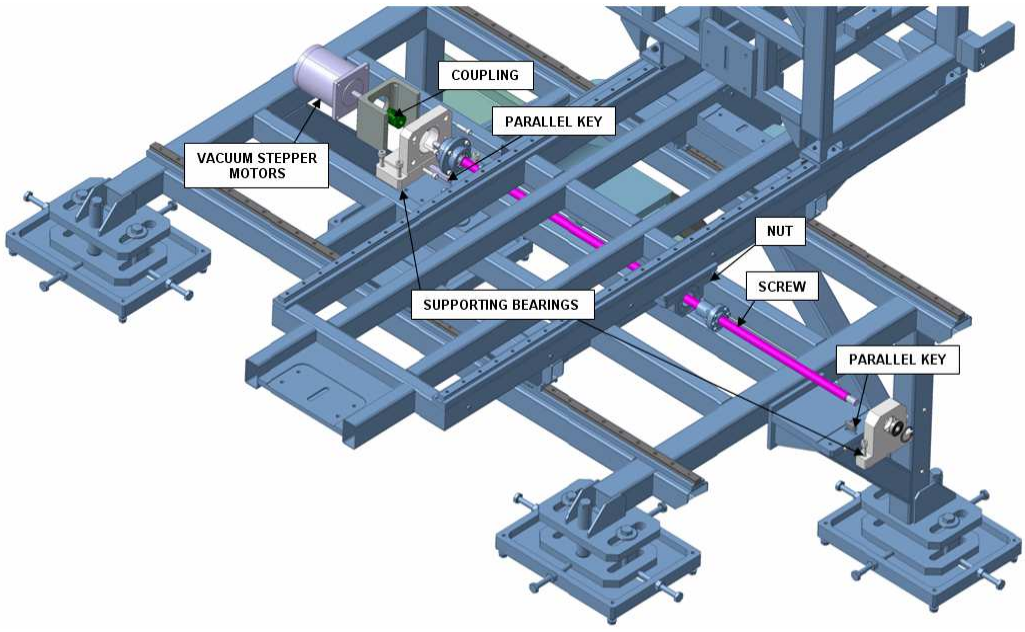

Figure 3.12: Motors for moving system along x axis.

The panels support frame are mounted on the trolley by means of two linear guides, as shown in Figure 3.13, to realised the open/close movement of the panels in the y direction.

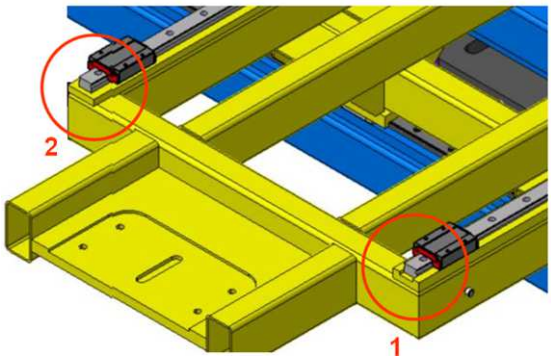

Figure 3.13: Basement frame and trolley with linear guides for the open/close movement along y axis.

The y moving system (Figure 3.14) will be mounted similarly to the assembly of the x moving system, but it differs because it shall accommodate the thermal expansion of the supporting structure frame; furthermore the transmission between the screw and the frame shall not be "fixed". An emergency release mechanism (Figure 3.15) allows the manual release of the nut of the ball screw, by moving up the two jaws so the frontal nut plate will be unlocked from the ball screw.

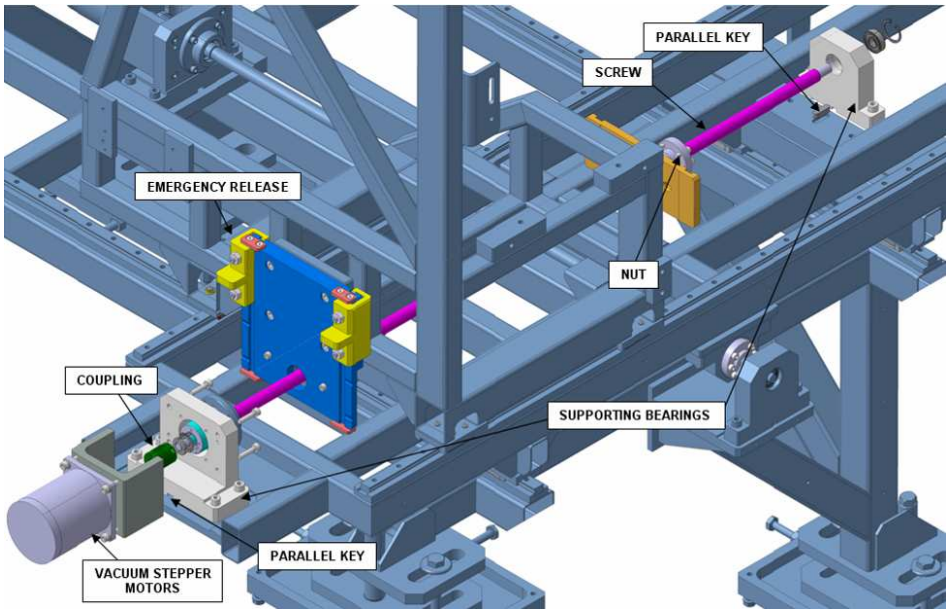

Figure 3.14: Motors for moving system along y axis.

Electric motors can be used in moving systems, both for the trolley and for the support structure, and they have to be equipped with encoders in order to have an absolute position measurement. Either DC or stepper motors can be chosen.

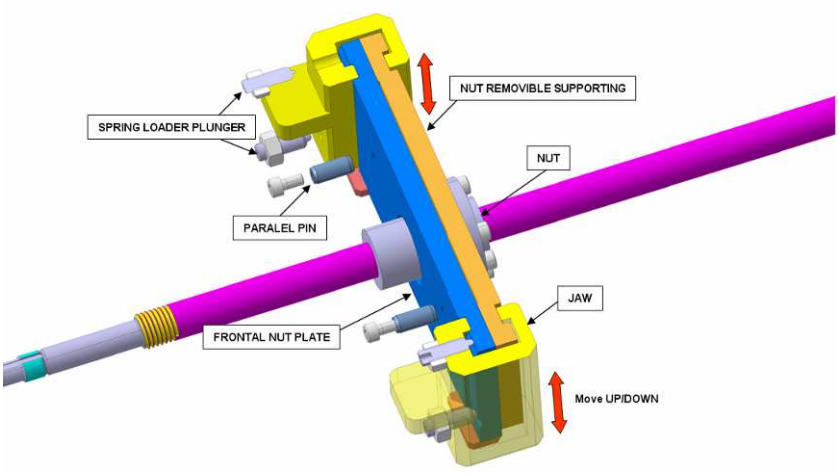

Figure 3.15: Emergency release mechanism.

Adjustments are incorporated in the supports of the basement frames allowing for ±30mm displacement of the basements frames along the three axes, as shown in Figure 3.16.

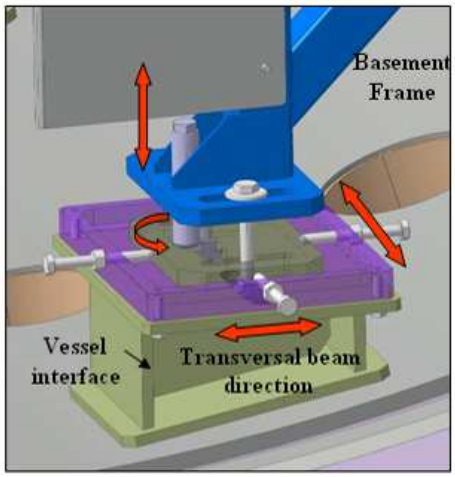

Figure 3.16: Basement frame adjustment.

The panel support structure is fixed on the carriages of the linear guides. In Figure 3.17 the two fixing systems used to attach the panels support structure to the trolley are shown. In order to allow the free thermal expansion between the STRIKE panel support structure and the carriages of the linear guides, the external bolted junction (see top-left zoom in Figure 3.17) is equipped with sliding carriage bushings and washers.

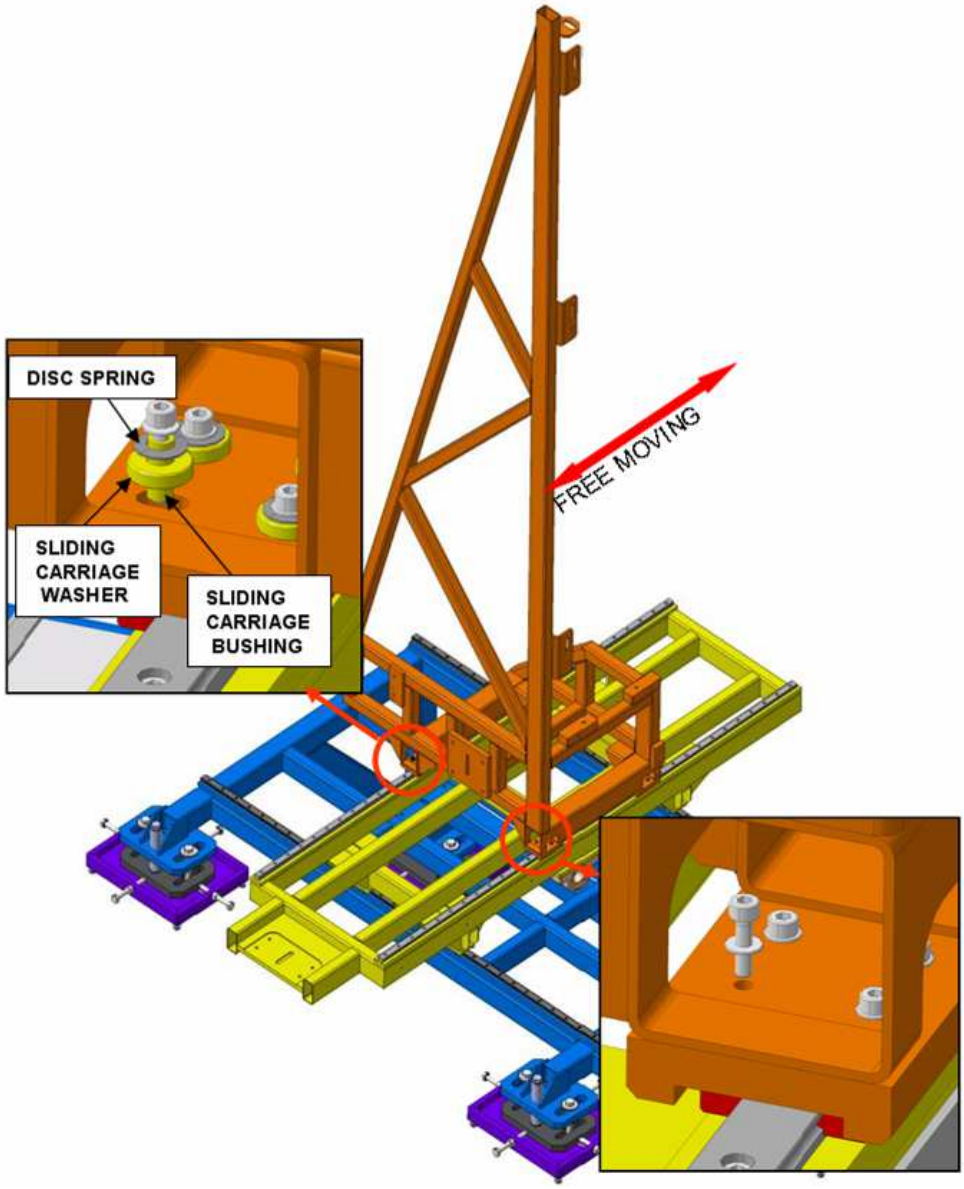

Figure 3.17: Fixing system and adjustment of the support structure frame.

The position adjustment of the panel frame, with respect to the panel support structure is guaranteed by the presence of suitable screws, as described in Figure 3.18. This system can also accommodate the thermal expansions of the panel frame.

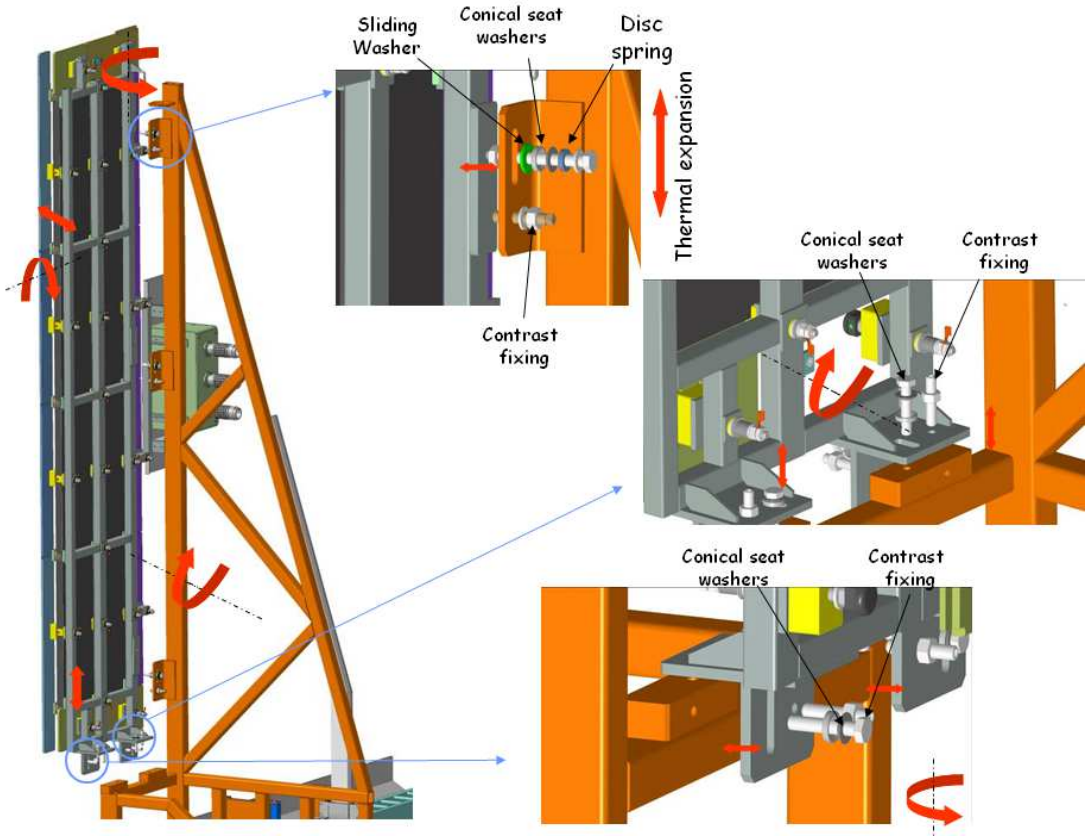

Figure 3.18: Adjustment of the panels.

In order to avoid that the two panels comes in contact when STRIKE is closing, possibly causing damages on the tiles or kerbs, a mechanical safety block (Figure 3.19) is foreseen.

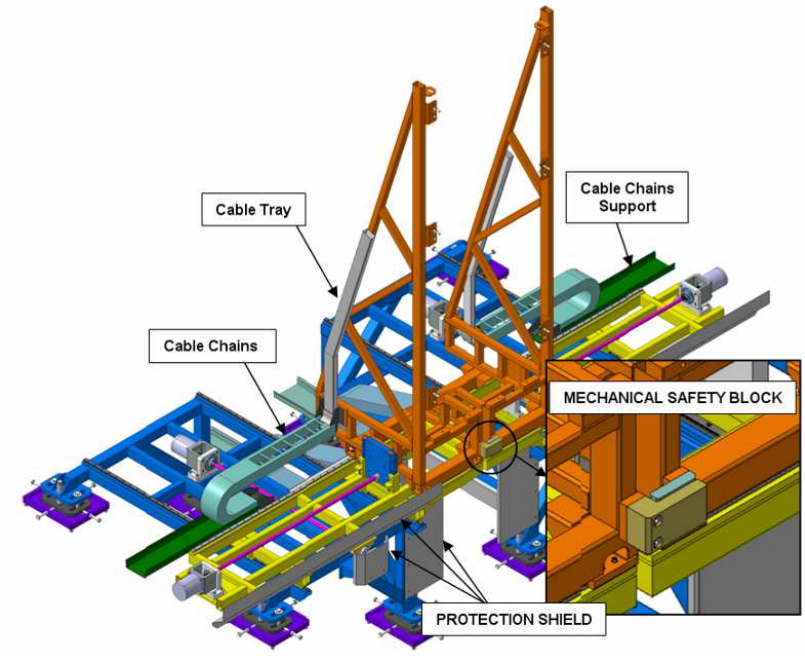

Figure 3.19: Mechanical safety block.

3.2 Diagnostic systems dedicated to STRIKE

Two thermal (IR) cameras are used to observe the thermal pattern on the rear side of STRIKE tiles. The IR cameras shall measure the two-dimensional temperature map of the entire beam cross section. From the results of the numerical simulations, the expected operating range of the IR cameras is 20-2000°C; the requirements of IR cameras are given in [44].

To observe the rear side of STRIKE panels by the thermal cameras, two ports will be used. The thermal cameras will be installed in air and will have an angled view of the tiles, as sketched in Figure 3.20, right hand side. One thermal camera will use one of the four upper ports on the SPIDER front lid (Figure 3.20, left), looking downwards; the other thermal camera will be installed on one of the three lower ports on the SPIDER front lid, looking upwards.

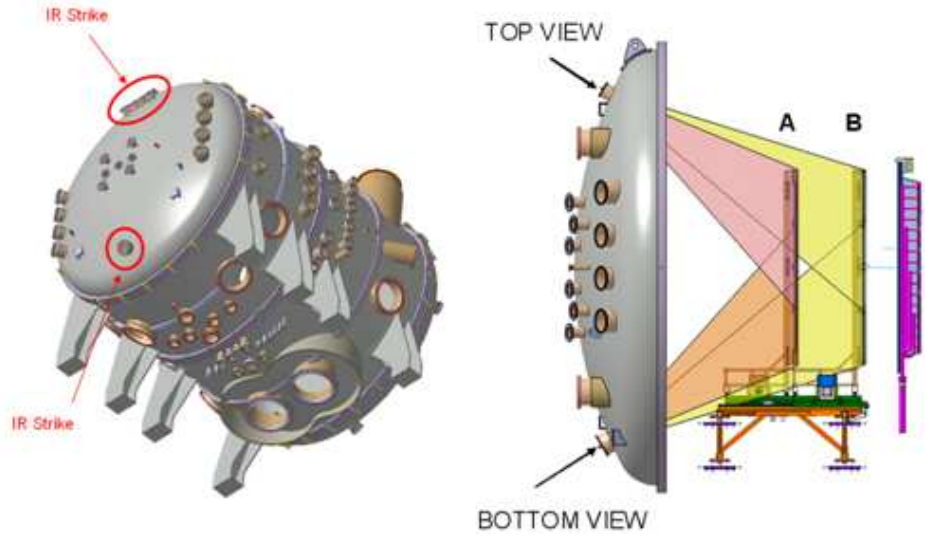

Figure 3.20: Thermal camera view ports.

The viewing field of the bottom thermal camera is sketched in Figure 3.21. Since the sensors of thermal cameras are usually slightly rectangular (e.g. the pixel number is 480x640) they will be aligned so that the longer side is in the vertical direction. Thus the viewing fields of the two cameras will overlap, providing a way for relative calibration. This is necessary to obtain homogeneity of the measurements and to provide the assessment of the deviation from uniformity over the whole beam cross-section.

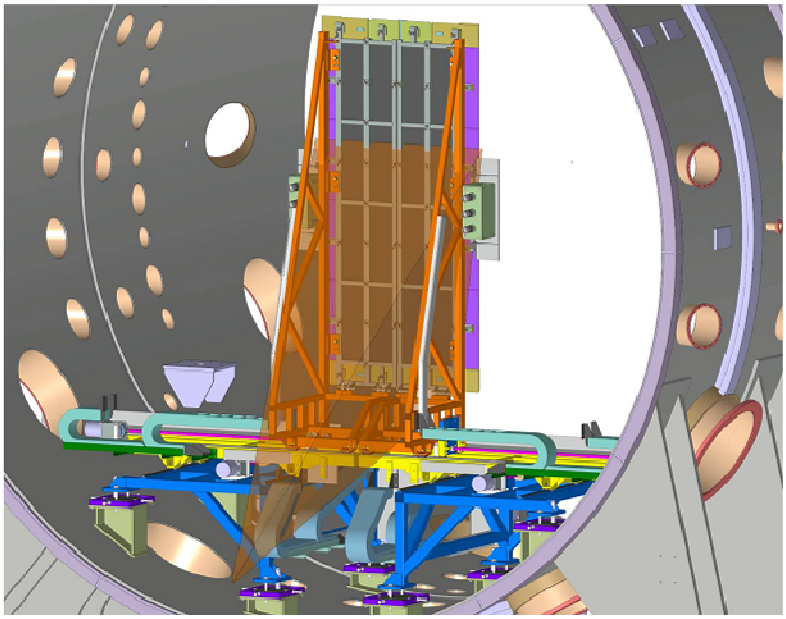

Figure 3.21: Area observed by the bottom thermalcamera.

In order to prevent secondary electrons from escaping the tile surface and hampering the current measurement, a voltage is applied to the tiles with respect to the vacuum vessel. Such biasing is provided by 2 suitable power supplies, whose ratings are: output voltage up to 300 V, total output current: 80A [45].

The current flowing into each tile will be measured to assess that the beam deviation from uniformity is lower than 10%; hence the current meters will have to measure a current up to 5A, with 1kHz bandwidth and accuracy better than 1%; the current meter must be insulated at least up to 500V with respect to the tiles [46].

The electrical contact with the tile is provided by the system shown in Figure 3.22: a stainless steel sheet located below the tile and insulated from the panel frame, with a crimping connection to the cable.

Also the current flowing through each kerb and strip elements shall be measured, to help in assessing the halo contribution, particularly in the case of large beam deflection. The current meters shall be able to measure a current up to 0.5A, with 1kHz bandwidth and accuracy better than 1%; the current meter must be insulated at least up to 500V with respect to the tiles.

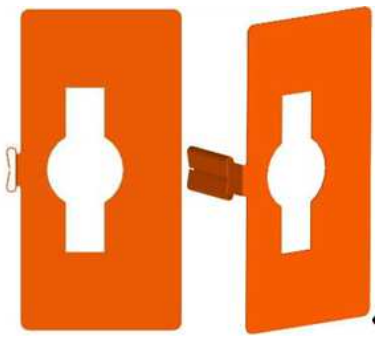

Figure 3.22: Thin sheet to current measurement.

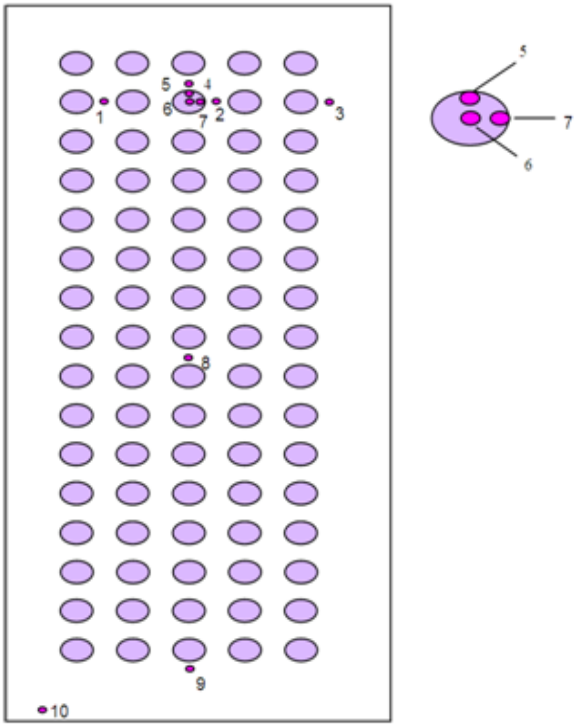

Figure 3.23: Thermocouple arrangement to identify beamlet profile.

Some thermocouples will be installed on the tiles. Their function is to provide a calibration for the thermal cameras and, possibly, to help in the reconstruction of the temperature profile [42]. For the former purpose, two measurement points are necessary to supply a reference in the whole temperature range (Figure 3.24); for the latter, a suitable arrangement has been developed for the first V-shape version (Figure 3.23) and it can be applied also for the final design of the calorimeter. It is difficult to realise because the thermocouple obscure the thermal camera view and in particular the instrumented beamlet (on the second row with 3 thermocouples on the beamlet footprint and 2 more thermocouples close to the beamlet).

The fixing system is sketched in Figure 3.24: the image in the centre shows a thermocouple measuring in a hot point that is the expected position of a beamlet; the right hand side image shows a thermocouple measuring in a cold point that is at the edge of the tile, outside the expected beam footprint.

Additional thermocouples are used: each kerb and strip shall be equipped with one thermocouple, to monitor its temperature during the operation and to help in assessing the halo contribution, particularly in the case of large beam deflection; some thermocouples will be installed in the frame to monitor its temperature.

Since the thermocouples are electrically connected to the surfaces which can be away from the ground potential, the measurements system will have to withstand an insulation voltage of 500 V [46].

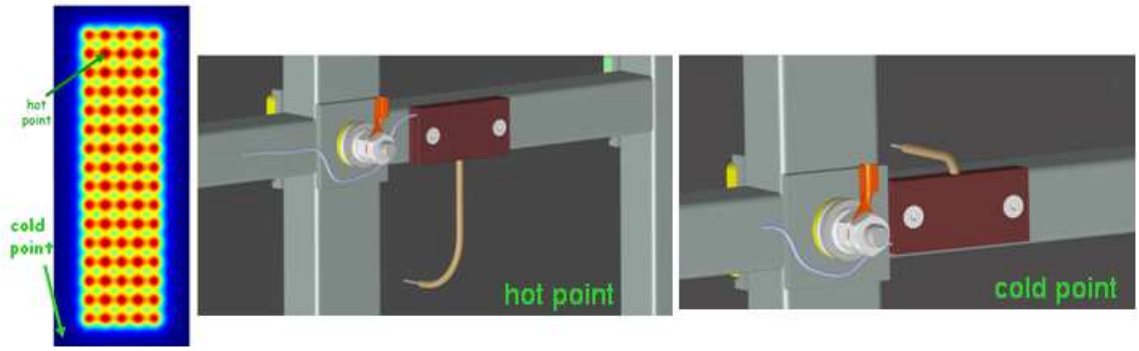

Figure 3.24: Thermocouples position and fixing system.

To characterise the plasma in front of STRIKE, 2 electrostatic probes shall be installed in each panel. The structure of the probes is displayed in Figure 3.25. The electrode is the link from the electrode plate, directly exposed to the plasma and the metal disc in which the electrical cable to extract the signal is soldered. To fix the electrode to the electrode plate, a screw is used. The insulating support is in this way compressed between these two elements. Inside the insulating support there are the electrode, the spring and the metal plate. The signal cable can be extracted through a slot obtained between the insulating support and the probe cover, to reach the frame.

These sensors are installed in kerbs at the top and bottom of the panels (Figure 3.25, left). They provide the measurement of plasma parameters like charge density, electron temperature and plasma potential. The first quantity is obtained by applying a constant voltage between the probe and the kerb and measuring the current; to obtain all quantities a voltage ramp is required and the whole current-voltage characteristic curve must be analysed [47].

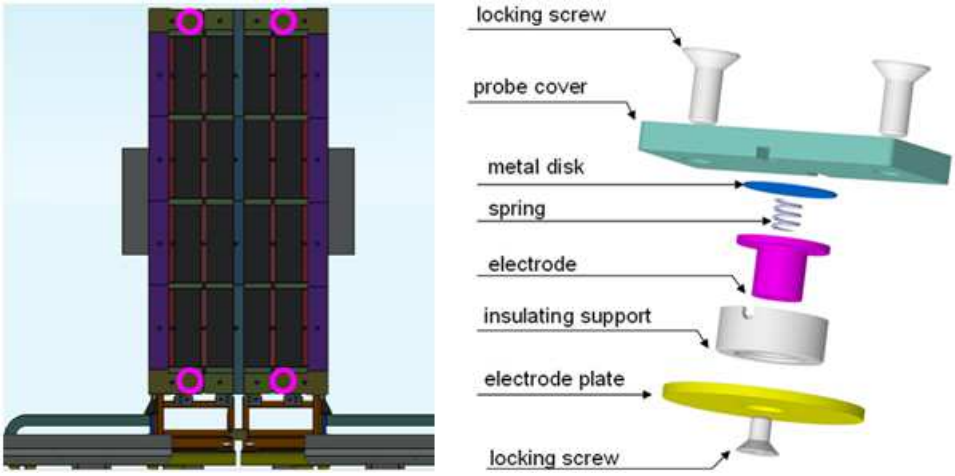

Figure 3.25: Electrostatic probes positions and assembly.

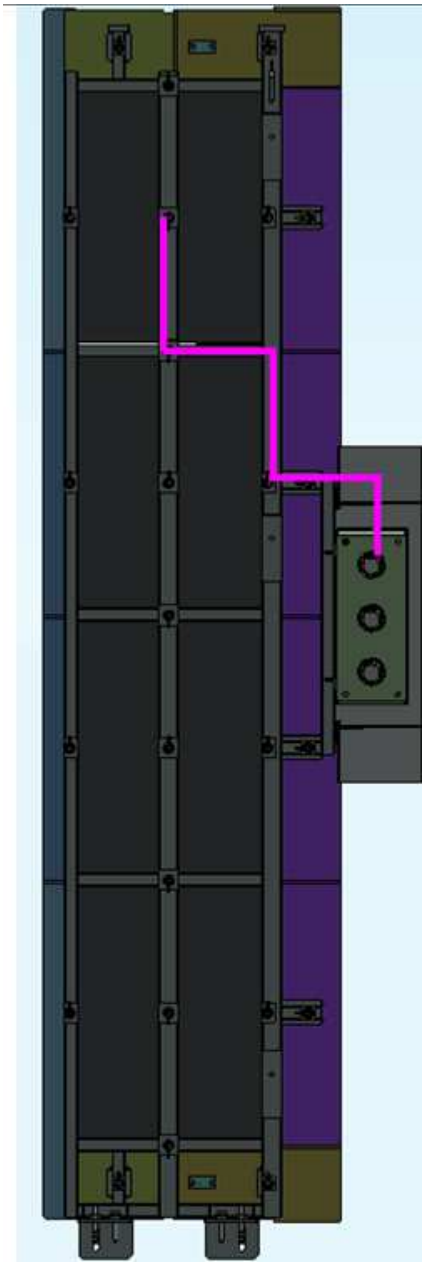

Figure 3.26: Cable path from the frame to the box.

Inside of SPIDER vessel, all cables follow the tubular pipe of the frame, from the sensor to the box (Figure 3.26). Each frame is provided with a Cable Box in which each insulated cable is terminated. These Boxes house thermocouple terminations as well as the connectors for all cables. The choice to use collecting points embedded in the Frames is useful in case of panel disassembly: the movable connector remains with the Supporting and Positioning System.

From the Cable Box to the feed-throughs all cables follow the same path within the cable runs along the supporting and positioning system (Figure 3.27).

SPIDER vessel will be provided with dedicated feed-throughs, located in dedicated flanges, for the extraction of several types of cables (for thermocouples, tile biasing, electrostatic sensors). The feed-through pins are insulated at 500 V from the vessel and from each other.

Outside of SPIDER vessel and bioshield, STRIKE cables reach an electrical cabinet where data conditioning and acquisition is performed. The cable runs must accommodate all STRIKE cables due to the RF applied to the source and breakdown events in the accelerator; the path and features of the cable runs must be suitable for preserving the signal integrity against noise, both along the cables and in the cabinets. The detail design is in progress.

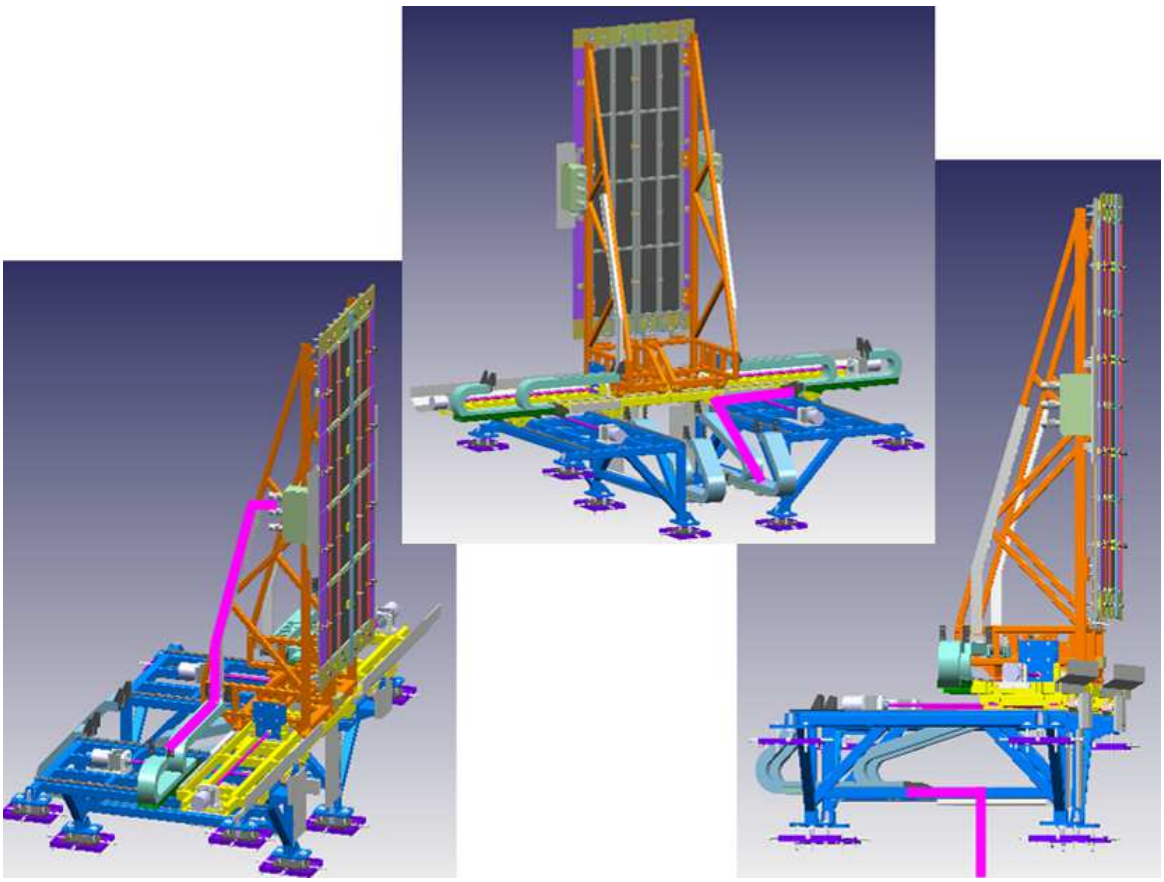

Figure 3.27: Cables path inside the vessel.

3.3 Simulations dedicated to the design

3.3.1 Thermal simulations

Thermal transient 2D and 3D simulations have been carried out by the finite element code COMSOL [48], with non linear material and including radiation. The geometry of the model represents only a quarter (0.08x0.198x0.02m^3) of beamlet group: due to the symmetry it is possible to reduce the computational time. The view factor for radiation is 1 for both surfaces, the one hit by the beam and the opposite surface observed by thermal camera. It radiates towards 300K because STRIKE is surrounded by surfaces around room temperature. The applied load corresponds to the superimposition of the beamlet described as a Gaussian. The maximum temperature on the rear side has been reached about 150ms after the end of the beam pulse.

It is also verified the code response with dedicated simulation: the asymptotic temperature, resulting from a low power application to consider as constant the thermal properties, has been compared with the analytical result.

3.3.1.1 Consecutive pulses

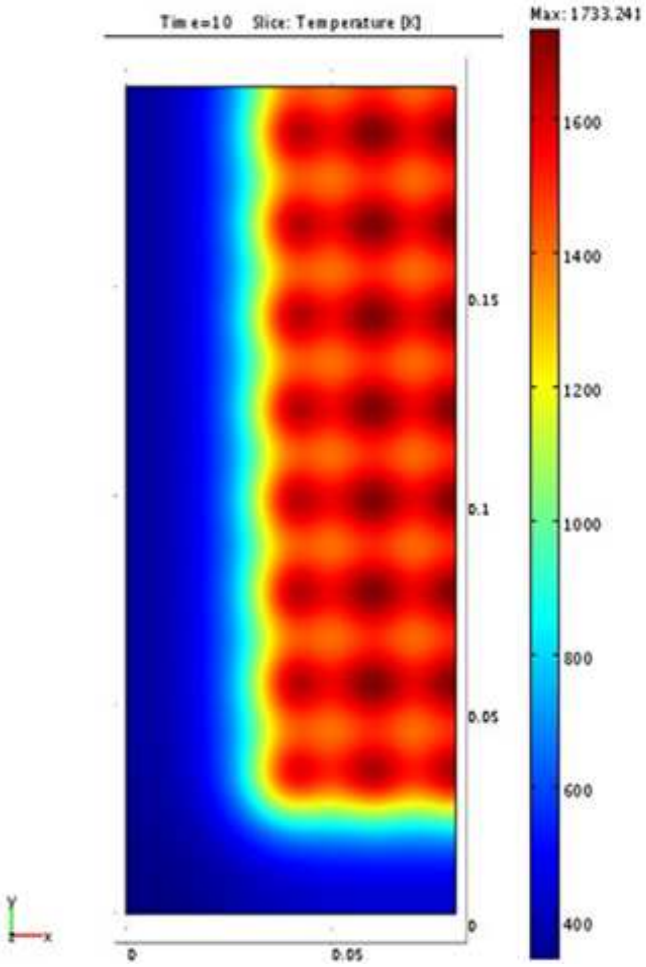

Figure 3.28: 2D temperature map at the rear side after 10s beam application.

Figure 3.28 shows a quarter of beamlet group where single beamlets can be observed, at the end of the first 10s beam pulse. Three consecutive pulses have been simulated with 20 minutes in between the pulses.

Previous studies on the V shape calorimeter, using same pulse duration and waiting time in between the pulses, have demonstrated that three pulses are sufficient to reach a kind of temperature upper limit (Figure 3.29) due to larger efficiency of radiation at high temperature. The cyan curve represents the temperature increase without radiation in the model, the red curve take radiation into account and the pulse duration is 5s, the violet curve take radiation into account and the pulse duration is 10s. The following figure refers to the V shape calorimeter.

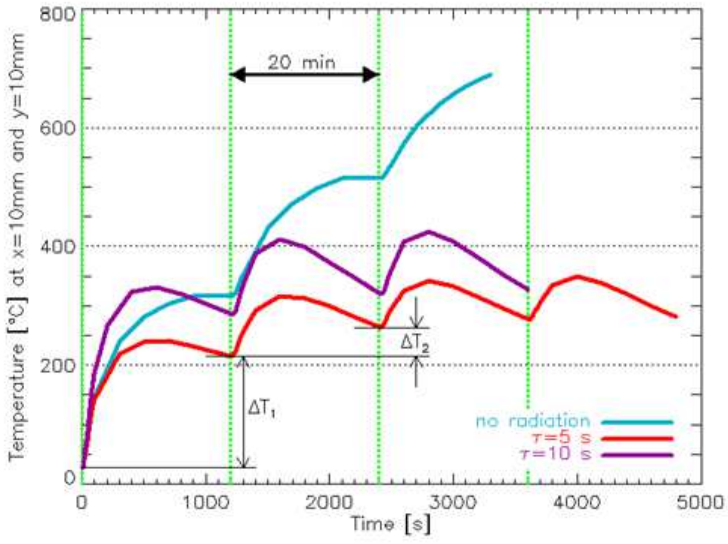

Figure 3.29: Temperature increase of three subsequent pulses.

Table 3.1 shows that the temperatures are very high but lower than the maximum allowable material temperature (2800°C).

	T front at the end of beam pulse [K]	T back at the end of beam pulse [K]	T front just before the successive beam pulse [K]
1st pulse	2657	1733	497
2nd pulse	2753	1814	504
3rd pulse	2756	1893	504

Table 3.1: Summary of front and rear side temperatures.

3.3.1.2 Beamlet halo

As a first estimation of the effect of the *halo*, a comparison between the temperature profile of the reference case, which does not include beam halo, and the case when halo is taken into account, has been done. Beamlets can be described as a superposition of a core, carrying most of the energy, and a halo having a gauss curve trend:

$$G_g(x,y) = A_g\left(-\frac{(x-x_{0g})^2}{2\sigma^2{}_{xg}} - \frac{(y-y_{0g})^2}{2\sigma_{yg}{}^2}\right)$$

Gg is the power density associated to each beamlet;

σ_{xg} and σ_{yg} are respectively the beamlet half-widths in the x and y directions;

A_g is the amplitude of the beamlet power density at the maximum position (x_{0g},y_{0g}).

Assuming that the halo carries 15% of the total energy and possesses a 30 mrad divergence,

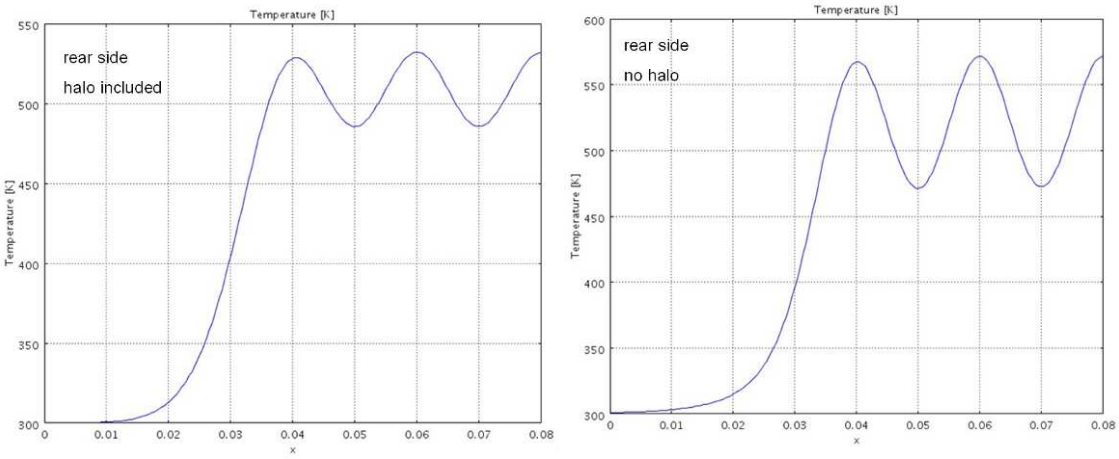

Figure 3.30: Temperature profiles with halo and without halo.

Figure 3.30 shows the temperature profile along a line passing thorough the centre of the central row of beamlets in a beamlet group.

As expected, if halo is included the peak temperature decreases, the radius of the single beamlets increases and the beamlet footprint is less recognizable due to larger superposition.

3.3.1.3 Beam uniformity

A study of *uniformity* has been performed, including radiation from the calorimeter, exposed orthogonally to the beam. Simulations have been carried out with +5% and -15% with respect to the reference power per beamlet. A comparison between the three cases has been done with the same colour code for the temperature. Figure 3.31 shows the comparison on the front side and Figure 3.32 on the rear side.

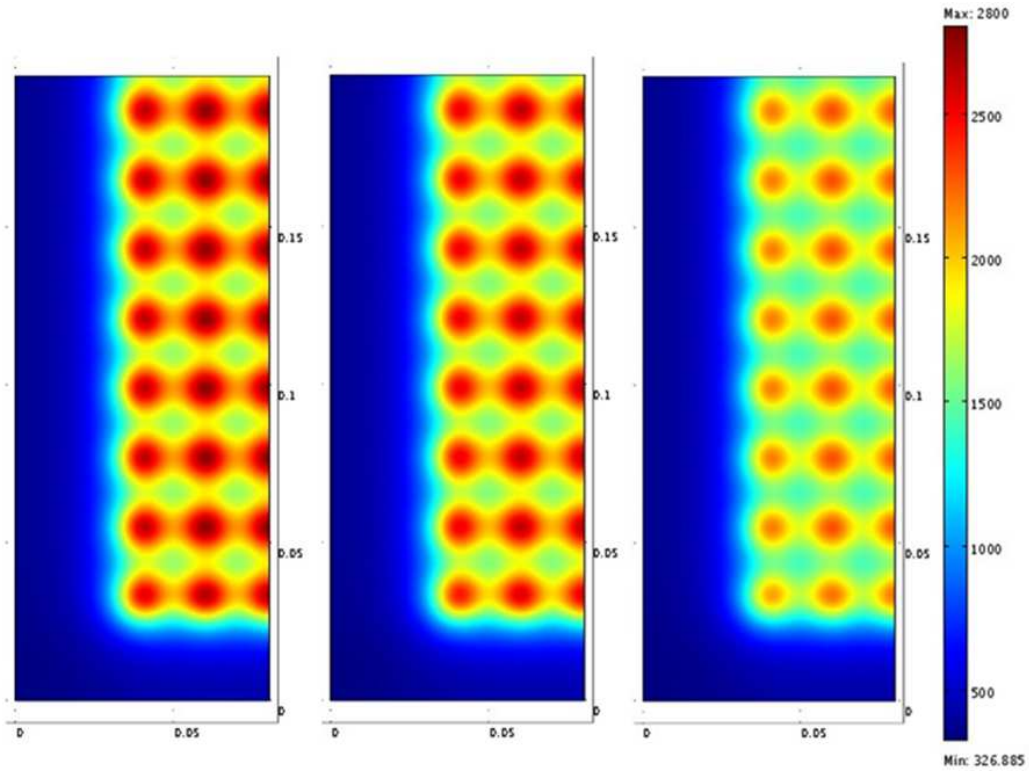

Figure 3.31: Thermal pattern on the front side of STRIKE: +5% on the left, reference case in the centre, -15% on the right.

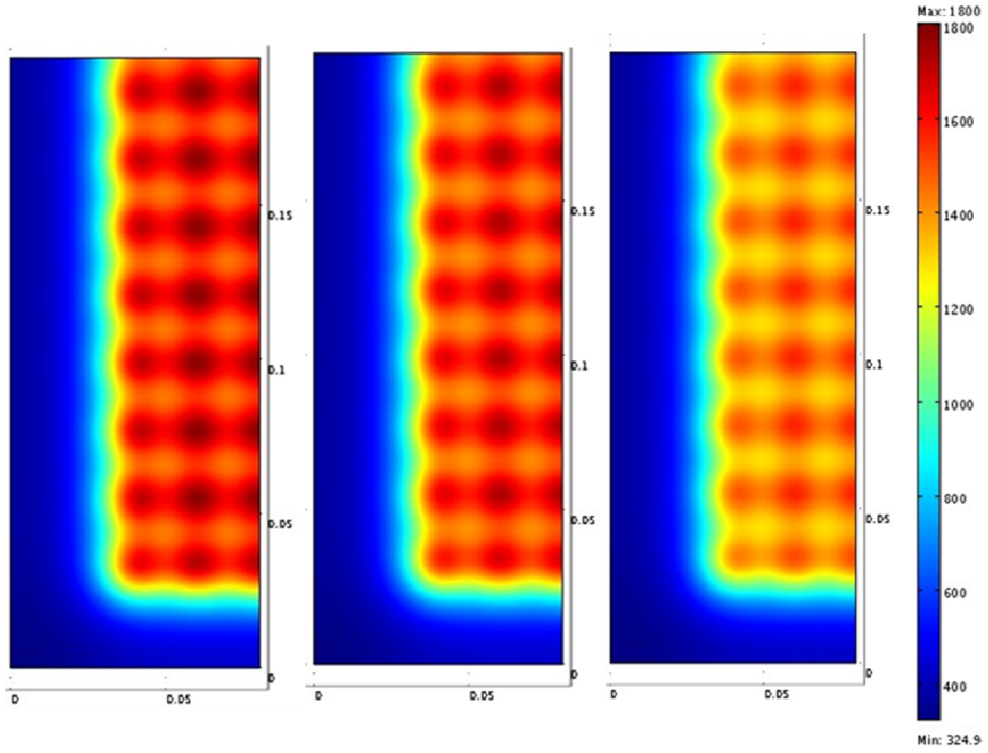

Figure 3.32: Thermal pattern on the back side of STRIKE: +5% on the left, reference case in the centre, -15% on the right.

With increasing power per beamlet, the maximum temperature increases. The maximum temperature on both sides of the tile is summarised in Table 3.2, along with the percentage variation of the temperature and the temperature increase (about 10 K) for a variation of the power density of 1%. Such a temperature increase should be detectable with a thermal camera.

reference case		+5% wrt reference		-15% wrt reference	
front temp. [K]	rear temp. [K]	front temp. [K]	rear temp. [K]	front temp. [K]	rear temp. [K]
2657	1733	2765	1783	2310	1572
	percent variation	+4.6%	3.5%	-14.7%	-11.2%
	temperature increment per 1%	21 K/%	10 K/%	-23 K/%	-10.7 K/%

Table 3.2: Summary of the temperature with respect to the power density variation.

3.3.1.4 Change of the acceleration voltage

Off-normal conditions concerning the *perveance* (see section 1.2) have been simulated. The acceleration voltage has been decreased from 100kV of the reference case of the SPIDER design to 50kV and 70kV to study the expected signals at constant perveance, as a consequence also the extracted current has been changed. The beamlet divergence is 3mrad in all cases. Three

successive pulses lasting 10s and 1200s elapsed time in between the pulses have been simulated. Figure 3.33 compares the thermal pattern on the rear side, at the end of 10s beam pulse. If particles are more energetic, due to a higher acceleration voltage, also the temperature at the calorimeter is higher and the single bemalet is more recognizable.

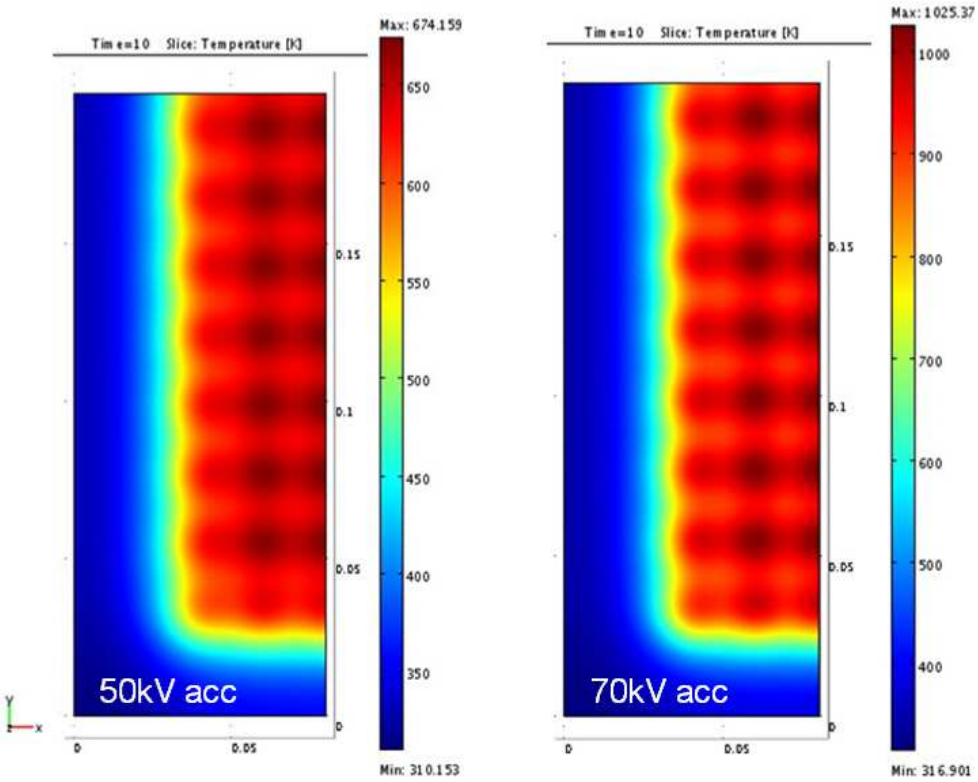

Figure 3.33: Temperature map at the rear side at the end of 10s pulse.

Table 3.3 and Table 3.4 summarise the maximum front side and rear side temperatures at the end of 10s beam pulse, together with the temperatures at the end of the interval in between the pulses, just before the successive beam pulse.

	T front at the end of beam pulse [K]	T back at the end of beam pulse [K]	T front just before the successive beam pulse [K]
1st pulse	744	674	376
2nd pulse	786	713	384
3rd pulse	791	718	385

Table 3.3: Summary of temperatures, 50 kV acceleration voltage.

By comparing results for both simulated conditions it can be noticed that temperature variations, with respect to 300K room temperature, are appreciable even if the beamlet profiles are quite overlapping.

	T front at the end of beam pulse [K]	T back at the end of beam pulse [K]	T front just before the successive beam pulse [K]
1st pulse	1259	1025	406
2nd pulse	1316	1073	412
3rd pulse	1320	1076	413

Table 3.4: Summary of temperatures, 70 kV acceleration voltage.

The maximum temperature reached at the rear side in the reference case of 100kV acceleration voltage is 1733K; compared with the unfavourable case of 70kV acceleration, which gave the minimum temperature difference, and considering that, as previously highlighted, a temperature variation of 10K corresponds to a power density variation of 1%, the studied cases are well distinguishable.

Set of issues have been faced from the preliminary design to the buil-to-print design, in order to refine the project. During the design phase, simulations were devoted to the realisation of the instrumented calorimeter for the SPIDER experiment. In particular, the capabilities of STRIKE as a diagnostic of beam uniformity and of beamlet divergence have been studied.

Simulations show that it will be possible to verify experimentally whether the beam meets the ITER requirement about the detection of the maximum allowed beam non-uniformity (below ±10%).

3.3.2 Electrostatic simulations

Impact of ions and neutrals on material surfaces induces the emission of secondary electrons; the coefficient of secondary emission depends on the projectile-target pair; for instance, for the hydrogen energy of 100keV, relevant for SPIDER, impinging on graphite it is 2.55. Such electrons have an energy distribution function which is peaked around 2-4 eV (see 2.1.2.1 and [49]).

As electron emission can affect the measurement of the beam current, two- and three-dimensional electrostatic simulations have been carried out by COMSOL code to assess the necessary conditions for secondary electrons to be re-absorbed, by positively biasing STRIKE

surfaces with respect to vessel and grounded grid. The voltage gradient in the vicinity of the tiles must guarantee that electrons emitted from one tile are attracted back to the same tile, so that the current profile measurement is not affected.

The model represents STRIKE as a parallelepiped inside the vessel. STRIKE is polarised at 200 V [50] and the vessel is grounded, namely at the same potential as for the grounded grid and the beam dump. The length of the vessel in the model is shorter than the real SPIDER vessel length: to further simplify the computation, the ends of the vessel in the model correspond to the grounded grid (and the electron dump) on one side and to the beam dump on the other side, as presented in Figure 3.34 by the red dashed vertical lines. This simplification is motivated by the fact that, within the vessel, the relevant region is just a few centimetres away from the STRIKE surface, so that the detailed structure of distant objects is negligible. STRIKE can operate at two different distances from the grounded grid (section 3.1 and [51]); for the simulations the calorimeter is positioned in the forward position. In this way the electric field between the grounded grid and STRIKE is lower than in the case with STRIKE in the backward position. The secondary electron trajectories are less affected by the electric field and this is the worst case.

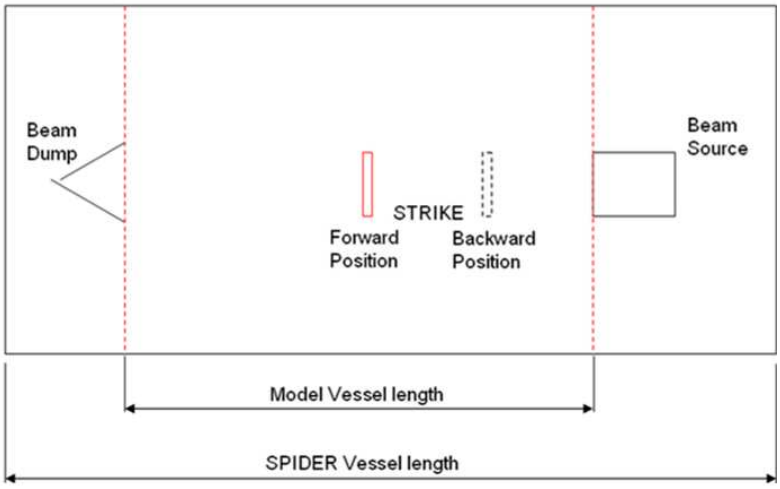

Figure 3.34: Scheme of the adopted geometry for the model.

The scope of the 3D analysis is to verify that the secondary electrons can not go farther than few centimetres away from the calorimeter. The reference frame is in

Figure 3.35: the STRIKE surface lies on the (x,y) plane, y being the vertical direction, pointing upwards; z points outside of the STIKE surface.

The polarization value of 200 V is derived from the previous electrostatic study with a simplified STRIKE geometry.

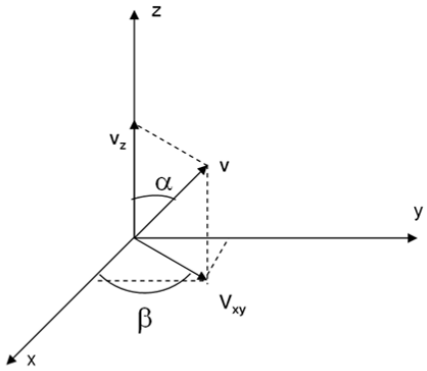

Figure 3.35: Reference frame for the 3D electron trajectories computation.

The electron trajectories are evaluated along lines at different x and y coordinates, in correspondence to an area close to the centre of the calorimeter and also near the edge, where the electric field is concentrated, as indicated in Figure 3.36.

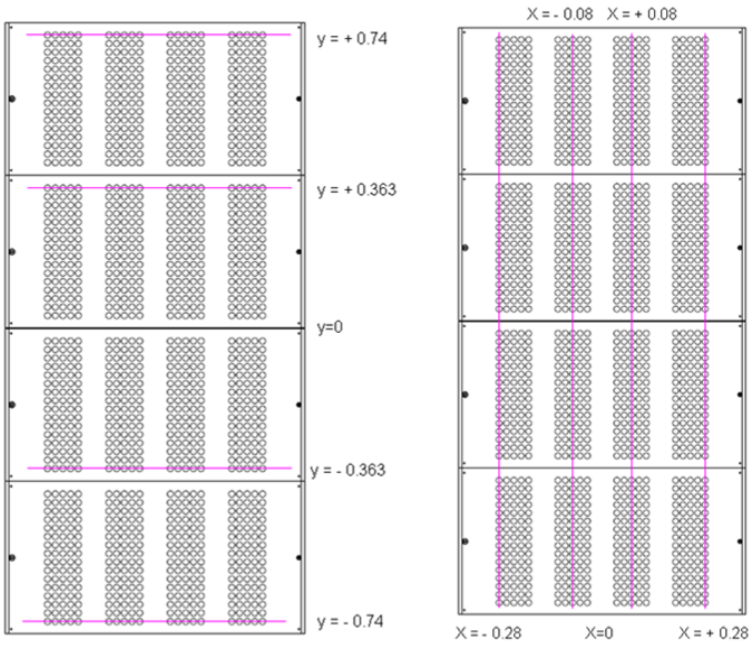

Figure 3.36: Lines along which the electron trajectories are evaluated.

Several combinations of α and β angles have been analysed; an example of trajectories related to $\alpha = \pi/4$ and $\beta = \pi/2$ is shown in Figure 3.37: the maximum range is about 19 mm and the maximum height of the trajectory is about 5 mm.

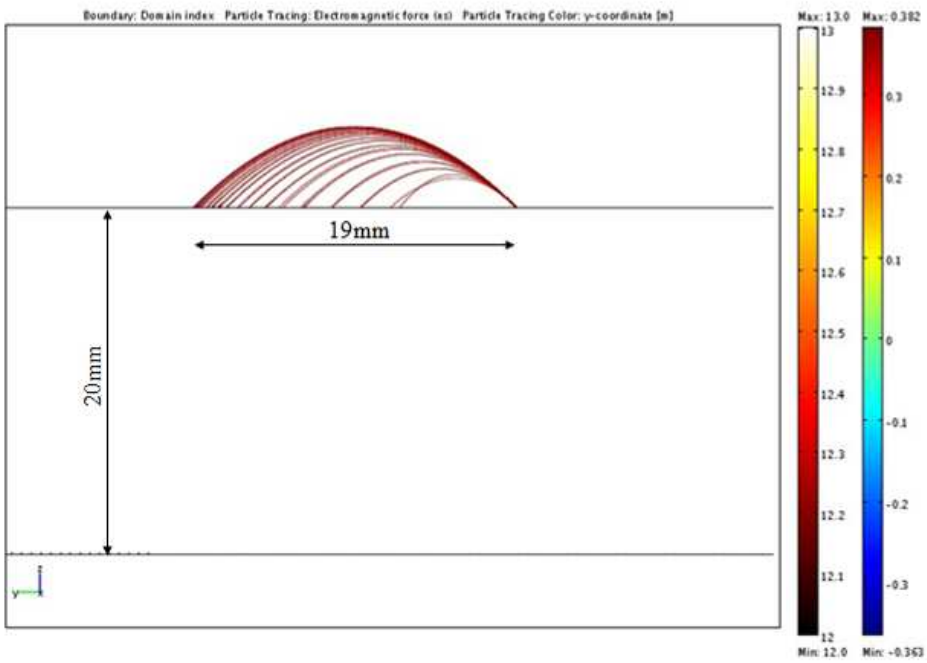

Figure 3.37: Zoom of the secondary electron trajectories; view in the plane yz.

From 3D electrostatic analyses it results that electrons are decelerated in a distance from the surface of the STRIKE calorimeter that corresponds to less than 3V. This verification permits to refer to the 2D model.

The real geometry of the calorimeter has been studied: the two-dimensional analysis has been performed with a model representing the equatorial plane of the calorimeter inside the vessel. The starting positions of the particles, corresponding to the region of the panel hit by the beam, is sufficiently far away from the edges that a 2D approximation is acceptable; this in turn allows a more detailed representation of the real structure of STRIKE. The scope of this analysis is to evaluate the most proper polarization combination of the different parts constituting STRIKE.

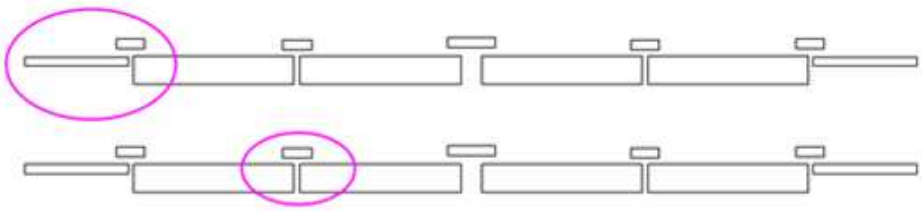

Figure 3.38: Sketch of the parts of the calorimeter quoted in other figure.

The vessel is grounded, the tiles of the calorimeter are polarised at 200V and the kerbs and the strips [52] can be grounded with the vessel or polarised at 200 V like the tiles.

In [20] the expected energy range of the secondary electrons is from 3eV to 10eV. The two-dimensional analysis has been performed considering secondary electrons exiting with energy of 3eV or 10eV and with different angles, including 45°, which corresponds to the maximum range.

Figure 3.39 on the left hand side shows the external left edge of the calorimeter and the electric field distribution between kerb, tile and strip (as indicated on the upper part of Figure 3.38) when only tiles are polarised at 200V with respect to vacuum vessel, strips and kerbs. The electric field is higher at the corner but the model does not represent the rounding off of the corner. Figure 3.39 on the right hand side shows the electric field distribution on external lateral kerb when all parts of the calorimeter panel are polarised at 200V with respect to the vacuum vessel.

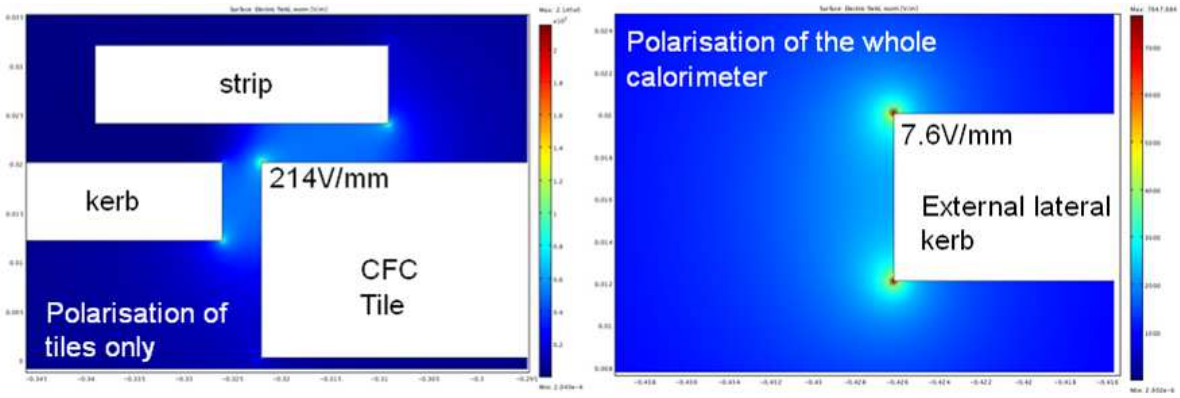

Figure 3.39: Electric field intensity.

The results depend on the strip bias (0V or 200V) as well as on starting energy and angle of electrons. If the strips are at the same potential as the tiles, electrons can be collected by the surrounding strips and tiles, as shown in Figure 3.40; this is more prominent for higher energies (the cases with 3eV and 10eV have been studied) and at 45°, where the range is maximum.

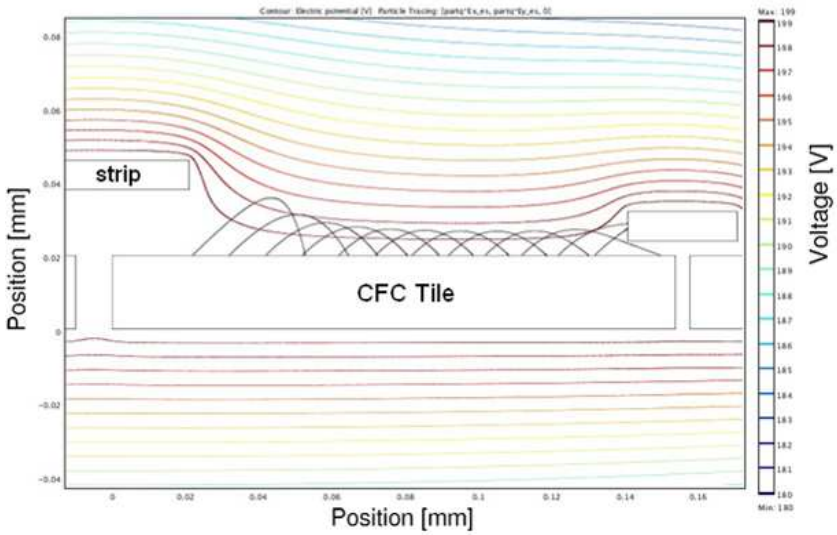

Figure 3.40: Equipotential lines and trajectories of electrons emitted at 45°: tiles and strips at 200V and 3eV electrons.

Figure 3.41 shows the fraction of the current of secondary electrons which is not collected on the starting tile; it is clear that 10eV electrons are essentially lost; however even for 3eV electrons the lost fraction is not negligible. For emission energy of 3eV, considering a cosine distribution of the emitted electrons, the percentage of "lost" current is 18%; this figure slightly increases if beamlet halo is included.

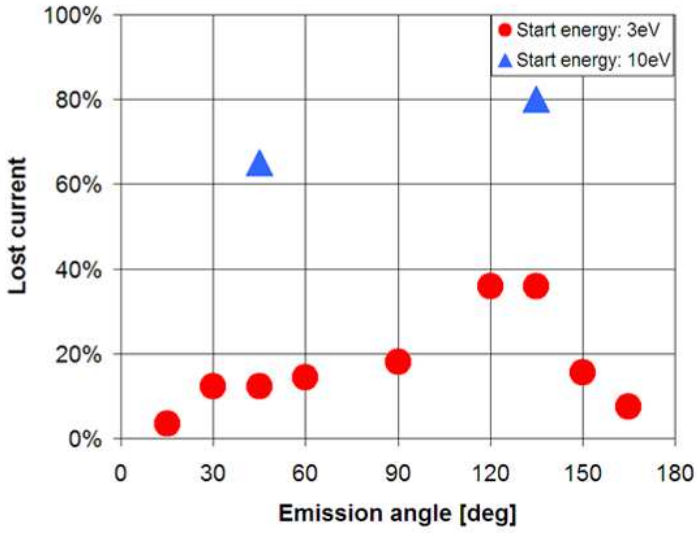

Figure 3.41: Secondary electron current not collected on the emission tile as a function of the emission angle; tiles and strips at 200V.

Conversely, if the strips are grounded, secondary electrons are always re-absorbed on the tile they were emitted from. It is worth noting that with grounded strips a lower bias voltage (<200V) is sufficient, since particles are confined by the very structure of equipotential lines (Figure 3.42 at 10eV). An influence of the electrons of the plasma in front of the calorimeter is also expected.

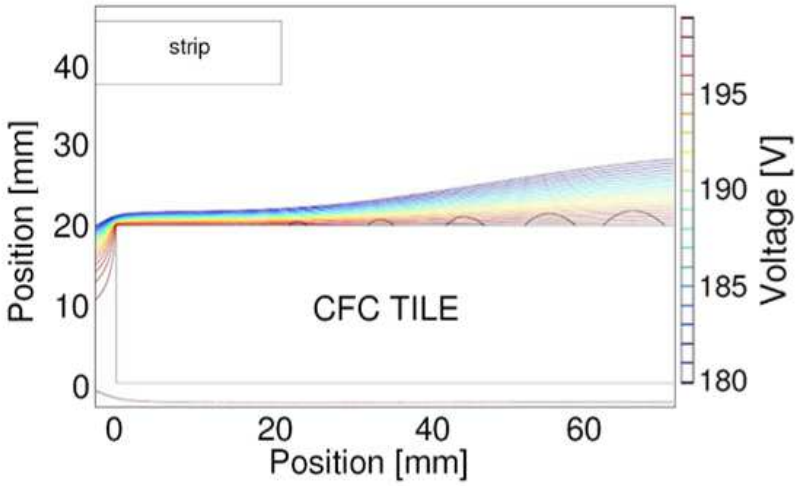

Figure 3.42: Equipotential lines and trajectories of electrons emitted at 45°: tiles 200V, strips grounded and 10eV.

4 CFC Characterisation

The CFC results to be the suitable material for STRIKE tiles. The manufacturing process is delicate and requires controlling several parameters (section 4.1). Moreover, only few suppliers are available. Considering these uncertainties, it has been decided to contact the producers and to purchase some small-scale prototypes. The companies contacted to check their interest on this project are Mitsubishi Plastic (Japan) and Mersen (France), suppliers of tiles named “B” and tiles named “A” respectively. Seven prototypes of the tiles have been collected and tested from 2010 to 2012: B1, B2, B3, A4, A5, A6 and A7. The dimensions of the tiles are:

- A4: 196 × 91.5 × 22 mm;
- A5: 62 × 62 × 20 mm;
- A6: 138x91x18 mm;
- A7:123.5x75x17.8 mm;
- B1: 120 × 90 × 20 mm;
- B2: 120 × 90 × 20 mm;
- B3: 125.6x91.2x12.5 mm.

The tests of the prototypes were performed by a power laser, to characterise the thermal parameters of the tiles, and by particle beams, to verify the diagnostic capabilities of the system and to assess the thermo-mechanical behaviour of the material.

4.1 Carbon Fibre Carbon Composite

The CFC is a carbon-carbon composite: carbon fibres are laid in a carbon matrix. Different are the known production processes of the fibres, the choice between PAN fibres (obtained by graphitization of polyacrylonitrile) and pitch fibres (obtained from pitch) depends on the mechanical and structural characteristics to be preferred, for instance the stress-strain behaviour, the Young moduli, the porosity, etc. The fibres used to produce the future STRIKE tiles and their prototypes, to be tested, are made of pitch fibres. These fibres exhibit high thermal conductivity. Also for the manufacturing of the composite different techniques can be followed: the matrix can be obtained by chemical vapour infiltration (CVI) or by liquid impregnation [53]. In the CVI, fibres are arranged in preform and positioned inside an isotherm and low pressure furnace; a hydrocarbons gas flows along the fibres, diffuses and deposits carbon inside the carbon fibres preform. In the case of the impregnation technique, the one used at least by the producer A, the fibres are arranged in two-dimensional fabric before the impregnation with the

matrix material and a 1D compression is performed between the fibre sheets. The matrix in the composite is carbonized (at about 1000°C). During this process the matrix loses mass and densifies; the consequent volume shrinkage is constrained by the fibres but matrix microcracks and void formation occur inside the material. To improve the stiffness of the matrix and to achieve high density, the phases of impregnation and carbonization are cyclically repeated. At the end of the cycles or in between, after carbonization, the composite is subjected to graphitization (at 2500°C), to provide structural stability and better thermal shock resistance.

In carbon-carbon composites, the strain to failure of the matrix is lower than the one of the fibres, moreover, the matrix is usually microcracked from processing stress and due to the similarity of the moduli between fibres and matrix, the load is shared evenly.

The interface between fibres and matrix is very important: the fracture behaviour depends on their coupling. A good coupling causes immediate fibre failure due to the pre-existing cracks of the matrix and the composite resistance is reduced, as it is dominated by the matrix properties. A poor coupling provides the composite with high strength and fracture resistance if the load is parallel to the fibre axis. Exceeding the failure strain of the matrix it cracks and debonding occurs between fibres and matrix. Due to this cracks the stiffness of the composite decreases and with further increases of the applied load also the fibres crack and pull out of the matrix.

Weak fibre-matrix interfaces allow the fibre strength to dominate the composite strength parallel to the fibre axis, but the off-axis strengths such as shear and transverse tension, are very degraded.

Supplier A explained that specific heat is independent from graphitisation process (it is the same as for graphite); instead thermal conductivities do depend on the graphitisation process (large graphitisation turns into high thermal conductivity).

4.2 Fibre and voids

The fibres composing the CFC are tied up together to make the bundles. These bundles make up the material. The bundles host a number of single fibres with circular cross-section and the room in between the fibres; so also the room in between different bundles can affect the thermal behaviour of the tiles.

To evaluate the effect of the room in between different bundles, an estimate of its surface with respect to the whole bulk has been done.

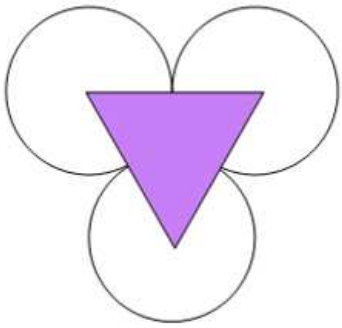

Figure 4.1: Equilateral triangle helping in the following computations.

From the area of the triangle highlighted in Figure 4.1:

$$A_{triangle} = \frac{1}{2} * 2R * \sqrt{3}R = \sqrt{3}R^2$$

the area of the circular sector is subtracted:

$$A_{circular-sector} = \frac{1}{6}\pi R^2$$

to obtain the area A_{in}, highlighted in Figure 4.2:

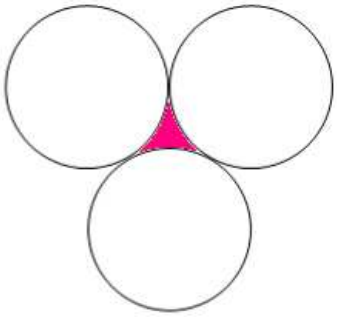

Figure 4.2: Area in between the fibres, A_{in}.

$$A_{in} = \sqrt{3}R^2 - 3 * \frac{1}{6}\pi R^2 = R^2\left(\sqrt{3} - \frac{1}{2}\pi\right)$$

Upon assuming that for each fibre there is a room corresponding to A_{in}, the equivalent area of a single fibre becomes:

$$A_{fibre} = \pi R^2 + R^2\left(\sqrt{3} - \frac{1}{2}\pi\right) = R^2\left(\frac{1}{2}\pi + \sqrt{3}\right)$$

So the area of a single bundle made of n fibres is:

$$A_{bundle} = nR^2\left(\frac{\pi}{2}+\sqrt{3}\right) = \pi r^2$$

and the resulting equivalent bundle radius is:

$$r^2 = \frac{n}{\pi}R^2\left(\frac{\pi}{2}+\sqrt{3}\right)$$

The same considerations can be done for the bundle and the room in between the bundles. The area in between the bundles results:

$$A_{in-bundles} = r^2\left(\sqrt{3}-\frac{1}{2}\pi\right) = \frac{n}{\pi}R^2\left(3-\frac{\pi^2}{4}\right)$$

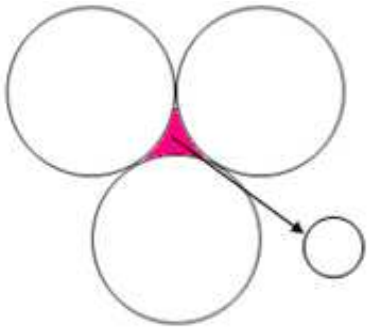

Figure 4.3: the area in between the bundles is converted into a circle with equivalent radius R_{eq}.

With this computation, depending on the number of fibres composing a single bundle, the real area of CFC composed by matrix and by fibres, which has the needed thermal parameters, can be deduced, as shown in Table 4.1.

n	no.of fibres	R[μm]	r [μm]	A_{in} bundles [m^2]	R_{eq} circle [μm]
2K	2000	5	2.293E+02	8.477E-09	5.194E+01
4K	4000	5	3.242E+02	1.695E-08	7.346E+01
6K	6000	5	3.971E+02	2.543E-08	8.997E+01
12K	12000	5	5.616E+02	5.086E-08	1.272E+02
2K	2000	5.5	2.522E+02	1.026E-08	5.714E+01
4K	4000	5.5	3.567E+02	2.051E-08	8.081E+01
6K	6000	5.5	4.368E+02	3.077E-08	9.897E+01
12K	12000	5.5	6.178E+02	6.154E-08	1.400E+02

Table 4.1: Radius of the fibre bundles with different number of fibres per bundle.

4.3 Profilometry

To investigate the prototype tile structure, colleagues of ICIS (Istituto di Chimica Inorganica e delle Superfici), CNR-Padova, have helped by performing profilometry analyses to quantify the fiber bundles cross-section dimension, the room in between the fibres and the room in between the fiber bundles. The scope of this measurement is to evaluate the status of the surface and to compare the results with the optical investigations. The tip of the profilometer can move vertically, in contact with the surface, to set the "zero level", and horizontally, to perform the measurement. The maximum path length of the profilometer tip on the surface of the specimen is about 8mm, longer path have been obtained by starting from the end of the previous measurement. The first measurement has been repeated to be sure that the tile was not damaged by the contact of the tip. Scans have been done both on vertical and horizontal directions, on the edge region of the prototype and in the centre of the tile (usually the impact point of the laser). In the following, two series of data are reported: the step heights analysis showing the original data, as recorded from the measurement device; and roughness analysis, in which the original data are levelled, to avoid a trend due, for instance, to the non planar surface of the specimen.

Figure 4.4: profilometer device (left hand side) and test on prototype (right hand side).

Typical findings for prototypes B1 and A4 are presented below: Figure 4.5 refers to data of prototype B1 and Figure 4.6 the results for B1 after data analysis; Figure 4.7 shows the raw data of A4 and Figure 4.8 shows the results after data analysis of A4 are displayed.

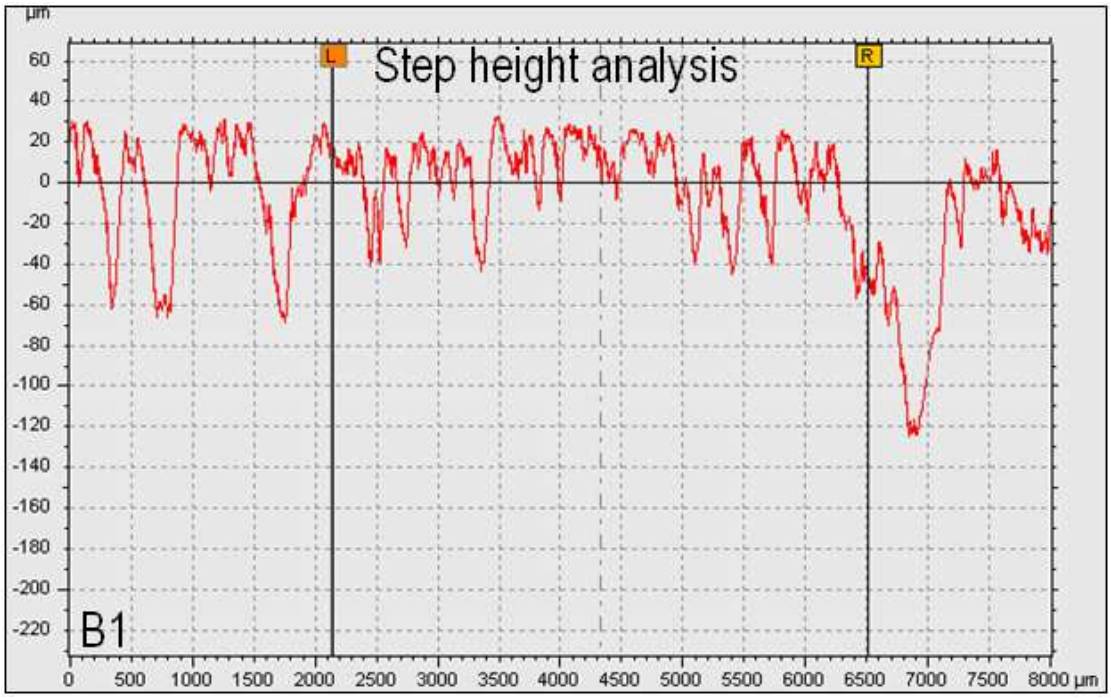

Figure 4.5: B1 raw data.

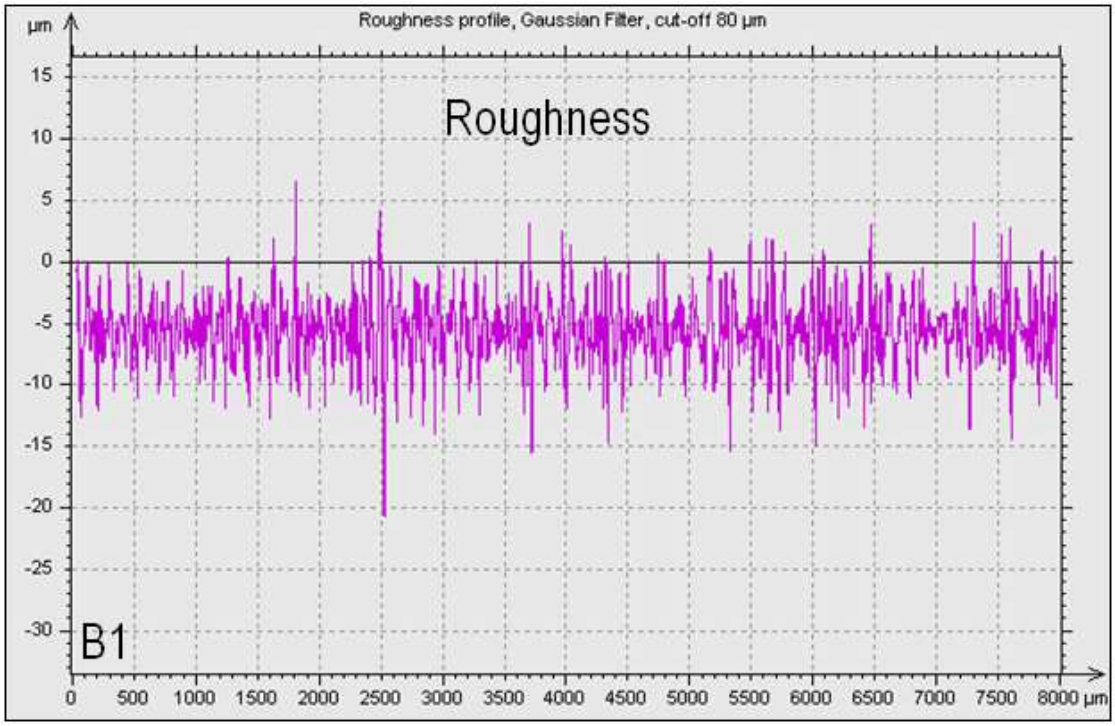

Figure 4.6: Results of the data elaboration for B1.

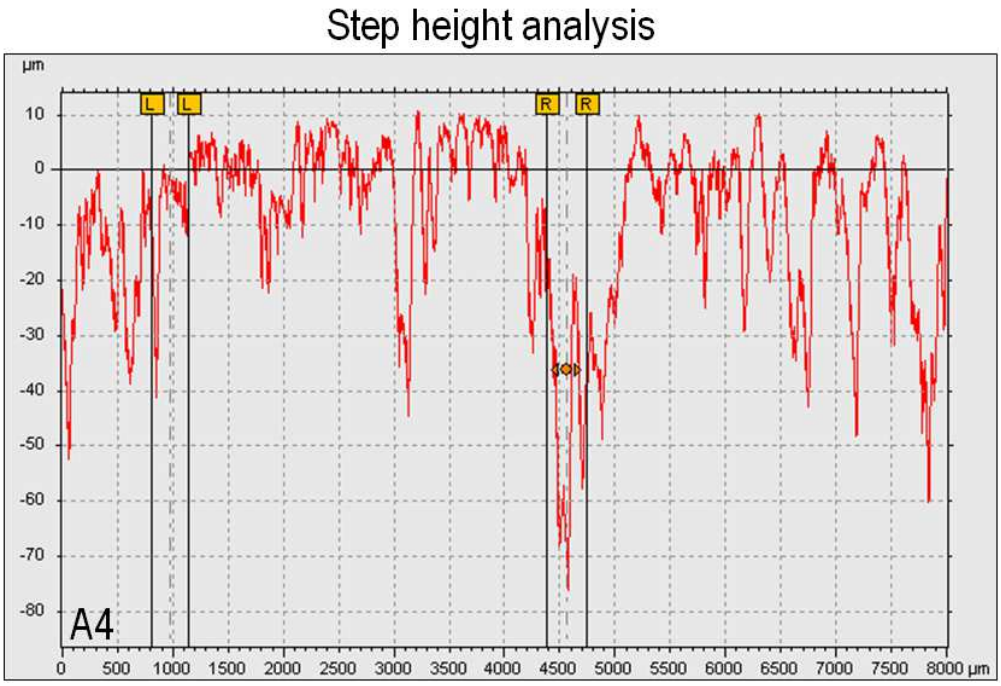

Figure 4.7: A4 raw data

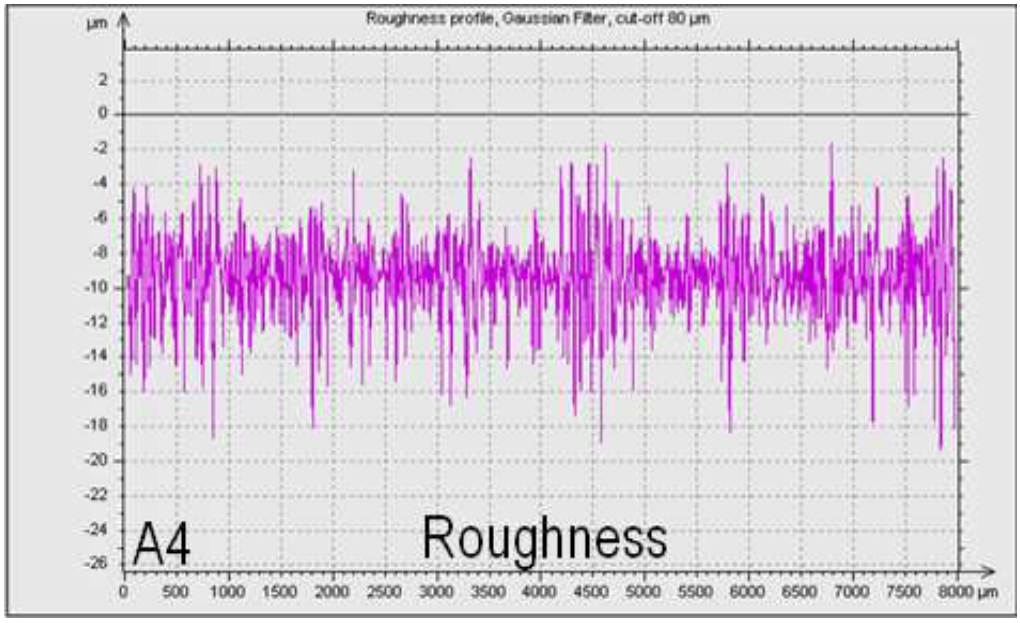

Figure 4.8: Results of the data elaboration for A4.

About the prototype A4, two different superimposed behaviours can be found: a regular smaller scale trend of ~20µm deep, ~100µm wide, and a periodicity of 100µm along the tile; and a larger scale trend of 40-50µm deep, 300-500µm wide, and a periodicity larger than 0.5mm along the tile. Similar results can be found also for B1 prototype.

Supplier A explained that profilometry findings on smaller scale are linked to fibre type: 200μm is the scale of the fibre bundles (fibre bundles used are 12K: 12,000 fibres per bundle), concerning the larger scale trend, it can be due to machining.

By microscopic observation of the prototypes, the structure of the tiles from different producers do not seem very different.

In any case, for diagnostic use, no problems are expected for the data interpretation on the beamlet spatial scale, and these results can be considered acceptable.

4.4 X-ray Diffraction (XRD)

X-ray diffraction analysis (XRD) is performed inside a device equipped with an X-ray source, a support for the sample and a collector. The X-rays are produced when electrically charged particles of sufficient energy are decelerated [54]. Electrons produced inside an X-ray source, accelerated by the high voltage between the electrodes of the source, reach the sample. As the electrons impact with the sample, X-rays are produced and radiate in all directions. As the X-ray clash with the crystal lattice planes, they are scattered (Figure 4.9). In most positions the scattering rays interfere destructively; if scattering rays in a certain direction are in phase with scattered rays from other atomic planes, constructive interference (diffraction) occurs. Due to the characteristic atomic structure of each crystalline material, there is a unique diffraction pattern of the X-rays, so it is univocally related to the material analysed. The diffracted radiation is collected by a detector. The method used to carry out this analysis is the θ 2θ procedure: the sample holder and the detector are mechanically coupled: the specimen is angled of θ with respect to the source and the detector is angled of another θ angle with respect to the specimen, as shown in Figure 4.9.

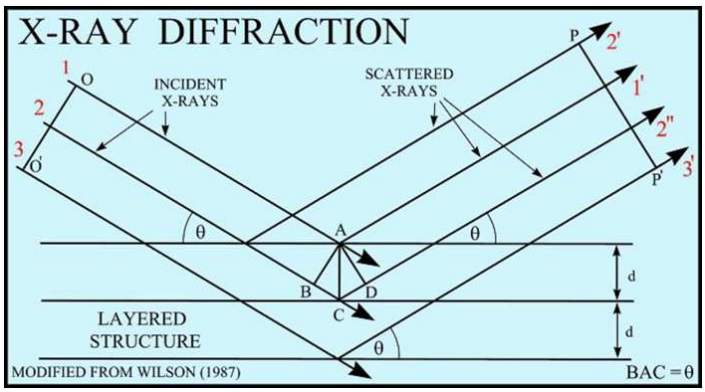

Figure 4.9: Scheme of the X-rays diffraction.

Two specimens coming from the A supplier have been analysed: a sheet of fibre bundles, the starting sheet to produce the material, and a piece detached from the A4 tile, when the manufacturing process was completed. These samples are shown in Figure 4.10.

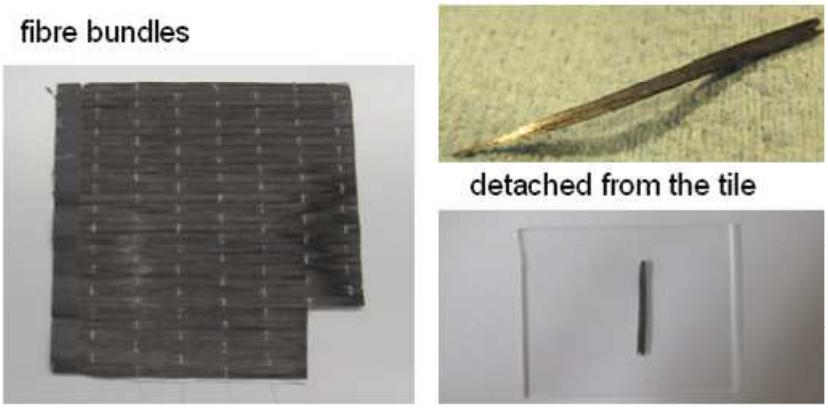

Figure 4.10: Samples for XRD analysis: fibre bundles (left hand side) and a splinter detached from the CFC tile (right hand side).

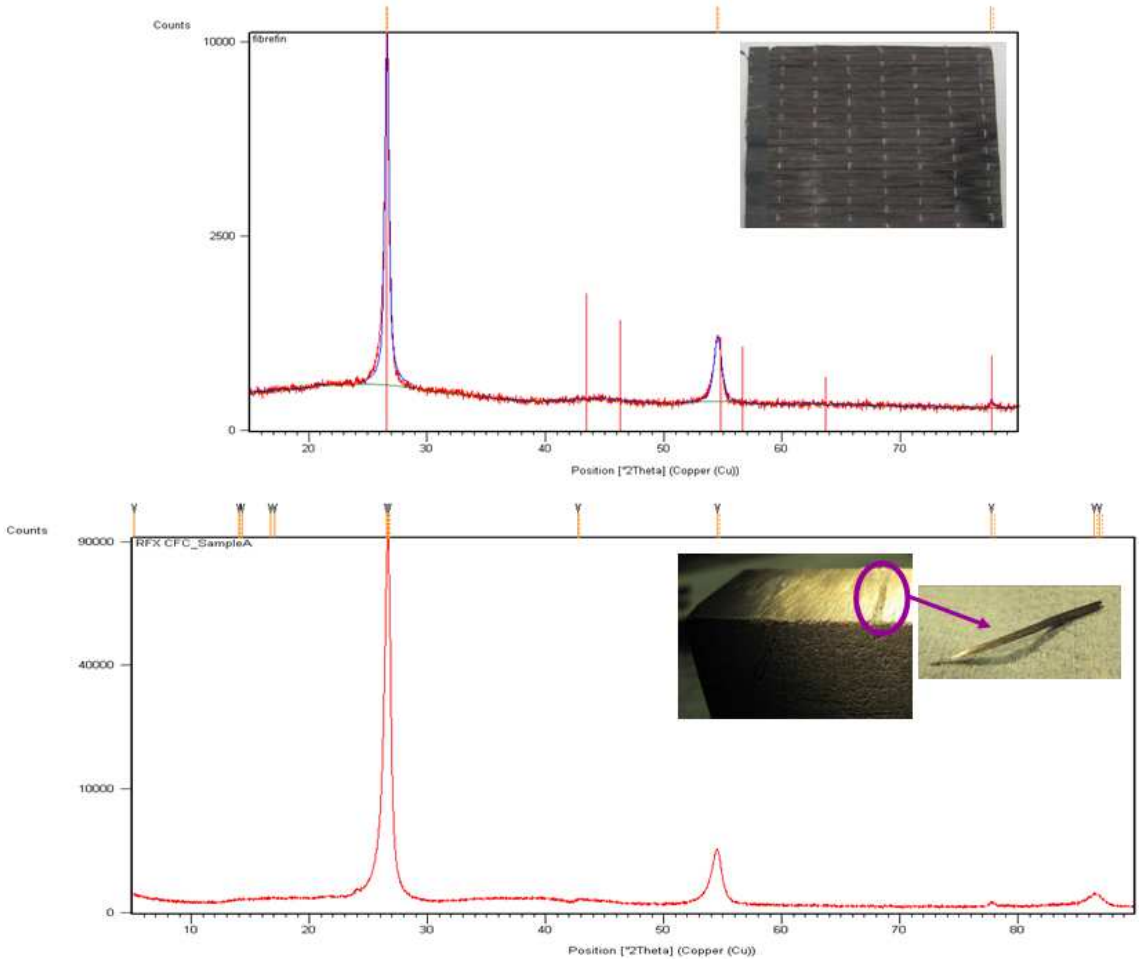

Figure 4.11: XRD results for fibre bundles (up) and the splinter detached from the CFC tile (bottom)

In the upper profile, the red line represents the experimental data, the blue line represents the fit made by the software and the vertical red lines indicate the position of the graphite coming from the literature.

The size of the crystallites is 200 Å for the fibre bundle sheet and 270 Å for the CFC; values relative to the peak of the maximum intensity at 2θ =26.6°. The preferential orientation of the crystallites is along the {111} plane family.

Similar results are obtained from fibre sheet and final material, demonstrating that during the production process no extraneous material has been added to graphite.

The presence of the asymmetrical peaks and shifts at angles different with respect to the literature reveal stresses and lattice defects.

4.5 Optical analyses

Prototypes B1, B2, B3, A4 and A5 have been subjected to an optical analysis, to better understand the findings previously described. For tile B, only the B1 has been tested because B2 is from the same batch and of the same dimension of B1, whereas B3 is also from the same batch but is thinner than the other two. In particular, the A5 has been produced with the aim of improving the production process and with particular attention to the stack of fibre bundles: A4 has had a larger graphitisation rate at 3000K.

Figure 4.12 shows both sides of the tile named A4, as Figure 4.13 for A5 and Figure 4.14 for B1:

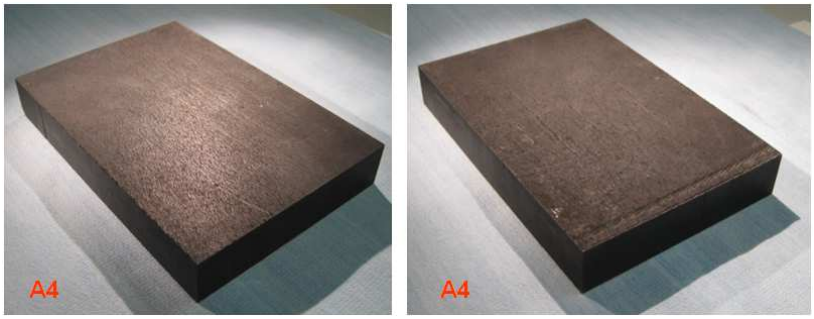

Figure 4.12: Prototype A4: both sides.

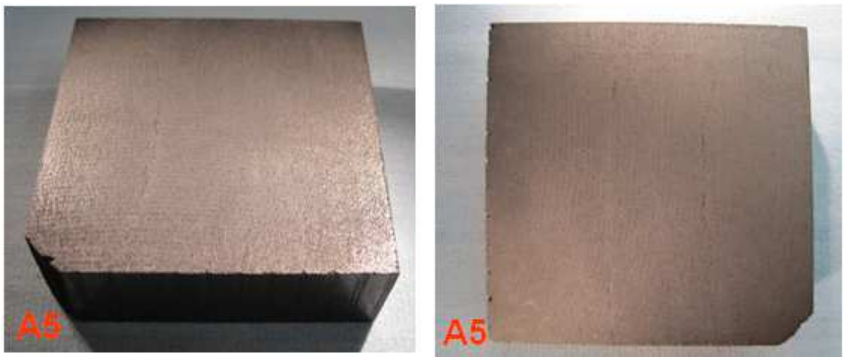

Figure 4.13: Prototype A5: both sides.

Tiles A4 and A5 were made by the same supplier and A5 is expected to be better than the previous tile produced A4.

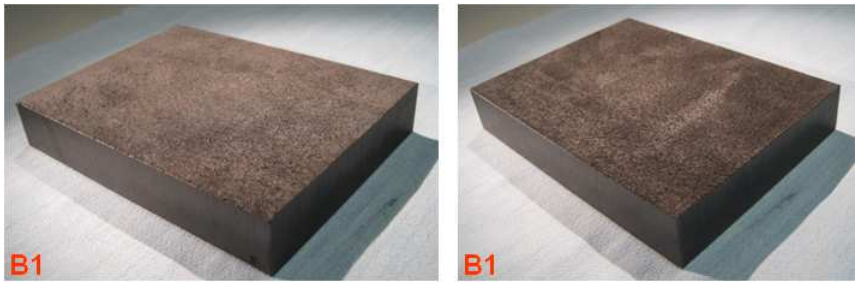

Figure 4.14: Prototype B1: both sides.

The first observations of tile A4, by means of laser pulse (chapter 5), have highlighted some linear patterns in the thermal images; due to this findings, the surfaces of the tile were carefully observed. Corresponding to the lines in the thermal image, the tile surfaces present linear scratches and a study of the small scale structure of such scratches was suggested. The scope of this analysis is to characterise the status of the prototype surfaces by looking for defects or specific areas that might affect heat propagation in the bulk causing deformation of the thermal pattern while passing from the front side, hit by the laser, to the rear side, observed by the thermal camera. The first system used for optical analysis of tile prototypes was a microscope (Nikon SMZ-2T, 10*21 lens), shown on the left hand side of Figure 4.15. It provides the following magnification: 2x, 3x, 4x, 5x and 6.3x. The details on the tile are illuminated by an optic fibre lamps and the optic fibres are suitably positioned to illuminate the observed area. The image of the area under investigation is displayed on a dedicated monitor.

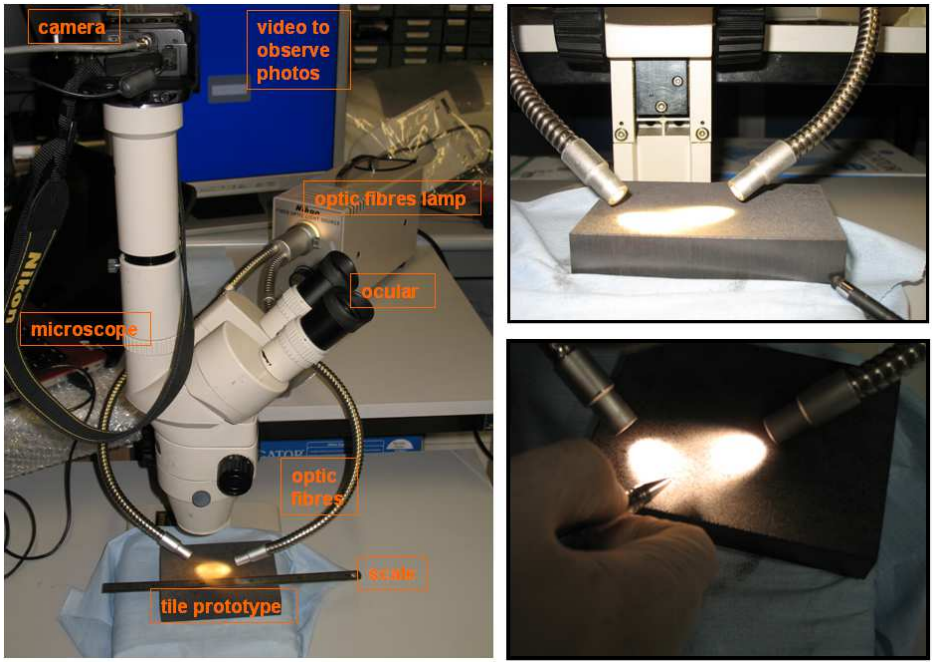

Figure 4.15: Microscope set-up.

Examples of photos for tile B1 are shown in Figure 4.16. Images refer to the extremes of the magnification range of the microscope; in both images, on the left hand side the scale is indicated by a ruler: every notch corresponds to 0.5mm.

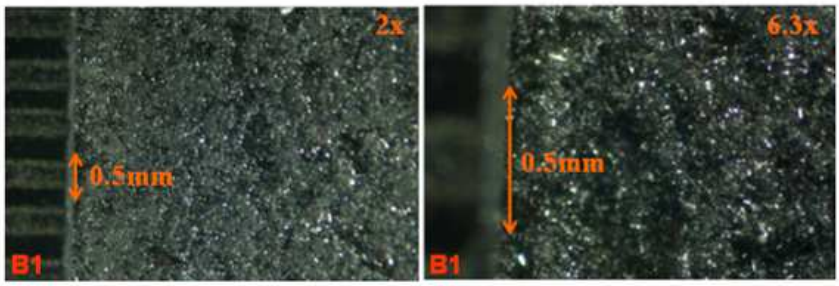

Figure 4.16: Microscope image of prototype B1.

To improve the magnification, a new device was used, with an optical system that allows reaching 18.4x. This system is shown in Figure 4.17: the magnification of the picture depends on the relative position of the lenses contained in the bellows: at the maximum extension the maximum enlargement is possible, as the bellows are completely compressed, the minimum magnification can be obtained; precise positioning of the bellows is provided by a fine adjustment screw. The image is recorded by a camera and can be seen on a monitor.

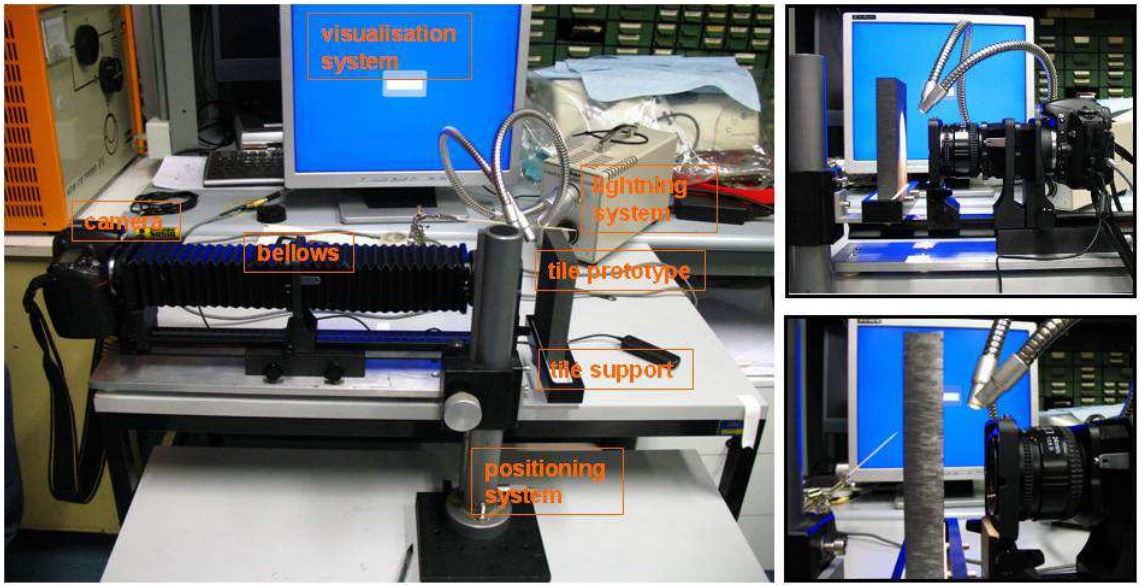

Figure 4.17: Set-up for the larger enlargement.

A comparison between images taken with these two different systems is shown in Figure 4.18:

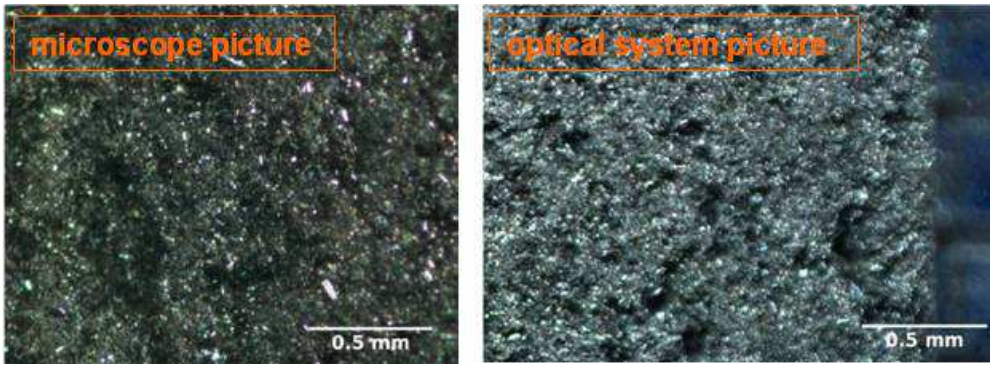

Figure 4.18: Comparison between images from microscope (left hand side) and optical system (right hand side).

The pictures shown in the following were taken by the optical system, which allows higher magnifications and clearer images.

To evaluate the depth of the scratches, the focus was in turns changed from the crest to the valley of the structures on the sample surface, and from the difference of the prototype positions, the depth of the scratch can be estimated.

B1 prototype:

The surfaces of this prototype look uniform and compact and no relevant regions were identified.

A4 prototype:

Figure 4.19 shows the area in which the observation was focalised. The image on the right hand side is the specular one. Some signs are present on both surfaces and are highlighted: considering that they correspond to the linear patterns in the thermal images, it might be deduced that the signs are cracks, extending in the bulk of the tile from one side to the other one. Some examples of these scratches are reported in the following: the scratch B, in Figure 4.20, whose width is 0.1-0.2mm; in Figure 4.21 the scratch C, which seem deeper than B but its width is comparable: about 0.1-0.2mm; and at last scratch D, the width is of about 0.5mm and it is visible also on the other side.

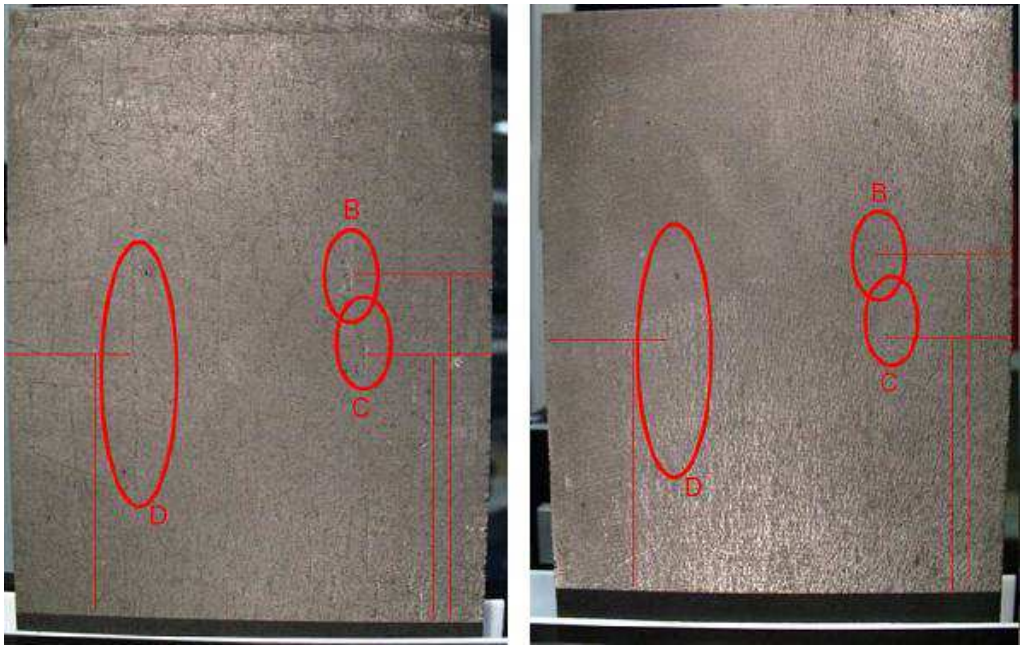

Figure 4.19: Signs on both sides of prototype A4.

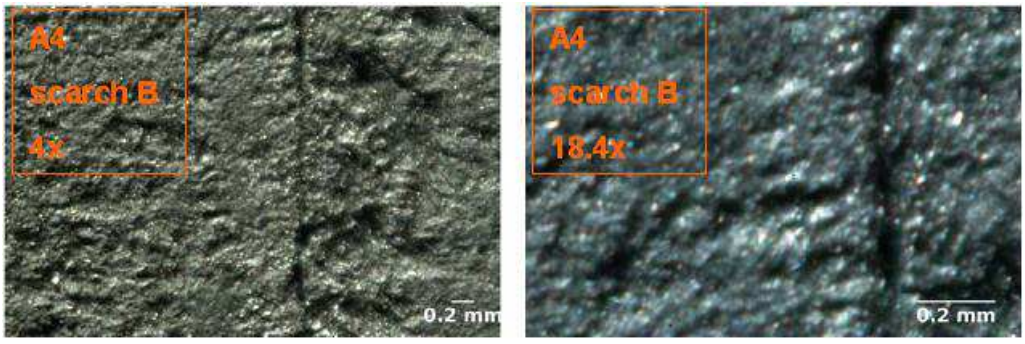

Figure 4.20: 4x (left), 18.4x (right), scratch B, prototype A4.

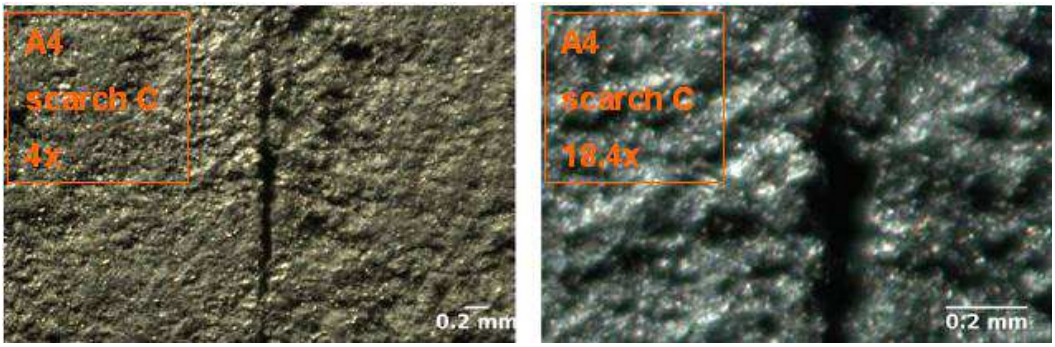

Figure 4.21: 4x (left), 18.4x (right), scratch C, prototype A4

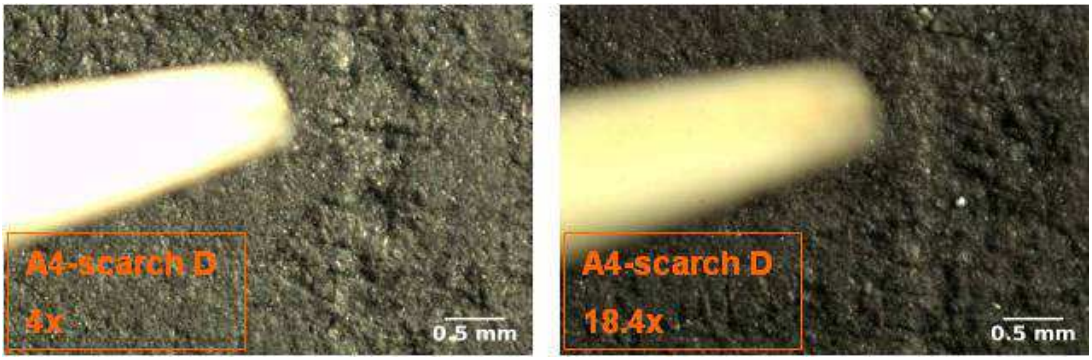

Figure 4.22: 4x (left), 18.4x (right), scratch D, prototype A4.

A5 prototype:

To remove this defect, another prototype has been produced and optically analysed. Unfortunately, also in this prototype scratches can be observed on both sides and some of them seem to be in correspondence from one side to the other. Figure 4.23 shows scratches on both sides. The image on the right hand side is the specular one.

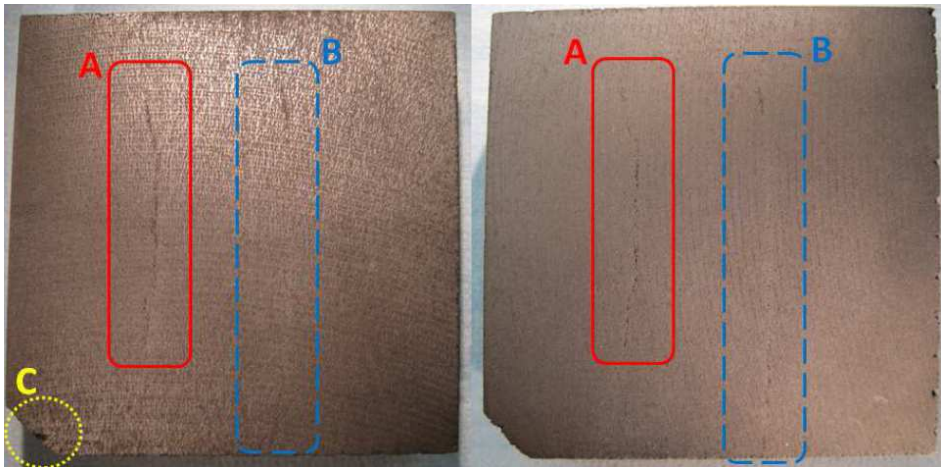

Figure 4.23: The studied regions of the A5 prototype.

In the following, details of these scratches are shown. In Figure 4.24 the scratch A of prototype A5 is shown. This scratch analysed is on the surface shown on the left hand side of the previous picture. The width is about 0.5mm, the central part of this scratch is deep but changing the focus to highlight the bottom of this scratch, it can not be seen. This means that the scratch would be too deep to be seen with the used instrumentation (light cannot penetrate deep enough to illuminate the bottom of the scratch).

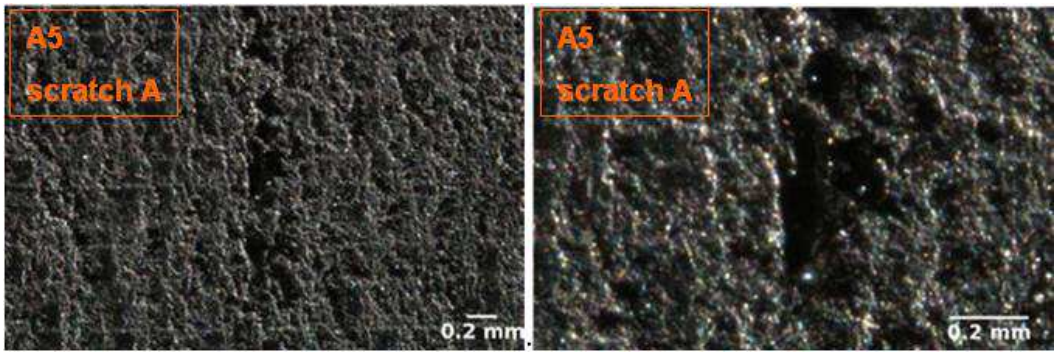

Figure 4.24: Scratch A of prototype A5.

The scratch B, on the surface shown at the left hand side of Figure 4.23, is shown below (Figure 4.25); the sign is of 0.4-0.5mm width and also a smaller and deeper one can be noticed, of about 0.1mm width.

Figure 4.25: Scratch B of prototype A5.

The scratch B on the other side of the tile is shown in Figure 4.26: it can be concluded that on this side scratch B is not evident: imperfections are present but the slit does not affect the whole bulk.

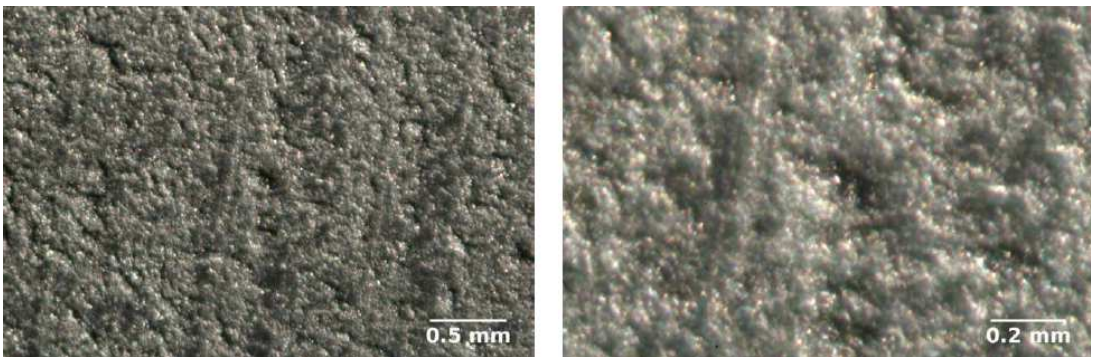

Figure 4.26: Magnification of prototype A5.

In Figure 4.27 focus is on the crest (left) and on valley (right side) of position C (left hand side of Figure 4.23): the distance indicated with the red arrow is 1.5-2mm and the one indicated with the green arrow is about 0.5mm. The distance between crest and valley is 0.48mm.

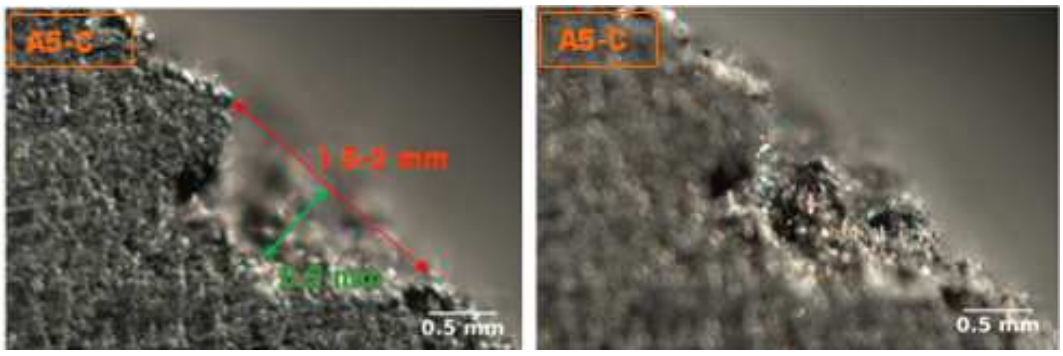

Figure 4.27: corner of A5, position C.

This analysis has highlighted that for tiles A4 and A5, macroscopic signs can be found and for both prototypes the typical dimensions are 0.1-0.2mm width and lengths of several centimetres. About prototype B1, no particular signs have been found.

Supplier A explained that scratches-defects are linked to the arrangement of fibres before the heating procedure; the scratch-defect is produced during one of the heating phases; unfortunately it cannot be detected before the end of the production process.

5 Tests on CFC prototypes by power laser pulses

The laser tests have been performed to reproduce the SPIDER conditions in terms of maximum power density of a single beamlet and with patterns on the same spatial scale as beamlet. A CO_2 power laser (nominal λ=10.6μm) was used, with power ranging from 20W to 100W; the laser light was focussed by a lens system reaching power density between about 6 to 32 MW/m^2. The application of the heat load was varied from some tens of seconds to one minute.

These tests permit to get confidence with the experimental conditions and to characterize the CFC in terms of its thermal behaviour. The characterization of the prototypes was achieved by reconstructing the experimental data with the simulated data, obtained by varying the thermal characteristics of the material with respect to the reference values provided by the supplier.

All prototypes have been tested with the laser.

5.1 Layout for laser test

To perform the tests, the laser beam was routed by suitable optical system onto the CFC prototype surface. The layout is shown in Figure 5.1. The observation of the CFC is performed at the rear side, the opposite surface with respect to the illuminated one, as foreseen by the calorimeter design. The CO_2 laser is dedicated to a particular diagnostic for the experiment RFX-mod, so for the tests the original layout was modified as little as possible: the only variation is the last mirror that deviates the CO_2 laser beam onto the tile instead of letting it enter the second laser for infrared polarimetry [55] of the RFX-mod experiment. The shutter can intercept the laser beam if necessary, between successive pulses (section 5.3); the mirrors deviate the beam and the lens is used to focalize the 1cm diameter laser beam at the exit of the device on the tile surface, to have a point-like thermal load: the laser spot diameter was 2mm, much smaller than the thermal pattern on the rear side, which is larger than 10mm.

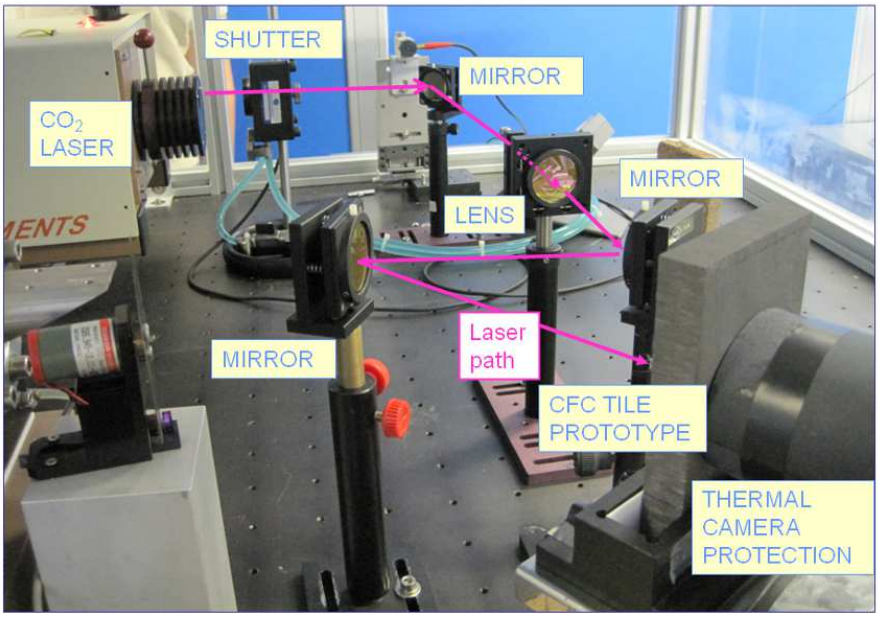

Figure 5.1: Laser test set up.

5.2 Thermal analysis

Thermal camera images recorded during laser tests show that the scratches observed and studied during the optical analysis are visible in the 2D thermal map (Figure 5.2) and a clear temperature gradient appears in correspondence of those scratches, as shown in Figure 5.3. In Figure 5.2 a) the large circle due to the thermal camera protection (Figure 5.1) is also recognisable.

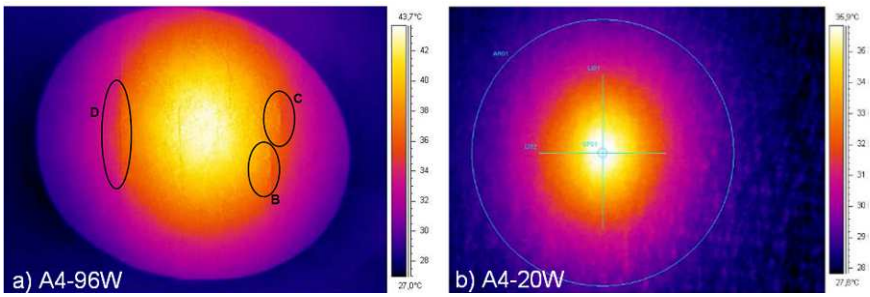

Figure 5.2: a) scratches observed in the thermal images; b) elliptical thermal pattern.

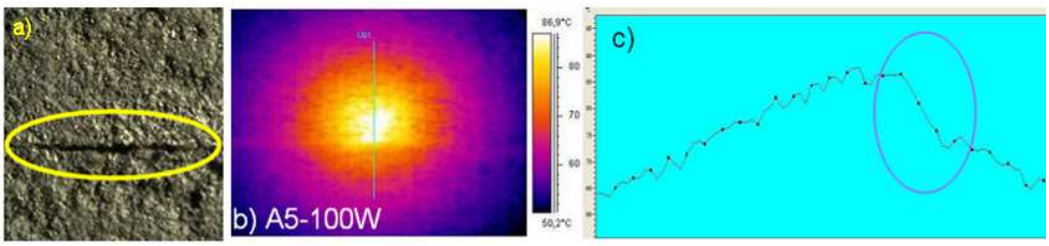

Figure 5.3: Temperature gradient on the scratch.

During the first laser test campaign another evidence was found: the ellipticity of the thermal pattern as observed on the rear side of the tile, as shown in Figure 5.2, b). This parameter played an important role in the CFC characterization and has been widely studied. It is very important in the discussion with the producer A to refine the manufacturing process. The assessment of the ellipticity will be an acceptance criterion for the supply of STRIKE tiles.

Scratches and ellipticity have been observed on the first prototype A4 and on the second A5, realised with the aim to improve the manufacturing process. Such defects have not been observed on the prototypes supplied by the producer B.

5.3 Comparison between experimental data and simulation data

In the optimization procedure the experimental data are reproduced by means of non-linear transient thermal simulations performed by the finite element code COMSOL [48]. Thermal radiation is applied to all sides towards surfaces at 300K. Simulations are adapted to the experimental data collected during the laser power application (20s) by varying the thermal parameters of the simulated material; other effects can also play an important role: for instance, as the thermal front propagates, it will reach the edges of the tiles, affecting the width of the thermal pattern and more generally distorting it; this is much more conspicuous when no more heat is supplied.

Notwithstanding the high ratio between thermal conductivities of the CFC, while transferring from the front to the rear side of the tile, the heat diffuses laterally so on the back side of the tile, which is the side observed by thermal camera, the thermal footprint is larger than on the front side; so much so that the focalized laser can be considered as a point-like source.

The amount of experimental data is quite large, resulting from several hundreds of frames having 480x640 pixels. So to compare experimental and simulated data a representation by suitable fitting functions is adopted. To this purpose, several functions have been tested: the Gauss curve, monodimensional in eq. 5.1 and two-dimensional in eq. 5.2:

$$y(x) = a_0 \exp\left(-\frac{(x-a_1)^2}{2a_2^2}\right) \quad \text{eq. 5.1} \qquad z(x,y) = a_0 \exp\left(-\frac{(x-a_1)^2}{2a_2^2} - \frac{(y-a_3)^2}{2a_4^2}\right) \quad \text{eq. 5.2}$$

a_0: maximum temperature that corresponds to the peak of the curve;

a_1 and a_3: widths of the curve;

a_2 and a_4: centre of the curve.

The modified Lorentz curve: 1D in eq. 5.3 and 2D in eq. 5.4:

$$y(x) = \frac{a_0}{1 + \left(\frac{|x - a_1|}{a_3} \right)^{a_5}} \qquad \text{eq. 5.3}$$

$$z(x,y) = \frac{a_0}{\left(\sqrt{\left(\frac{x - a_1}{a_3} \right)^2 + \left(\frac{y - a_2}{a_4} \right)^2} \right)^{a_5} + 1} \qquad \text{eq. 5.4}$$

a_0: maximum temperature that corresponds to the peak of the curve;

a_1 and a_2: centre of the curve;

a_3 and a_4: curve half widths at half maximum.

The most suitable one resulted the modified Hubbert curve (Figure 7.33) (eq. 5.5 for the 1D description and eq. 5.6 for the 2D description), which is capable of properly representing the thermal profiles at several instants, during laser application as well as after the application of the heat load, when the heat diffuses into the bulk of the tile.

$$y(x) = \frac{a_0}{\left[\cosh\left(\frac{|x - a_1|}{a_2} \right) \right]^{a_3}} \qquad \text{eq. 5.5}$$

$$z(x,y) = \frac{a_0}{\left(\cosh\left(\sqrt{\left(\frac{x - a_1}{a_3} \right)^2 + \left(\frac{y - a_2}{a_4} \right)^2} \right) \right)^{a_5}} \qquad \text{eq. 5.6}$$

The most important parameters in the data analysis are the peak of the curve, namely the maximum temperature that corresponds to the a_0 parameter; parameter a_1 determines the centre of the curve; the width of the curve, in particular the half width at half maximum (HWHM) that gives information about the shape of the thermal pattern after propagation inside the bulk material and is related to the parameters a_2 and a_3; the ellipticity defined as the ratio between vertical and horizontal HWHMs, a parameter “created ad hoc” to describe the experimental evidence observed on the thermal pattern at the rear side of the tile since the first laser tests (Figure 5.2, b).

The analyses were performed in 1D (considering data along vertical or horizontal lines passing through the temperature peak) and 2D, using programmes developed in the Interactive Data Language (IDL).

The temperature variation depending on the power density has been studied: the relation that links the temperature increase to the incident power density (q) on the surface, with q independent from time and thermal parameters independent from temperature, in a one-dimensional approximation, is:

$$T(x,t) - T_i = \frac{2q\left(\frac{\alpha t}{\pi} \right)^{1/2}}{k} e^{-\frac{x^2}{4\alpha t}} - \frac{qx}{k} erfc\left(\frac{x}{2\sqrt{\alpha t}} \right)$$

where

- T(x,t) [K] = temperature at time t, in a point at distance x from the surface hit by the power density;
- T_i [K] = initial temperature;
- q [W/m^2] = incident power density on the surface;
- α [m^2/s] =$k/(\rho c_s)$ = thermal diffusivity;
- k [W/m K] = thermal conductivity;
- ρ [kg/m^3] = density;
- c_s [J/kg K] = specific heat.

So, the relation follows a linear law, once x (the rear side of the tile) and t are fixed.

In this way, the temperature increment as a function of the laser power can be obtained from the data. Comparing the angular coefficients of the lines resulting from experimental data and from simulated data, yields a feedback on the correctness of the simulations. An example for prototype A4 is shown in Figure 5.4 for the experimental data and in Figure 5.5 for the synthetic data, at 20s that corresponds to the end of the heat load application. The angular coefficient resulting from the fit of the experimental data is 0.75±0.02 K/W and for the simulation is 0.773 K/W.

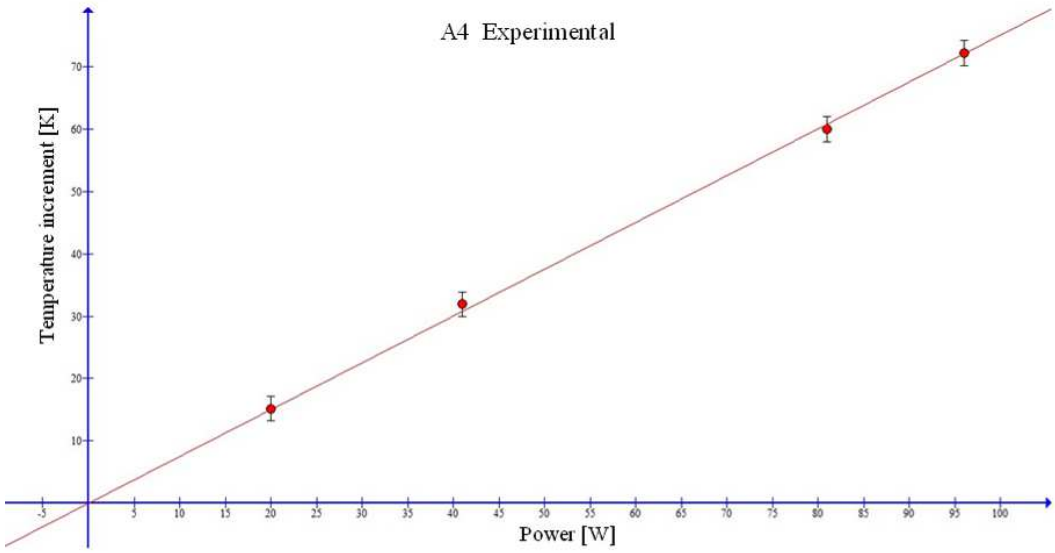

Figure 5.4: A4 fit of the experimental data, t=20s.

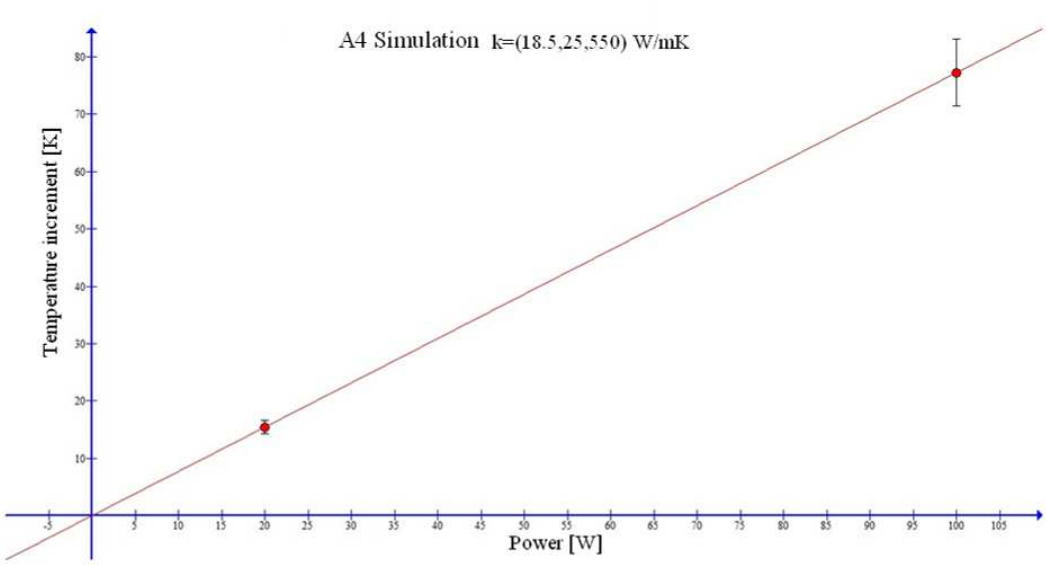

Figure 5.5: A4 fit of the simulated data, t=20s.

The producer A has supplied values for thermal parameters only at room temperature: 767 J/kgK for the specific heat, 550W/mK for the thermal conductivity parallel to the fibres (along tiles thickness) and the in-plane thermal conductivities of 25W/mK, the density ρ = 1950 kg/m^3. This is not the better solution but due to the lower increment of tile temperature during laser tests the simulation result introducing the previous parameter has been considered reliable.

To reconstruct the ellipticity of tile A4, thermal conductivities orthogonal to the fibre direction (in-plane thermal conductivities, k_x and k_y) have been varied with respect to the values provided by the producer. The higher the three thermal conductivities, the lower is the maximum temperature; the higher the in-plane thermal conductivities, the higher are the HWHMs, so several combinations have been tried.

In Figure 5.6 the results of simulations with different thermal parameters are compared with the experimental data for prototype A4 and the best fitting thermal parameters are given; it appears that to reproduce the experimental value of ellipticity 1.2, a ratio of about 1.4 between the vertical and horizontal in-plane thermal conductivities is required. Also the high value of the ratio between parallel and in-plane thermal conductivities of tiles A should be highlighted, with respect to tiles B (15 from data sheet). Experiment and simulation data of amplitude, vertical HWHM and ellipticity for A4 are shown in Figure 5.6; arrows indicate the direction of the fitting procedure. The first parameter set (red line) can not reproduce very well the peak and the ellipticity; to increase the ellipticity, the vertical thermal conductivity was increased and in fact the ellipticity, at least during the pulse, is similar to the experimental value (green line) but in this case the maximum temperature further decreases. The best results (cyan line) has been

obtained by decreasing the horizontal thermal conductivity and at the same time by increasing the vertical thermal conductivity with respect to the supplier data, while maintaining a ratio of 1.4 between the two values.

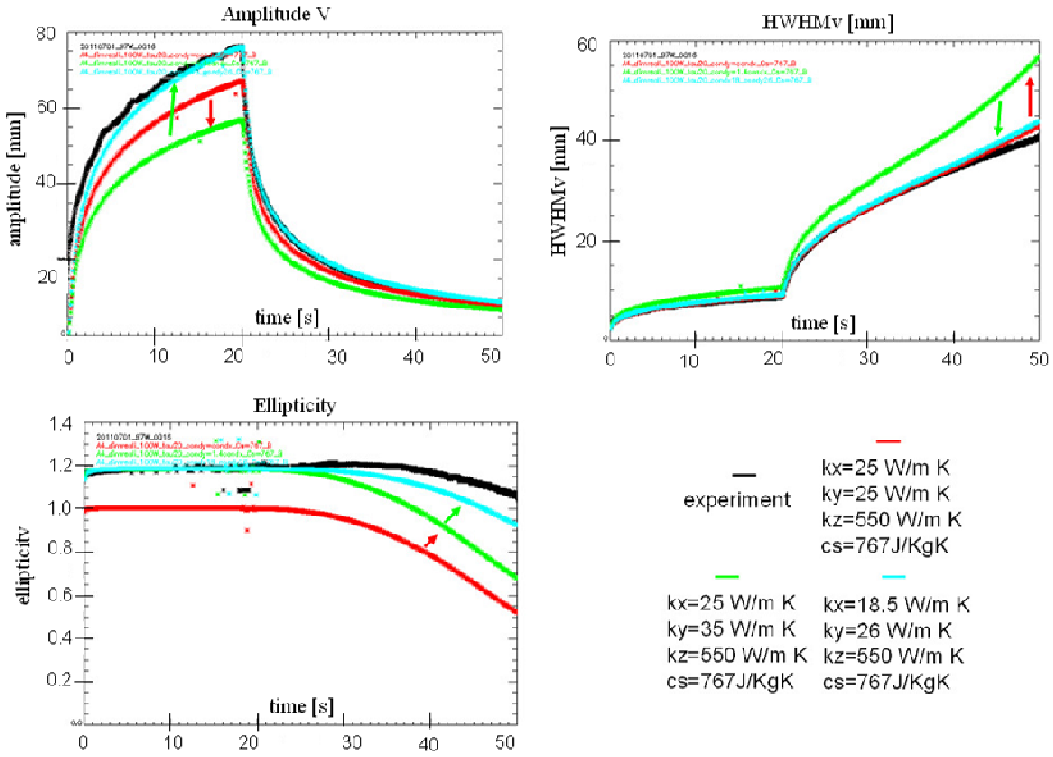

Figure 5.6: Experiment and simulation data of amplitude, vertical HWHM and ellipticity for A4.

The resulting thermal parameters for tile A4 are18.5W/mK, 26W/mK and 550W/mK for the horizontal, vertical and parallel thermal conductivities.

The same procedure was followed for A5 tile, starting from the thermal parameters found for A4 since the supplier is the same but no mach between experiments and simulations had been found.

Experimental values to be matched, derived from a mean of several experiments at 100W, are:

Tmax [K]	HWHMx [mm]	HWHMy [mm]	e
350	8.03	9.20	1.15

Table 5.1: Values to be matched for A5.

Variation on the vertical thermal conductivity k_y was performed to match the maximum temperature but the ellipticity could not be reconstructed, as shown in Figure 5.7 for the laser application of 20s at 100W. The red and black curves represent data displaying the maximum

and minimum temperature obtained among all experiments on A5; the green curve shows the simulation result considering k=(25, 65, 550)W/mK; with this value for the thermal conductivity the simulation matches the value of the peak; the ellipticity is not well reproduced.

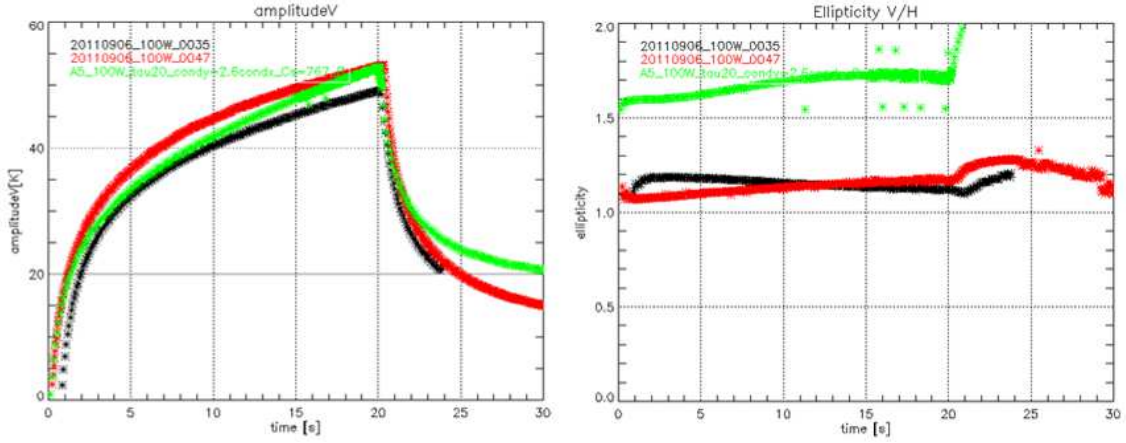

Figure 5.7: Example of no match between experimental data and simulation for A5.

In the attempt to maintain the matched maximum temperature and at the same time to find a correspondence also for the ellipticity, other simulations were run by keeping constant the ratio between the in-plane thermal conductivities k_y/k_x and changing also the thermal conductivity parallel to the fibres k_z and the specific heat c_s. Aiming at quantifying the optimization through the combination of the three thermal conductivities and of the specific heat, a figure of merit was defined:

$$F = \sqrt{\left[\frac{(T_{\max})_s - (T_{\max})_e}{(T_{\max})_e}\right]^2 + \left[\frac{(HWHM_x)_s - (HWHM_y)_e}{(HWHM_x)_e}\right]^2 + \left[\frac{(HWHM_y)_s - (HWHM_y)_e}{(HWHM_y)_e}\right]^2}$$

Considering the trends of the figures of merit, an indication of the way to change the thermal parameters of the tile in the simulations has been suggested. F tends to minimize the difference of the simulation results with respect to experimental ones simultaneously for all parameter evaluated to assess the goodness of the reproducing simulation.

But also in this case no match was found, as shown in the examples for amplitude and ellipticity reported in Figure 5.8.

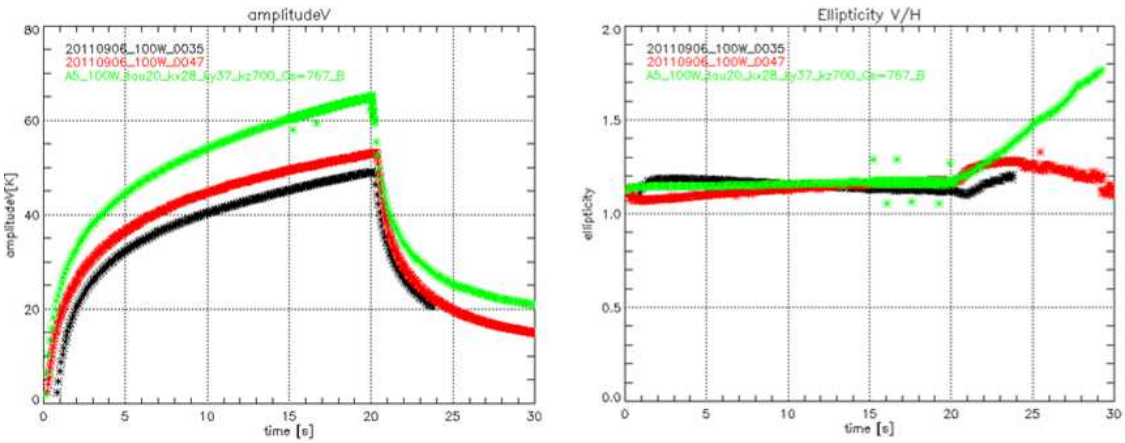

Figure 5.8: Example of no match between experimental data and simulation for A5.

Graphs in Figure 5.8 were obtained with no variation of the specific heat; the ellipticity is well reproduced but the maximum temperature is not: it was observed that the specific heat directly affects the temperature, so some simulations should be done increasing this parameter. Moreover, further considerations have been done about the experiments: it is possible that during the tests some amount of the incident laser power has been lost so the real incident power is less than 100W. This could have occurred due to:

- Optical system: it could absorb and diffuse power during the transmission of the laser. To assess this contribution a test was performed: measuring the power at the beginning (just outside the laser) and at the end (at the tile) of the optical path, no difference can be observed. This cause of loss has been discarded;
- Light diffusion from the tile surface: a small amount of the power can by diffused by the tile towards the surrounding environment; during a dedicated check, however, no diffused power was detected by the measurement instrument (within the instrument sensitivity). This cause of loss was discarded;
- Light reflection at the tile surface: the tile is no blackbody, its emissivity is lower than 1 so part of the laser beam can be reflected. Experimental evidence of reflection was found: a paper sheet in front of the tile shows burn signs, confirming the reflection. Figure 5.9 shows two signs: the big one is due to the laser spot and the small one is the reflected beam.

Consequently on these findings, the measurement of the reflection was performed on all tiles. The reflected power for tile A5 is 5% of the incident power. As shown previously, the maximum temperature is proportional to the absorbed power and the reflected part can explain the impossibility to well reconstruct the data, as described before. The measurement on tile A4 has highlighted a reflection on the incident power of about 1.4%, corresponding to some

thousand mW, negligible for the comparison between simulations and experimental data, explaining why experimental data were reproduced by the simulations.

Moreover, the thermal camera error (±2K) was considered in the analysis together with 7.5% instrumental error for the measurement of the reflection power (the instruments were not absolutely calibrated).

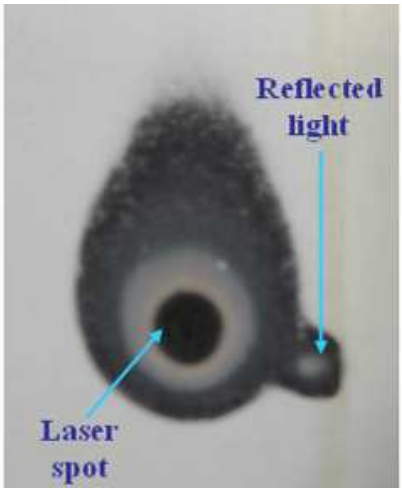

Figure 5.9: Measuring of the reflected power.

Including the previous considerations, a set of suitable thermal parameter for tile A5 can be obtained: thermal conductivities k=(25, 32, 550)W/mK and specific heat c_s=1000J/kgK. Figure 5.10 shows the final results concerning the maximum temperature, including the error bars. The analysis of tile A5 was not continued further, as the tile anyway has a size much smaller than the other samples.

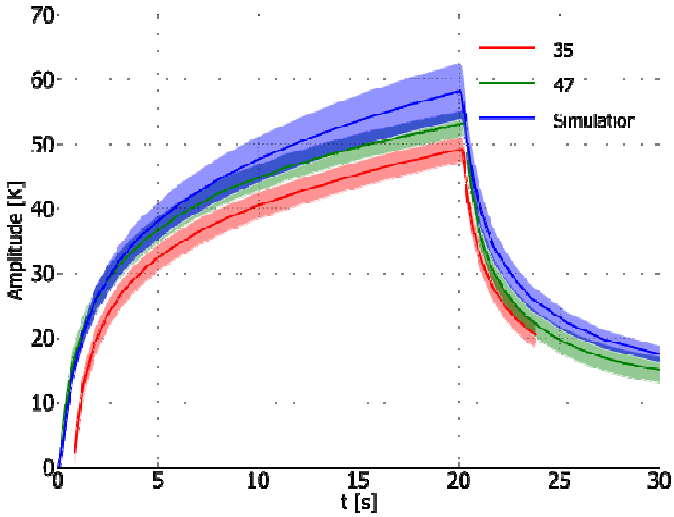

Figure 5.10: Compatibility between simulation end experiments on maximum temperature.

Concerning tile A6, reflection depends on the side illuminated by the laser: there is a large reflection on one side, the smoother one, of 18%, and a moderate reflection on the other, the rougher side, of 2.5% (Figure 5.11).

Figure 5.11: Smooth side and rough side of A6 tile.

If on both sides of the tile the reflection measured is the same, the parameters can be univocally obtained, but if the reflection depends on the incident point, as in the case A6, a pulse which impacts on the smoother side of the tile does not lead to the same thermal profile as a pulse with the same characteristics impacting on the rougher side. Moreover, due to different reflectivity coefficient of the surfaces, a different emissivity has to be set on the thermal camera: for instance, if the beam impacts on the rough surface, in the simulations the energy of the beam must be reduced, considering a coefficient of reflectivity equal to 2.5%, at the same time in the parameters of the thermal camera, observing the opposite side an emissivity equal to 0.82 must be set for the temperature map.

Experimental values to be matched, derived from a mean concerning all experiments on A6 at 100W power laser, are:

Tmax [K]	HWHMx [mm]	HWHMy [mm]	e
113	6.3	6.9	1.095

Table 5.2: Values to be matched for A6.

As a first tentative, the specific heat and the thermal conductivity perpendicular to the tile surface (k_z) were considered known parameters, since it was the same manufacturer who supplied them and they were confirmed by the comparison with the simulations of tiles A4 and A5; the values of thermal conductivity in the two directions parallel to the tile surface (k_x and k_y) were then searched for; the values of these parameters which lead to the best correspondence between experimental data and numerical analyses are: thermal conductivities k=(16, 19.5, 550)W/mK and specific heat c_s=767J/kgK. Figure 5.12 shows the reconstruction of experimental data by means of simulation with the thermal parameters previously defined: the green line refers to the simulation; red and black lines instead represent the extreme values of the range obtained by all experiment on A6. In the following figure also 2D results are displayed about ellipticity.

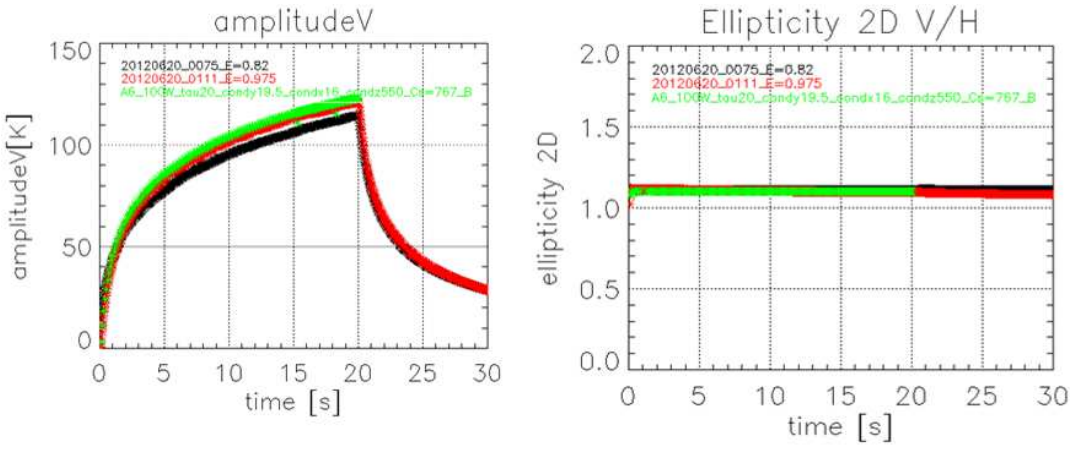

Figure 5.12: Matching between experiment and simulation for A6.

Reflection measurements on tile A7 has led to a negligible reflection power on both sides; the comparisons with numerical simulations on this tile have not been performed up to now.

Tiles B1, B2 and B3 are the most similar to each other since they derived from the same batch. In particular, it is important to characterize and compare B1 and B2 prototypes; they have also the same dimensions, to get a good knowledge of the tiles to be used to study the BATMAN beam during the foreseen experiments (chapter 7). No correction to the thermal parameters was applied in the simulations with respect to those received from the supplier; thermal parameters are introduced in the model as functions of temperature, with trends and descriptive formulas as in Figure 5.13.

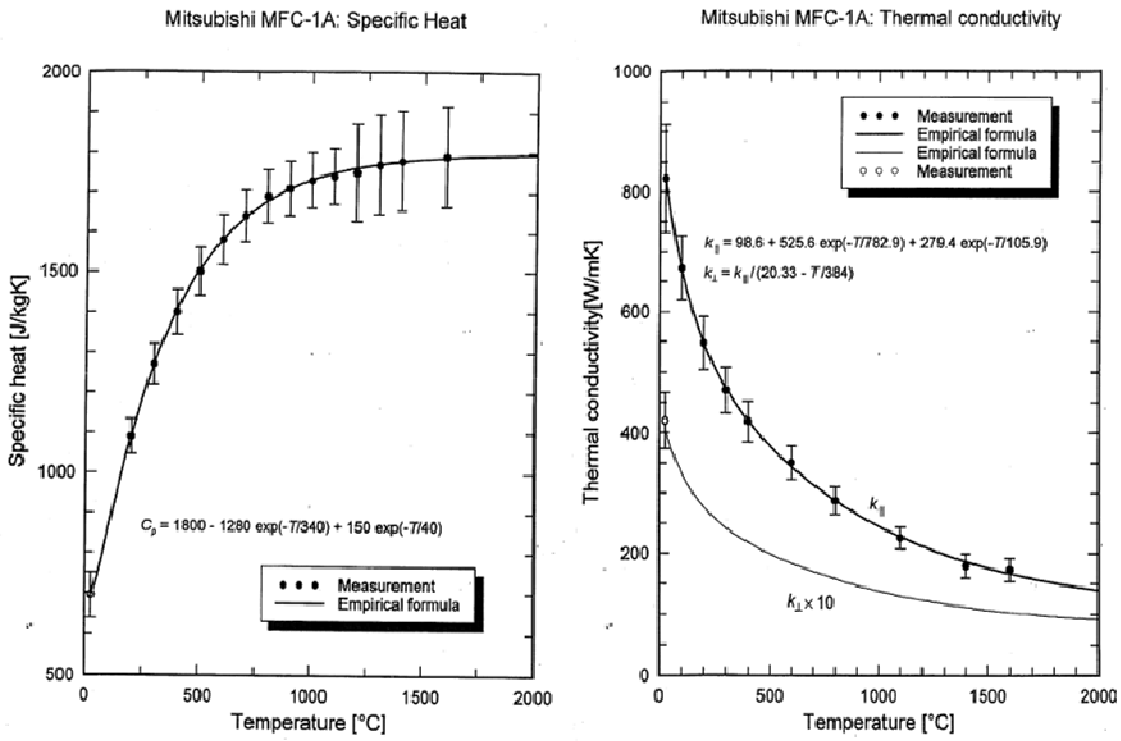

Figure 5.13: Thermal parameter for tile B.

So at 50°C, the maximum observed during the experiments, the specific heat is 738J/kgK and the thermal conductivity parallel to the fibre 766W/mK and the in-plane thermal conductivities 38W/mK.

The trends of temperature peak and ellipticity, from 2D data analyses, are presented in Figure 5.14: the green trend refers to the simulation, the red one to the experimental data for tile B1 and the black one to experimental data for tile B2. It is clear that the simulation fits the data very well.

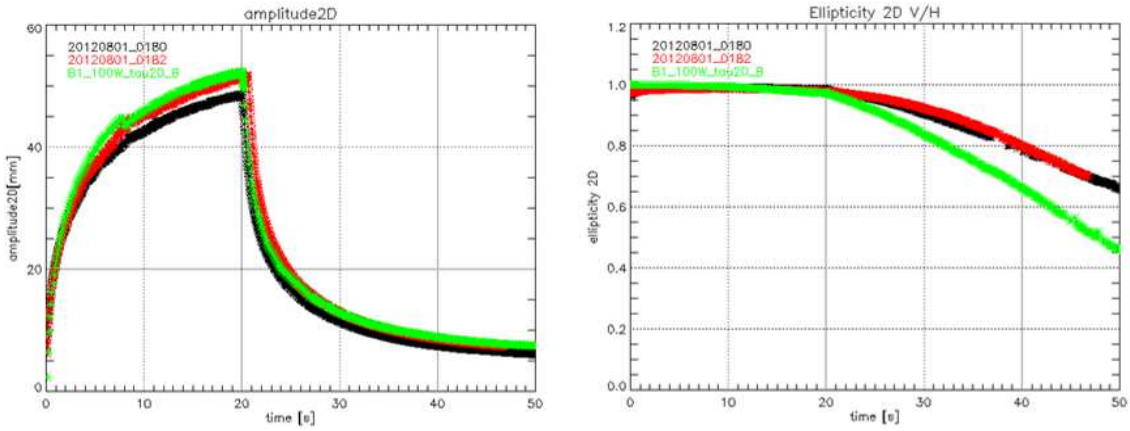

Figure 5.14: Comparison between B1 (red) and B2 (black) experimental data and simulation (green) data.

Measurement of the reflection at the prototype surface should be considered, but for B tiles the reflectivity ranges only from 0.05% to 0.35%, corresponding to some tens of mW, so this component has been neglected on both sides of all prototypes B. Instead, some issues, as for the other prototypes, have been taken into account: ±2° measurement error by thermal camera and ±7.5% estimated error of laser power meter. The following table compares the maximum temperatures from experiments and from simulations, by applying the aforementioned corrections: the results are in good agreement.

	T_{max}	error	resulting range
B1	51 K	±2 K	49-53 K
B2	48 K	±2 K	46-50 K
simulation	52 K	±7.5%	48-56 K

Table 5.3: Summary of maximum temperatures for B1, B2 and related simulation.

The same analysis has been performed on the third prototype B3 and the same results, temperature peak and ellipticity, from 2D data analysis, are shown in Figure 5.15. Also for this prototype experimental data and simulations are in good agreement. The higher maximum temperature with respect to B1 and B2 is due to the smaller thickness.

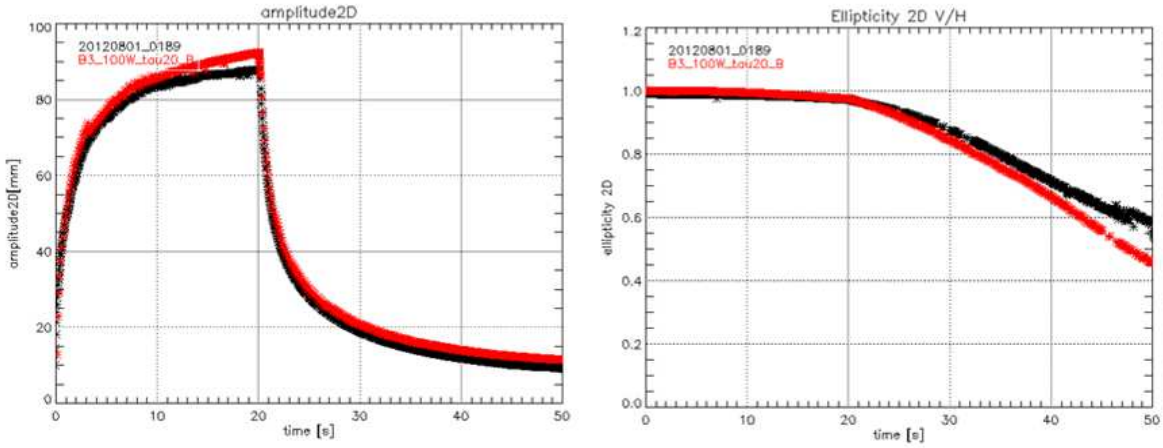

Figure 5.15: comparison between B3 experimental data and simulation data.

The following table shows maximum temperature from experiments and simulations, including the corrections.

	T_{max}	error	resulting range
B3	87 K	±2 K	85-89 K
simulation	92 K	±7.5%	85.1-98.9 K

Table 5.4: Summary of maximum temperature for B3 and related simulation.

6 Validation of the design

The design of STRIKE has been accompany by a series of validation documents and tests. These activities have contributed to the project of STRIKE and to the optimization of the design to reduce the possible failure risks.

According to the PMBOK® Guide, risk is “an uncertain event or condition that, if it occurs, has a positive or negative effect on a project’s objectives” [56].

This replies to the ISO 9001 requirements about preventive actions within a project.

In particular, quality in the design includes some actions:

verification: confirmation, through the provision of objective evidence, that specified requirements have been fulfilled (for instance by mean of simulations, tests, experiments);

validation: confirmation, through the provision of objective evidence, that the requirements for a specific intended use or application have been fulfilled (for instance by means of series of tests covering all the operating conditions and operating procedures);

review: activity undertaken to determine the suitability, adequacy and effectiveness of the subject matter to achieve established objectives, for instance by mean of a meeting with involved parties (internal, external) where the design status is presented (verifications and validations included) and decisions are taken about problems and risks.

In this chapter, an overview of the quality documents drawn up for the STRIKE calorimeter and of the validation tests is presented.

6.1 Risk analysis

The risk analysis is the first step in estimating the impact of the risks: usually the risk analysis is done at the beginning of the project, and when significant decisions are made; it has the aim of minimizing and controlling the risks linked to the project and concerns the project management risks.

The risks identified in the risk analysis document are classified according to the following categories [57]:

- technical risks (customer requirements, product performances and safety, design and development processes, new technologies, production processes, “special processes”, complexities, interfacings, …);
- external risks (suppliers, laws and rules, market, customers, catastrophic events, lack of natural resources, …);

- organizational risks (resources, links with other projects, organizational priorities, …);
- project specific risks (estimates of times, costs, resources, problems on the control of the project status, communication issues, …).

The identified risks are recorded in the Risk Management and Preventive Actions Form, represented in Table 6.2 for STRIKE; their impact on the project and their probability of occurrence can be estimated.

Risks are treated according to the following Table 6.1 [57].

Probability and impact are rated according to the risk management and preventive actions form.

probability	10					
	8					
	6					
	4					
	2					
		2	4	6	8	10
	impact					

Table 6.1: Probability and impact matrix.

The results of the intersection between probability and impact can have different importance:

- if the intersection results in a red box, risks require urgent or near term response;
- if it is an orange box, risks require additional analyses and response action (that can be planned, not urgent or near term);
- a yellow box means low priority risks, periodically reassessed but no action is needed.

Risks shall be monitored and controlled by an iterative process of risk identification, assessment and treatment.

A scheme of the process that leads to the risk analysis document is shown below [56]:

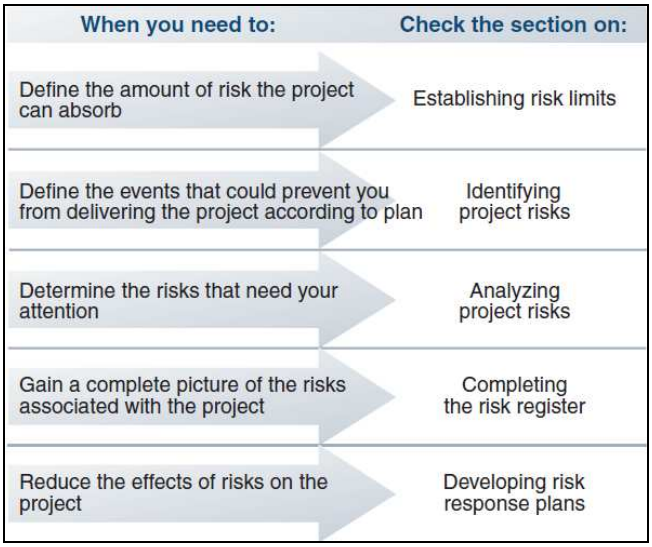

Figure 6.1: Scheme to the reduction of the risk analysis document.

The risk analysis for STRIKE was carried out by identifying the kind of risks that might be expected for the component and detailing specific items for each type of risks. To each item the impact and probability indices are associated and their combination gives the risk number.

RISK DESCRIPTION (POTENTIAL NONCONFORMITY) AND ITS EFFECTS (functions, peformances, quality in general; costs; schedule and time; interfaces, impact on other teams)	Impact	ROOT CAUSES	Probab	Risk	POTENTIAL RESPONSES AND PREVENTIVE ACTIONS	Responsibility & Target Completion Date	Action Results			
							Verification (action completed) and Validation (effectiveness)	Impact	Probab	Risk
EXTERNAL RISKS				0						0
requirement changes by customer	4	improvement or external restrictive requirement	2	8	implement in the design the possibility to upgrade the system	WPM				0
supplier: time	4	delivery delay	4	16	verification of the supplier schedule and milestones	WPM+PP				0
supplier: quality	4	no conformity to standards required or to quality plan	2	8	implement in the Tec. Specs. Adequate test phases	WPM+QM				0
sub-suppliers: time	4	delivery delay	4	16	verification of the supplier and sub-supplie schedule and milestones	WPM+PP				0
sub-suppliers: quality	4	no conformity to standards required or to quality plan	4	16	implement in the Tec. Specs. Adequate test phases	WPM+QM				0
ORGANIZATIONAL RISKS										
project dependencies: availability of buildings and gen. services	8	building delay or building unfit for use	2	16	coordination with building and general services WPM	WPMs				0
project dependencies: vessel and source	8	vessel and source system delay or unfit for use	2	16	coordination with vessel and source system WPM	WPMs				0
resources: overallocated	6	delay of projects that cause overlapping	6	36	planning and monthly control of resources	WPM				0
funding:	0	not applicable	0	0						0
PROJECT MANAGEMENT RISKS										
cost estimating	4	cost underestimate	6	24	cost cross check	WPM				0
planning	4	activity delay	4	16	coordination and meeting with WPM	PL+WPM+PP				0
controlling	4	lack of control	4	16	coordination with WPM, monthly report with project leader	PL+WPM+PP+QM				0
communication	4	lack of communication	4	16	coordination and meeting with WPM, team	PL+WPM+QM				0

Table 6.2: STRIKE Risk Analysis.

For instance, the external risk concerning the supplier time involves a delay in the delivery of STRIKE components. This condition is judged as having a medium-low (4) impact and a medium-low (4) probability of occurrence, so the risk due to delay in the delivery is not so high. This external risk can be controlled by verification of the documentation prepared by the supplier, such as the milestones in the schedule.

About organizational risks, the over-allocation of the resources has the highest risk. If this condition is verified a delay in the project occurs and this may cause overlapping with other activities. So a good planning and a monthly control of the resources have to be applied.

Regarding the project management risks considered for STRIKE, the highest impact and probability of occurrence are expected for cost estimation. The underestimation of the cost could be a problem for this component so careful estimation and cross-checking of the costs are needed.

6.2 FMEA

The diagnosis of the SPIDER ion beam is the primary scope of STRIKE: the real capability of investigating the whole beam, directly related to the system integrity, and the capability of deducing the beam parameters, requiring good alignment with respect to the beam source, are of primary importance for this diagnostic. The failure mode and effects analysis (FMEA) was applied to identify the potential causes of failure and to study how to detect and possibly prevent the consequent failure modes.

A FMEA is an analytical technique that can be described as a systematic group of activities intended to:

- recognize and evaluate the potential failure of a product/process and the effects of that failure;
- identify actions that could eliminate or reduce the chance of occurrence of the potential failure;
- document the entire process.

It is complementary to the process of defining what a design or process must do to satisfy the customer [58].

A guideline to write the FMEA is shown in the following figure:

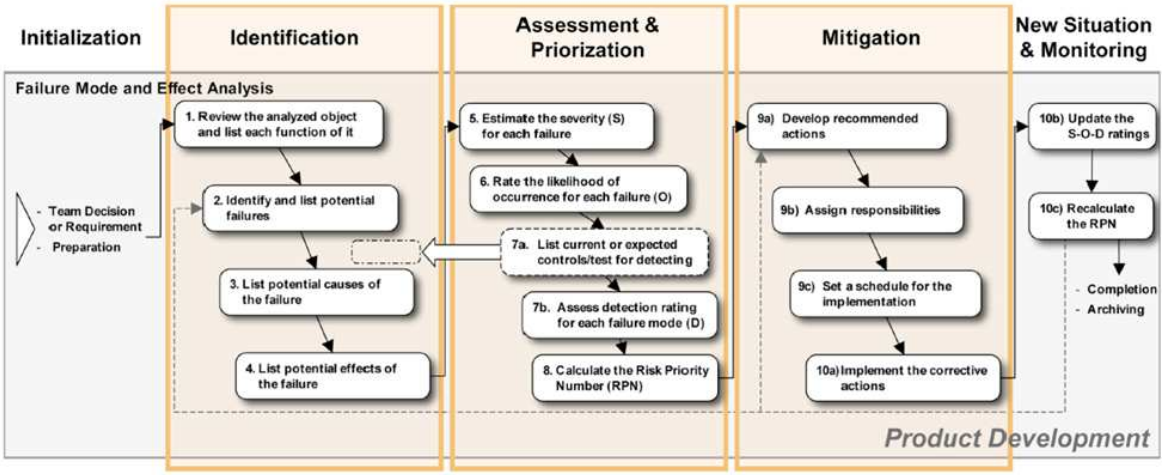

Figure 6.2: Schema for the drawing up of the FMEA [59].

The potential causes of failure for STRIKE are related to different areas, e.g., vacuum compatibility, system integrity, diagnosis of beam performances, and positioning. For each of the causes, the potential failure modes and their effects can be identified, together with detection methods and precautionary measures during manufacturing, maintenance, and periodical tests. To each potential cause of failure three numbers are associated whose product gives the risk priority number (RPN). RPN is an index of the gravity of the failure and it is the result of the ranking of severity (severity is the rank associated with the most serious effect for a given failure mode), occurrence (occurrence is the likelihood that a specific cause/mechanism will occur during the design life), and detection (detection is the rank associated with the best detection control listed in the design control) of the potential causes of failure [60]. Some examples of how the FMEA is compiled are described in the following.

A short circuit between tiles represents a potential cause of failure whose effect is the loss of the electrical insulation; the related failure mode is the reduction of the diagnostic capabilities of STRIKE. Another example can be done about the vacuum: an air leakage through STRIKE viewing windows or STRIKE feed-throughs can allow impurities to enter the vessel, the breakdown probability to increase, the pressure to go out of range etc., so that the air leakage into the vessel is not only involves the calorimeter but the entire SPIDER operation. Another example concerns the system integrity: the break of a tile, the loss of a screw, the detachment of a panel etc. can cause impediment to the movement, or damages to the pumping system or damages to the observation windows.

The FMEA has also to indicate methods to control the potential failure modes, both as prevention and survey, during the operation. Among the prevention actions identified for STRIKE, some example can be the ordinary maintenance, the monitoring (for example foreseeing installation of thermocouple in points like the stainless steel frame of the panels) and

a suitable design; it can be noticed how the verification of the design by means of suitable mock-ups (described in the following of this chapter) is an essential activity accompanying the design phase.

The detection methods are for instance the data analysis with which signal noise can be identified or using the calorimeter diagnostics; for example the FMEA, shown in the appendix, shows how the diagnostics of STRIKE can contribute to signalling potential risks. For example, the overheating of panels can compromise the system integrity by causing damages to tiles, panels, or cables. These failures (e.g., broken tile) can induce the detachment or the fall of some components (e.g., the tile). The thermal cameras can thus be used as a detection method for anomalies, also confirmed by thermocouples. Another way for checking the system integrity is through the current and the electrostatic probe measurements: in fact, if these measures become irregular, or absent, the electrical cables could be disconnected or have connection problems. Distinguishing electrical disconnection from tile detachment can be achieved by cross-checking with thermal measurements. Thermal cameras constitute the main diagnostic for evaluating the beam performances: the non-planarity of the panels or the frame, due to manufacturing, to thermal expansion, or as a result of internal stresses caused by thermal loads, can be reconstructed by analyzing the thermal pattern of the beam as seen on the rear side of the tiles. The accuracy of the axial positioning of STRIKE is ±5 mm: this allows to limit the error induced by the beamlet pattern below ±5‰, to recognize with a sufficient confidence whether the beam non-uniformity is within 10%. This requirement implies also a limit to the exposure angle accuracy: the beam facing surfaces of the tiles of each panel shall lie within two parallel vertical planes spaced by 10 mm.

The STRIKE Failure Mode and Effects Analysis table is shown in the appendix.

6.3 Control Plan

The Control Plan [61] defines the verifications, reviews and validations that ensure the quality of the deliverables and the control of the processes.

Among these activities those related to the safety are identified in a special column of the control plan (SRA column).

According to ISO 9001 (adopted ad standard for the quality of the management of the PMS project) verifications and validations are useful in several phases of the project, as illustrated in the following:

- in the design and development, to ensure the quality of the design against the requirements;

- in the procurement of materials, products and services, to ensure the quality of the supply;
- to validate the process and monitor the process parameters therefore ensuring the quality of the process output;
- on the products (deliverables), to accept and monitor the product quality.

The control plan is a tool to reduce the risk of nonconforming product.

For this reason the control plan takes into account the results of the FMEA Analysis and of the Risk Analysis: it implements the control actions identified in the FMEA, planned to avoid the failure foreseen.

The Control Plan is prepared by the project team, verified by the quality representative and approved by the quality representative and the project manager or the sponsor (at discretion of the sponsor). In Table 6.3 the STRIKE Control Plan is shown.

For instance, the control plans requires some verifications of the design, like tests on the thermocouple fixing system, whose detailed description can be found in section 6.5 as well as the test of the prototypes, which is reported in section 7.2.

Supplier			F4E	Notes & acronyms	
Prepared	Verified	Approved	Acceptance	D = Document Review V = Design Verification R = Review (e.g. Design Review, Project Review, Progress Review) W = (Monitor or) Witness NP = Notification Point ATP = Authorisation to Proceed Point HP = Hold Point S = Surveillance (S1:100%, S2:Random or Spot)	TP/NB = Third Party Inspection Authority (TP) / Notified Body (NB) or French Safety Authority (FSA) F4E = F4E or it's representative Other = Interested Party (specify)
			Name & Date		

Oper.#	Activity (verification, manufacture, inspection,...)	Specification (procedure, drw,...) and/or Standard	Acceptance Criteria	SRA (Y/N)	Verification by								Records (report, NCR, ...)	Observations
					RFX		F4E		TP/ NB		Other			
					Name, Sign & Date		Name, Sign & Date		Name, Sign & Date		Name, Sign & Date			
1	Internal review of STRIKE design	System Requirement Document; Work instructions requirements management	compliant to		R									
2	Test of thermocouple fixing system	System Requirement Document	compliant to		V									
3	Test of tile fixing system	System Requirement Document	compliant to		V									
4	Test of CFC prototypes	System Requirement Document												
5	Deformation verification													

Table 6.3: STRIKE Control Plan.

The control plan is used also to record the results of the verifications and validations; where these results need a specific report, the control plan refers to the report.

6.4 Design Review

The definition of review is the following: activity undertaken to determine the sustainability, adequacy and effectiveness of the subject matter to achieve established objectives [62].

At several stages of the design of STRIKE, design reviews have been performed, together with the project team, customer (F4E) and experts, to assess and discuss the present project and to validate the design, in the way towards the final design.

6.5 Mock-up of thermocouple fixing system

Tests on a mock-up were performed to complete the STRIKE design in terms of the thermocouple fixing system and of the position of the thermocouples on the tiles. The thermocouples used are the same as foreseen for STRIKE: type N, Inconel sheet, transition to kapton cable, 1mm external diameter. Both thermocouple design positions were: Figure 6.3 shows the mock-up, which reproduces a part of the frame of STRIKE panels as well as the thermocouple fixing system [63]; the thermocouples will be installed inside stainless steel pipes providing the elastic force for a sufficient thermal contact between the thermocouple junction and the tile surface (Figure 6.4, left); the thermocouple is held in place by a plate exhibiting a suitable housing for the pipe (Figure 6.4, right); the plate is fixed to the STRIKE frame (in the mock-up a piece of stainless-steel tubular pipe is used).

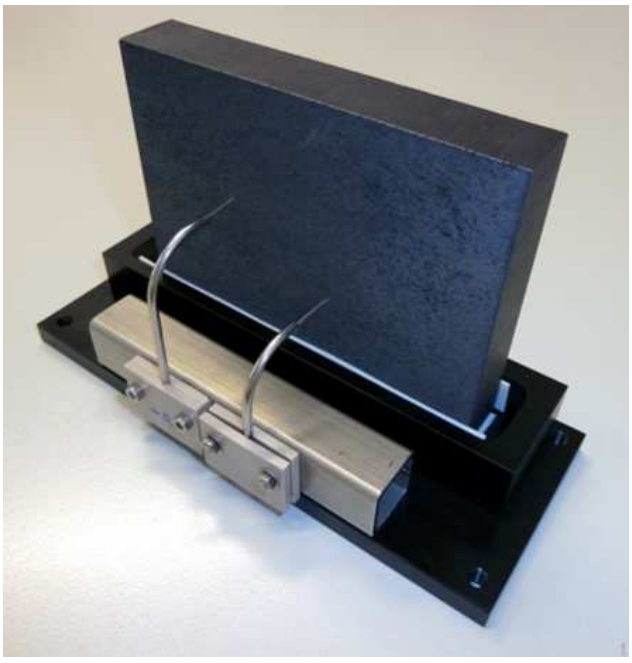

Figure 6.3: Mock-up for the thermocouple fixing system: global view.

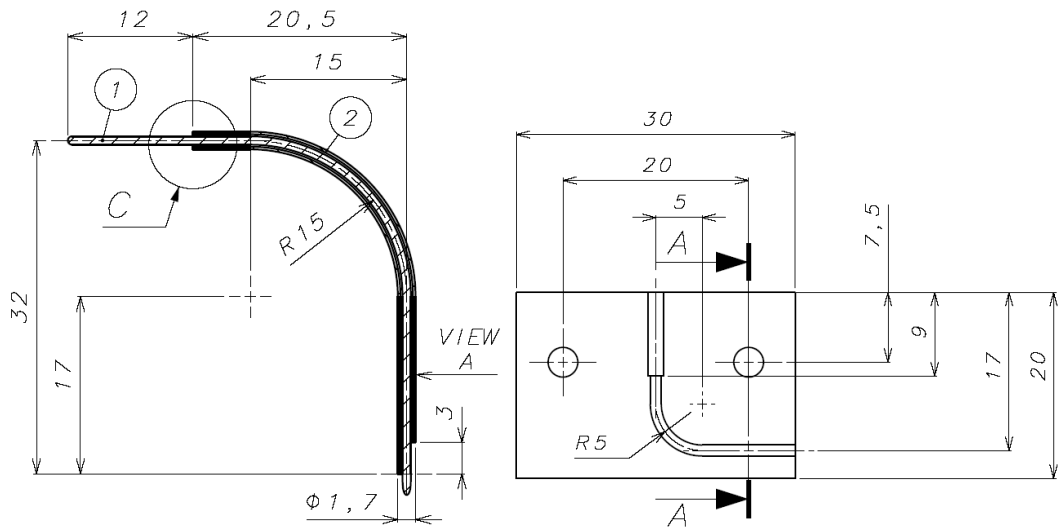

Figure 6.4: Mock-up for the thermocouple fixing system: thermocouple inside the pipe (left); fixing system of the pipe (right).

Different thermocouple positions with respect to the tile (the same as in STRIKE design for a hot point and a cold point), several values of heat loads and different ways of manufacturing the thermocouples have been analysed.

Several systems have been realised and compared to identify the suitable method to fix the stainless steel pipe to the thermocouple while guaranteeing the stiffness necessary for a good thermal contact without damaging the thermocouple.

6.5.1 Preliminary test on thermocouples

To guarantee that no damages result from manufacturing the connection of the thermocouples to the stainless steel pipes, a first preliminary measurement was carried out to verify that all thermocouples measure the same temperatures.

Thus, thermocouples were inserted into a climatic chamber, as shown in Figure 6.5.

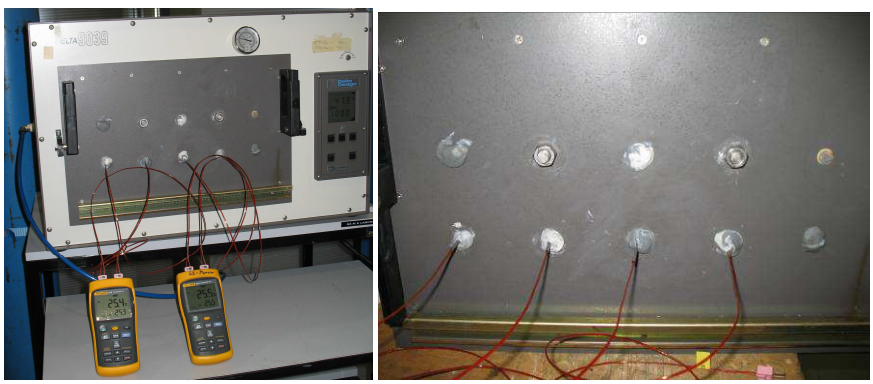

Figure 6.5: Climatic chamber for test of thermocouples (left), particular of the introduction of the thermocouples inside the climatic chamber (right).

To assure that differences in measurements are not depending on the thermocouple positions inside the chamber, thermocouple junctions were inserted into a copper body, mounted on the internal face of the chamber lid and visible in Figure 6.6.

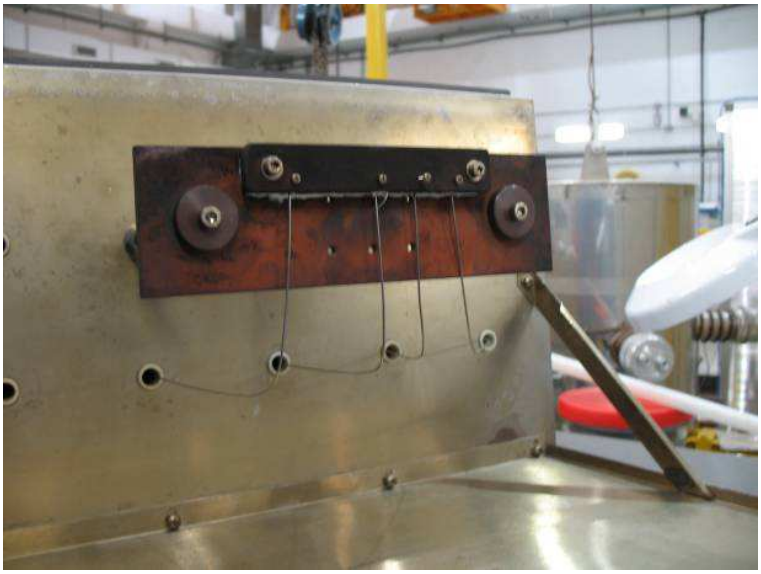

Figure 6.6: Positioning of thermocouples for the preliminary test.

The temperature of climatic chamber was pre-set at 300 °C and during the temperature increase, from room temperature to the pre-set one, thermocouple measurements were recorded every second.

Since the temperatures collected are in a good agreement with each other, we proceeded with the manufacturing of the junction.

6.5.2 Studies for connection of thermocouples to stainless steel pipes

The next step was manufacturing on thermocouple: curvature and fixing to a stainless steel pipe to guarantee the thrust of the thermocouple junction against the tile, like in the design (see Figure 3.24).

Several fixing systems were compared: Figure 6.7 shows the low temperature braze welding system on the thermocouple (identified as T1); even if it is not suitable for the operation temperatures expected at the rear side of STRIKE this type of connection was investigated because the brazing alloy can be substituted with one with higher temperature range.

Figure 6.7: Thermocouples braze welded to stainless steel pipe.

Another sample was realised by fixing the thermocouple to the stainless steel pipe by spot welding (thermocouple identified as T3), see Figure 6.8.

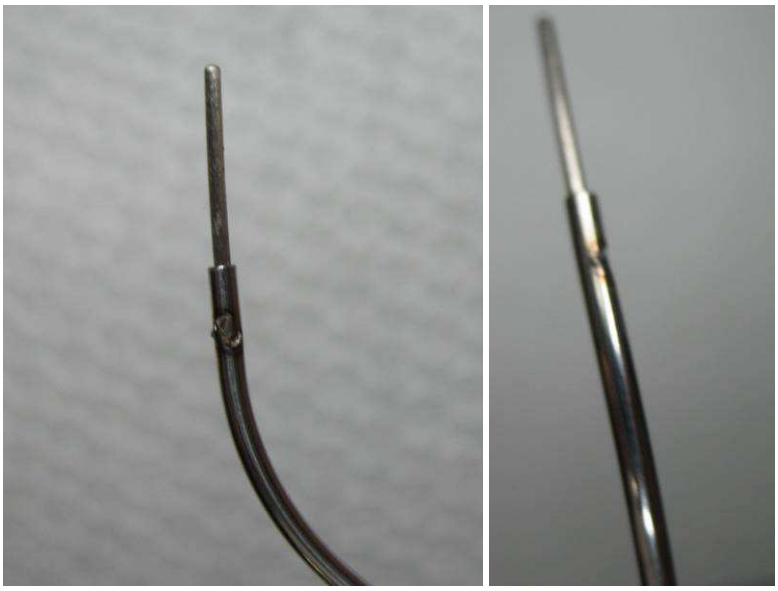

Figure 6.8: Thermocouples spot-welded to stainless steel pipe.

The third method was a sort of crimp on the thermocouple (identified as T2). In Figure 6.9 on the right, an expansion of the tip of the final system is shown: it looks like a triangle, because of the shape of the tool used to compress the stainless steel pipe around the thermocouple, as shown better in Figure 6.10, together with the tool employed for manufacturing.

Figure 6.9: Thermocouples crimped to stainless steel pipe (left); expansion of the tip (right).

Figure 6.10: System used to crimp the thermocouple (left) and crimped thermocouple cross-section.

After the manufacturing phase, the thermocouples were tested again in the climatic chamber, to verify that no damages had occurred. The position of each thermocouple was the same as the previous test.

Temperatures were in a good agreement with each other and with the first test performed.

6.5.3 Set up of the tests on thermocouple mock-up

Thermocouples were positioned as designed for STRIKE tiles; the stainless steel pipes were held in position by the insulating plates (Figure 6.11).

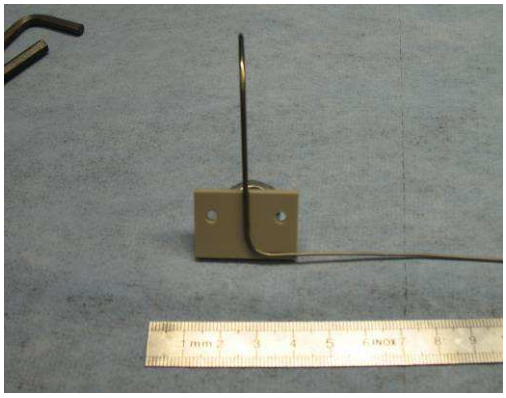

Figure 6.11: Fixing system for the thermocouples according to the preset design.

The tests consisted in measuring the temperature on the rear side of the tile prototype. The complete layout is shown in Figure 6.12.

Figure 6.12: Test set-up.

The heat load was applied by an air blower (Figure 6.13). A thermal camera was used for comparison the results, but the thermal camera data are not reported here. Two more thermocouples, as shown in Figure 6.14 and Figure 6.15, were used to have indications about the temperature of the air reaching the tile surface and the air temperature just outside the air blower, to be used as references for the applied power which can only be regulated by selecting different switch positions of the air blower. The thermal camera sensor was protected by a screen from the hot air produced by the air blower. Several experimental conditions were tested by changing heat load power (by the correspondent switch position) and the contact force between thermocouples and tile.

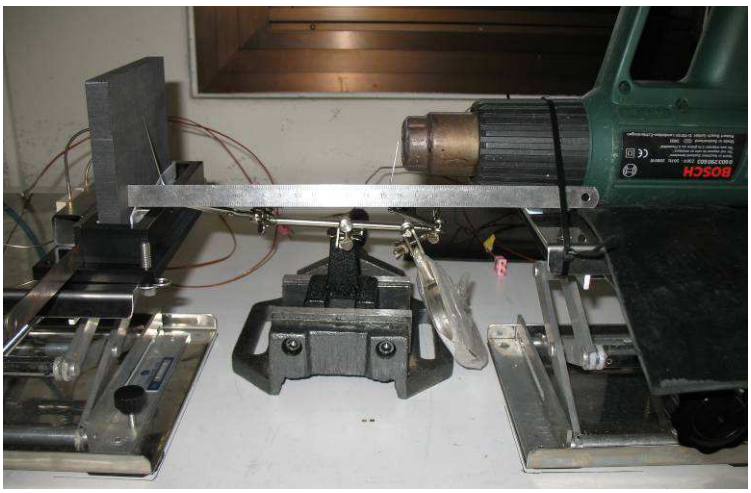

Figure 6.13: Detail of the test set-up.

Figure 6.14: Thermocouples positioning for tests.

Figure 6.15: Measurement of the temperature of the air blower.

An image recorded by thermal camera showing the position of T2 and T3 thermocouples is following.

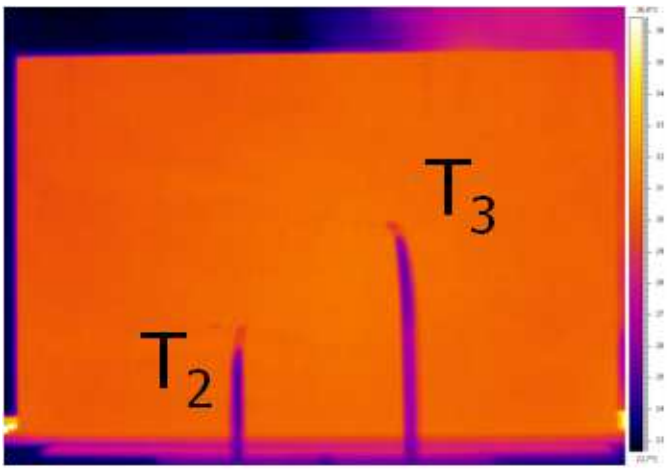

Figure 6.16: Frame from the thermal camera.

6.5.4 Results of the tests on thermocouple mock-up

Table 6.4 and Table 6.5 summarise the conditions of the tests carried out. Table 6.4 corresponds to tests on crimped and spot-welded thermocouples, while Table 6.5 corresponds to tests on the same crimped thermocouple and the braze-welded one. Only two positions of the switch, and correspondingly two powers, have been used: the maximum (pos.15) and an intermediate value (pos. 5). Moreover, care should be taken about the thermal contact and its influence on the measurement; to verify the effect of the thermal contact, several compressions between tile and thermocouple junction were tested.

N° test	switch	D
10	15	0.3 compression
11	5	0.3 compression
12	15	0.2 compression
13	5	0.2 compression
14	15	0.1 compression
15	5	0.1 compression

Table 6.4: Summary of the test using crimped and spot welded thermocouples.

When the thermocouples are just in contact with the tile surface, without exerting any pressure on it, the distance between tubular pipe and tile support is 6.9 mm (see D parameter in Figure 6.17). Different pressures and correspondingly different thermal contacts are provided by reducing such distance by the amount given in the tables before fixing the relative position of all parts.

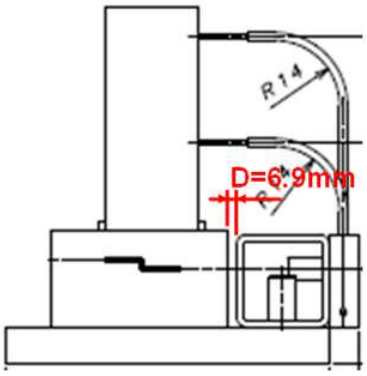

Figure 6.17: Lateral view of the mock-up; distance between tubular pipe and tile support.

In the following, measurements comparing crimped and spot-welded thermocouples are presented.

Figure 6.18 compares measurements due to different compressions of the T3 thermocouple junction on the tile, with the same nominal heat load.

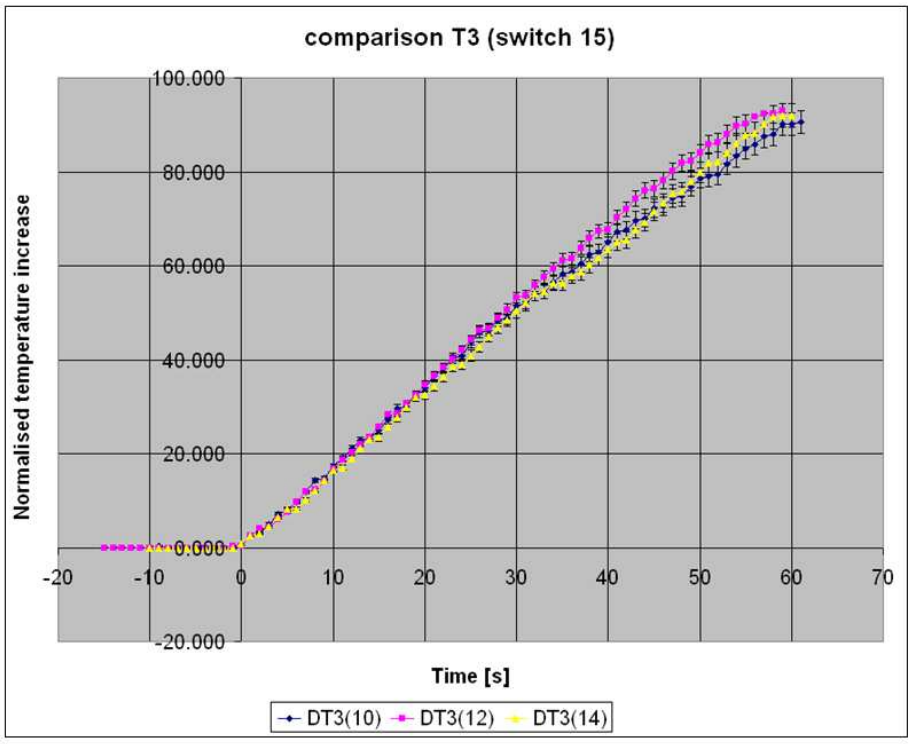

Figure 6.18: Spot welded thermocouple measurement as a function of the pressure of the thermocouple on the tile (test numbers as in Table 6.4).

The data shown in Figure 6.18 and Figure 6.19 have been analysed to take into account the initial temperature (vertical offset), the time delay after the experiment start (horizontal offset)

and the non reproducibility of the heat load. This has been done using the thermal camera data as the reference: each curve was normalised to the temperature provided by the thermal camera (the difference between the maximum temperature averaged in an area near the thermocouple and the average temperature in the same area just before the beam pulse).

Some indications can be drawn from the slope of the curves: the most responsive pressure seems to be the one corresponding to 0.2mm compression; it is not clear why 0.1mm and 0.3mm should behave similarly.

Analogously, Figure 6.19 compares measurements due to different compressions of the crimped thermocouple (T2) junction on the tile, with the same nominal heat load.

The same behaviour as for thermocouple T3 can be found also for thermocouple T2.

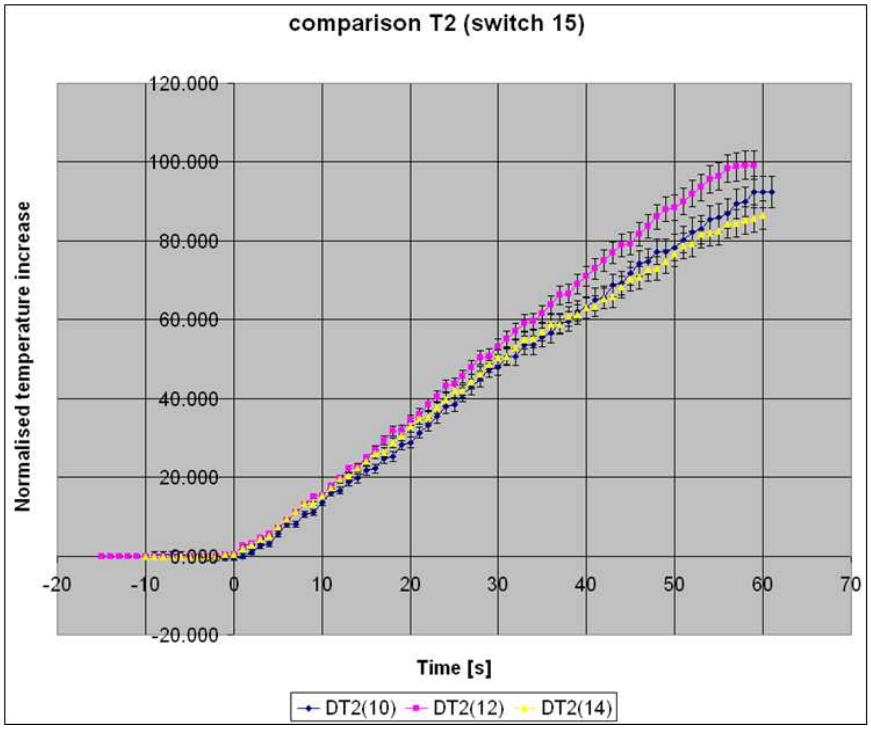

Figure 6.19: T2 measurement as a function of the pressure of the thermocouple on the tile.

Figure 6.18 and Figure 6.19 show temperatures at the same time.

Comparison between the crimped thermocouple T2 and the braze-welded thermocouple T1, at the same compression 0.2mm and at the same thermal load (switch 15) in given in Figure 6.20.

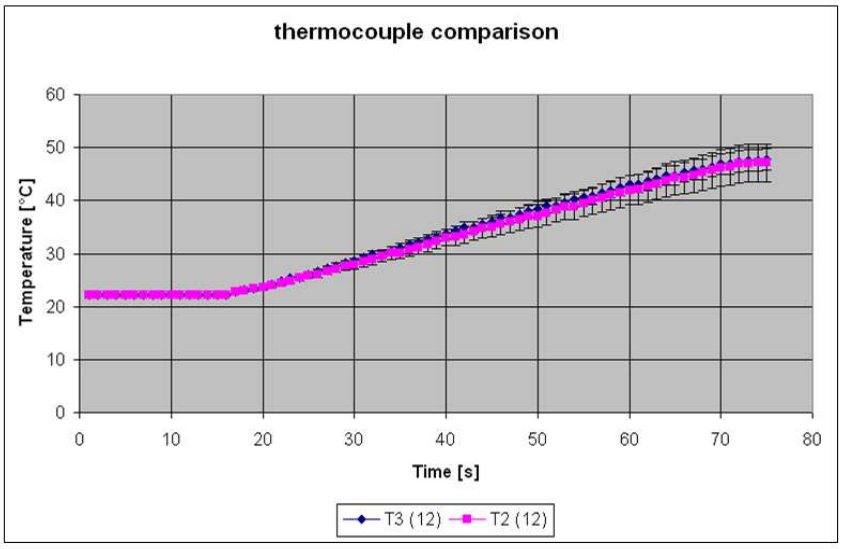

Figure 6.20: Comparison between T1 and T2 in the same conditions.

The trends are quite the same. In Figure 6.21, an expansion of the previous figure is given to highlight the temperature difference for the two thermocouples.

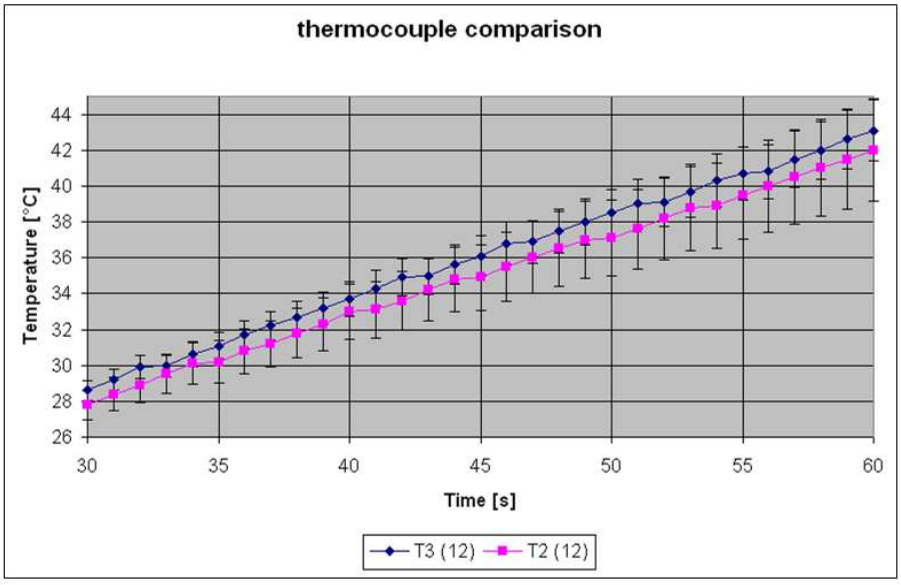

Figure 6.21: Expansion of Figure 6.20.

From the expansion, it can be observed that the temperature differences between the two thermocouples is not relevant (lower than 1°C) to this measurements and this small difference remains constant during time. Thus, in the same operation conditions no effects of the manufacturing can be noticed between crimping and spot-welding.

As mentioned previously, another test has been performed by comparing crimped thermocouple (T2) and braze-welded thermocouple (T1). In this case the temperatures were only recorded every minute.

N° test	switch	D
1	15	0.3 compression
2	5	0.3 compression
3	5	0.2 compression
4	15	0.2 compression
8	5	0.1 compression
9	15	0.1 compression

Table 6.5: Summary of the test using braze-welded and crimped thermocouples.

Comparison between the braze-welded thermocouple T1 and the crimped thermocouple T2, at the same compression 0.2 mm and at the same thermal load (switch 15).

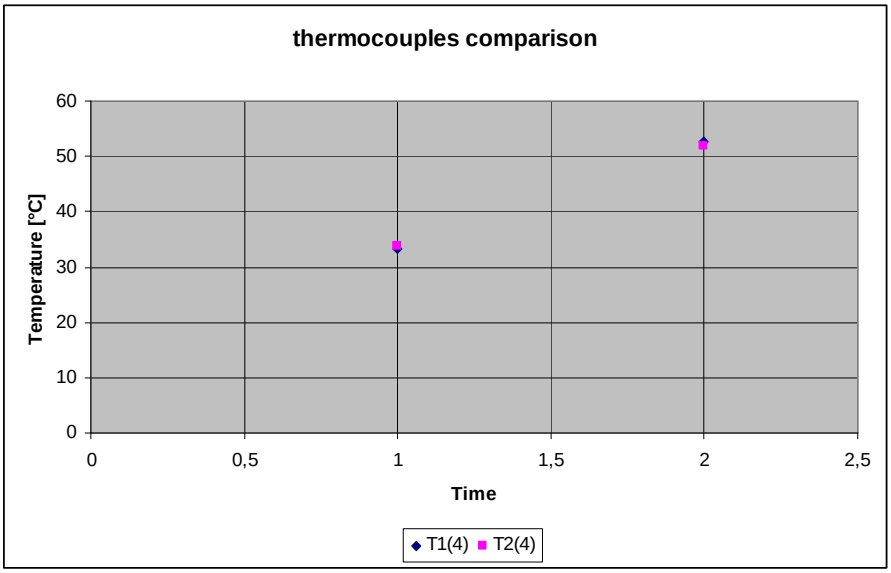

Figure 6.22: Comparison between braze-welded T1 and crimped T2 in the same conditions.

Like for the comparison of the crimped thermocouple T2 and the spot-welded thermocouple T3, also in this case no relevant temperature differences can be observed by comparing, in the same operation conditions, crimped thermocouple T2 and braze-welded thermocouple T1.

Another fixing system of the stainless steel pipe to the thermocouple was tested: laser welding. It seems to be the most suitable way, particularly for the expected operating temperature. The laser welded thermocouples. The laser welded thermocouples (Figure 6.23)

were delivered too late for this test to be performed but they were used in BATMAN (section 7.1)

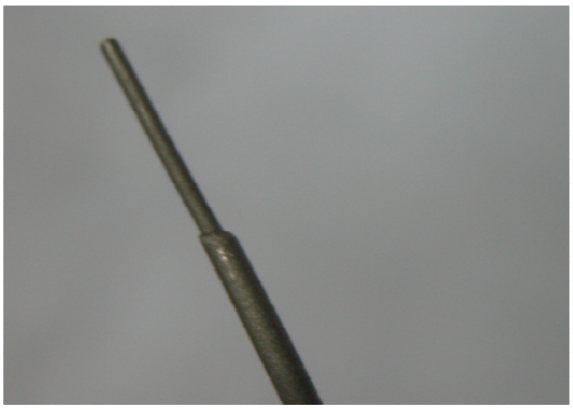

Figure 6.23: Laser welded thermocouple.

Crimping is a viable alternative method to fix the thermocouple to the stainless-steel pipe; so a refinement of the system to perform the crimping was studied, by changing the number of contact points between thermocouple and stainless steel pipe, as shown in Figure 6.24.

Figure 6.24: Thermocouple crimped in 4 points.

What works out from these tests is that neither the compression nor the fixing method can affect the thermocouple measurement so this design solution for the thermal contact is a good for STRIKE.

6.6 Thermal camera discretisation

The aim of these analysis regarding the discretisation of thermal images introduced by the thermal camera, is to explore realistic operational conditions and their effect on the temperature profile of the beamlets and on the thermal pattern along the tile.

To perform the measure of the beam divergence, STRIKE can be placed at a distance from the thermal camera from ~2m and ~3m. The sensor of the thermal camera is subdivided in

640x480 pixels that correspond to about 1.4x1.9 mm/pixel at a distance of 2m and to about 1.8x2.4 mm/pixel at a distance of 3m with a field of view of 25ºvertically × 19ºhorizontally (Figure 6.25).

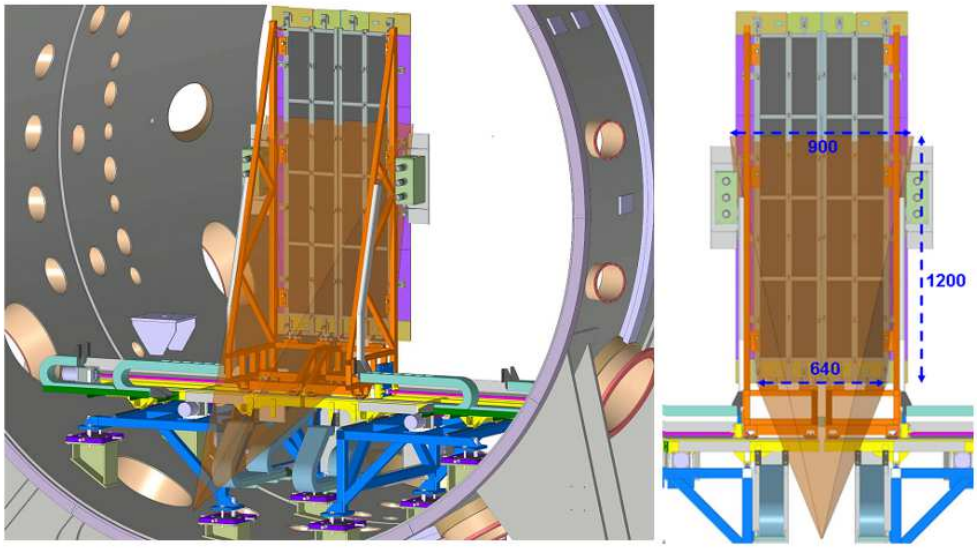

Figure 6.25: Area of STRIKE observed by the thermal camera at the bottom.

Several pixel dimensions, corresponding to distance from STRIKE and thermal camera, have been simulated by resampling the thermal image: from less than 1×1 mm^2 to 1.4×1.4 mm^2, 2×2 mm^2, 2.4×2.4 mm^2, 3×3 mm^2, 4×4 mm^2, 5×5 mm^2, 6×6 mm^2, 8×8 mm^2, 10×10 mm^2. In the following, only few examples are reported. The resampling has been applied at different heat load conditions: considering beamlets with 3mm initial radius and 3mrad divergence and also corresponding to power density of beamlets with 3mm initial radius and 7mrad divergence.

In fact, the numerical simulations have been shown with the lower divergence, the two-dimensional pattern of beamlets is clearer than the one with higher divergence that results blurred. The fit of data are evaluated along three horizontal lines, one of them is a line passing through the centre of the central row of beamlets and the other two correspond to neighbouring lines (like in section 2.5). Such expected operational conditions have been simulated numerically by dividing the continuous thermal pattern into squares and by computing the average of the energy flux over the single squares [64]. Figure 6.26 on the right hand side shows the 1D fitting of the numerical data with a sum of 5 Gauss curves, to simulate the experimental procedure of deducing the beamlet parameters from the measured data. The red line represents the continuous heat load profile; other lines represent the reconstruction of the profile on the basis of data coming from the discretisation (Figure 6.26 on the left hand side). This example is referred to the 3x3mm^2 resampling and 3mrad divergence.

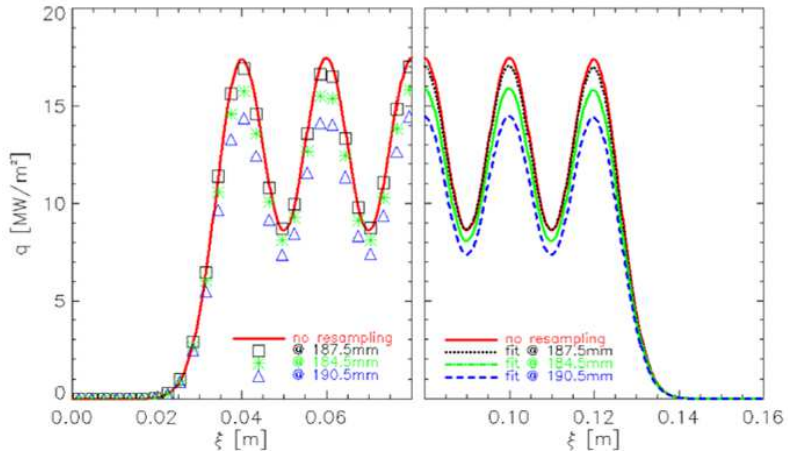

Figure 6.26: Fitting curves to reconstruct the data.

The width simulated parameter was reconstructed by data obtained by applying different size of the discretisation pattern .The reference case (6mm) can be well reproduced, within 5%, up to 6mm pixel size.

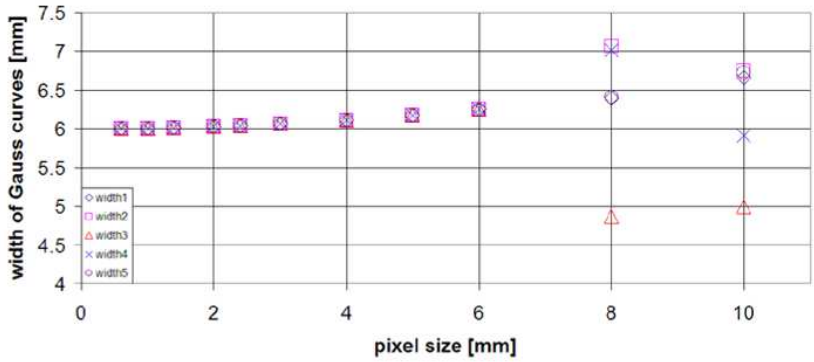

Figure 6.27: Reconstruction of the simulated beamlets width.

Comparing these results with the pixel size in the expected SPIDER operation conditions allows to conclude that the resampling introduced by the thermal camera should provide good measurements of the 2D thermal pattern.

This aspect was also investigated by experiments (section 6.7).

6.7 "SPIDER like" data analysis

An experimental campaign on CFC tile prototypes for STRIKE was performed by simulating the measurement conditions expected in SPIDER: the tiles were observed on the rear side, at about 2m and 3m distances and at different angles, as indicated in Figure 6.28. The aim of this test is to get confidence with the experimental conditions and the dedicated data analysis, and to assess the diagnostic capability in conditions similar to the real SPIDER situation.

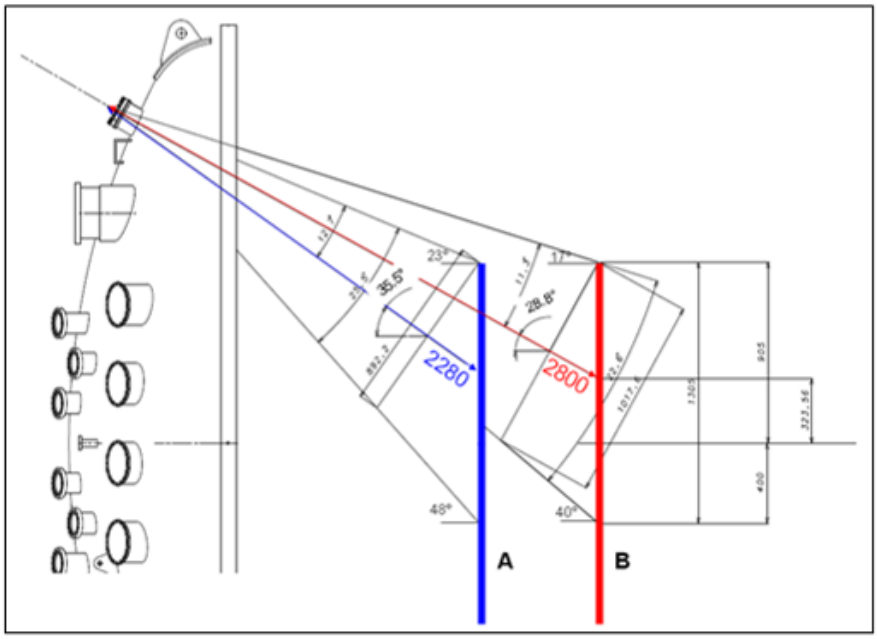

Figure 6.28: Distances and angles between thermal cameras and STRIKE panels.

Figure 6.29 shows the system realized to support and to protect the thermal camera from stray infrared radiation. The length of the polyethylene tube is 1m; adaptation to the required distance is provided by a further paperboard tube.

Figure 6.29: Support and protection structure.

An aluminium slab is used. The holes on this slab are made to fix and adjust the position with respect to the rear side of the tile, which is the observed one. The moving systems are shown in Figure 6.30: on the left, a polyethylene slab to be fixed to the system support, permits the transversal movement; on the right hand side, the disk that provides the rotation.

Figure 6.30: Translation system (left) and rotation system (right).

The disk is mounted on the polyethylene slab, as shown in Figure 6.31.

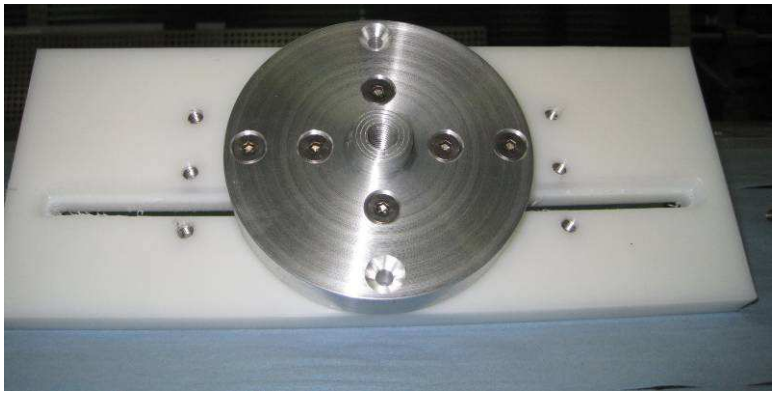

Figure 6.31: Structure of the moving system.

Figure 6.32 represents the aluminium slab mounted on the two moving systems.

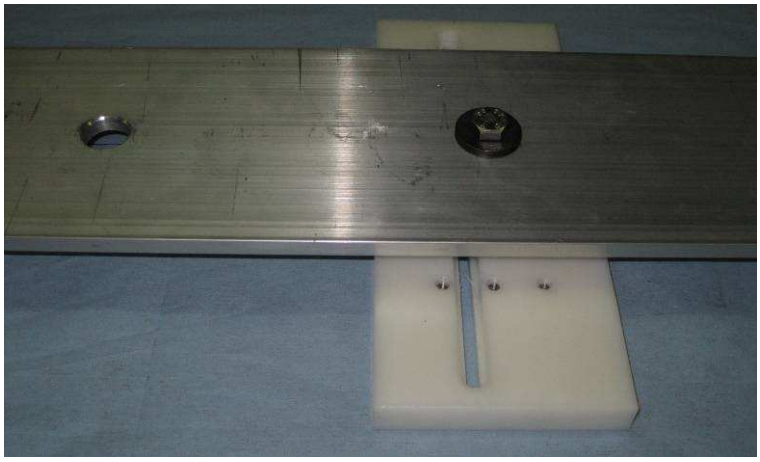

Figure 6.32: Aluminium slab mounted on the two moving systems.

At one end of the protecting polyethylene tube the thermal camera is installed, as shown in Figure 6.33, to observe the rear side of the tile; it can be rotated to angle the thermal camera with respect to the tile and to adjust the height by aligning it with respect to the tile.

In reality, during the preparation of the set-up, it seemed to be better to angle the tile instead of the whole thermal camera system.

Figure 6.33: Thermal camera installed on the tube.

The experimental set-up in the farther position is shown in Figure 6.34.

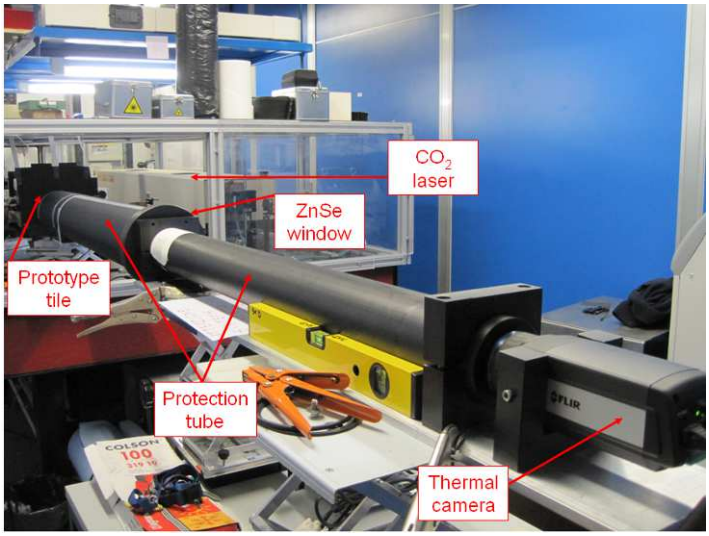

Figure 6.34: Experimental set-up for laser tests, reproducing distances and angles as in SPIDER.

When STRIKE is in position A (Figure 6.28), at 1100mm from the grounded grid, the middle point is at 2280mm from the camera and here the surface is seen at an angle of incidence of 35° to the normal, the angles at the extreme of the view cone are 48° and 23° [65].

When STRIKE is in position B (Figure 6.28), at 500mm from the grounded grid, the middle point is at 2800mm from the camera and here the surface is seen at an angle of incidence of 30° to the normal, the angles at the extreme of the view cone are 40° and 17° [65].

Laser power, tile, distance and observation angle were varied in this campaign and in some cases also the vacuum infrared window (Figure 6.35) was installed.

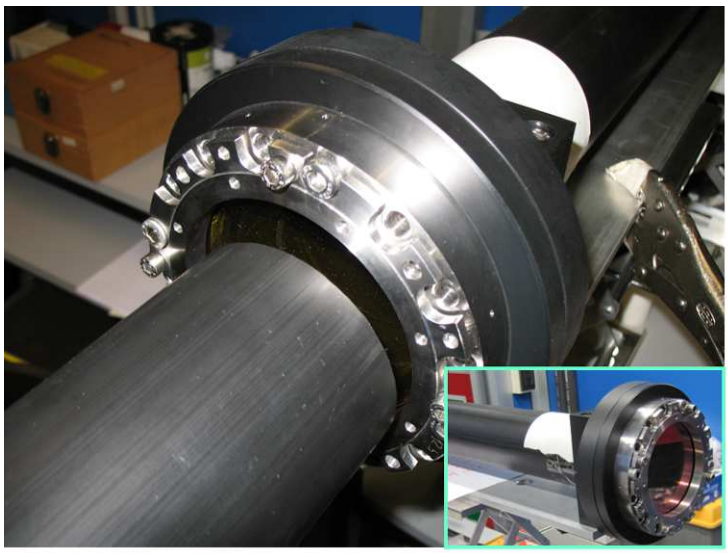

Figure 6.35: Vacuum infrared window installed.

Tiles B1, A4 and A5 were tested at different distances, angles, laser powers, with and without the IR window.

The thermal image has a resolution given by the size of the sensor pixels; at large distance, previous simulations showed (section 6.6) that the diagnostic capabilities of the system are heavily reduced only when the pixels of the thermal camera correspond to 6mm-side squares [66]. In the present case, the discretisation is due to the distance between thermal camera and tile (Figure 6.36). Notwithstanding the small amount of the thermal camera sensor used, Figure 6.37 shows the resulting data discretisation to be sufficient for the fit in the same spatial case as the beamlets, relevant for SPIDER.

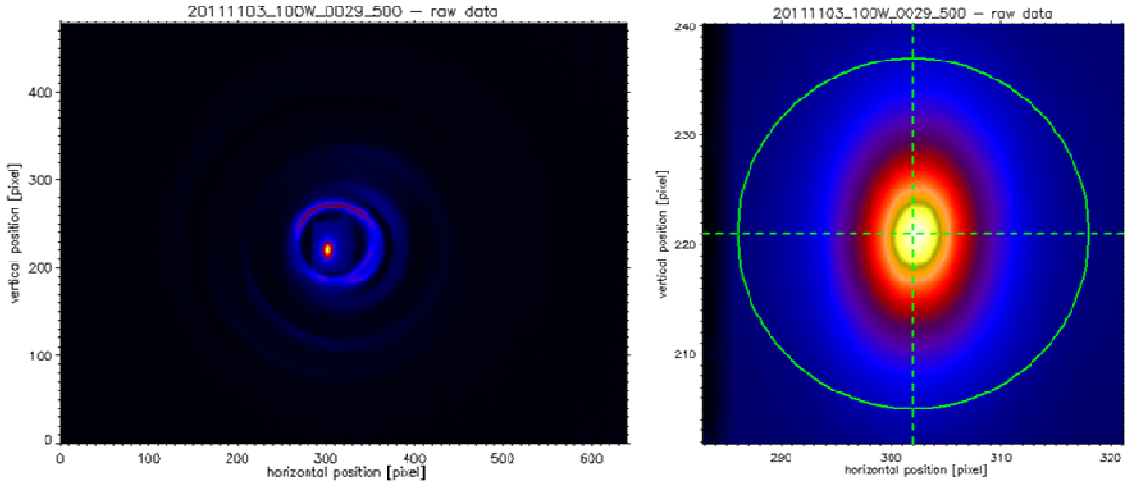

Figure 6.36: Image collected by the thermal camera (left) and portion used in data analysis (right).

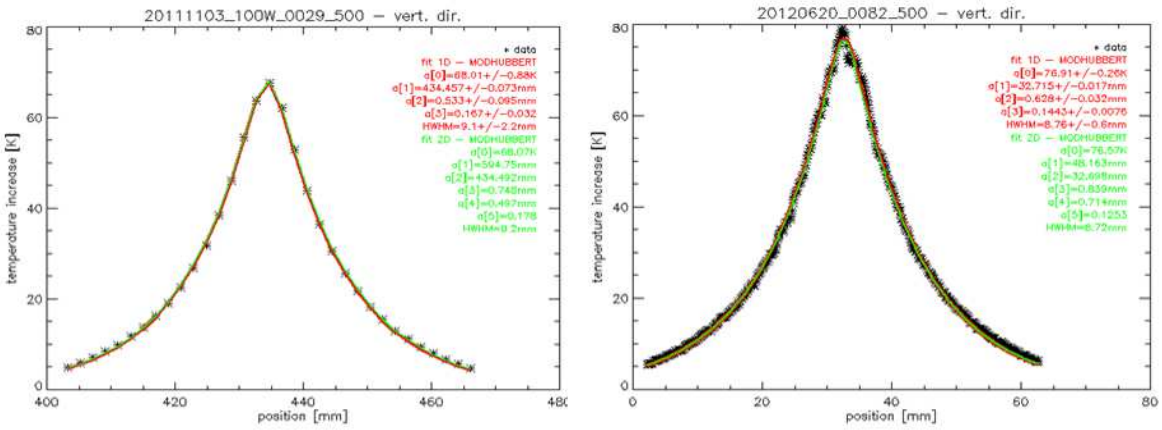

Figure 6.37: Data and corresponding fitting 2.8m (left) and 0.25m (right) from the thermal camera.

As an example, at 2.28m from the thermal camera, the exposure angles in SPIDER will be 17° (closest point), 30° (image centre) and 40° (farthest point). The measured ellipticity increases correspondingly (Figure 6.38); by applying a geometrical correction to the data, the original value of the ellipticity is recovered, so the beamlet ellipticity can be detected even with a tilted tile. It can be concluded that the information about the shape of small-scale structures in the thermal pattern was preserved despite the exposure angle and the distance; due to the variable exposure angle depending on the position on the STRIKE panel, projecting the observed area onto the sensor will yield a trapezoidal shape.

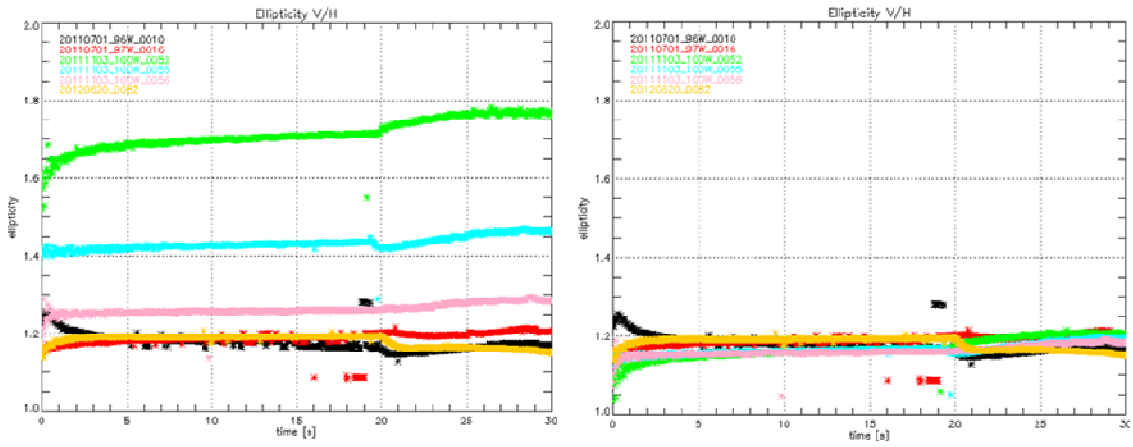

Figure 6.38: Apparent ellipticity due to tilted tile (left); same after geometrical correction (right).

Hence, even if observation of the STRIKE tiles in SPIDER will be tilted, the measurements should give correct indications about spatial profiles.

7 Tests in particle beams

Concerning several aspects of the project, the CFC is the proper material for the tiles of STRIKE. Unfortunately, it is a very anisotropic and delicate material. To validate the use of CFC, several experimental campaigns have been planned to verify the response of the whole diagnostic system in a negative ion source as well as the thermo-mechanical behaviour under high energy flux. These tests were carried out in two experiments in operation at IPP (Max-Plank-Institut für Plasmaphysik) Garching, Germany, in the framework of the activities for the Work Programme 2012 with F4E. Both experimental campaigns were concluded at the beginning of December; data analysis has just started; hence only some examples of the experimental findings are presented.

7.1 Test at IPP-BATMAN

The experimental campaign in BATMAN experiment was carried out to investigate the use of the CFC as a real beam diagnostic, in a source of the same type as the SPIDER source.

BATMAN (BAvarian Test MAchine for Negative ions) source has the aim to optimize the extracted current densities in hydrogen and deuterium at low pressure and the electron/ion ratio, with a small extraction area (<0.01m^2) and short pulses (<6 s) [18].

The acceleration system from which the ions and electrons are extracted is composed by three grid system. Magnets are located in the extraction grid (to deflect electrons). The pulse length in BATMAN has a maximum of only about 5 s (limit due to the power supply).

Some important findings on BATMAN and in RF source, are summarised in the following.

From Figure 7.1, that shows the horizontal (blue) and vertical (red) beam profile, it can be noticed that the two profiles have different half widths at half maximum; this is due to the source geometry, whose extension is larger in the vertical direction than in the horizontal direction.

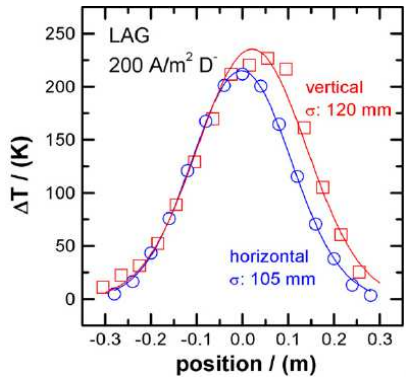

Figure 7.1: Beam temperature profiles.

The shift in the position of the maximum means that the beam is slightly deflected upwards, which is found to be related to the magnetic filter field.

The following figure shows the trend of the ion current and the electron-to-ion ratio depending on the source pressure and on the RF power. A comparison has been done between the caesium-free source, in which the production of negative ions is a volume process, and a caesiated source in which also surface production occurs. Caesium is found to have the effect of increasing the production of negative ions and to decrease the electron-to-ion ratio; moreover the negative ion current density is little affected by the source pressure.

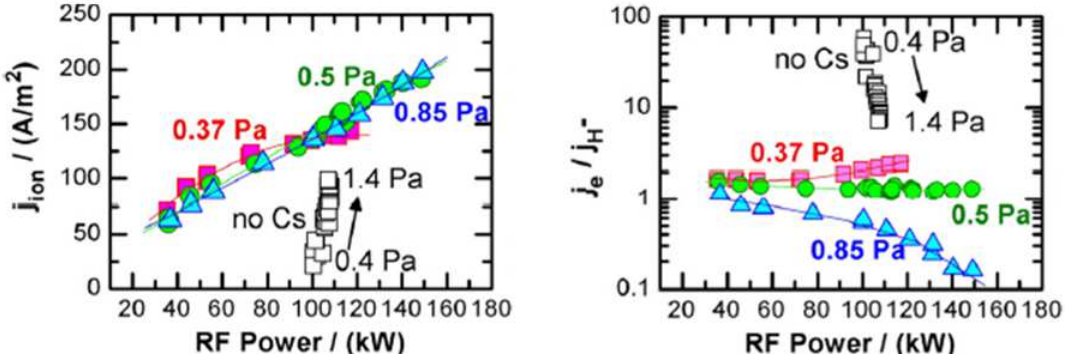

Figure 7.2: Pressure and power dependence of the current density and electron-to-ion ratio with and without Cs evaporation.

A further method implemented in the source to reduce the co-extracted electrons [67] is a positive bias of the plasma grid with respect of the source body (some tens of volts), together with a proper filter field across the plasma grid.

7.1.1 Design of CFC tile support

To evaluate the diagnostic capability of the STRIKE project, a small-scale diagnostic calorimeter, named mini-STRIKE, was designed as a prototype of the full size diagnostic. So, the CFC tile samples, observed at the rear side by a thermal camera, have been used. Thermocouples on the prototypes are also used and their fixing system is the same adopted for STRIKE; this way also a field test of the thermal contact design for STRIKE can be tested.

In order to get a good knowledge of the BATMAN beam, the prototypes selected for this campaign were B1 and B2: the most similar ones as confirmed by the laser characterisation (section 5.3).

The experiments in BATMAN aimed at characterizing the beam produced with the large area grid (LAG, Figure 7.3), featuring 8mm diameter apertures and about 12 mm pitch [68]. The grid

has 126 apertures, resulting in an extraction area of 63cm^2. The upper and lower halves of the grid are inclined by an angle of 0.88°. The source operates with a sequence of pulses 5s long, every 3 minutes; with a current density of 300A/m^2 up to 25kV, and 2° divergence.

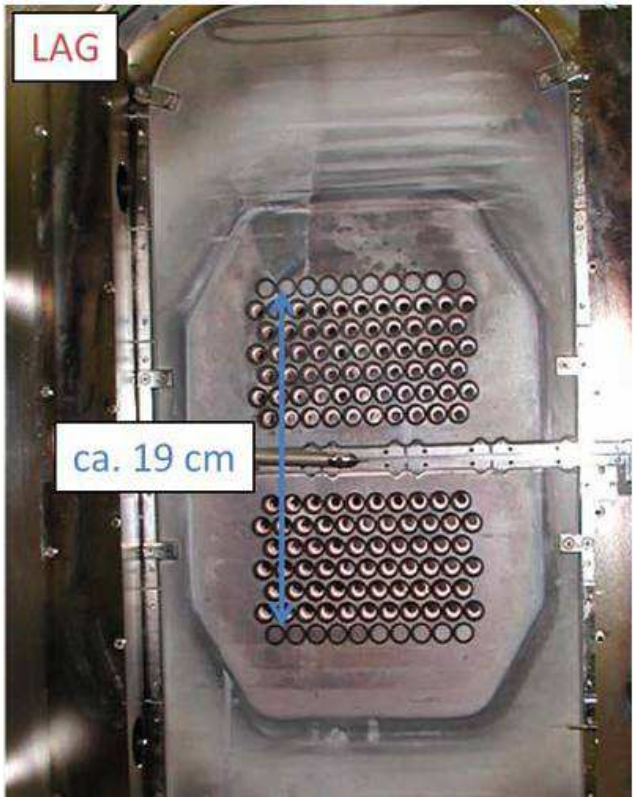

Figure 7.3: LAG grid.

Figure 7.4 and Figure 7.5 show some examples of the beamlet pattern at 0.1m and 1m from the source, respectively. The prototype tile positions with respect to the beam are also shown in cyan. On the left hand side of these figures, the 2D map of the beam power density is represented, together with some horizontal lines along with the beamlet profiles are evaluated; on the right hand side the beamlet profiles along those lines are shown.

In the case nearer to the source, single beamlets are clearly separated; on the contrary, due to the high divergence of the BATMAN beam and the observation at the rear side of the prototypes, the footprint of the single beamlets can not be resolved at 1m from the source, resulting in a flat temperature profile.

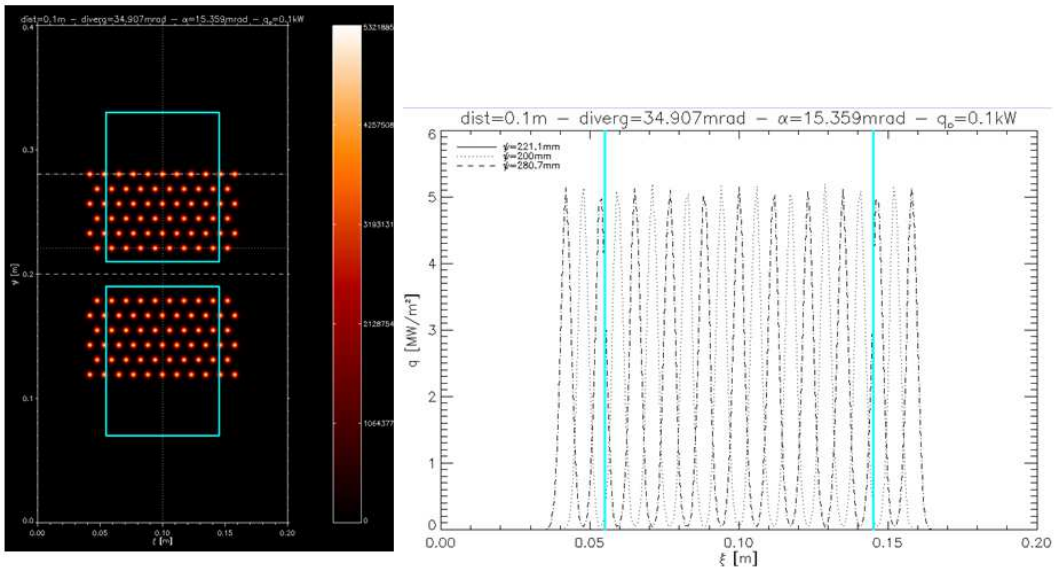

Figure 7.4: Beamlet patterns at 0.1 m from the source.

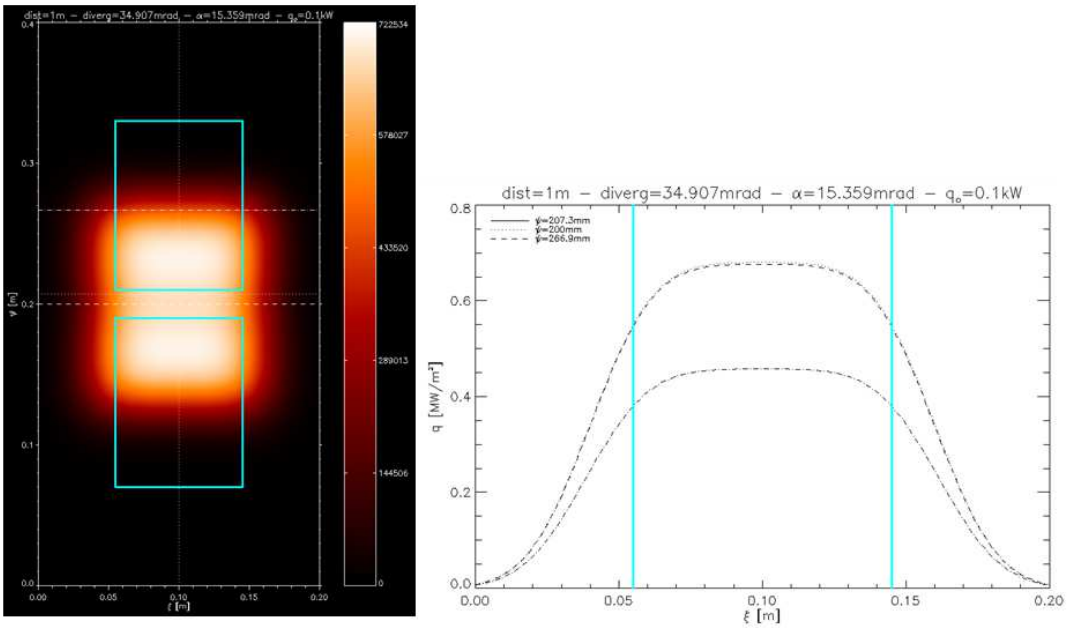

Figure 7.5: Beamlets pattern at 1 m from the source.

Although the investigation of the beamlet features would require a smaller distance of the calorimeter from the beam source, to avoid graphite contamination of the source, the mini-STRIKE had to be installed at 1m from the source. So a mask in front of the prototypes, provided with 8 apertures has been adopted to create a SPIDER-like geometry (Figure 7.6). The holes of the mask have 10mm diameter and 30mm pitch.

Figure 7.6: Mask to create beamlet geometry.

To investigate the vertical BATMAN beam homogeneity and its dependence on the plasma homogeneity in the source, a topic of this collaboration, the majority of the mask holes are positioned in the vertical direction. The geometry of the mask has been improved by implementing the results obtained by thermal, transient simulations. With a preliminary geometry of a 5mm thick copper mask, maximum temperatures reached on the surface directly exposed to the beam are summarized in Table 7.1.

	T_{max} front (5s)	T_{max} front (180s)
1st beam pulse	588 K	420 K
2nd beam pulse	704 K	509 K
3rd beam pulse	792 K	565 K

Table 7.1: Summary of the 5 mm thick copper mask front temperatures without cooling system.

Figure 7.7 shows the simulation results: the front side of the copper mask at the end of the first beam pulse (left hand side) and at the beginning of the forth beam pulse (right hand side). The centre of the beam is in correspondence of the bottom hole of the upper series.

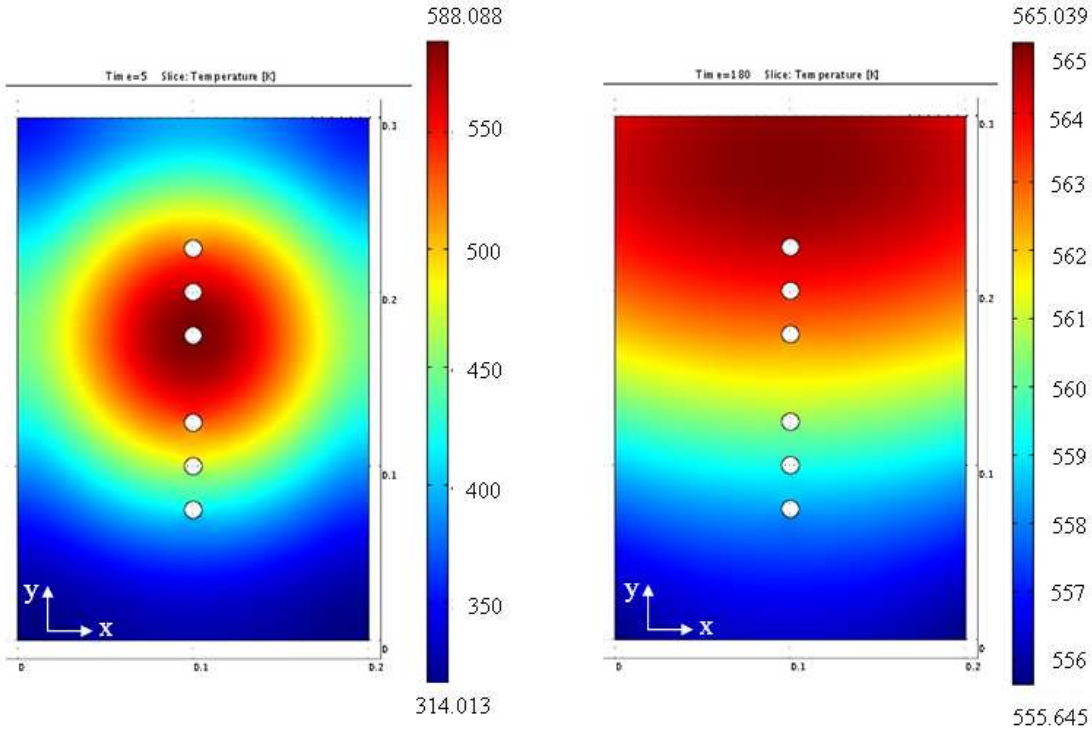

Figure 7.7: front side at the end of the first beam pulse (left hand side) and at the beginning of the forth beam pulse (right hand side).

Too high temperatures and the tendency to increase of the temperature just before the next beam pulse (memory effect), suggest that active cooling is required. Some simulations with the same mask geometry have been performed, including a simplified model for cooling: some areas along the pipe path are kept at a fixed temperature (300K). At the beginning of the successive beam pulse the maximum temperature on the mask should be back down to about room temperature (308K) as shown in Table 7.2:

	T_{max} front (5s)	T_{max} front (180s)
1st beam pulse	586 K	308 K
2nd beam pulse	593 K	308 K

Table 7.2: Summary of the 5 mm thick copper mask front temperatures with cooling system.

Figure 7.8 shows the simulation results: the front side of the active cooled copper mask at the end of the first beam pulse (left hand side) and at the beginning of the third beam pulse (right hand side). The centre of the beam is in correspondence to the bottom hole of the upper series.

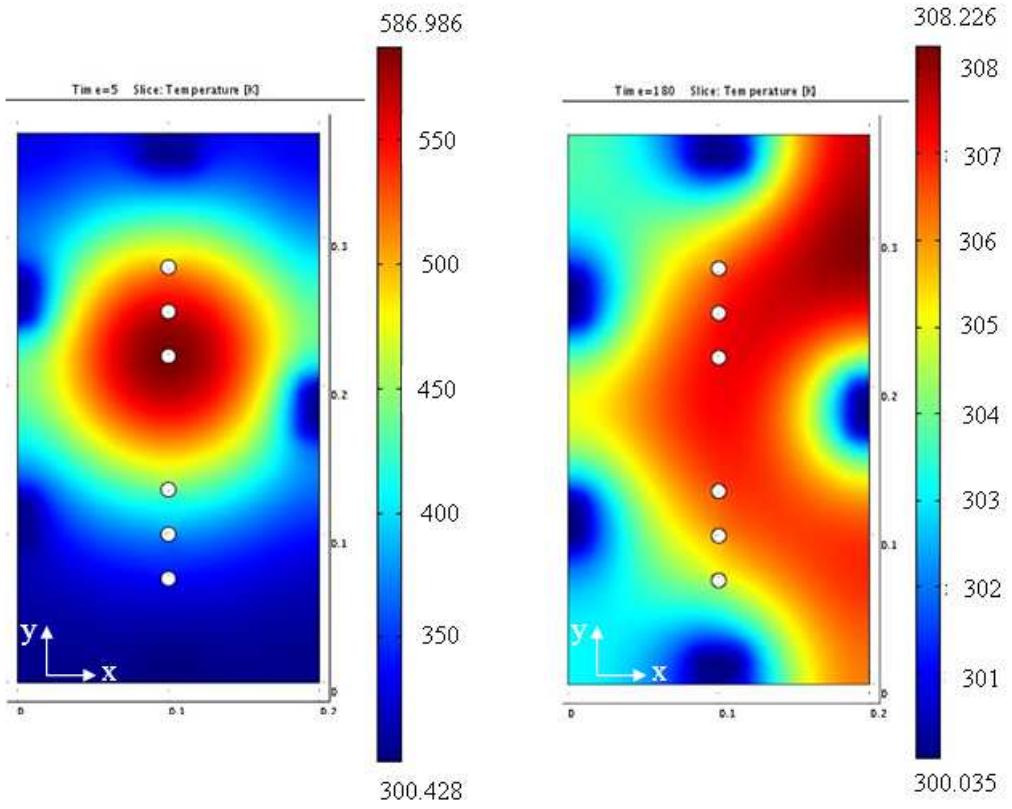

Figure 7.8: front side at the end of the first beam pulse (left hand side) and at the beginning of the third beam pulse (right hand side).

Based on these results and to house the cooling pipes, the final thickness of the mask was increased to 10mm. The geometry was further changed in order to hide the whole system from the direct exposure to the beam without increasing too much the overall weight of the mask (Figure 7.6 and Figure 7.10).

To validate the use of soft brazing to fix the cooling pipe to the mask, a simulation of the optimized mask geometry has been performed in the worst case: without cooling; the maximum temperature at the rear side is 392K in the centre of the mask; at the edges, along the cooling tube path, it is about 320K (Figure 7.9, left) Hence soft brazing, which can withstand up to 485K in continuous use, was adopted and the mask is shown on the right hand side of Figure 7.9. The expected centre of the beam should be the centre of the mask.

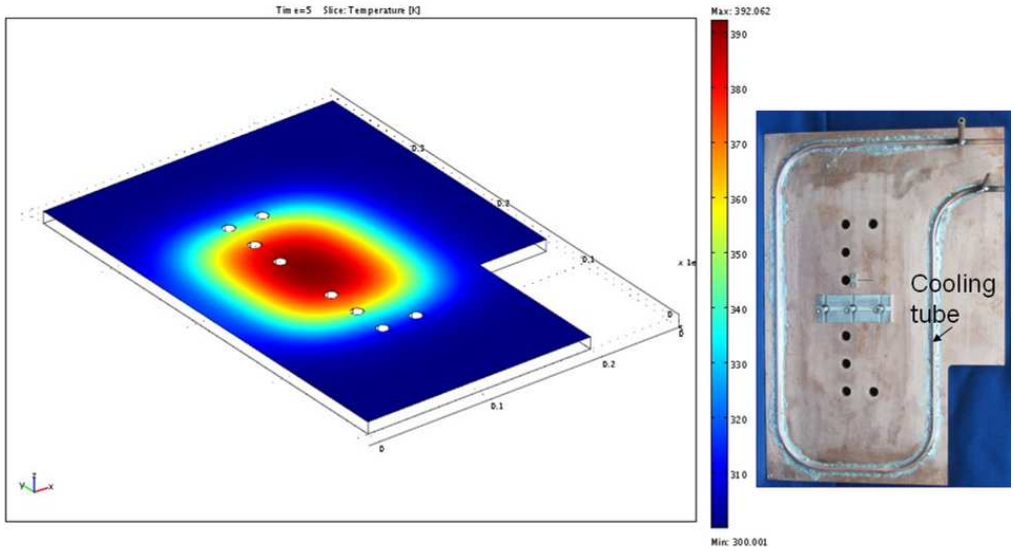

Figure 7.9: Mask simulation results at the rear side without cooling (left) and the realized component (right).

In the final design the mini-STRIKE will simultaneously expose to the beam two tiles, housed in a dedicated frame, connected to a supporting arm attached to the large BATMAN vacuum flange and arriving into the beam. The actively cooled mask is located just in front of the tile. CAD (Computer Aided Design) images of the whole system inside the BATMAN vessel are shown in Figure 7.10. A plate is required at the bottom to protect the tiles against particles coming from the titanium pump located just below.

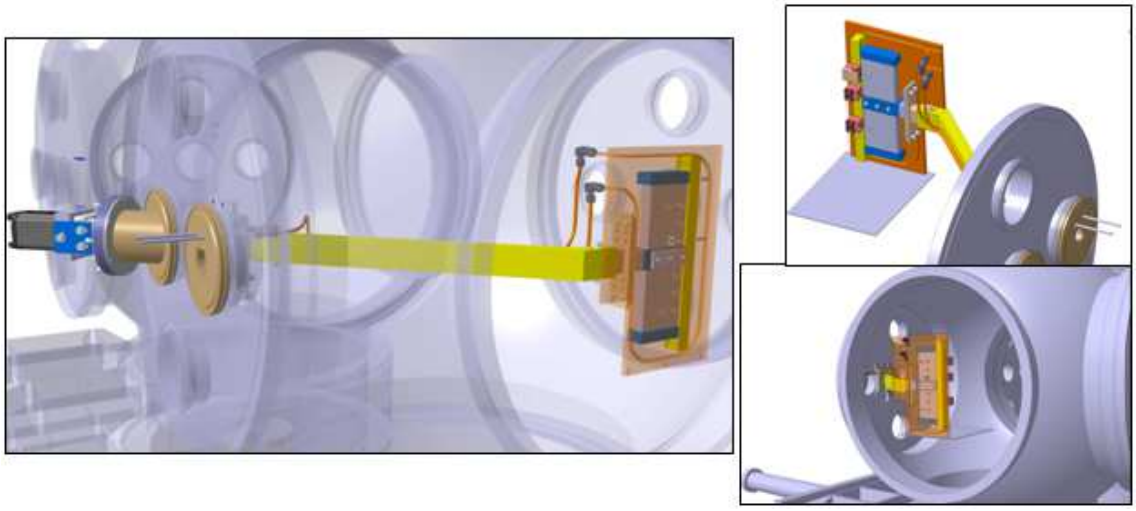

Figure 7.10: mini-STRIKE in BATMAN.

Several position adjustments are present: ±30mm vertically at the large BATMAN flange for the arm (Figure 7.11), and ±30mm vertically and horizontally at the tiles (Figure 7.12). Also a ±30mm adjustment of the distance between tiles and source can be obtained (Figure 7.11).

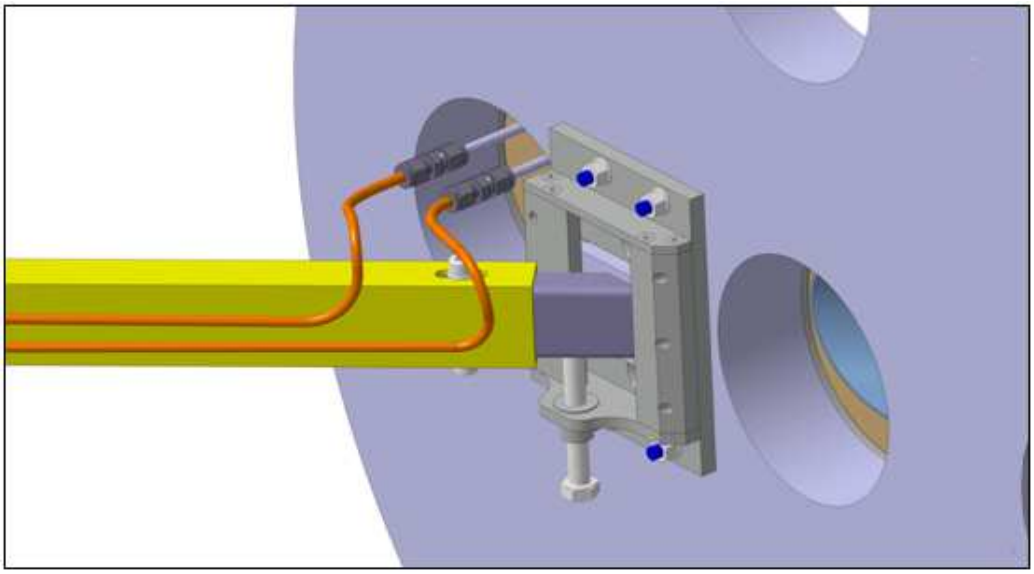

Figure 7.11: Vertically adjustments at the large BATMAN flange.

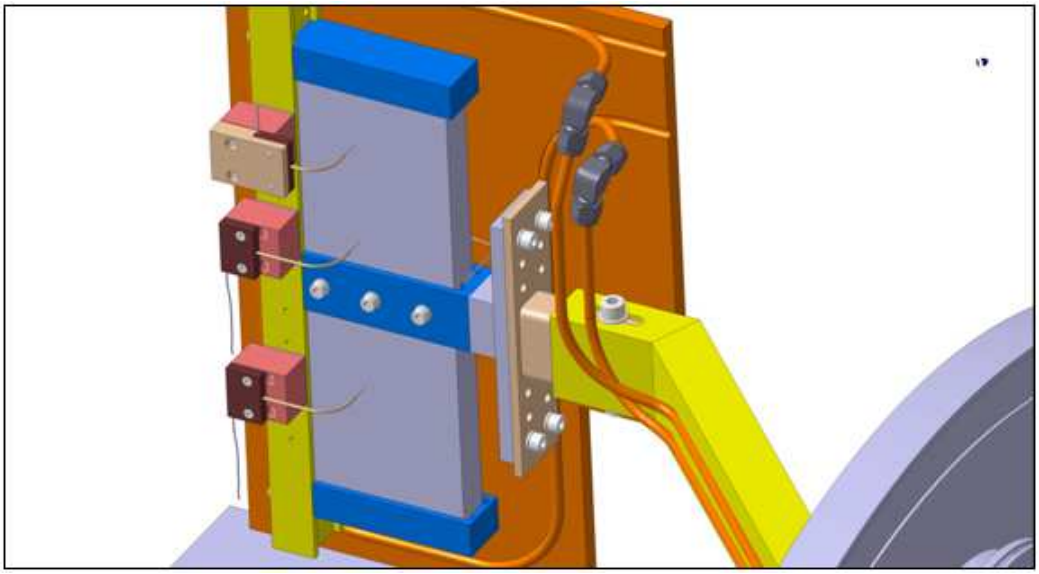

Figure 7.12: Vertically and horizontally adjustments at the tiles.

An exploded view of the assembly is shown in Figure 7.13 in which also the thermocouple on the mask and on the tiles are is visible.

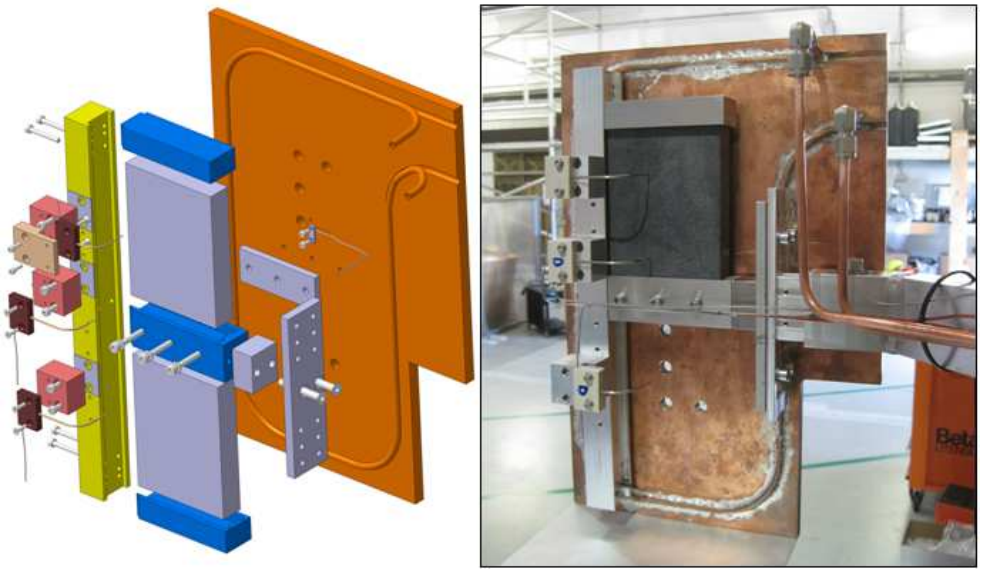

Figure 7.13: Exploded view of the mini-STRIKE (left); partially assembled system (one of tiles is missing).

The rear side of the tiles is observed by a thermal camera mounted on a viewport (Figure 7.14) of the large vacuum flange, through a zinc-selenide window.

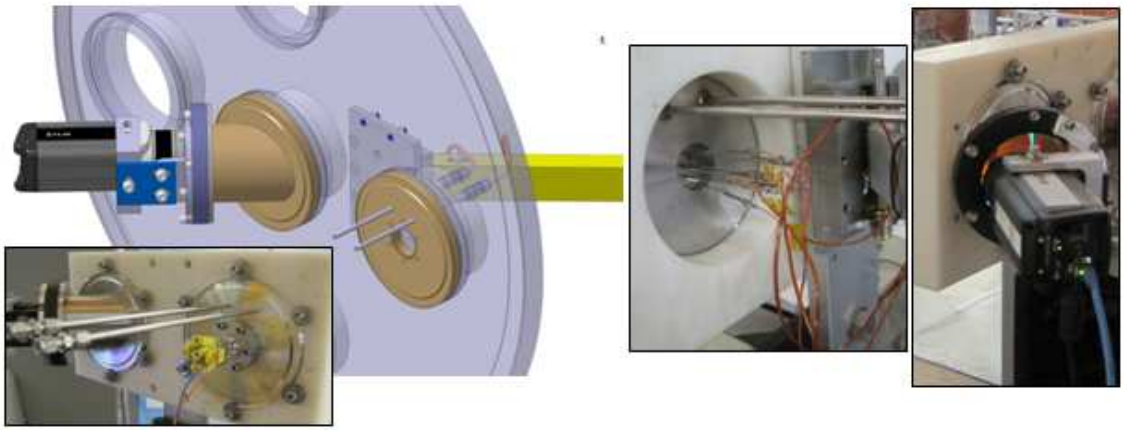

Figure 7.14: Flanges for thermal camera and signals extraction.

The angle of the thermal camera axis with respect to the beam is 50°. Notwithstanding the small room available to the thermal camera view, due to the angled position of the thermal camera itself, the view cone is not obstructed, there are no interferences with the viewport internal surfaces and the whole system can be observed (Figure 7.15).

Figure 7.15: Thermal camera view cone.

A second porthole is dedicated to extraction of thermocouple signals and cooling tubes (Figure 7.14). Three thermocouples are mounted at the rear side of the tile, to calibrate the thermal cameras. One further thermocouple is installed at the rear side of the mask, in the proximity of the beam power density peak, to monitor the copper temperature.

7.1.2 In-house tests on mock-up

Before the installation of the mini-STRIKE in BATMAN, some tests have been carried out in-house. Some of them are functional tests, as the verification of the cooling of the mask; with others are dedicated to protect BATMAN, like for instance the vacuum tightness.

Outgassing of the mask

To verify the compliance of the mask with the BATMAN vacuum prescription (0.3 Pa), an outgassing test has been performed inside a vacuum chamber (Figure 7.16, left). The viton gasket, the previous nitrogen ventilation of the chamber and also some devices installed on this chamber, are responsible for a high background noise. A calibration of the chamber has been performed, to clean the chamber from the nitrogen adsorbed at the chamber walls. The minimum pressure reached with the gate valve opened so as to connect the chamber to the vacuum system was 10^{-6} mbar and the pressure at the end of the pressure increase phase, with the gate closed, was 10^{-3} mbar. Afterwards the mask was inserted and a cycle of pressure drop and a pressure rise was performed. The pressure at the end of the decrease phase was 10^{-7} mbar and the pressure at the end of the rise phase was 10^{-2} mbar (Figure 7.16, right). The measured pressures with the mask inside the chamber are the same obtained during the calibration test.

The outgassing test indicates that the degassing rate of the mask does not exceed the sensitivity of the measuring instrument.

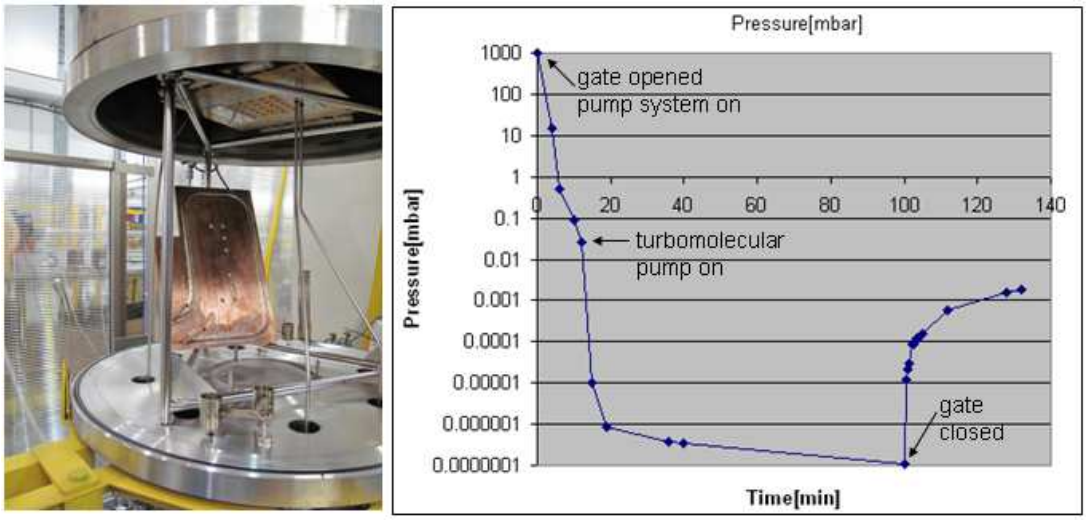

Figure 7.16: Mask outgassing test.

Mask cooling system test

Figure 7.17, shows the set-up of the test of the mask cooling system. The mask was heated by an electric hot plate. The rear side of the mask was observed by a thermal camera. Thermocouples had been installed in a hot point and in a cold point of the mask (corresponding to the centre and to the edge of the mask) and in the inlet and outlet of the cooling system. Two pressure gauges were also mounted to measure the pressure of the cooling water at inlet and outlet (Figure 7.18). To verify the efficiency of the active cooling, the mask was heated to a quite high temperature, 96°C, and then the electric hot plate was removed and the water circuit opened.

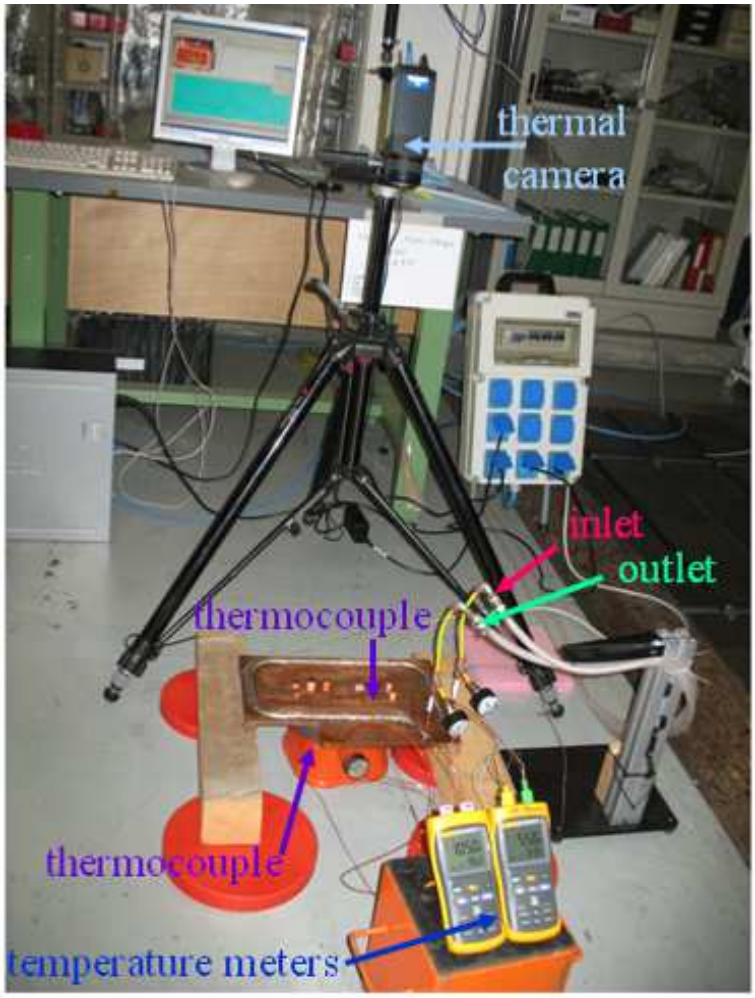

Figure 7.17: Mask cooling system test.

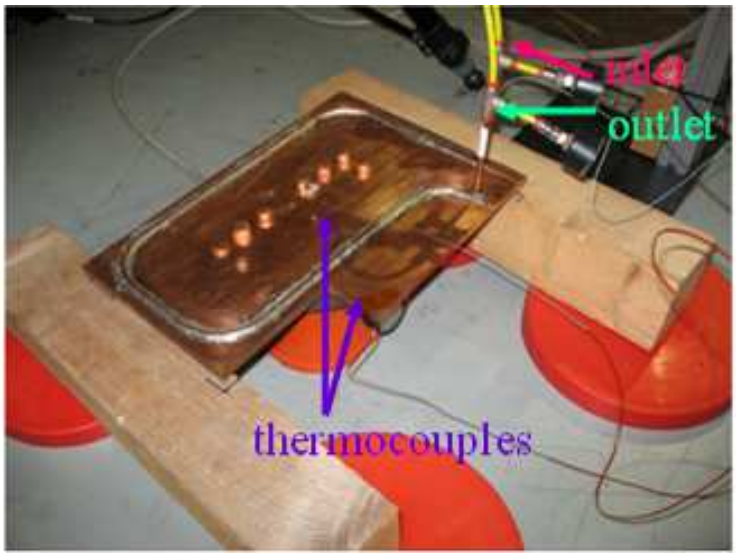

Figure 7.18: Mask cooling system: thermocouples and water inlet and outlet.

The cooling down was measured both with thermocouples and thermal camera.

A first test was made with cooling water in a closed circuit, and by means of thermocouples installed on the mask, the cool down was monitored. As shown in Figure 7.19 the temperature came back to the room temperature in about 4 minutes. The typical repetition time of BATMAN shots is 3 minutes but water flow control is provided.

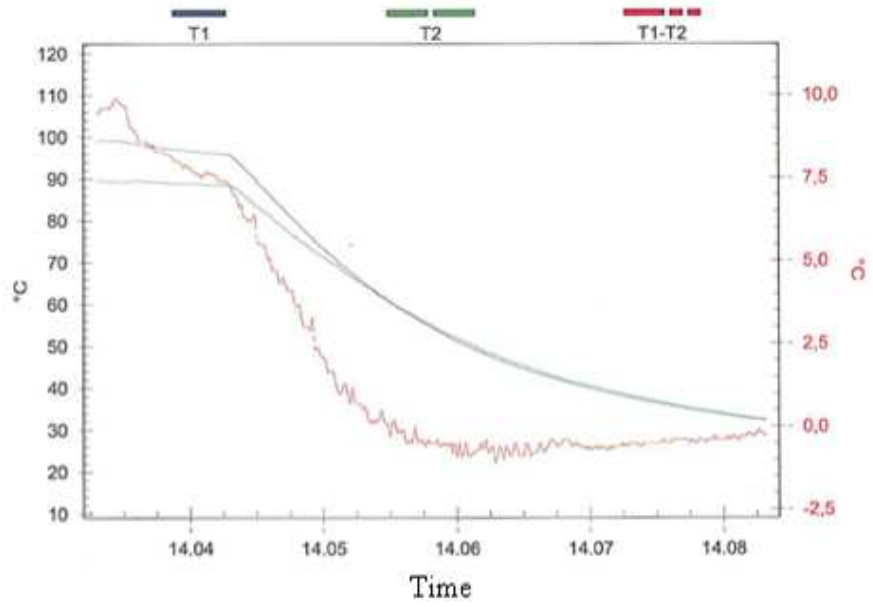

Figure 7.19: Temperature trend with the cooling water in a closed circuit.

The second test was carried out with the cooling circuit open and the outlet at atmospheric pressure. The cooling water in this configuration was collected into a container. Starting with the mask temperature at 96°C, the same as the previous test, the cooling is more efficient with the open circuit: the mask temperature came back to room temperature with a rate of one degree per second and the time to cool down the mask is halved, as shown in Figure 7.20.

In the case of closed cooling system the pressure difference between the inlet and the outlet of the cooling system is lower than 0.2 bar lying in the range of measurement error of the pressure gauge used. With the water circuit opened, the difference of pressure is about 1.3 bars and, as a consequence, the cooling of the mask results much more efficient.

As a conclusion of this test, with the pressure difference guaranteed from the BATMAN cooling circuit, the cooling of the mask can work efficiently, removing the heat deposited by the beam on the mask in between the pulses.

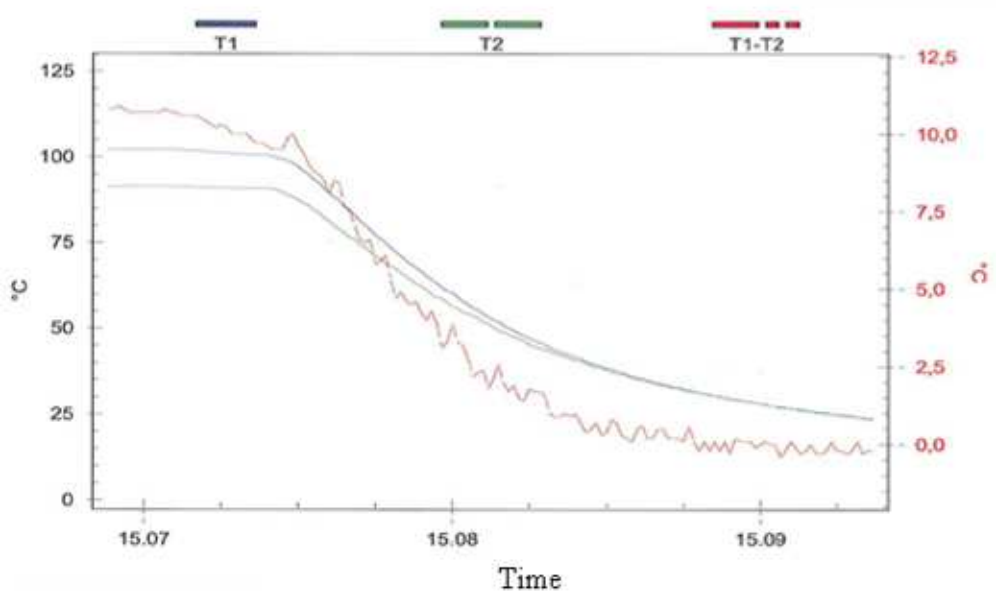

Figure 7.20: Temperature trend with the cooling water in an opened circuit.

Pressure tests

The cooling system was kept for 1h with compressed air at 5bar; at the end of the test no change in the pressure was observed, so no losses occurred.

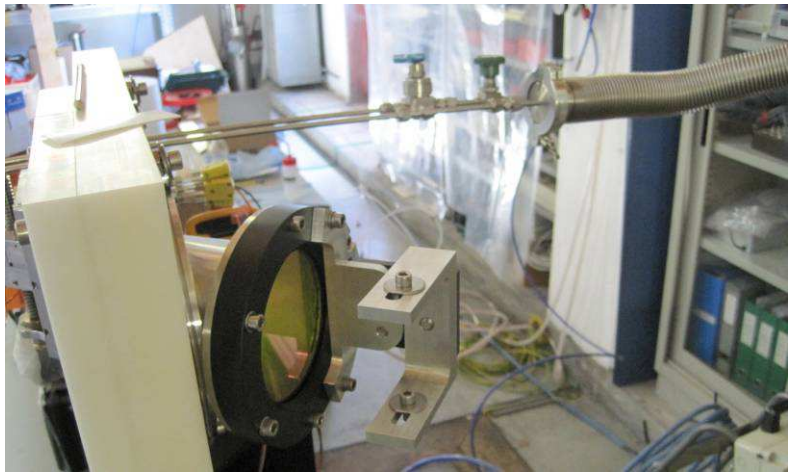

Figure 7.21: Leak test of the cooling system.

Leak tests

The cooling system was subjected also to the vacuum tightness test: the leak rate was less than 6 10^{-10} mbar l/s.

The same test was performed on the infrared camera window: the result is comparable with the background noise of the measurement device: less than < 10^{-10} mbar l/s.

Figure 7.22: Set-up for the vacuum tightness of the infrared camera window.

Electrical continuity

The continuity and low-voltage insulation were verified by a tester and the results were above the measurement limits of the equipment, in accordance with the expectance.

Cleaning

Materials to be introduced in the vacuum vessel have to be previously cleaned. Depending on the material, there is different procedure to be followed [69]. For instance, copper has to be cleaned manually with alcohol and acetone, and then with a known solution of HNO_3; it has to be rinsed with demineralised water, dried with nitrogen flow and has to be outgassed in vacuum at 350°C. For the aluminium the procedure is simpler: it has to be cleaned manually with alcohol and acetone, rinsed with demineralised water and dried with nitrogen flow. For the steel, the procedure is the same as for aluminium. The deep cleaning of the material is achieved by means of ultrasonic bath, to exploit a combination of the mechanical action of water and ultrasounds together the chemical action of the detergent; moreover, heat helps the dissolvability of impurities and mineralised water minimises the deposition of calcium carbonate.

Figure 7.23: Ultrasonic tank.

7.1.3 Simulations

To investigate the expected experimental conditions, several simulations were carried out with different beam characteristics: 2° and 3° divergence and vertical disuniformity of 0%, 3%, 5%, 10%.

Figure 7.24 shows the 2D temperature map on the front side and on the rear side of the upper tile for 2° divergence and 0% beam disuniformity. Two numerical models were studied, the first one representing the prototype located at the top of the system and the second one representing the prototype housed on the lower part. The models have the same dimension as the prototypes.

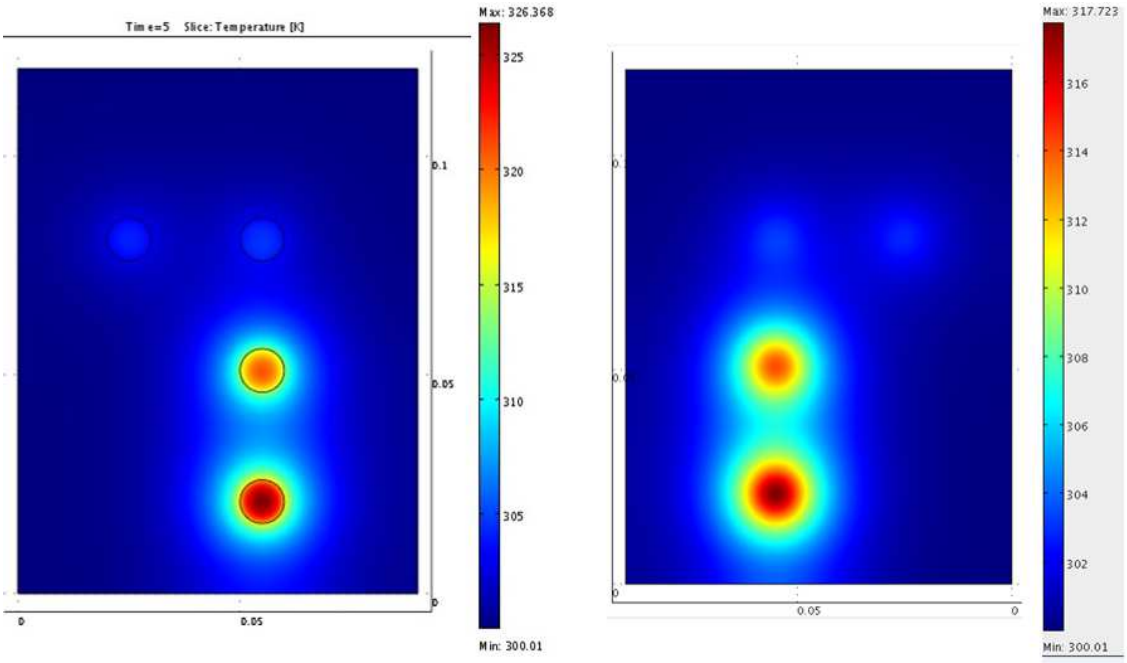

Figure 7.24: Front side (left) and rear side (right) of the upper tile, 2° divergence and no beam disuniformity.

The mesh elements are adapted to the single parts of the model: care was dedicated to the mesh size, particularly for the exposed areas and the observed surfaces. Radiation towards surfaces at 300K is included on all surfaces, except on the one facing the mask; room temperature is 300K; the thermal load application lasts 5s. The temperature increase is quite low, due to the low energy flux.

Due to such little temperature increases, changes in beam uniformity are difficult to be characterized: Figure 7.25 shows the tile temperature profiles for 2° divergence, no disuniformity and 2° divergence 10% disuniformity. Careful analysis of the data is required to obtain indications about the degree of beam disuniformity.

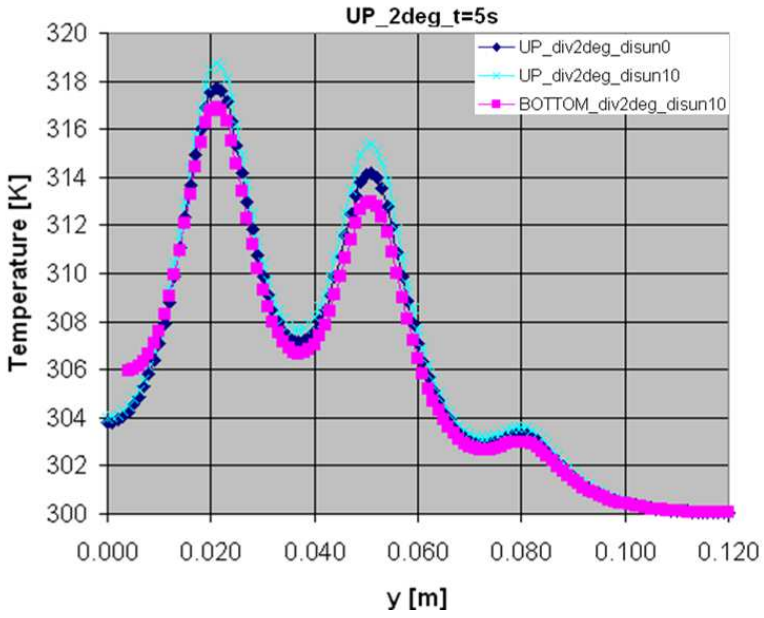

Figure 7.25: Tile temperature profile with 2°divergence and no disuniformity (blue line); top tile, 2°divergence and 10 % disuniformity (cyan line); bottom tile, 2°divergence and 10 % disuniformity (magenta line).

7.1.4 Measurements and data analysis

After the tests to evaluate the vacuum tightness of the components, the whole system was mounted inside BATMAN vessel, as shown in Figure 7.26.

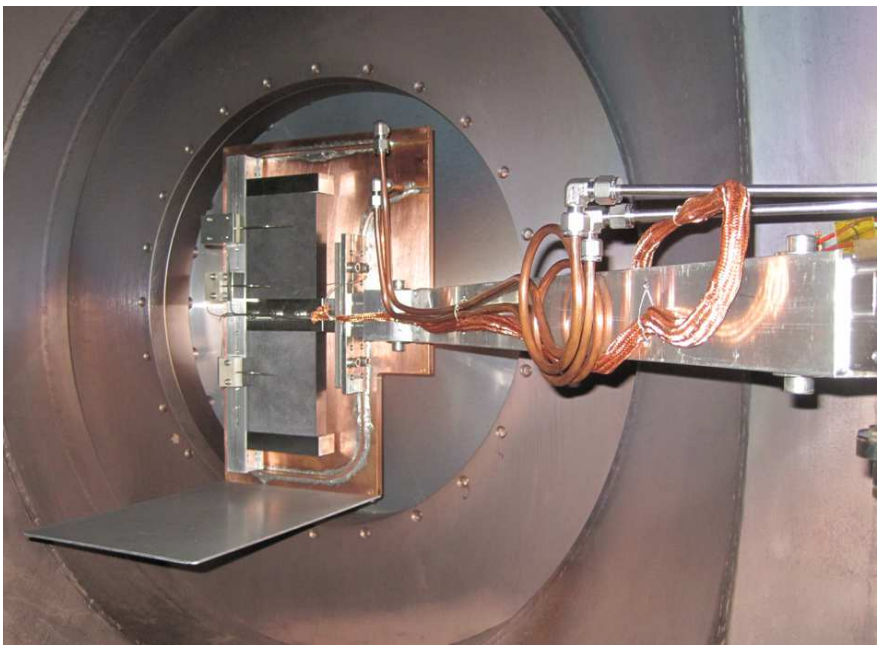

Figure 7.26: Assembly of mini-STRIKE inside the vacuum vessel of BATMAN.

The experimental campaign in BATMAN was performed by varying several parameters:

- U_{bias}: the polarization of the plasma grid with respect to the source wall; this enhance the negative ion yield and reduces the co-extracted electrons;

- the magnetic filter field: by changing the intensity, the position and the polarity of the field, and without magnetic filter field. Figure 7.27 shows different positions of the magnet bars;

- extraction voltage;

- acceleration voltage;

- gas plasma: hydrogen and deuterium;

- source pressure;

- RF power;

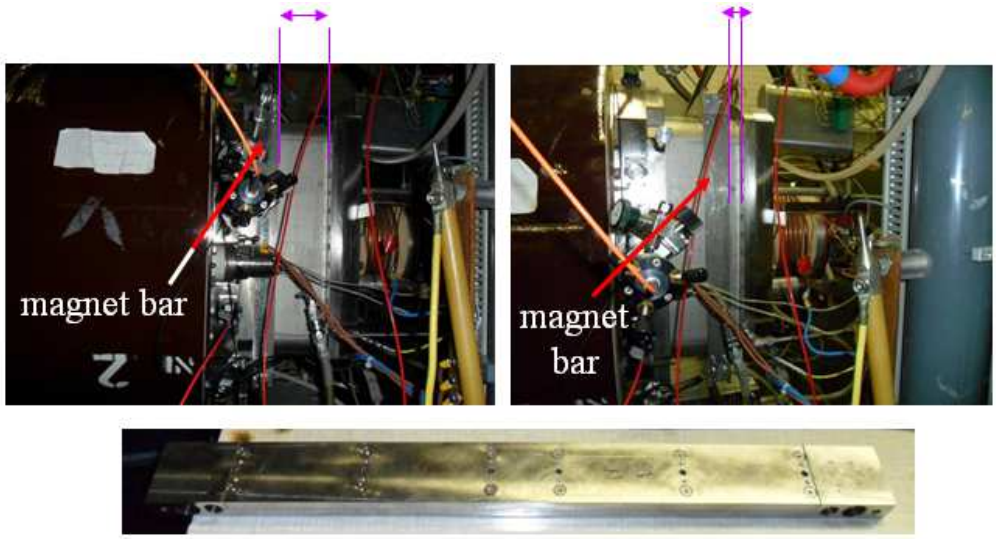

Figure 7.27: Different positions of magnet bars and a dismounted magnet bar.

An example of BATMAN signals is reported in the following figure: for a deuterium pulse at 15kV acceleration and 5kV extraction. The important trends are the measured co-extracted electrons (magenta line) and the deduced current associated to the extracted negative ions (red line).

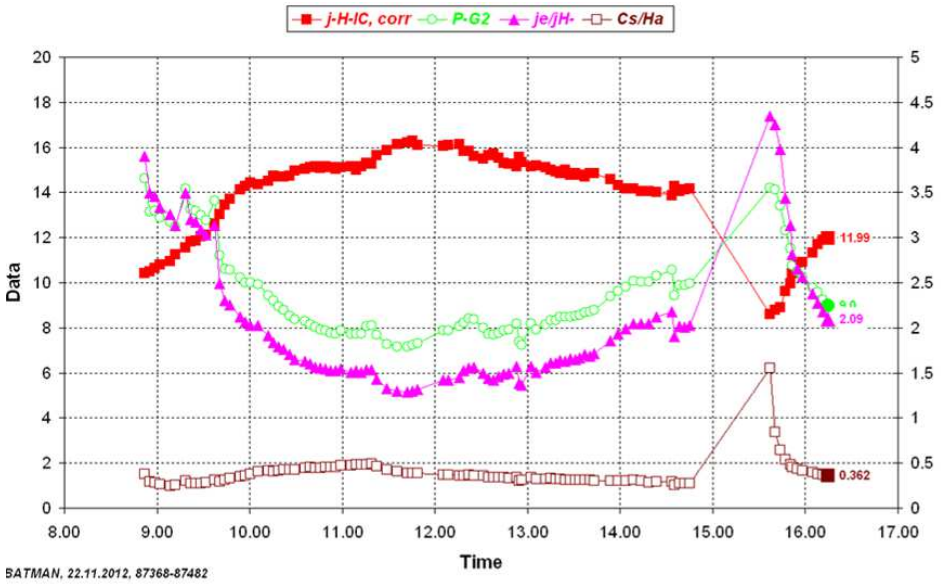

Figure 7.28: Example of BATMAN data.

The infrared view (Figure 7.29, left hand side) during a pulse shows the beamlets on the rear side of the tile, created by the mask holes. In the image, also the thermocouples are visible; they have been used to calibrate the thermal camera, setting the emissivity of the tile. As already

reported, a beamlet structure of the type expected in SPIDER can be obtained and studied with an analogous experimental procedure that will be adopted in SPIDER by deducing the beamlet parameters from the measured data. The same Figure 7.29 shows also the beamlet footprint left on the tile, on the hit surface hit by the beam.

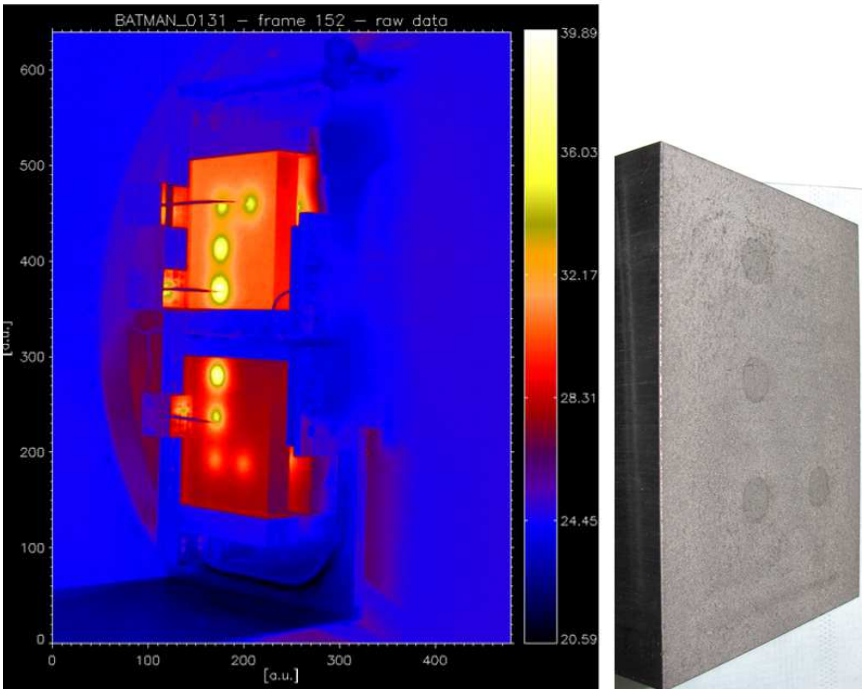

Figure 7.29: Example IR image of mini-STRIKE in BATMAN; mini-STRIKE tile after exposure to the BATMAN beam.

From the 2D map temperature data, the study of the beamlets can be performed, along a vertical line passing through the beamlet centre. Figure 7.30 shows the data analysis results of the experimental data (missing data can be noticed in correspondence to the thermocouples) and of the simulation made to reconstruct the experimental findings (in the centre of the figure).

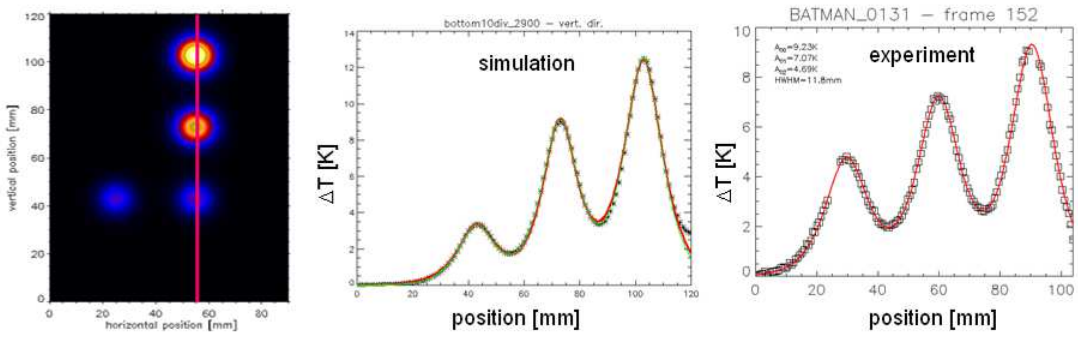

Figure 7.30: Data analysis on the vertical profile of beamlets.

To investigate the beam features in the vertical direction, the following data analysis procedure is applied: the frames of the IR film preceding the beam are averaged and the result is subtracted from the image in all subsequent phases of the data analysis (Figure 7.31); the area surrounding each beamlet in the thermal image is isolated and the portion affected by the shadow of the thermocouples is removed (Figure 7.32); to each beamlet a two-dimensional fit with the modified Hubbert curve is applied and the parameters of the fit procedure are recorded (Figure 7.33, left).

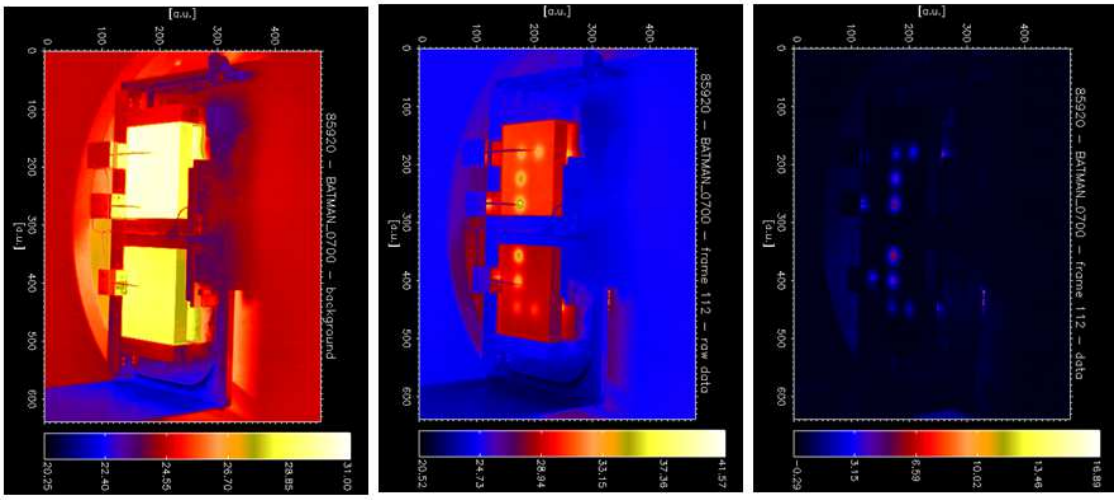

Figure 7.31: Background image; raw data; image resulting from the subtraction of the background to the raw data.

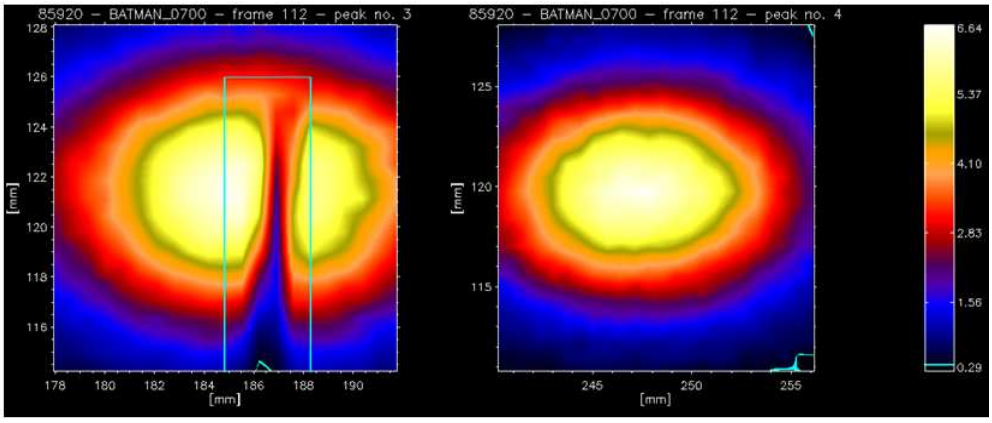

Figure 7.32: Thermocouple shadow; thermal image after removing the thermocouple shadow.

The superposition of the peak values of the single beamlets are gathered together and (Figure 7.33 on the left hand side) the profile of the whole beam in terms of the temperature induced in the tile can be reconstructed, as shown in Figure 7.33 on the right hand side.

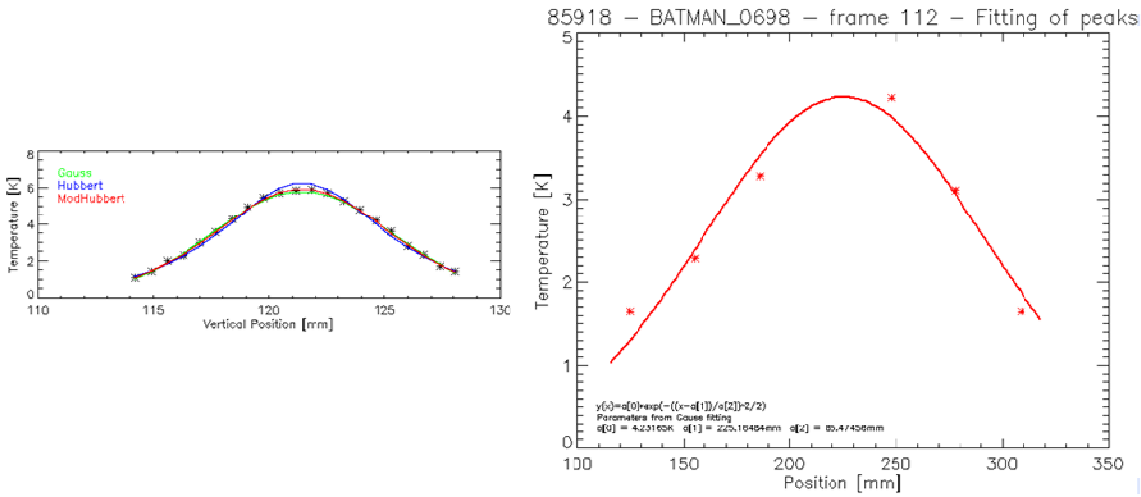

Figure 7.33: Profile of a single beamlet and the superimposition to obtain the beam profile.

The resulting parameters of the beam can be plotted as a function of time. In Figure 7.34, the centre, the amplitude and the width of the reconstructed beam profile at the rear side of the CFC tiles, are shown. It can be noticed that during the pulse the position of the beam centre is stationary, the amplitude increases as expected and the beam does not broaden (the first points correspond to the formation of the image; then a stationary equilibrium is reached between heat deposited on the tile and perpendicular diffusion).

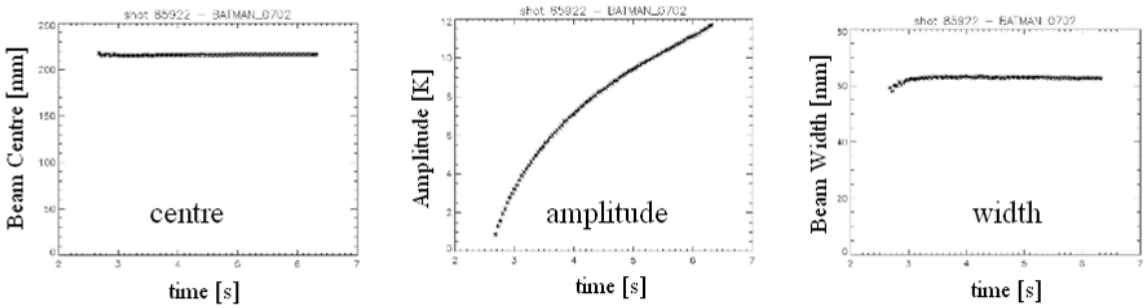

Figure 7.34: Example of BATMAN beam results.

Data analysis is still on going and this is why in the following only some examples are reported. In several years of BATMAN operations, it has been found that the magnetic field strength in front of the plasma grid plays an important role in the extraction of negative ions [70]. The positive ion density is higher at the driver exit than in front of the plasma grid, as

shown in Figure 7.35, this depends on the source zone observed and on the position of the external magnets for the filter field: in particular the positive ion density is higher when the field is more strength to the plasma grid (z=9cm). Moreover, it was also found in the negative ion sources that a positive bias of the plasma grid with respect to the source walls [18] can help in reducing the co-extracted electrons and in increasing the negative ion yield.

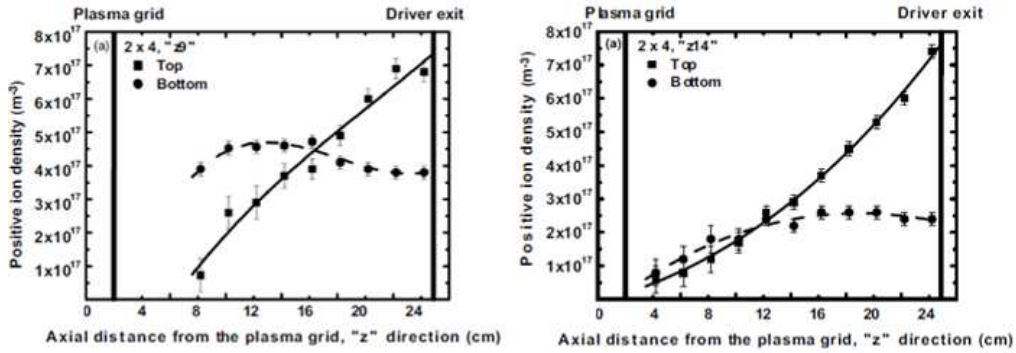

Figure 7.35: BATMAN measurements: positive ion density [70].

Measurements done with the mini-STRIKE can reconstruct the BATMAN beam profile using information coming from single beamlet created at the tile by the mask. Figure 7.36 shows the peak of the hydrogen beam in two different magnetic configurations; with the same number of magnets, near to the plasma grid (z=9cm) and away from the plasma grid (z=14cm). Measurements were performed by increasing the voltage applied to the plasma grid, except for the last pulse of each series, which has the same parameters as the first pulse of the same series, to verify if the beam conditions were stationary during the parameter scan. The acceleration voltage was 15kV and the extraction voltage 5kV. The biasing value of the plasma grid can influence the extracted current; the corresponding increase in the electrostatic repulsion might explain the behaviour with the higher filter field (z=9cm). Moreover, the experimental findings show a stronger dependence of the temperature increase on the U_{bias} when the permanent magnets are closer to the plasma grid. The total positive ion density near the plasma grid is higher in the z=9cm case and in this condition the calorimeter measures a higher temperature.

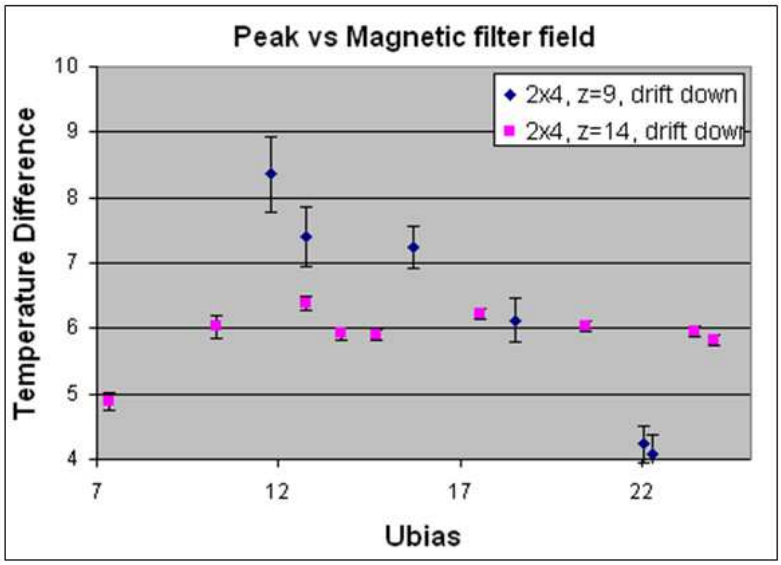

Figure 7.36: mini-STRIKE measurement: maximum temperatures on the rear side of the tile.

If no filter field is applied, the positive ion density inside the source, near the plasma grid, has the same order of magnitude that the condition ad with magnet far away from the plasma grid (z=14cm), as in Figure 7.37. Moreover, the electrons close to the plasma grid are more energetic than with the filter field (temperature are comparable both for z=9 cm and z=14 cm).

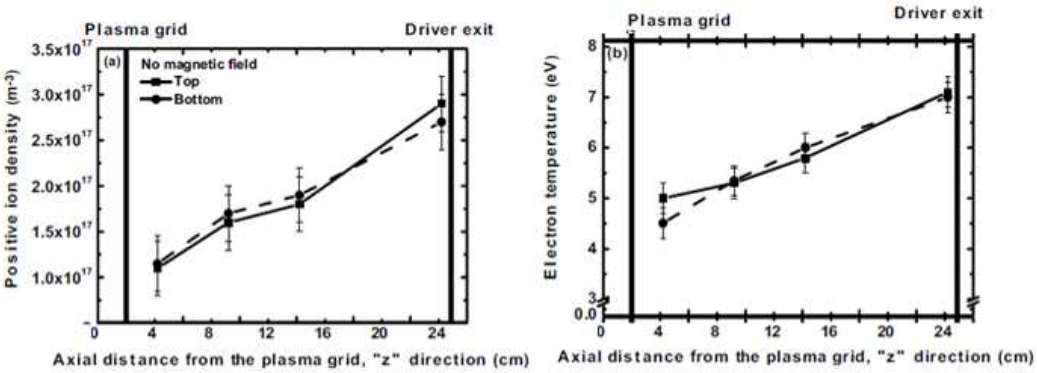

Figure 7.37: BATMAN measurements: positive ion density and electron temperature without filter field [70].

From BATMAN measurements, in this condition the electron-to-ion ratio is about 11: very high. Fast electrons can destroy the negative ions and less positive ions are facing the extraction region with respect to previous cases. The pulse chosen to plot the temperature in Figure 7.38 has the same acceleration voltage, extraction voltage and negative ion current. The U_{bias} which is positive with respect to the source walls, has the aim of facilitating the extraction of negative ions. The absence of the filter field has the effect of no deflection for the electrons, so they are

extracted together with the negative ions, and collected to the calorimeter. As the U_{bias} increases, more and more negative charges are extracted so the measured temperature increases.

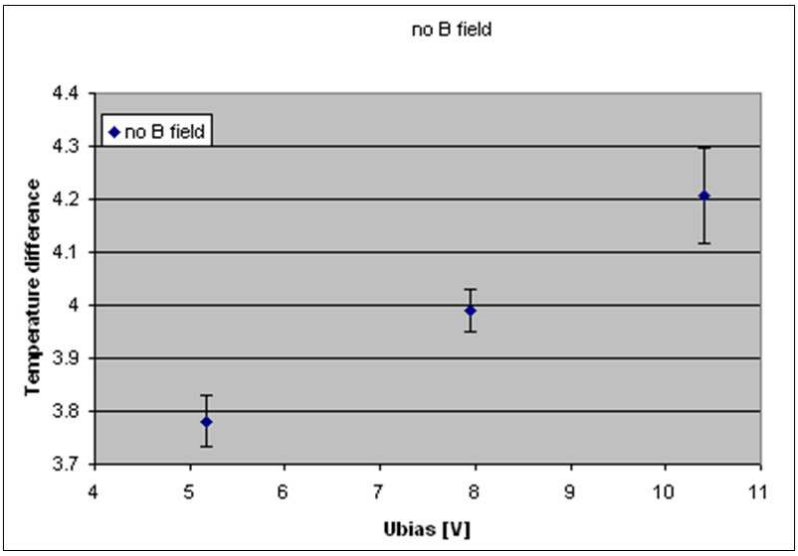

Figure 7.38: mini-STRIKE measurement: maximum temperatures on the rear side of the tile without filter field.

Figure 7.39 shows the trend of the temperature measured on the rear side of the CFC sample as a function of the perveance (section 1.2). As shown in Figure 7.40, this measurement has been done with perveance values laying on the left branch of the curve, this means that also the divergence is decreasing, in fact the temperature measured with increasing perveance is also increasing.

Moreover, with increasing U_{bias} the measured extracted current is decreasing, so the temperature measured on the rear side of the CFC tile is also decreasing (Figure 7.39).

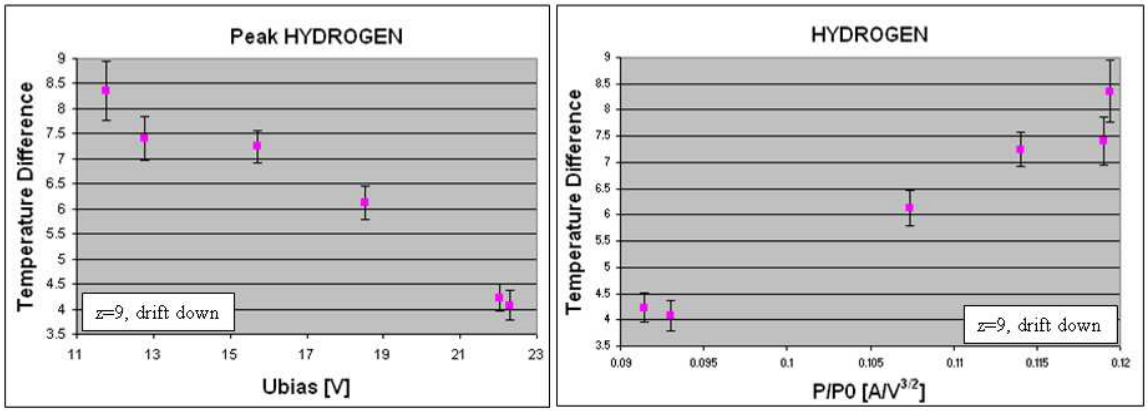

Figure 7.39: mini-STRIKE measurement: maximum temperatures on the rear side of the tile as a function of the normalised perveance for hydrogen.

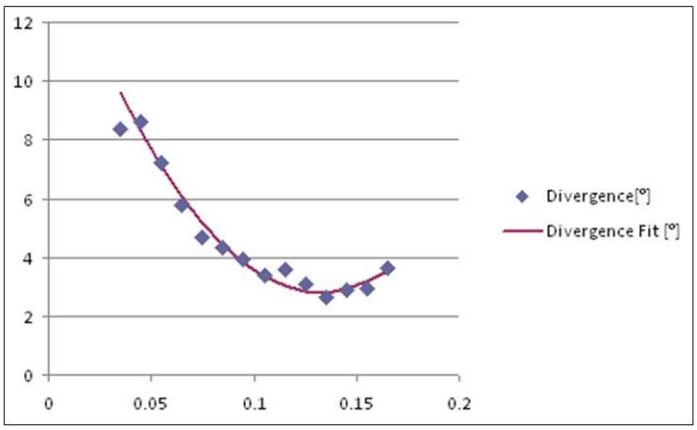

Figure 7.40: Hydrogen divergence as a function of normalised perveance [71].

As previously described, during this scan the divergence decreases so the width measured with the mini-STRIKE is expected to decrease; however this trend is not well recognizable from Figure 7.41.

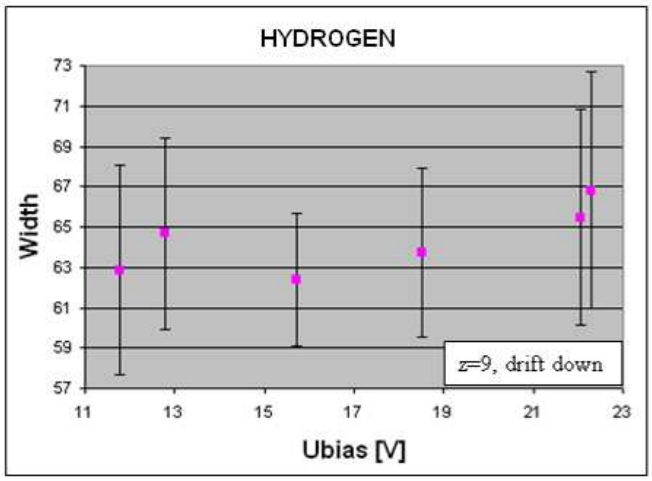

Figure 7.41: Width of the temperature profile on the rear side of the CFC.

Similar trends has been found also in deuterium operations as shown in Figure 7.42 for temperature increase as a function of the U_{bias} and as a function of the normalised perveance and in Figure 7.43 for the width.

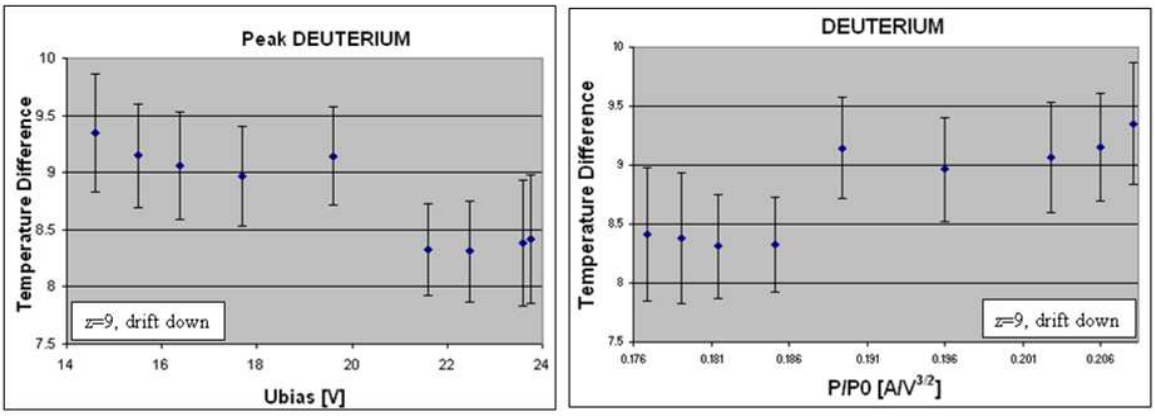

Figure 7.42: mini-STRIKE measurement: maximum temperatures on the rear side of the tile as function for deuterium.

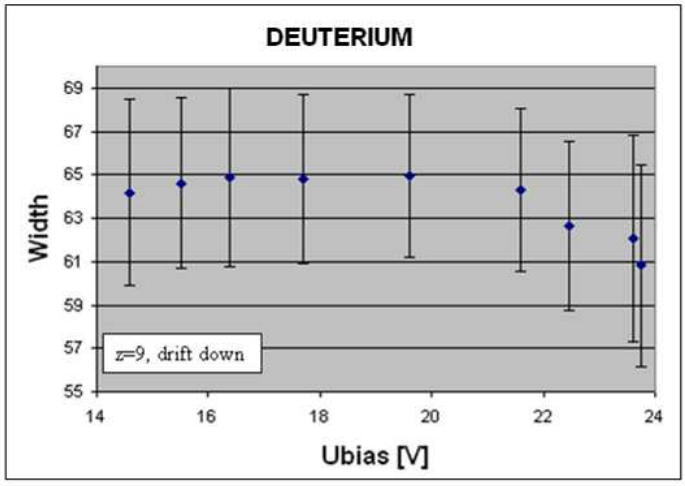

Figure 7.43: Width of the temperature profile on the rear side of the CFC.

From recent experimental findings in BATMAN [72], it seems that the negative ion beam distribution is related to the density distribution of neutrals inside the source and not to the density distribution of positive ions. With this assumption, if the pressure increases inside the source, it is possible that a higher number of neutrals impinge on the plasma grid, where, upon receiving an electron they become negative ions. If the negative ion density increases, due to the repulsion of charged particles of the same sign also the divergence increase (Figure 7.45) and consequently the temperatures measured on the rear side of the mini-STRIKE decrease, as shown in Figure 7.44, except for one point. In fact, as the perveance increases, the perveance decreases (left branch of Figure 7.40). A confirmation is found also from Figure 7.44 on the right hand side: with increasing perveance the temperature increases.

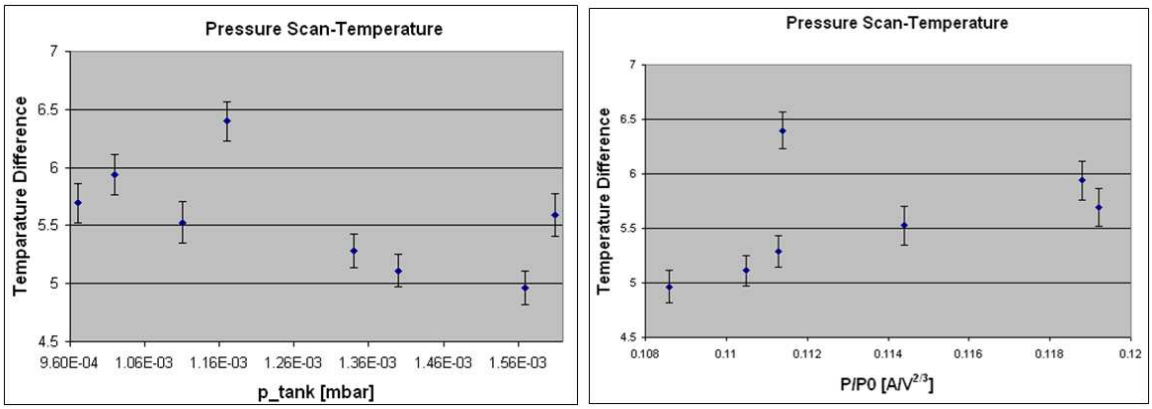

Figure 7.44: Temperature measurements on the rear side of the tile as a function of pressure.

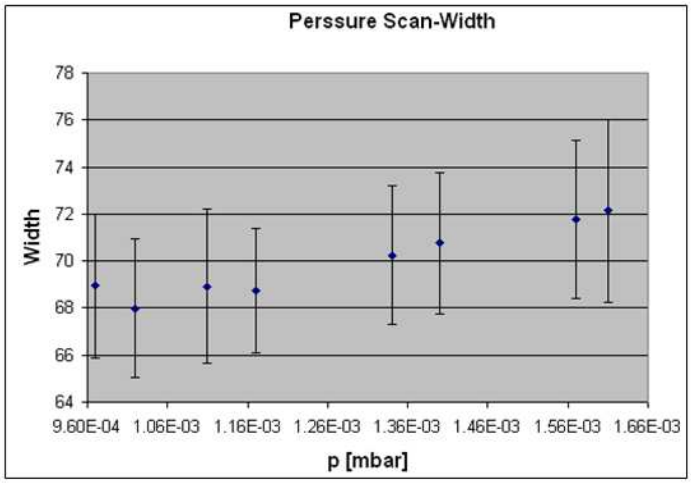

Figure 7.45: Width of the temperature profile on the rear side of the CFC.

The measurement with the mini-STRIKE of the temperature increment with increasing RF power (Figure 7.46) shows an increase also of the temperature measured at the rear side, in the same way as found in the BATMAN results shown on the left hand side of in Figure 7.2. This is probably due to the increase in the atomic hydrogen inside the source, assisted by the RF power, which heats the gas. Correspondingly to the increase of the temperature measured on the rear side of the tile, a clear decrease of the beam width is found (Figure 7.47).

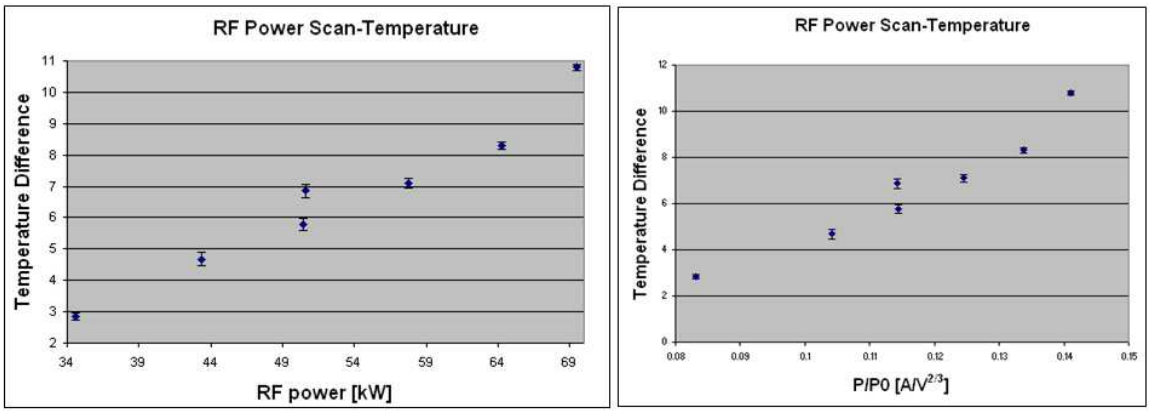

Figure 7.46: Temperature measurement as a function of RF power.

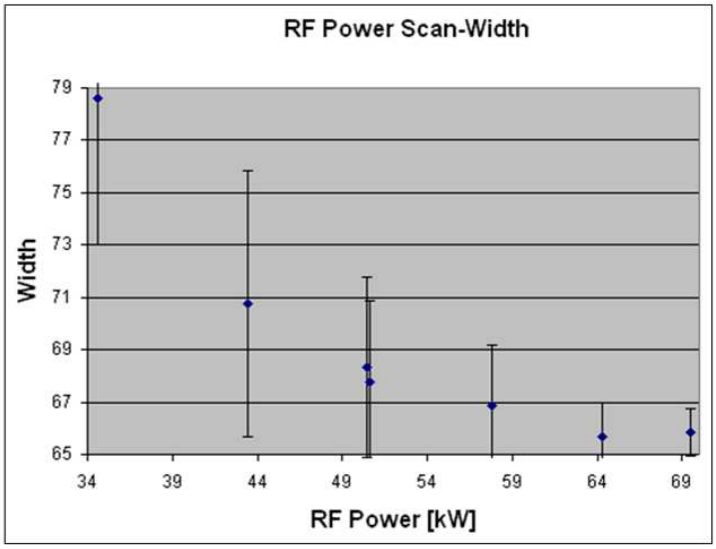

Figure 7.47: Width of the temperature profile on the rear side of the CFC.

Since the mask is actively cooled, calorimetric measurements were also performed in BATMAN, related to the overall intercepted beam energy. Moreover a local measurement of the mask surface temperature on the rear side was recorded. The in-vessel thermocouples are N-type, as foreseen by STRIKE design, so the acquisition system is set on N-type. The two thermocouples for calorimetry were instead K-type, so a "recalibration" of the K thermocouples was carried out in order to convert their measurements as if they were N-type. This procedure was made by measuring the temperature of water (starting from cold water and adding more and more hot water) with the two K-type together with an N-type thermocouple as reference. An example of the resulting calibration curve is shown in Figure 7.48, along with the calibration relationship.

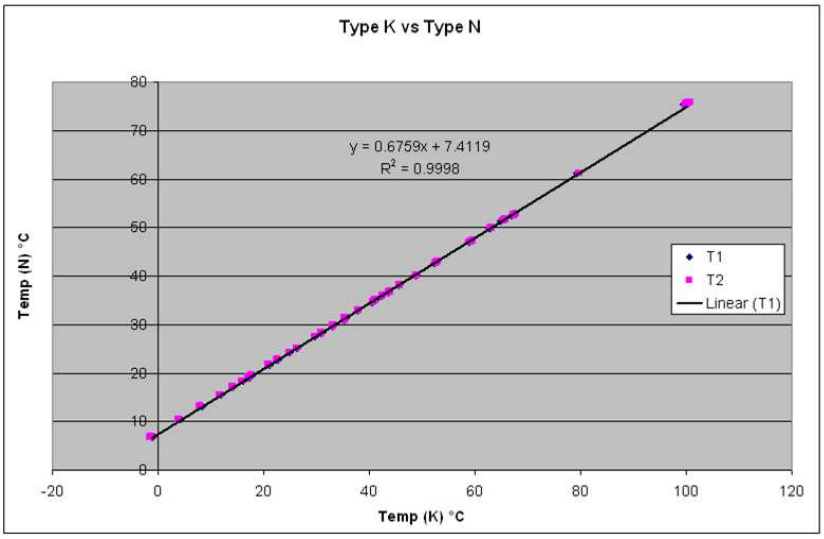

Figure 7.48: Calibration of one of the K-type thermocouples.

To verify the behaviour of the K-type thermocouples, other two N-type thermocouples have been purchased and mounted, together with the previous K-type ones, numerically corrected, in the inlet and outlet. In Figure 7.49 the difference in the corresponding measurements is shown, they are quite constant during time and of about 1.3°C.

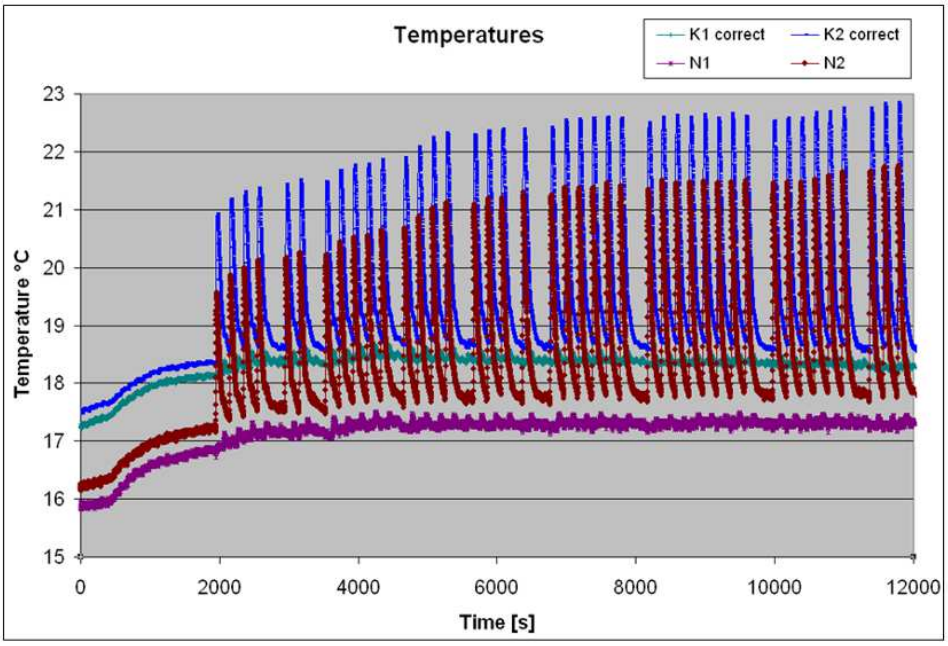

Figure 7.49: Comparison between N-type and numerically corrected K-type thermocouples for mask coolant temperature measurement at inlet and outlet.

As shown in Figure 7.50, from the measurement of water mass flow ($\dot{m}$) and the inlet and outlet temperatures as functions of time, the instantaneous cooling power, P, transferred from the beam to the mask (except for the beamlets on the tile) is obtained:

$$P = \dot{m} \cdot c_p \cdot \Delta T$$

where c_p is the specific heat of water and ΔT is the difference between the coolant temperatures at outlet and inlet.

The cumulative energy removed by the coolant can then be calculated by numerical integration every 0.5s acquisition.

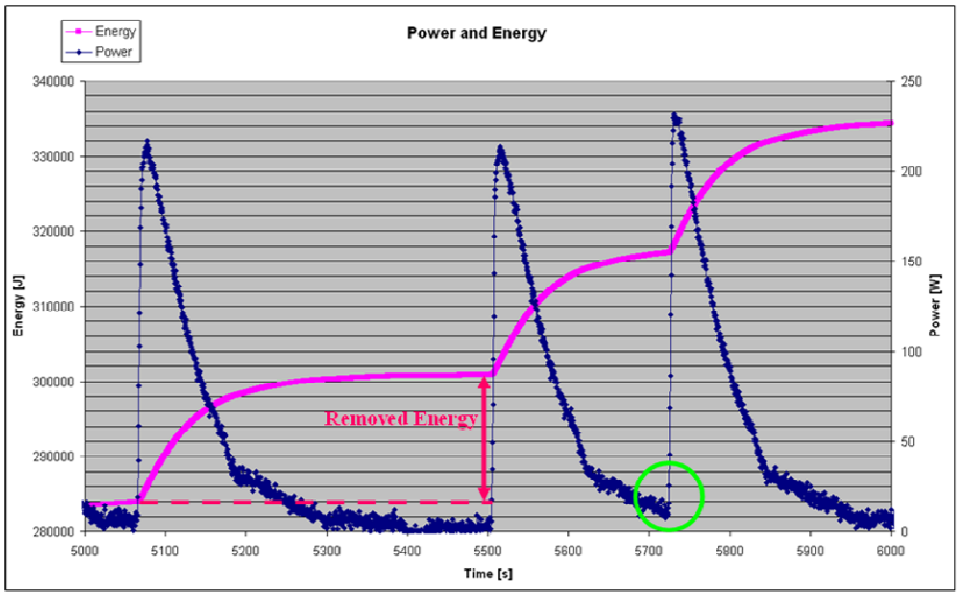

Figure 7.50: Instantaneous cooling power and cumulative energy.

When the cooling power comes back to the initial value at the beginning of the next beam pulse, the total beam energy was removed by the coolant and calorimetry yields the whole energy deposited by the beam on the mini-STRIKE mask; if the successive beam pulse starts before the coolant has completely removed the energy of the previous beam pulse (cooling power starts from a higher value), the calculated energy is not simply related to the intercepted beam. Also in these cases however, the whole beam energy can be reconstructed with the help of a similar pulse in which the calorimetry has been able to remove the deposited beam energy. The beam energy and cooling power of the pulse made at 5065s is compared with the successive beam pulse starting at 5504s in Figure 7.50.

As Figure 7.51 shows, the cooling power and the beam energy can be well superimposed. The first pulse has a higher number of data acquired after the end of the beam pulse; the energy

trend (yellow) tends to saturate: the energy removed by calorimetry is smaller and smaller; the energy removed, resulting from the shorter cyan trend, is the 98% of the whole beam energy, resulting from the yellow trend. Moreover, a fit to the data of the form (1-exp) has to be implemented; this method will be suitable for all pulses.

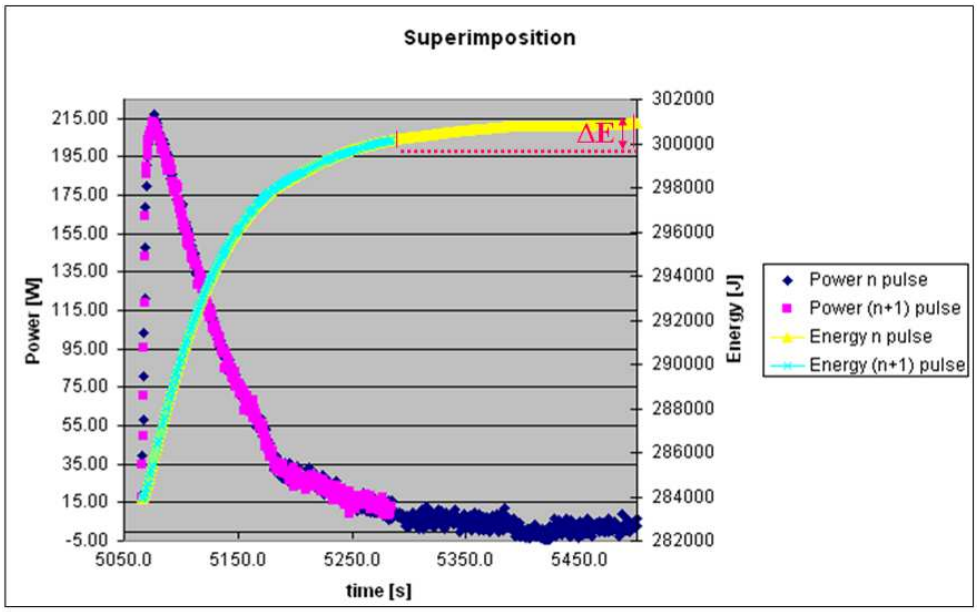

Figure 7.51: Comparison of pulses with same cooling power increment.

The previous considerations show also how from calorimetry it is possible to obtain information about the beam.

On the front side, the beam power density can be described by a Gaussian shape:

$$q(x,y) = \frac{P_{beam}}{2\pi\sigma_x\sigma_y}\exp\left(-\frac{(x-x_0)^2}{2\sigma_x{}^2} - \frac{(y-y_0)^2}{2\sigma y^2}\right)$$

where P_{beam} is the electrical power associated to the beam

$$P_{beam} = (V_{ext} + V_{acc})I_{H^-} = V_{tot}\,I_{H^-}$$

given by the product of the total acceleration voltage and the negative ion current, x_0 and y_0 are the coordinate of the centre of the beam, σ_x and σ_y are the half widths at half maximum in the x and y directions respectively.

Thermocouple T_1 is installed in the centre of the rear side of the mask; from the difference between the maximum temperature measured after the end of the beam pulse and just before the beginning of the beam pulse, the energy flux $q_{T1\ position}$, applied for a time t_{on}, in the position where T_1 is installed, can be estimated by inverting the relationship [73]:

$$\Delta T_1 = \frac{q_{T_1 position} t_{on}}{\rho c_s L}$$

where L is the thickness of the slab and the thermal parameters of CuCrZr are used: ρ = 8890 kg/m^2 is the mass density and c_s = 400 J/(kg K) the specific heat [74]. The assumption that $q_{T1position}$ has a flat profile in the neighbourhood of the position of the thermocouple T_1 was made and that the thermal radiation can be neglected, thanks to the low temperature increases.

Under these assumptions, the proportionality constant between the beam energy flux $q_{T1\ position}$ and the measured ΔT_1 is shown in Figure 7.52 and for t_{on} =4s and L = 10 mm it is 112.5 K/MW.

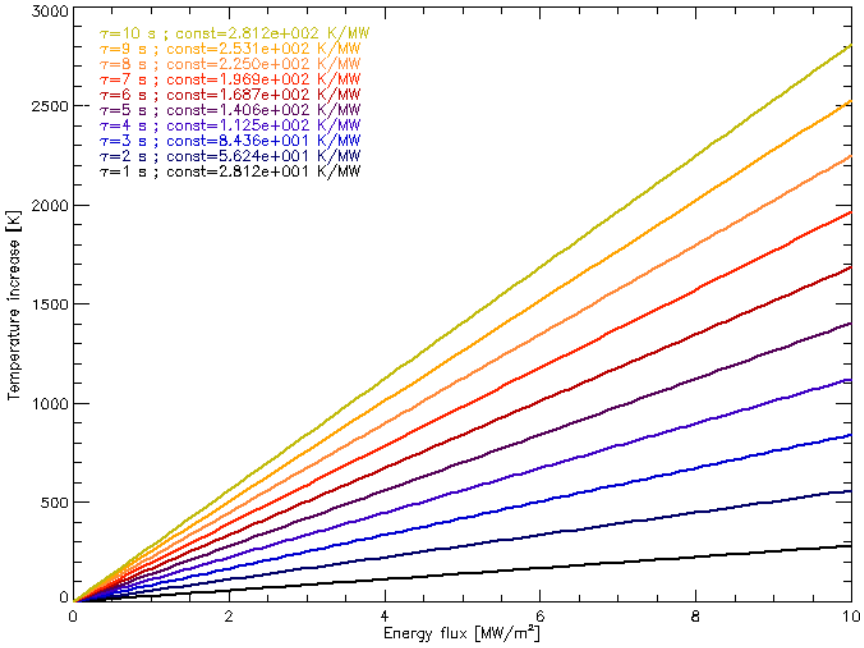

Figure 7.52: proportionality constant between the beam energy flux and the measured DT1.

Upon assuming the symmetry of the beam and that ΔT_1 is measured just in correspondence to the maximum of the beam power density, it can also be written:

$$\Delta T_1 = \frac{P_{beam}}{2\pi\sigma_x\sigma_y}\frac{t_{on}}{\rho c_s L} \cong \frac{P_{beam}}{2\pi\sigma^2}\frac{t_{on}}{\rho c_s L}$$

So the beam half width at half maximum can be obtained and plotted as a function of the total beam voltage (extraction+acceleration) in Figure 7.53, in other words, the dependence of the beam width on the beam perveance and expected divergence is shown in Figure 7.54 and Figure 7.55 respectively:

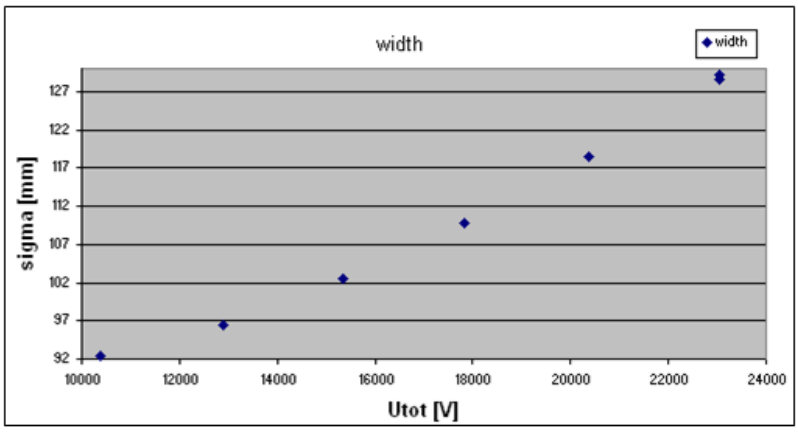

Figure 7.53: Beam width as a function of the total beam voltage.

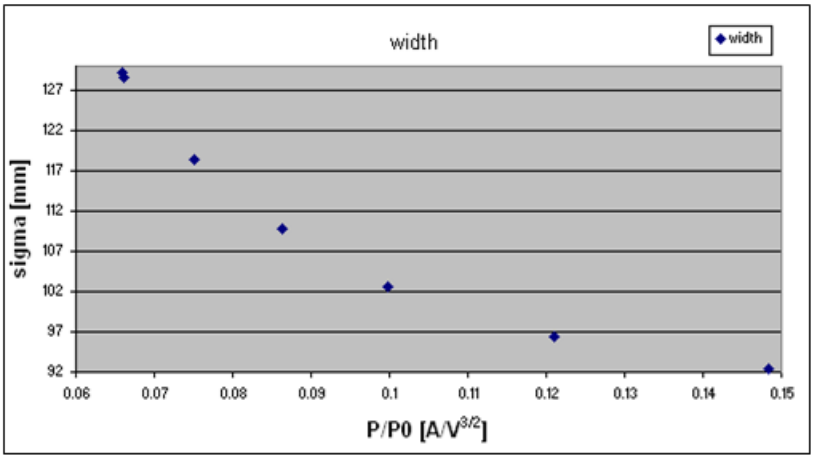

Figure 7.54: Beam width as a function of the ratio of the perveance.

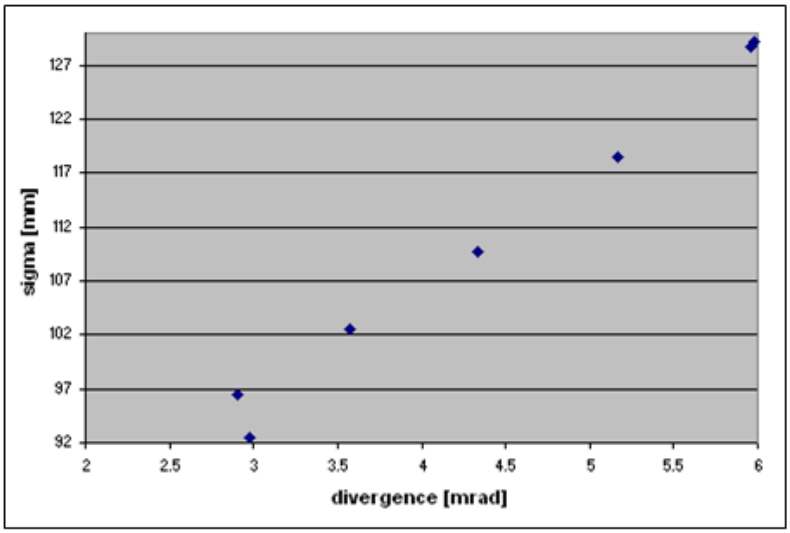

Figure 7.55: Width linear dependence from divergence.

If the beam voltage increases, a higher number of negative ions are extracted from the source; due to the space charge repulsion the beam broadens and its divergence increases, consequently also the beam width increases. As already seen, the optimum in the perveance ratio for hydrogen is 0.135: on the left branch of the perveance, as the perveance increases the divergence and likewise the beam width decreases.

The mean value of P_{mask} is known from the calorimetry on the mask: $E_{cal} = P_{mask} t_{on}$.

From the ratio P_{mask}/P_{beam}, the part of the beam intercepting the mask can be obtained. P_{mask}/P_{beam} is plotted in Figure 7.56. The experimental ratio between the powers is derived from measurement. As shown in Figure 7.57, the mask is too small to intercept the whole BATMAN beam. To interpret the experimental findings, the calculated power ratio is obtained from the beam width, as previously derived, considering also the geometry and inclination of the source. It can be noticed that the computed power ratio is larger than the experimental one; this might be due to: some loss of power during the flow of the water towards the position where the thermocouples are located; the possible contribution of thermal radiation from the front of the mask; the daily drift of the coolant temperature as more and more pulses are perfomed.

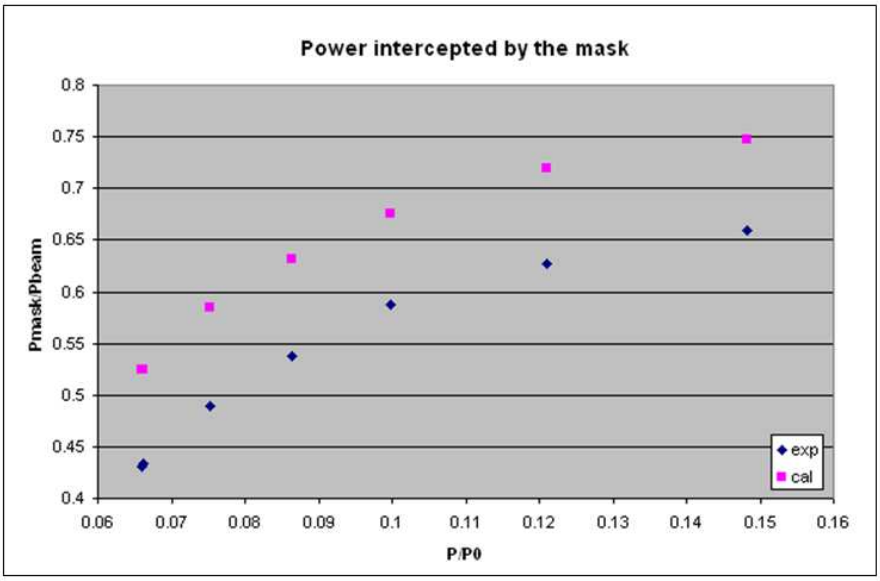

Figure 7.56: Experimental and calculated Pmask/Pbeam.

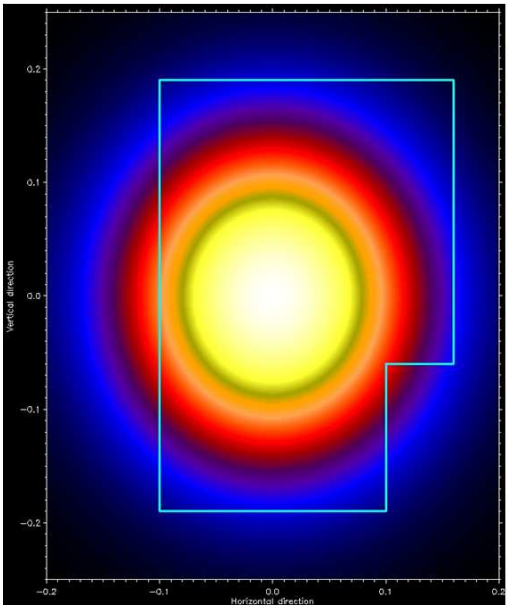

Figure 7.57: Beam footprint with respect to the overall dimension of the mask.

The experimental campaign in BATMAN has demonstrated that the diagnostic principle, on which the instrumented calorimeter STRIKE is based, is sound: all subsystems worked properly and some previous experimental findings concerning the BATMAN beam features were confirmed by this new device. Data analysis is still ongoing.

7.2 Tests at IPP-GLADIS

The expected energy flux expected in SPIDER is quite large, reaching up to 20 MW/m^2 at the beamlet centre. Considering that such heat deposition is very localised, depending on the beamlet size and the distance in between them, large thermal gradients can be expected and, correspondingly, large thermal stresses in the bulk of the tiles. To verify the suitability of the CFC samples to the final use, it was decided to carry out a series of tests in a large particle beam featuring high and localised power densities. Several electron beam facilities are in operation, but in the case of electron beam, reflection and formation of secondary electron reduces the deposited beam power; beams on the contrary provide complete absorption of the beam power on the surface of the tested material.

GLADIS (Garching Large Divertor Sample test Facility) [75] is a high heat flux (HHF) test facility constructed in the laboratory of IPP Garching. It has started operation in 2007 and this facility has the aim of testing actively cooled plasma facing components under high heat fluxes. GLADIS has two H^+ ion sources. The current is extracted from a water-cooled 3-grid system and at the end of the vessel an actively water-cooled beam dump is installed. The position of the

target plane is indicated in Figure 7.58 by numbers (1) and (2): the distance from the sources depends on the power density to be achieved at the target. Both ion sources are inclined at 8° to the horizontal axis of the facility. The preferred position of the target is 3 m downstream the ion sources at the intersection of the beams, as shown in Figure 7.58. GLADIS permits to investigate small material samples as well as full-scale water-cooled components (up to 2m lenght); GLADIS can provide up to 8.5 l/s of cooling water to the sample under test. The water-cooled vessel permits long operations.

Due to a complex magnetic ion removal system with deflection magnets, ion dumps and cryopumps are note necessary but due to the absence of the pumps in the source region, the hydrogen pressure in the main vacuum chamber reaches $1x10^{-3}$ mbar during the pulse. Hence the beam is largely neutralised at the target plane.

The parameters for GLADIS operation are: H_2 gas flow 6 6 mbar l/s, RF power 15–35 kW, high voltage 20–53 kV. The current extracted from the source varies between 5 and 22 A depending on both the RF power and high voltage settings. No ion neutralizer is used in and the beam divergence is 1.5°. Each source can deliver 1.1MW power each and every source generates heat loads between 3 and 55 MW/m^2 with a beam diameter of 70mm at the target position

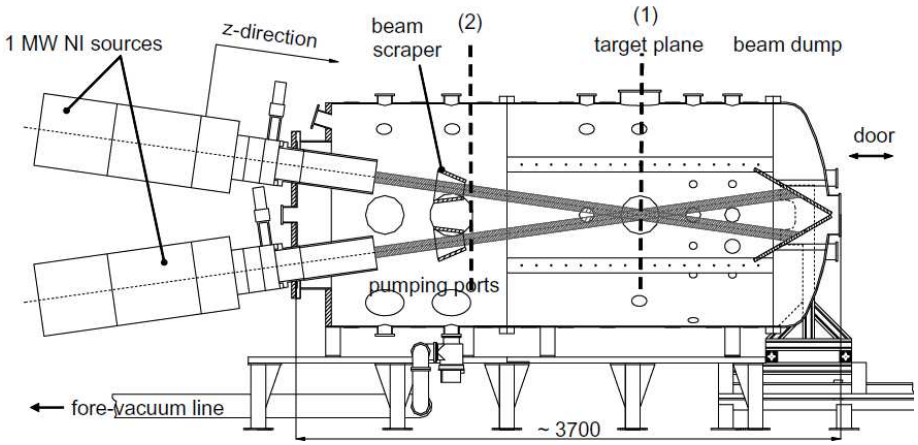

Figure 7.58: The cross-section of the HHF test facility GLADIS.

The power density distribution of the beam was measured at the target plane with an inertially cooled copper calorimeter. A 2D Gaussian fit to these data provides the beam profiles. An example is shown Figure 7.59: the beam profile recorded is related to a pulse with 876 kW beam power. The comparison of calculated and measured profile is also shown.

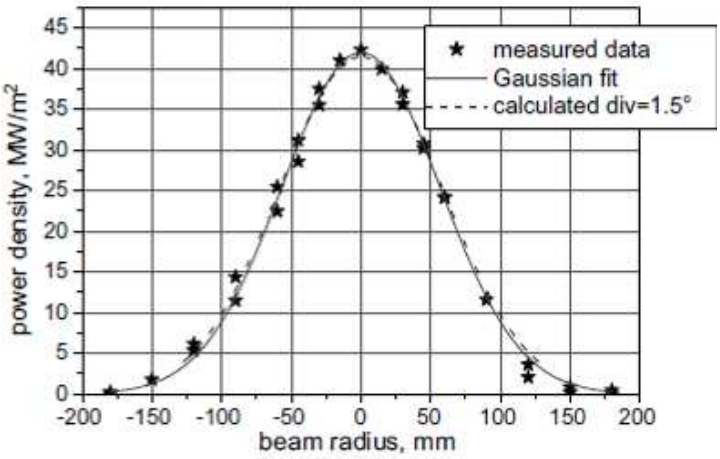

Figure 7.59: Beam profile with 876 kW power [75].

In Figure 7.60, several Gaussian fits are presented, corresponding to beam profiles measured in different beam conditions.

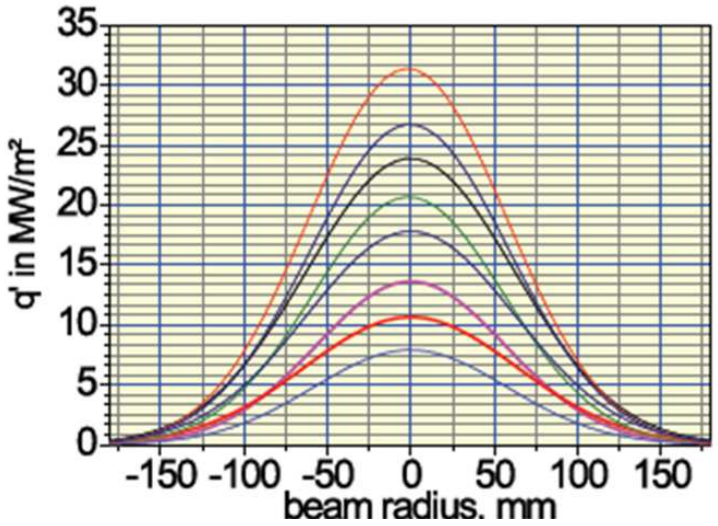

Figure 7.60: Heat flux distribution at the target position [75].

Testing the CFC tiles in GLADIS can also help for the qualification of the non-destructive examination methods of the material and for the definition of the acceptance criteria of the tiles procured for STRIKE.

7.2.1 Design of CFC tile support

The support of the tile under investigation must:

- support the tile and the thermocouples;
- - protect the supporting structure against the beam;
- - define a clear-cut separation between the area illuminated by the beam and the area protected from it;
- - allow the observation of the rear side of the tile by the thermal camera.

Two stainless steel supports (pockets number 6 and 7 in Figure 7.61) are used to hold the tile permitting the thermal expansions. To protect the stainless steel supports from the overheating due to the high power of the beam, two graphite shields have been used, indicated with the number 2 and 3 in Figure 7.61; one of them has also the role of creating a sharp boundary from the part of the tile hit by the beam, in this way the thermal gradient is very concentrated and the tile results very stressed. Since the tile is observed at the rear side by a thermal camera, the supporting structure has to hide as little as possible the rear surface of the tile. Parts number 4 and 5 in Figure 7.61 play the role of spacers and for each tile of different length a pair of those elements was used. Two thermocouples at the rear side, arranged as for STRIKE design, can measure in a hot point and in a cold point. The whole system presented in Figure 7.61 will be fixed to the manipulator arm by means of a plate appropriately developed; the element number 14. The same plate has a slot in the upper part for the extraction of the signal cables.

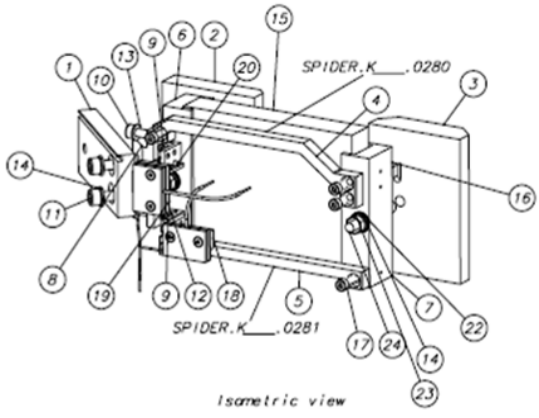

Figure 7.61: Tile supporting structure for test in GLADIS.

The graphite protection shield has a helicoil for a screw to fix it to the stainless steel support, and a slot, with a corresponding pin on the support, to avoid the rotation of these elements.

Figure 7.62: Rear side of the graphite protection shield.

The top view of the whole system is shown in Figure 7.63, where the graphite protecting shields can be clearly seen. It can be noticed that the plate coupling the tile support to the manipulator arm is inclined by 45° with respect to the tile.

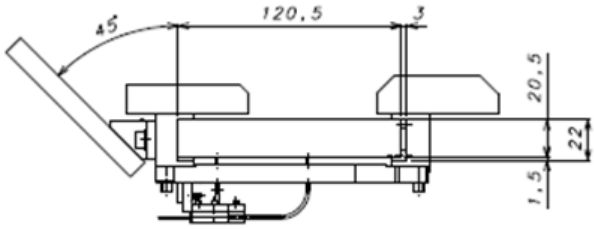

Figure 7.63: Top view of the supporting structure.

This arrangement permits the observation of the rear side by the thermal camera for an appropriate port window and to insert the whole system inside the vessel, through the manipulator porthole, as shown in Figure 7.64.

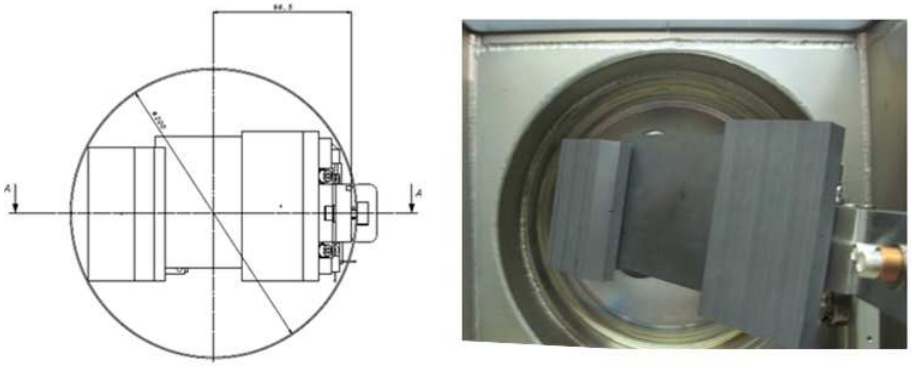

Figure 7.64: Insertion of the system through the manipulator porthole.

Figure 7.65 shows the whole system in position, inside the vessel and the corresponding infrared image, as seen by the thermal camera.

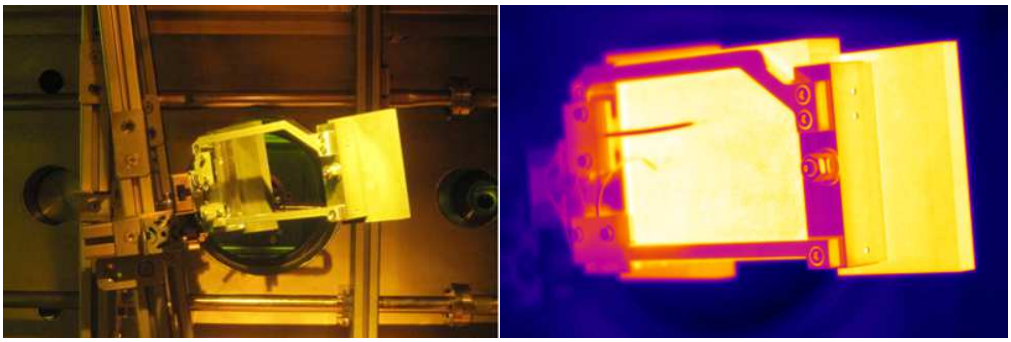

Figure 7.65: The final assembly of the system and an infrared image.

7.2.2 Comparison between simulations and experimental data

The experimental conditions have been simulated: a Gaussian heat load, with the same parameters as in GLADIS, hits only a limited part of the tile, due to the graphite protections. The following figures refer to the prototype type B; the emissivity is set to 1 and radiation towards surfaces at 300K is included for the entire model.

Figure 7.70 shows the temperature map of the front side of the tile, just after 2s beam application; the initial temperature is set to 510K to compare with a pulse executed in GLADIS.

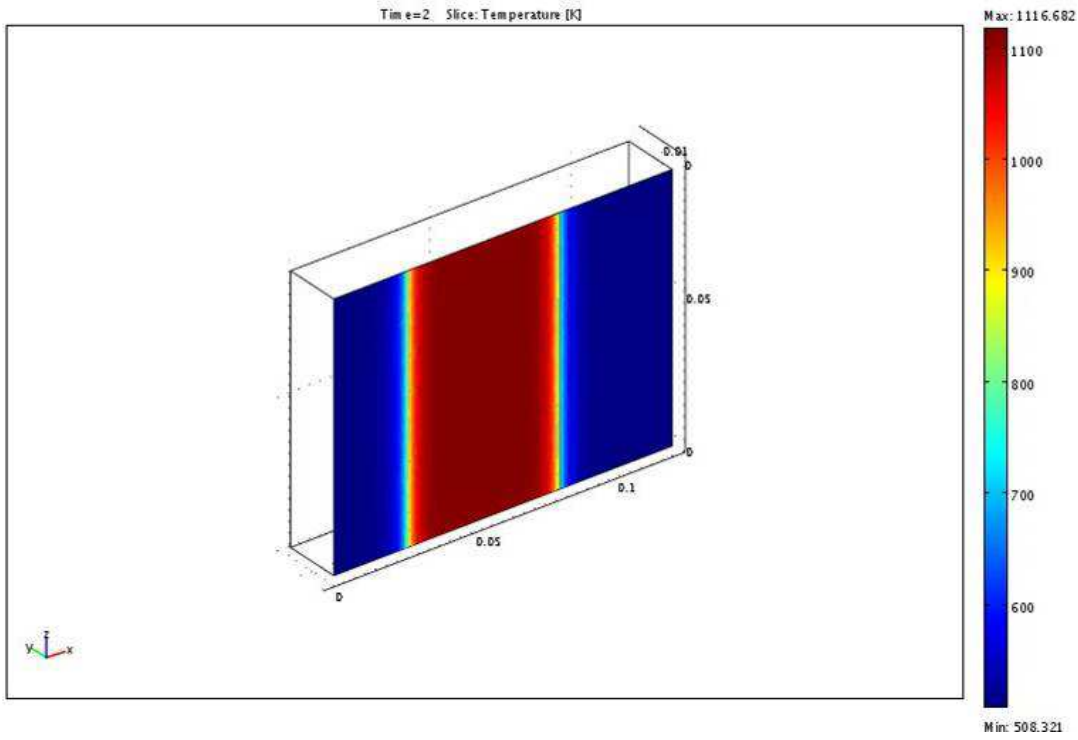

Figure 7.66: Front side after 2s heat load application.

Figure 7.71 shows the temperature profile along the horizontal direction obtained by simulation compared to the one obtained from experimental data: the results are in good agreement.

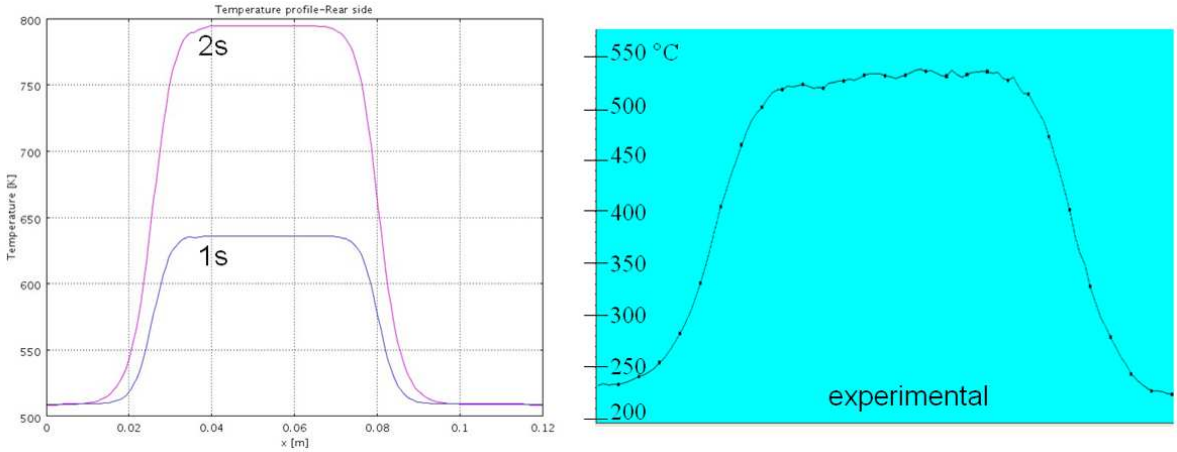

Figure 7.67: Comparison from synthetic data (left) and experimental data (right), sample B1.

The same comparison has been made also for tile A4 and A6. The thermal parameters introduced in the model are those worked out from the comparison between experimental results and numerical simulation made for laser tests (section 5.3). The thermal parameters for samples A are all constant: unlike B prototypes, the thermal properties are not given as functions of temperature. GLADIS experiment produced a power beam (15MW/m^2 in this campaign), so the CFC reaches high temperature also with short pulse duration. The temperature range is too wide to use constant values of thermal conductivities. Probably for this reason the temperature increases found in the experiment are very different from the temperature increases from the simulations, in which the same experimental conditions are reproduced, for both A4 (Figure 7.68) and A6 (Figure 7.69). Indeed, when temperature increases, the specific heat is also expected to increase like for tiles B, so that the experimental temperature variation is much smaller than in simulations.

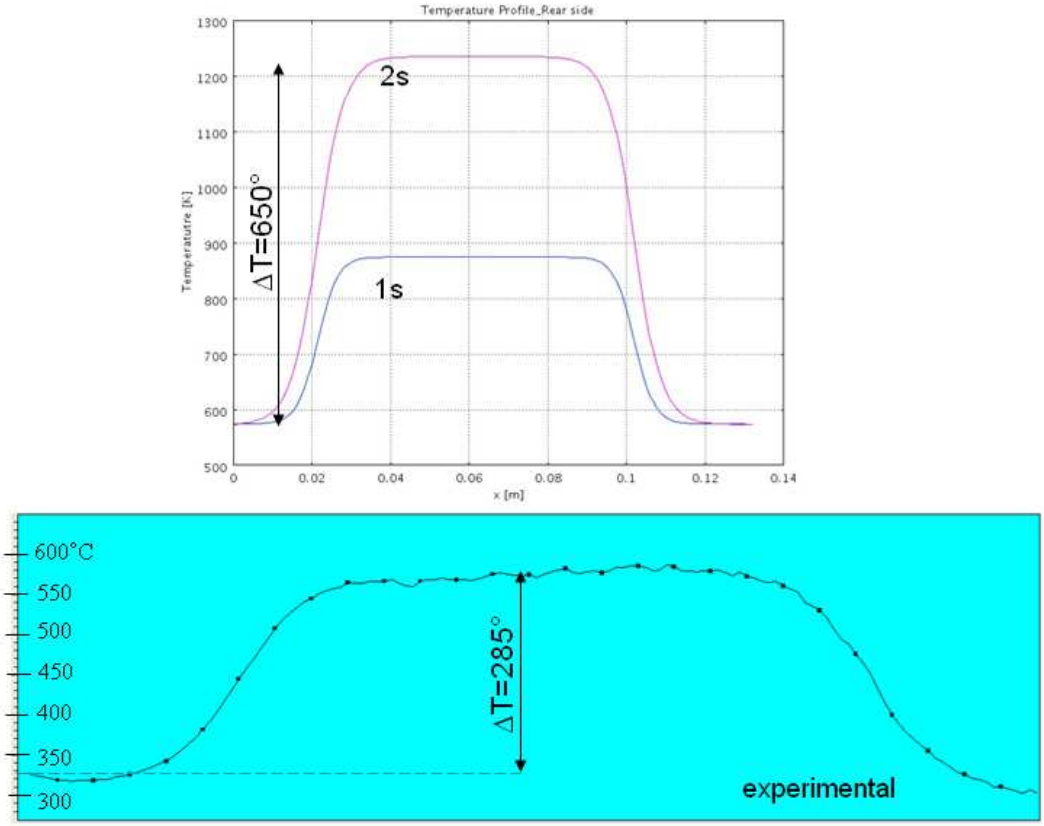

Figure 7.68: Comparison between synthetic data and experimental data, sample A4.

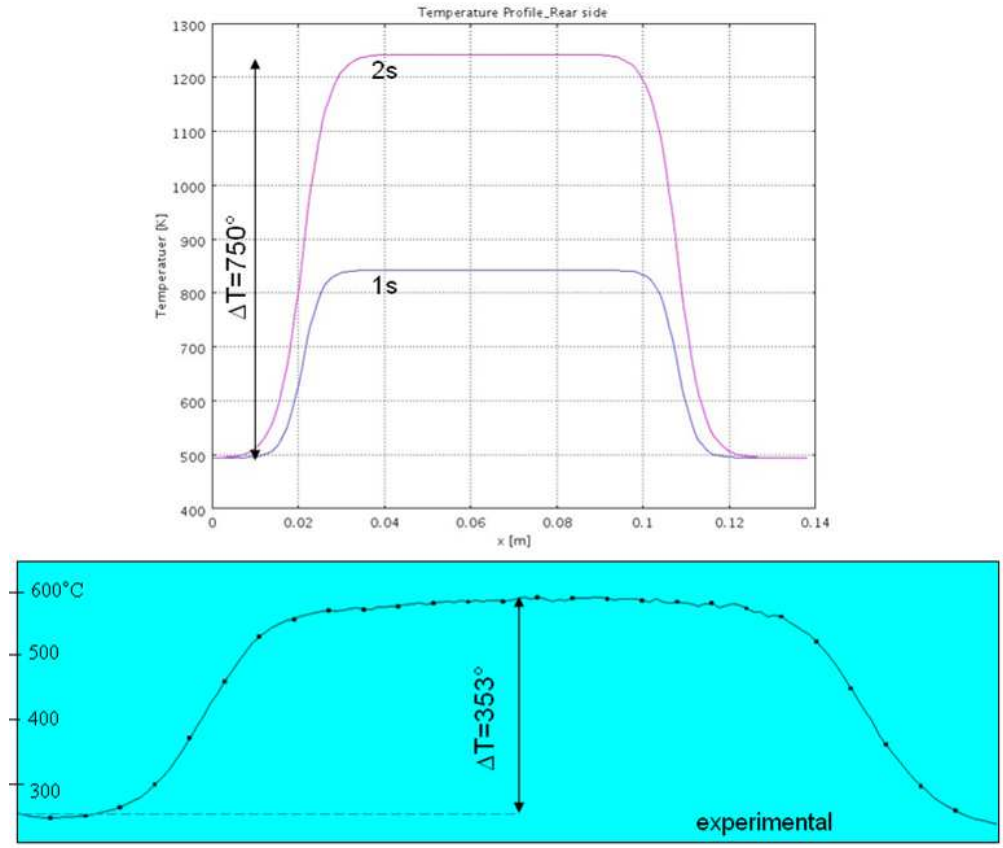

Figure 7.69: Comparison between synthetic data and experimental data, sample A6.

7.2.3 Measurement campaigns

The CFC tile was aligned by a prototype and a laser as shown in Figure 7.70.

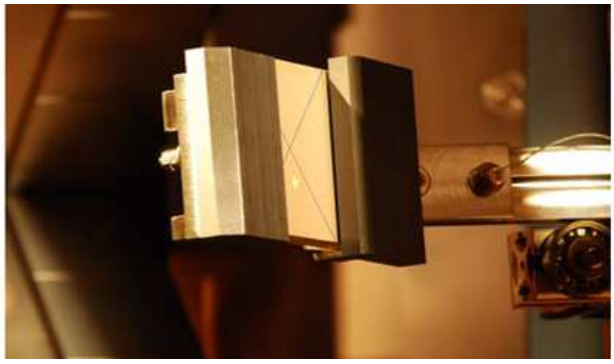

Figure 7.70: Alignment of the prototype.

After the verification of the proper position, the tile was mounted on the supporting structure and was installed on the manipulator head inside a chamber separate from the main vacuum vessel (Figure 7.71), starting pumping. After reaching the proper vacuum level, the gate valve is opened towards GLADIS vessel.

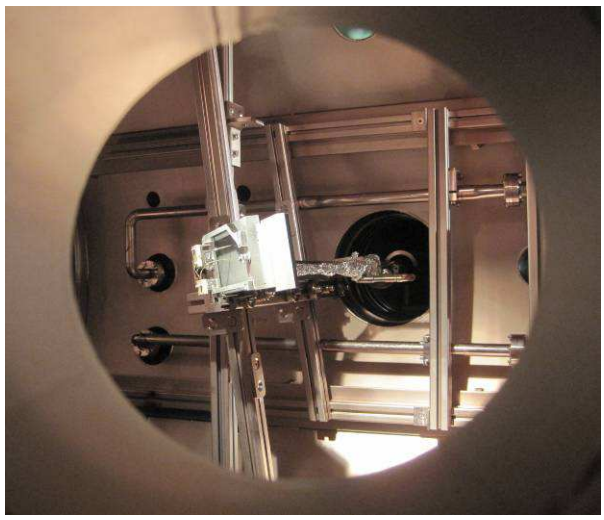

Figure 7.71: Introduction of the prototype inside GLADIS vessel.

Thermocouples are installed on the rear side of the tile and on the stainless steel support to monitor the temperature during the experimental campaign (Figure 7.72).

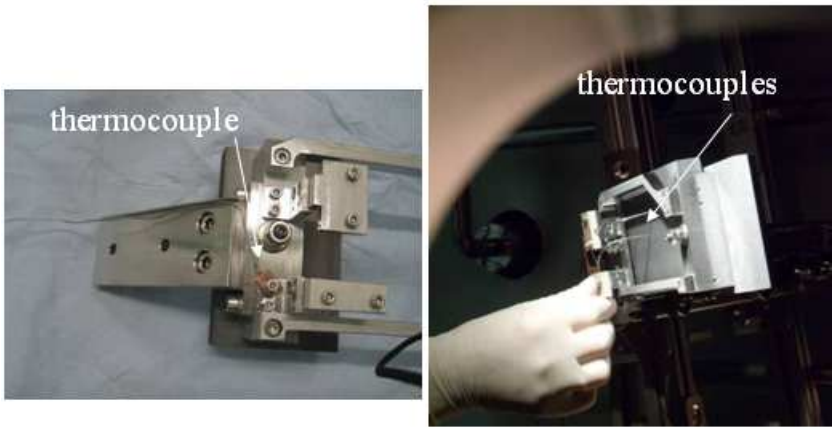

Figure 7.72: Thermocouple on the supporting structure (left) and installation of thermocouples on the tile (right).

Figure 7.73 shows the measurement systems used during the CFC tests: pyrometers and thermal cameras were observing both the front and the rear side of the tile; visible cameras were also present. The STRIKE IR camera is not visible in the figure: it was installed on a porthole opposite the manipulator. The KTR pyrometer was not operating.

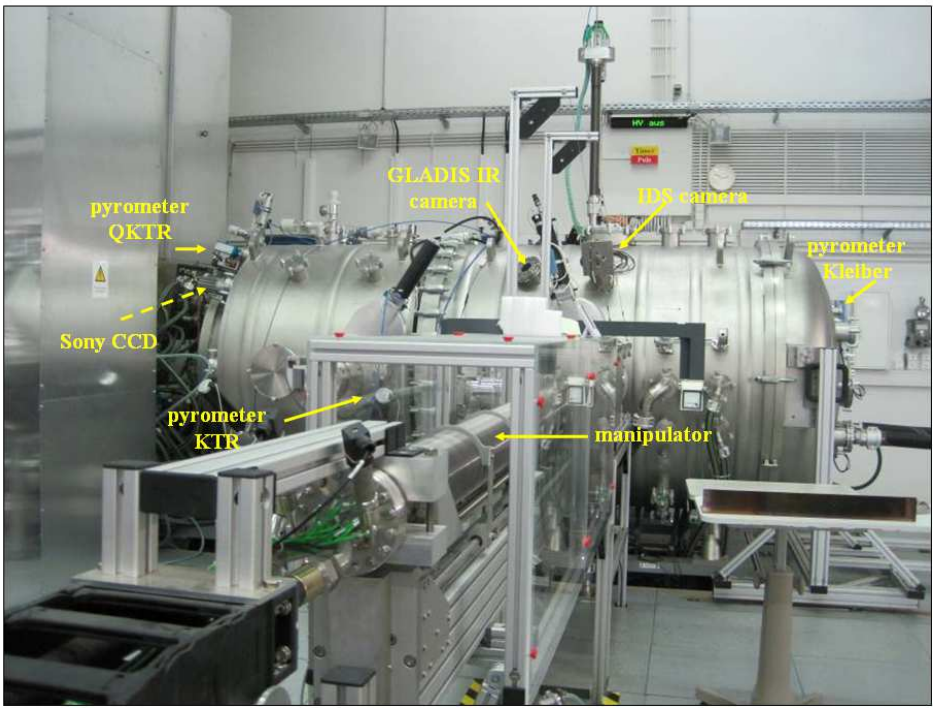

Figure 7.73: Measurement systems during the CFC tests.

Measurements in GLADIS were performed with a beam profile having a peak of 15 MW/m^2. For all tiles the exposure time was varied between 0.5s and 3s.

The measurements of the KTR pyrometer, measuring the temperature on the front side of the CFC tiles, and of the Kleiber pyrometer at the end of the vessel, performing the measurements on the rear side of the CFC tiles, are shown in Figure 7.74: the black curve represents the extraction current and it is included in this graphs to indicate the pulse duration; the magenta curve represents the local temperature on the front side and the blue trend is referred to the local temperature at the rear side: the maximum value on the rear side is reached slightly later than on the front side, due to the heat transfer time from front to back. In particular, the sharp increase of the front temperature and hollow trend is probably due to the overheating of the powder in front of the surface when the beam particles reach the surface; this powder is emitted from the surface in the first beam pulses, as show in Figure 7.76. Besides, the front pyrometer can record the temperature only for value over about 700°C. The front and rear temperature signals show the slow relaxing time of the tile temperature.

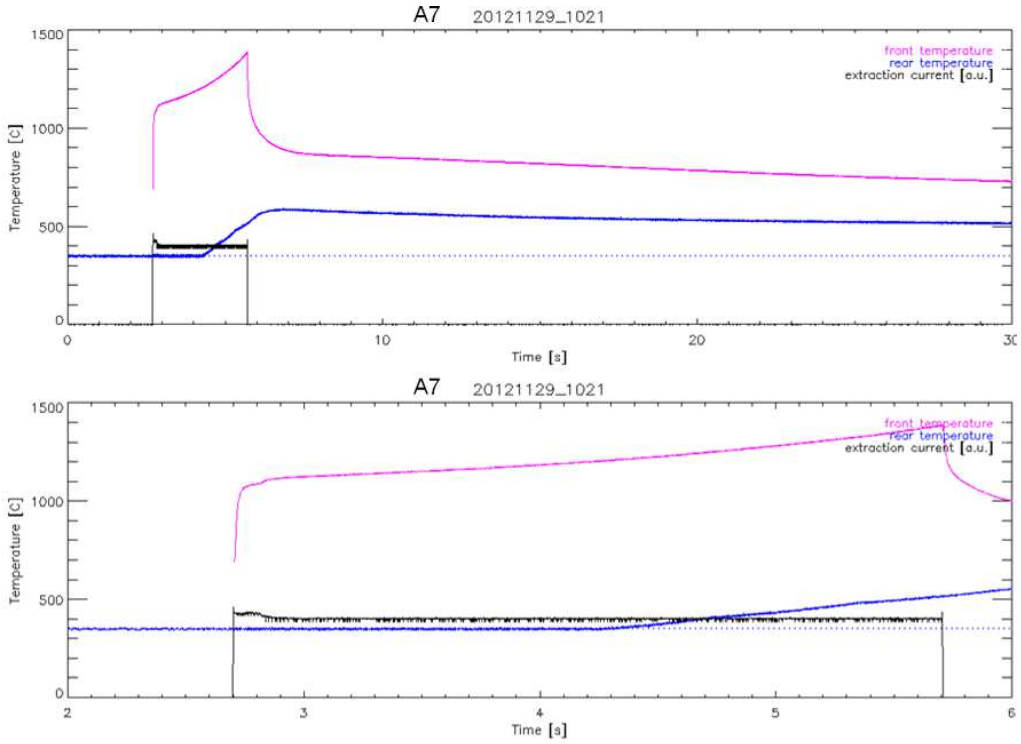

Figure 7.74: Measurement by pyrometer (up); zoom around the beam pulse (bottom).

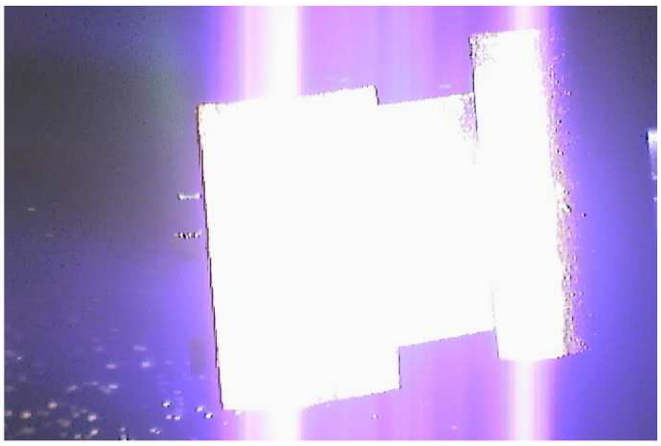

Figure 7.75: Graphite powder removed from the tile.

From the temperature profile measured by thermal camera, a high temperature variation can be observed: for tile A7 and with beam duration of 3s, the temperature gradient is larger than 19°C/mm.

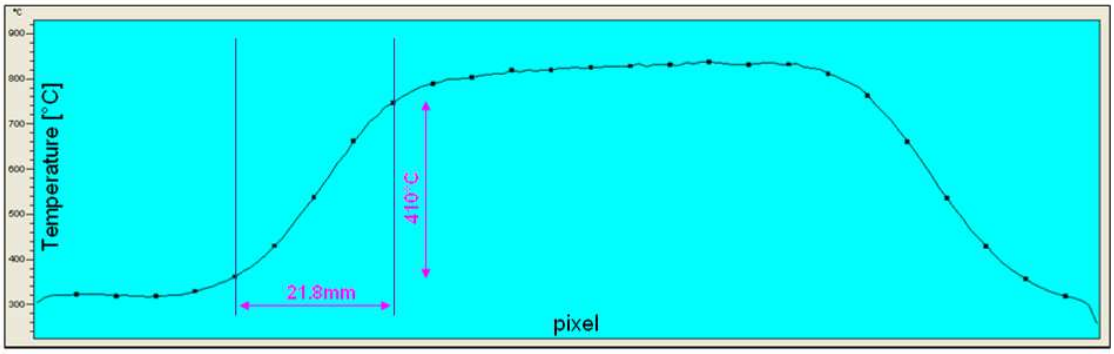

Figure 7.76: Temperature profile for 3s pulse duration, tile A7.

7.2.4 Preliminary remarks on CFC tiles exposed to GLADIS beam

At the end of the experimental campaign, all tested tiles have been observed. A wide campaign to investigate the effect of the GLADIS beam in the structure and the bulk of the tiles will be planned soon, but just by a simple visual observation damages can be seen.

A4 tile, notwithstanding its numerous signs on the surfaces, seems to have withstood well the exposure to the power beam. A comparison between the smooth side and the rough side, before and after the tests in GLADIS is shown in Figure 7.77 and Figure 7.78 respectively: only preexistent signs can be observed.

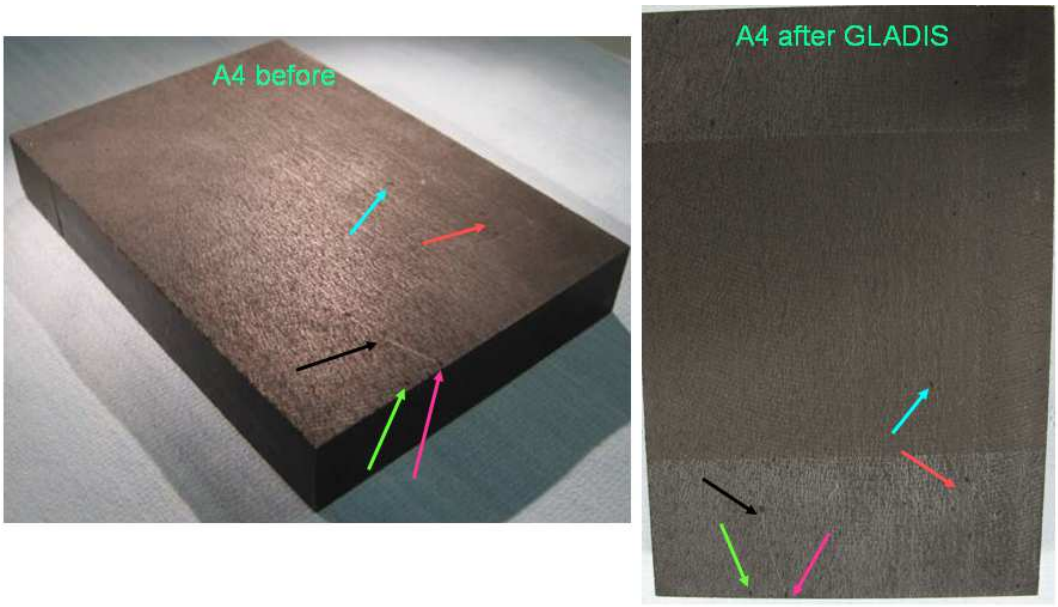

Figure 7.77: A4 smooth side, before and after exposure to the GLADIS beam.

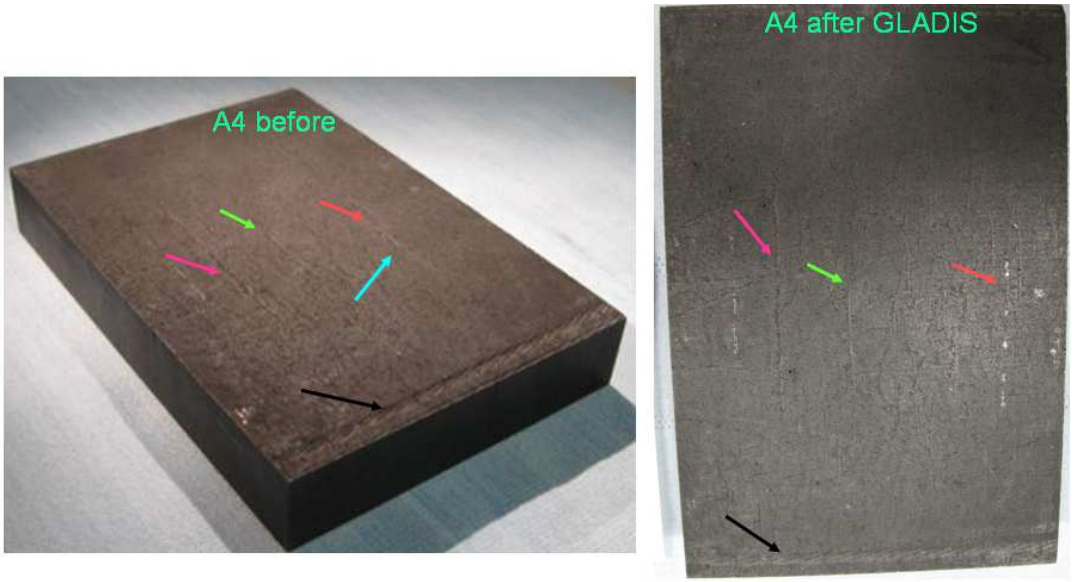

Figure 7.78: A4 rough side, before and after exposure to the GLADIS beam.

The same comparison was done for A6. On the smooth side some sings have correspondence but a crack in the tile after exposure in GLADIS can be observed, as shown by the red dashed arrow in Figure 7.79.

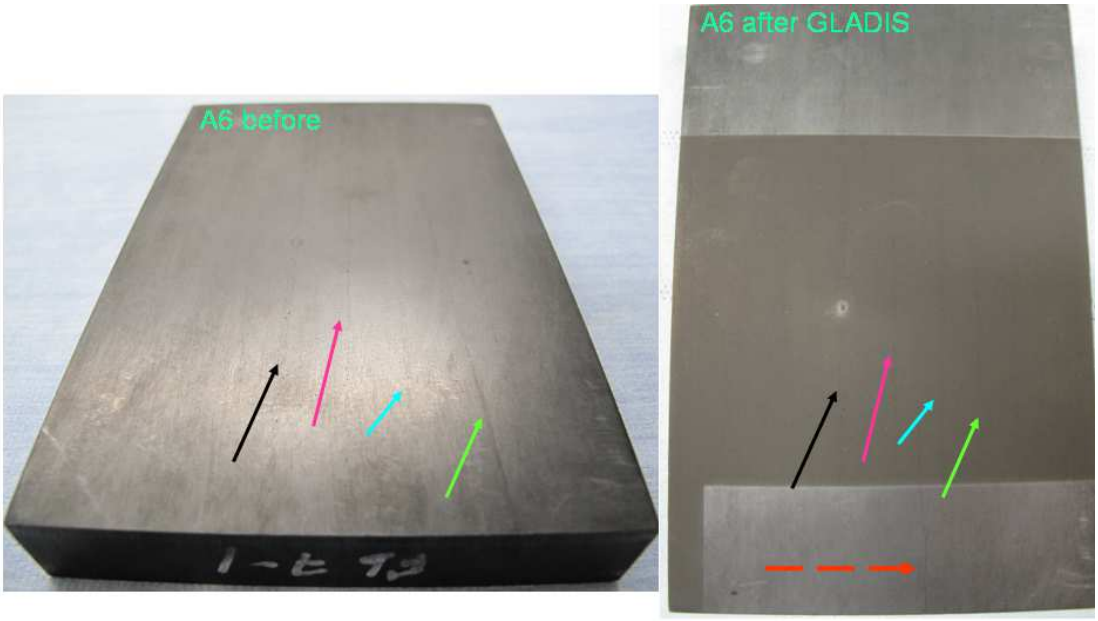

Figure 7.79: A6 smooth side, before and after exposure to the GLADIS beam.

This crack was investigated more in detail. Figure 7.80 shows that at least a sign was pre-existent; it was probably opened up by the exposure to the GLADIS beam.

All these signs and cracks are parallel to the sheets of fibre bundles (see section 4.4).

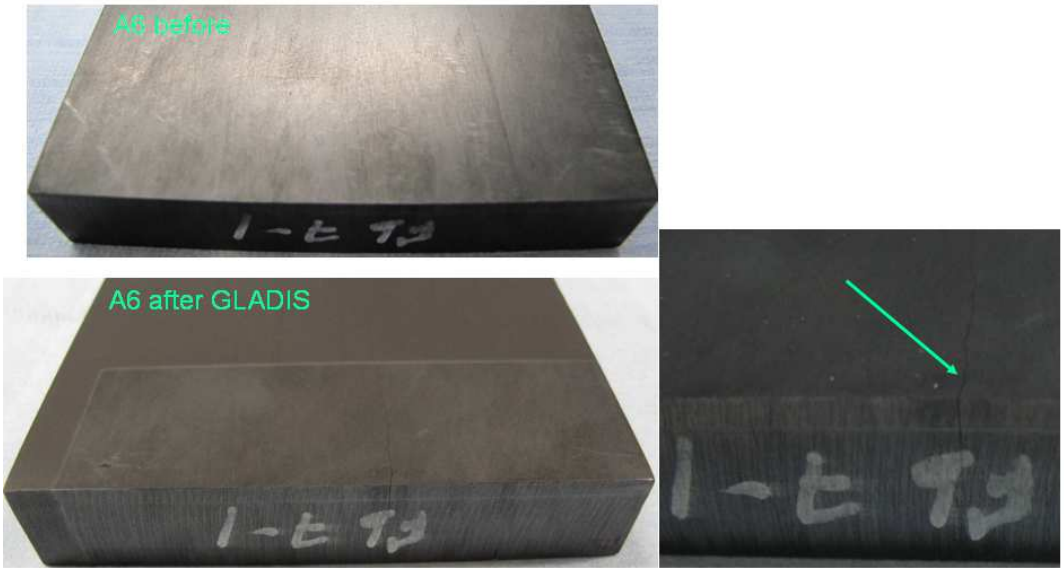

Figure 7.80: Details of crack in A6 smooth side.

Also on the rough side of the tile A6, as shown in Figure 7.81, a crack appeared. In this case the crack is perpendicular to the sheet of fibre bundles.

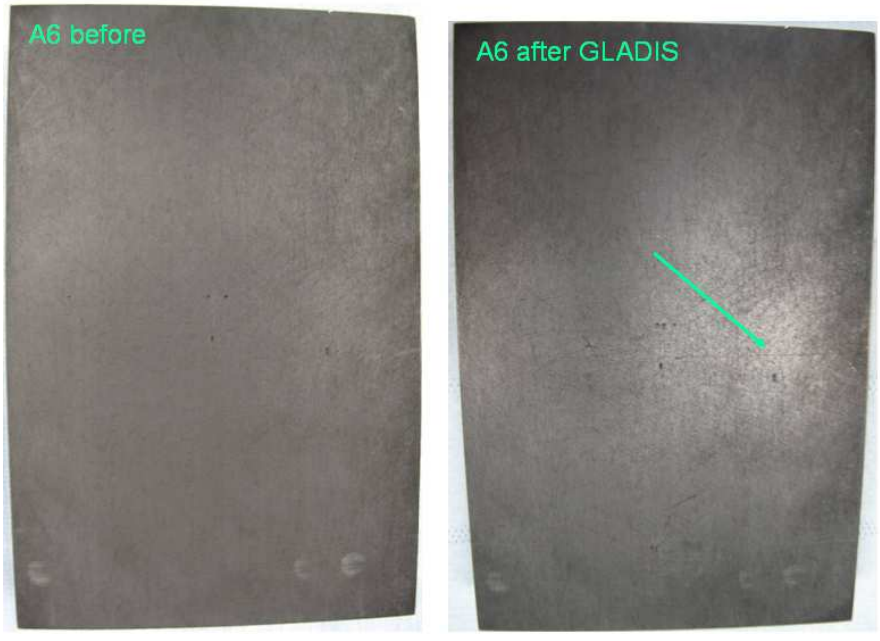

Figure 7.81: A6 rough side, before and after exposure to the GLADIS beam.

The tile A7 has shown visible fractures (Figure 7.82) and in some cases the crack is continuous in the tile: recognizable on one side, in the thickness and correspondingly on the

opposite side. The higher is the thermal expansion coefficient, 9.10^{-6} /K for A7 tile for the in-plane directions, the higher is the stresses in the material due to thermal expansion.

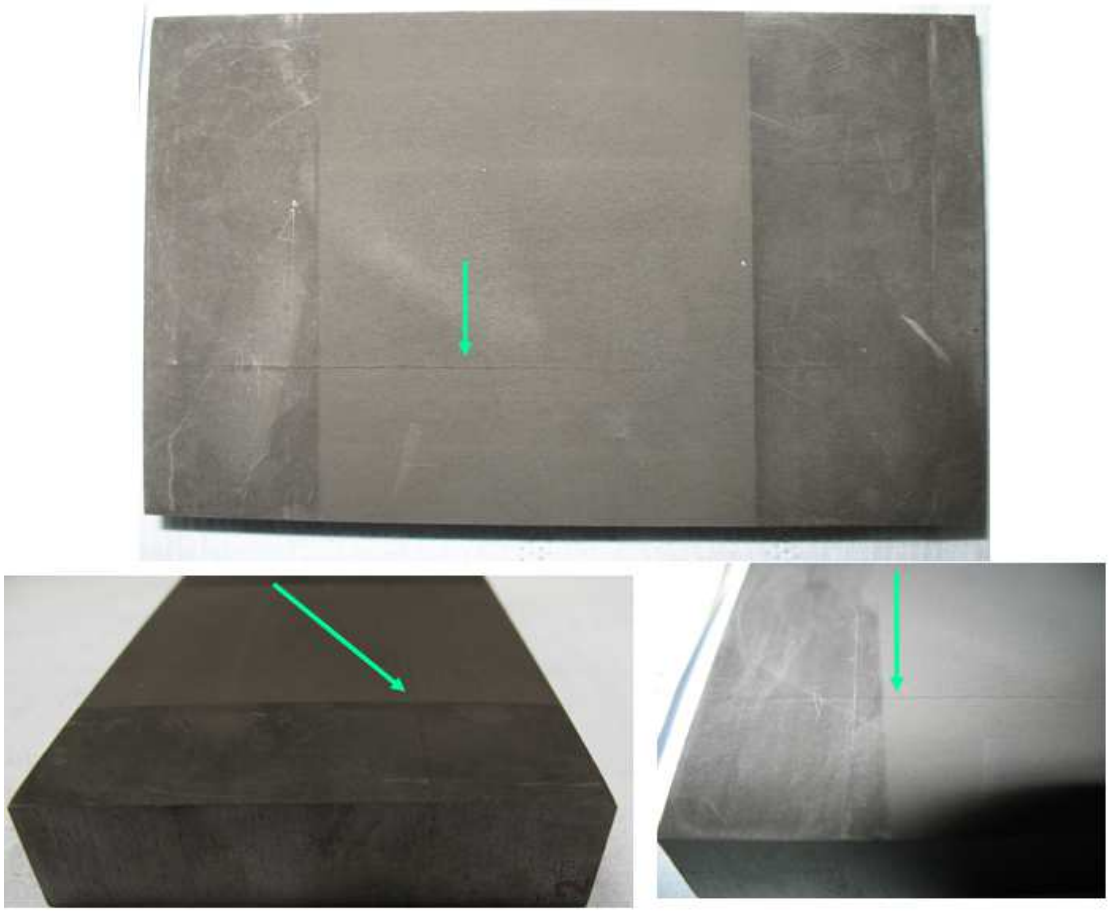

Figure 7.82: Fracture in tile A7 after experimental campaign in GLADIS.

A preliminary conclusion can be drawn for tiles A: the improvement of the construction process from A4 to A7 in terms of ellipticity, resulted in a slightly lower quality in terms of resilience of the composite product.

Tiles B exhibit better results: nothing appreciable can be noticed, either for tile B1 or for tile B2, as shown in Figure 7.83 and Figure 7.84.

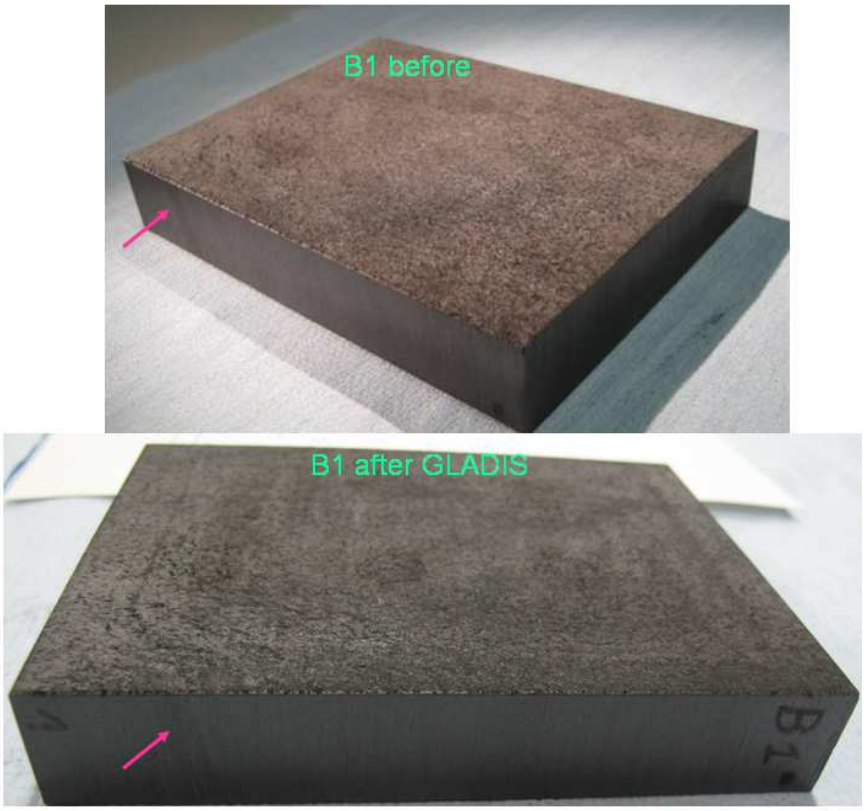

Figure 7.83: Comparison of B1, before and after exposure to the GLADIS beam.

Figure 7.84: Comparison of B2, before and after exposure to the GLADIS beam.

The cracks observed on the tiles A can be probably due to a non perfect compression between the fibre sheets or also in the densification phase. The cracks observed on the tiles are not parallel and this is due to the propagation in the matrix, between the fibre bundles. The differential thermal expansions occuring between the area heated by the beam and the colder areas shielded by graphite can cause stresses and cracks can form starting from seed points produced during the manufacturing process.

7.3 NIO1

NIO1 (Negative Ion Optimization phase 1) experiment [76] is a multiaperture radio frequency ion source based on the same concept as the one approved for the PMS project. This negative ion source is in the manufacturing phase and was developed as a collaboration between Consorzio RFX and Laboratori Nazionali di Legnaro of the Istituto Nazionale di Fisica Nuclear (INFN-LNL). The modular source aims at continuous operation. The inner walls of the source are completely covered by magnets, which can be changed to investigate several magnetic configurations. The studies of this source are focused on the efficiency of the magnetic filter and on the reduction of the co-extracted electrons by changing the configuration of the magnets; the uniformity of the extracted beam and the stability of its parameters, for instance the optics or the current density; the caesium consumption; the maximisation of the number of H^- coming from the production area (mainly the plasma grid) to the extraction region; the optimal combination between frequency and working pressure. NIO1 allows studying the scaled operation with respect to MITICA and SPIDER. This source is planned to come into operation at the end of this year, so it will be useful to have a fast feedback for the validation of source and accelerator codes.

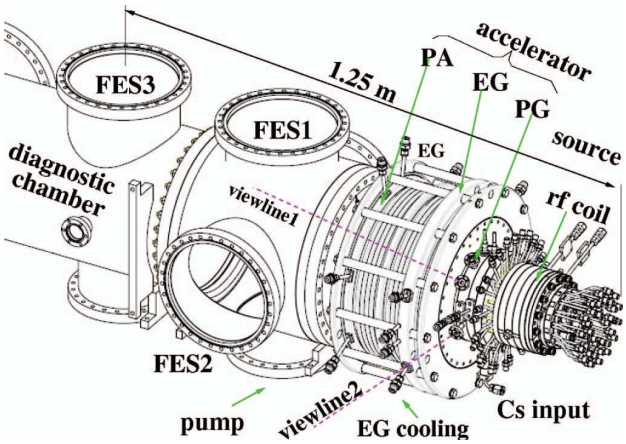

Figure 7.85: NIO1 beam source.

7.3.1 Description of NIO1 experiment

Figure 7.85 shows the ion source [77] design. The acceleration column is composed of three grids whose connections are in air: the plasma grid (PG,-60kV), the extraction grid (EG, -51kV) and the post acceleration grid (PA, ground potential); the total acceleration voltage is 60 kV. At the end of the acceleration grids, a repeller electrode (up to 150V) has been added, at the aim of optimize the space charge compensation beyond the post acceleration grid. The beam is formed by 9 H^- beamlets of 15 mA each. The extracted beamlets are arranged in a 3 x 3 matrix with 14 mm spacing.

The operational frequency of the rf source is 2MHz (instead of 1MHZ as in MITICA and SPIDER).

During my PhD, I managed the definition of the layout of the site hosting the NIO1 experiment. However, this activity is not reported herein.

7.3.2 Simulations of expected signals

The use of the CFC prototypes is foreseen also in the NIO1 experiment to characterise the beam produced.

A preliminary study of the beam footprint at different distances from the source (Figure 7.86) and the footprint at the CFC tile, have been carried out to choose a proper position for the installation of the tile inside NIO1 vessel and to evaluate the expected signals.

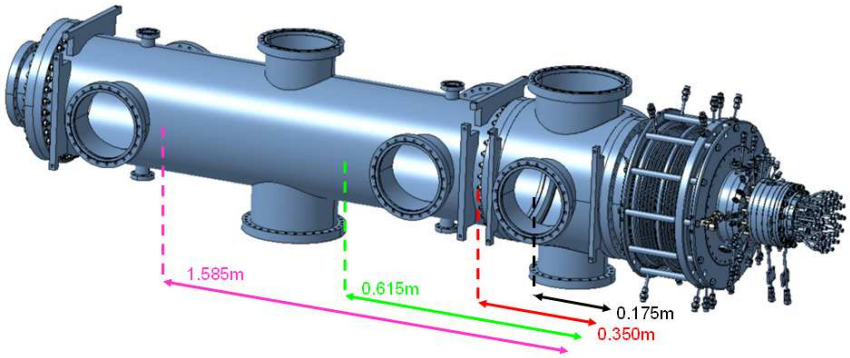

Figure 7.86: Possible CFC tile positions in NIO1 experiment.

Figure 7.87 shows the beam power density profile, due to the whole 3x3 beamlet arrangement, along a horizontal line and at different distances from the grounded grid. These profiles give information about the possibility to resolve the single beamlet. Tests were performed at 10mrad beam divergence and 3mrad beam divergence (only results for 3mrad

divergence are shown). Overlapping of the beamlets occurs even at the smallest distance from the source; moreover just 3mrad of beamlet divergence produce a less clear footprint. The farthest position, 1.585m from the source, should be avoided due to the flat profile of the power density in both divergence cases.

At lower divergence, the overlapping of the beamlets decreases, even if also for the nearest position overlapping can be noticed.

From these profiles it can be concluded that the whole beam should be intercepted by the tile.

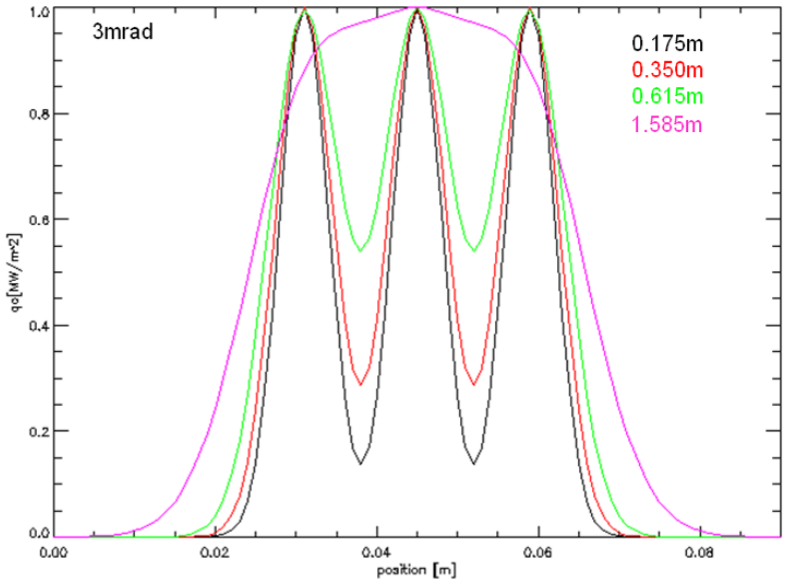

Figure 7.87: Beam power density at 3mrad divergence.

The previous tests carried out on the CFC tiles, made by illuminating the tiles with a CO_2 laser, shown that the tile named B had the best thermal response, so, to characterise the beam, a B tile was chosen. Figures shown in the following are related to the thicker tile, B3, whose dimensions are 120x90x12mm. The emissivity was set to 0.95 and radiation was imposed to all surfaces towards room temperature.

The application of the heat load occurs for 20s and it results from the superimposition of 9 gaussian curves, computed at different distances from the source. Room temperature has been set to 300K.

The elements of the mesh have different sizes: not to have a heavy model to manage, the boundary surfaces have finer resolution with respect to the subdomain (bulk); in particular, the surface correspondent to the one observed by the thermal camera and the surface hit by the beam. To further improve the spatial resolution, in this latter surface the mesh element size has been decreased in the area reached by the beamlets.

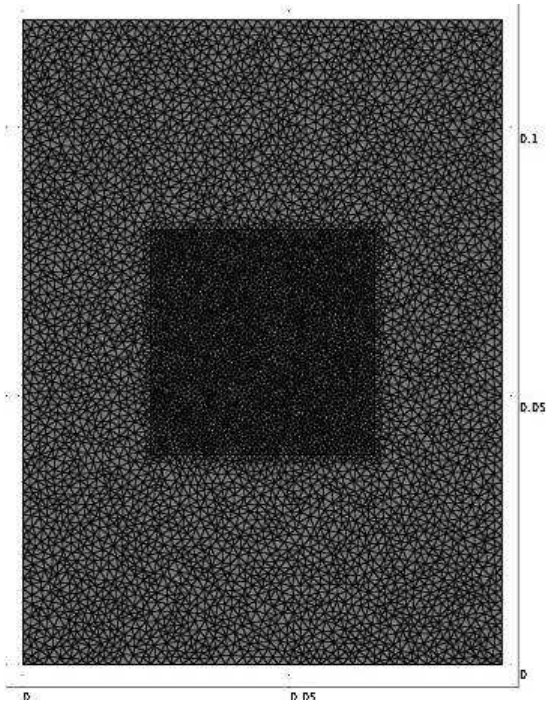

Figure 7.88: Elements of the mesh.

The power per beamlet, q_0, is about 867 W:

$$q_0 = \frac{V_{acc} \cdot I_{ext}}{n^o beamlet} = \frac{60 \cdot 10^3 \cdot 130 \cdot 10^{-3}}{9}$$

The power density to be applied to each beamlet is:

$$\frac{q_0}{2\pi\sigma_x\sigma_y} \exp\left(-\frac{(x - x_0)^2}{2 \cdot \sigma_x{}^2} - \frac{(y - y_0)^2}{2 \cdot \sigma_y{}^2} \right)$$

Where the center of beamlets has coordinates (x_0, y_0).

The radius r_b of the beamlet at the last accelerating grid of the source is 3mm. The mean quadratic radius at the last accelerating grid is: $\sigma_{x0} = \sqrt{(r_b)^{\frac{2}{3}}}$ and

$$\sigma_x = \sqrt{\frac{(r_b)^2}{3} + L^2 \cdot \sigma_d{}^2}$$

is the mean quadratic radius at the CFC tile; L is the distance from the tile and the source and σ_d the angular mean quadratic divergence.

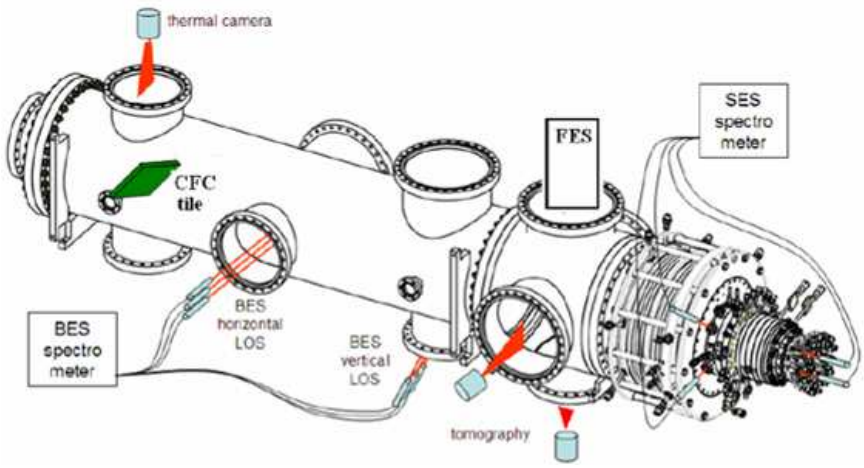

Figure 7.89: Tile position at 45° with respect to the beam.

Figure 7.90 shows the temperature profile on the front (left) and on the rear side (right) along a horizontal line passing through the centre on the beamlet central row. The tile is inclined by 45°, the beam divergence is σ_d=1mrad and the distance from the source is 1.585m. The single beamlet is not clearly identified.

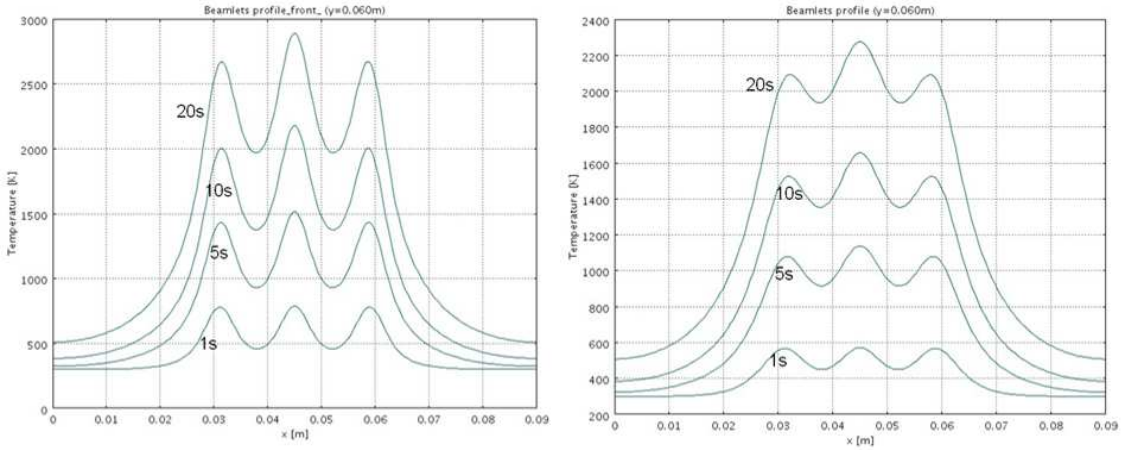

Figure 7.90: Temperature profile on the front (left) and on the rear side (right) along horizontal direction.

For comparison, the case with the tile orthogonal to the beam is presented in Figure 7.91, with 1mrad divergence and 3mrad divergence. The profiles are obtained for the rear side. If the divergence increases, the superimposition of the beamlets also increases and it is negative affected at the increasing of the distance between tile and source.

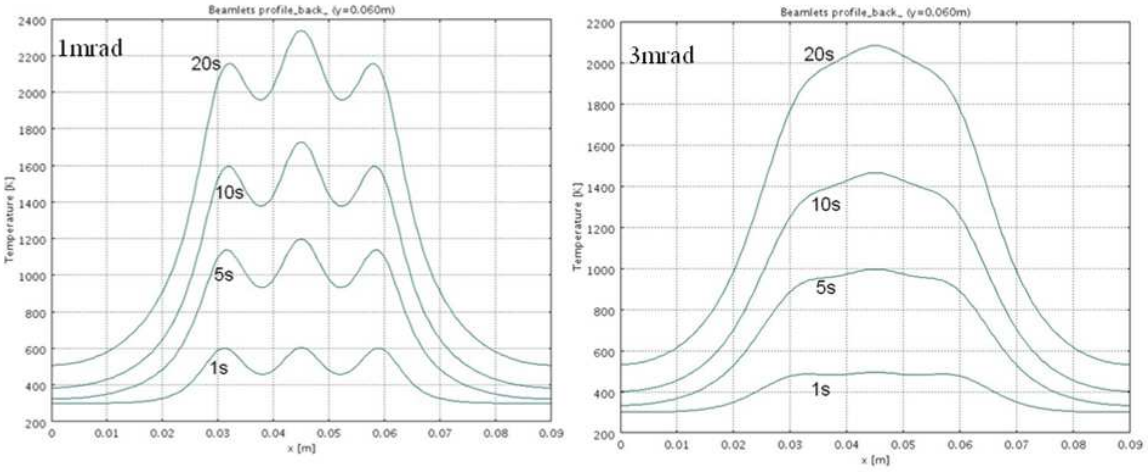

Figure 7.91: Temperature profiles along horizontal direction with 1mrad and 3mrad divergence.

Calculation of emitted radiation from the CFC was done, considering a maximum operating temperature of CFC T_{max}=1800K, the room temperature T_R=300K and the emissivity ε=0.95, the emitted radiation is about 5kW.

$$\varepsilon\sigma S\left(T_{\max}^{4} - T_R^{4}\right)$$

σ = 5.67 10^{-8} is the Stefan-Boltzmann constant; S is the tile surface.

From this preliminary sensitivity analysis it can be summarised that:

- in some case the temperature reached on the front side of the tile are higher than the maximum allowed temperature of the CFC, but with shorter pulse durations the temperature decrease.
- The typical operation using the CFC tile as diagnostic should be some seconds beam on/ some minutes break, as for STRIKE.
- The thinner tile is useful to highlight the beamlets profile at the rear side.
- It is better to install the tile near the source. However, due to different constraints, also the farthest position, at 1.585m from the source, is being considered. At that distance, the beam divergence has the principal role in providing information about single beamlet profiles: 3mrad beam divergence is too high and no beamlet profiles can be seen. The final position of the CFC tile is still under discussion.
- Tile exposed to 45° with respect to the beam could help to resolve the single beamlet profile: the peaks in the vertical direction are more distant than those in the horizontal direction: $\sqrt{2}14$ = 19.8mm instead of 14mm.

8 Conclusions

The work done during the PhD thesis has regarded the design and the assessment (simulation, verification and test) of a diagnostic calorimeter, STIKE, to measure the SPIDER beam features, in particular to verify whether the beam uniformity fulfils ITER requirements.

Three years ago, I started my PhD work as a continuation of the activity I performed during the graduate thesis (Laurea Specialistica), concerning the feasibility study of the diagnostic calorimeter and simulations dedicated to the design issues. At the end of this work, the design of the calorimeter involved two separated panels made of 16 unidirectional carbon fibre carbon composite (CFC) tiles, electrically insulated and exposed at 60° with respect to the beam axis. The active cooling could be avoided by maintaining the measurement time below 10s. The observation of the calorimeter by means of two thermal cameras was to be performed on the rear side. The calorimeter could be positioned at different distances from the SPIDER ion source and could be opened to permit long SPIDER pulses.

During the doctorate, economic considerations on the cost of the diagnostic calorimeter, in particular concerning the CFC tiles, made it necessary to revise the design of the STRIKE calorimeter.. At the end of this activity, the orthogonal exposure of the calorimeter to the beam was selected.

Numerical simulations were carried out: three-dimensional, transient, non linear thermal simulations of the CFC with radiation aiming to support and verify the design solutions. The evaluation of the maximum temperature of the CFC in the orthogonal configuration of the calorimeter, depending on the thickness of the CFC and on the pulse duration, is just an example. Thermal simulations were also dedicated to the assessment of the capabilities to diagnose the SPIDER beam, for instance to measure the divergence as well as to evaluate the behaviour of the diagnostic in off-normal conditions: change in the beam perveance and in the power per beamlet.

The secondary electron trajectories were studied in different conditions of starting energy and angle in order to evaluate a suitable polarisation voltage together with a proper combination of polarised and grounded elements of the calorimeter, to prevent electrons from being collected by a different tile from the one they were emitted from. The related electrostatic two-dimensional and three-dimensional simulations have been carried out aiming to evaluate the proper configuration for having a reliable beam current measurement, despite secondary electron emission.

The verifications of the design and of the operational conditions in SPIDER have been performed on mock-ups. This kind of tests confirmed the solutions adopted in the design.

At the end of this phase, the final design of the calorimeter was ready and the technical specifications were completed. To this purpose, I took care also of the project management of the calorimeter: the documents accompanying the design have contributed to the project of STRIKE, by implementing control actions in the design itself, and to its optimization, by reducing the possible failure risks.

The CFC tiles are the main component of the calorimeter. Two manufacturers have been identified as possible suppliers of the calorimeter tiles, but to better understand the behaviour of the CFC, several studies were realised on purchased prototypes. The first analysis conducted on this small size tiles was profilometry, to understand the superficial morphology. Thanks to this analysis, it was possible to highlight typical trends due to the fibre bundles used as preform to manufacture the matrix of this material; then a study of the proportion between the CFC fibres and the carbon matrix was carried out depending on the dimension of the single fibre bundles, to interpret the results of profilometry. The samples were subsequently subjected to the X-ray diffraction analysis to evaluate the structure and the chemical composition of the CFC before and after the manufacturing process, finding that essentially graphite planes are detected. By means of an optical analysis, the zoomed surfaces of the prototypes was studied. The most important and most extensive tests on the CFC have been carried out by a power laser aiming to characterise the thermal properties of all samples; several thermal simulations were dedicated to finding the values of the material properties capable of satisfactorily fitting the experimental results; to this purpose it was necessary to take the measured surface reflectivity into account. At the end of this series of investigations, the comprehension of the behaviour of CFC around room temperature had greatly improved.

Another important activity realised on the CFC samples has been the test in particle beams. My work involved designing the supporting structure of the tiles for the tests, performing simulations related to the design decisions and of the expected signals, overseeing the realisation and the in house tests. The prototypes were tested in the BATMAN experiment, to assess the diagnostic capability of the calorimeter, and in the GLADIS experiment, to evaluate the thermo-mechanical behaviour of the CFC. Moreover, the system realised for BATMAN measurements is planned to be used on other particle beam sources; in particular thermal simulations of the expected signals have been carried out for the installation in the NIO1 source, due to start experiments soon at Consorzio RFX.

Tests in BATMAN have proven the diagnostic capability of the system realized during the period of this thesis; calorimetric analysis was performed as well, demonstrating that by combining all measurements the beam parameters can be deduced. Tests in GLADIS highlighted the fragility of the tile material: some CFC prototypes experienced fractures after the application of the GLADIS power beam.

The whole data analyses concerning BATMAN and GLADIS are not concluded yet and they will be completed in the near future. Moreover, after the results in GLADIS, it is clear that an extensive investigation has to be made on the thermo-mechanical properties of CFC: there are still open issues on this material, and in particular on prototypes supplied by one of the manufacturer. Thus, other CFC samples should be produced and tested aiming to optimise the manufacturing process. This could also allow to complete the technical specifications as far as the tile material and the acceptance tests of the final supply of CFC tiles are concerned.

REFERENCES

[1] M. Kikuchi et al., Fusion physics, Vienna: International Atomic Energy Agency, 2012.

[2] J. Wesson, Tokamaks; 4th ed., International series of monographs on physics (2011).

[3] ITER website, www.iter.org.

[4] J.L. Luxon, "A design retrospective of the DIII-D tokamak", Nucl. Fusion **42** (2002) 614.

[5] R. J. Hawryluk et al, "Fusion plasma experiments on TFTR: A 20 year retrospective", Phys. Plasmas **5**, (1998) 1577.

[6] J. Paméla et al, "Overview of JET results", Nucl. Fusion **43** (2003) 1540.

[7] M. Yoshikawa, "An overview of the JT-60 project", Fusion Eng. Des.**5** (1987) 3.

[8] M. Kikuchi, "Overview of Modification of JT-60U for the Satellite Tokamak Program as one of the Broader Approach Projects and National Program", 21st IAEA Fusion Energy Conference (2006), http://www-naweb.iaea.org/napc/physics/FEC/FEC2006/talks/t_ft_2-5.pdf.

[9] R Aymar et al, "The ITER design", Plasma Phys. Control. Fusion **44** (2002) 519.

[10] Y. Shimomura et al, "ITER Overview", Nucl. Fusion **39** (1999) 1295.

[11] F. Wagner et al., "On the heating mix of ITER", Plasma Phys. Control. Fusion **52** (2010) 124044.

[12] T. Inoue et al, "Design of neutral beam system for ITER-FEAT", Fusion Eng. Des. **56–57** (2001) 517.

[13] R. S. Hemsworth et al., "Status of the ITER neutral beam injection system", Rev. Sci. Instrum. **79**, (2008) 02C109.

[14] R. S. Hemsworth et al., "Status of the ITER heating neutral beam system", http://www-naweb.iaea.org/napc/physics/FEC/FEC2008/papers/it_p7-7.pdf.

[15] R. Hemsworth, et al., "Status of the ITER heating neutral beam system", Nuclear Fusion **49** (2009), doi:10.1088/0029-5515/49/4/045006.

[16] M. Kuriyama, et al., "Operation of the negative-ion based NBI for JT-60U", Fusion Eng. Des. **39–40** (1998) 115.

[17] P. Sonato et al., "Status Of PRIMA, The Test Facility For ITER Neutral Beam Injectors", presented at "3rd International Symposium on Negative Ions, Beams and Sources", Jyväskylä, Finlandia, 3-7 September 2012, accepted for publication in AIP Conference Proceedings.

[18] E. Speth et al., "Overview of the RF source development programme at IPP Garching" Nucl. Fusion **46** (2006) S220.

[19] R. Hollinger, "Ion Extraction", in The Physics and Technology of Ion Source, edited by I.G. Brown.

[20] E.W. Thomas, Oak Ridge National Laboratory, Technical Report No. ORNL-6088, 1985.

[21] H.P.L. DeEsch, “Negative ion beam halo mitigation at the 1MV testbed at IRFM”, Fusion Eng. Des. **86** (2011) 363.

[22] M. Bacal, “Physics aspects of negative ion sources”, Nucl. Fusion **46** (2006) S250.

[23] D. Marcuzzi, M. Dalla Palma, M. Pavei, B. Heinemann, W. Kraus, R. Riedl, “Detailed design of the RF source for the 1 MV neutral beam test facility”, Fusion Eng. Des. **84** (2009) 1253.

[24] L. Svensson, SRD-53-PR, -MI, -MP, -SI, -SP (Neutral Beam Test Fscility), Version 1.2, IDM UID 2WCCSG, October 2009.

[25] P. Sonato et al., “The ITER full size plasma source device design”, Fusion Eng. Des. **84** (2009) 269.

[26] R. Pasqualotto et el., “Diagnostics of the ITER neutral beam test facility”, Rev. Sci. Instrum. 83 (2012) 02B103.

[27] U. Fantz, H. Falter, P. Franzen, D. Wünderlich, M. Berger, A. Lorenz,W. Kraus, P. McNeely, R. Riedl and E. Speth, “Spectroscopy—a powerful diagnostic tool in source development”, Nucl. Fusion 46 (2006) S297.

[28] A. T. Forrester, “Large ion beams”, Wiley, 1988.

[29] W. Eckstein and H. Verbeek, “Reflection of light ions from solids”, in Data Compendium for Plasma-Surface Interactions, edited by R. A. Langley et al., Nucl. Fusion special issue, 1984, p. 12.

[30] E. W. Thomas, “Secondary electron emission”, in Data Compendium for Plasma-Surface Interactions, edited by R. A. Langley et al., Nucl. Fusion special issue, 1984, p. 94.

[31] N. Schupfer et al., “Effect of particle-induced electron emission (PIEE) on the plasma sheath voltage”, Plasma Phys. Control. Fusion **48** (2006) 1093.

[32] J. Bohdanski, “Sputtering”, in Data Compendium for Plasma-Surface Interactions, edited by R. A. Langley et al., Nucl. Fusion special issue, 1984, p. 61.

[33] J. Roth, “Chemical effects in sputtering”, in Data Compendium for Plasma-Surface Interactions, edited by R. A. Langley et al., Nucl. Fusion special issue, 1984, p. 72.

[34] A. Miyahara, J. B. Whitley, “Thermal effects and other critical issues of plasma-facing components”, J. Nucl. Mater. **179-181** (1998) 19.

[35] R. A. Langley, “Evaporation”, in Data Compendium for Plasma-Surface Interactions, edited by R. A. Langley et al., Nucl. Fusion special issue, 1984, p. 55.

[36] Paulmier, M. Balat-Pichelin, D. Le Quéau, R. Berjoan, “Physico-chemical behaviour of carbon materials under high temperature and ion irradiation”, J. F. Robert, Appl. Surf. Sci. **180** (2001) 227.

[37] Y. Ueda, K. Shiota, Y. Kitamura, Y. Ohtsuka, M. Isobe, M. Nishikawa, "Detailed study of radiation enhanced sublimation of graphite under high flux beam irradiation", Fusion Eng. Des. **41** (1998) 55.

[38] M. Dalla Palma, M. De Muri, R. Paqsqualotto, A.Rizzolo, G. Serianni, "Report RFX_SPIDER_TN_096", Grant F4E-2009-GRT-032-01 (PMS-H.CD), T3.23/D2.2.

[39] G.Serianni, "Report RFX_SPIDER_TN_084", Grant F4E-2009-GRT-032-01 (PMS-H.CD), Task 6.

[40] M.De Muri, G.Serianni, "Report RFX_SPIDER_TN_081", Grant F4E-2009-GRT-032-01 (PMS-H.CD), Deliverable T6.2/D7.2.

[41] M.De Muri, G.Serianni, "Report RFX_SPIDER_TN_007", Grant F4E-2008-GRT-011-01 (PMS-H.CD), Deliverable T4.2/D1.2.4.

[42] M.De Muri, G.Serianni, "Report RFX_SPIDER_TN_008", Grant F4E-2008-GRT-011-01 (PMS-H.CD), Deliverable T3.9/D2.2.2.

[43] D. Ciric et al., "Beam Profile Measurement using a Unidirectional CFC Target and Infrared Imaging", Fusion Technol-JET (1994) 059.

[44] R. Pasqualotto, "STRIKE thermography - Technical specifications, Report T3.23-D3-RFX_SPIDER_TN_109", Grant F4E-2008-GRT-011-01 (PMS-H.CD), Deliverable T3.23/D3.

[45] M. De Muri, N. Pomaro, G. Serianni, "Diagnostic Calorimeter for SPIDER - Biasing of tiles and cable routing, Report RFX_SPIDER_TN_009", Grant F4E-2008-GRT-011-01 (PMS-H.CD), Deliverable T3.9/D2.2.3.

[46] S. Dal Bello et al., "Technical specification for the supply of the diagnostic calorimeter, STRIKE, for the SPIDER experiment, Report T3.23D1.2_RFX_SPIDER_TN_137", Grant F4E-2009-GRT32-PMS-H.CD, deliverable T3.23-D1.

[47] M. Spolaore, G. Serianni, A. Leorato, F. degli Agostini, "Technical specifications of the Electrostatic sensor system for the SPIDER experiment, Report RFX_SPIDER_TS_013", Grant F4E-2009-GRT32-PMS-H.CD, deliverable T3.18-D1.

[48] Comsol Multiphysics 3.5, (2009), http://www.comsol.eu.

[49] N. Schupfer et al., "Effect of particle-induced electron emission (PIEE) on the plasma sheat voltage" Plasma Phys. Control. Fusion 48, 1093 (2006).

[50] M. De Muri, N. Pomaro, G. Serianni, P. Veltri, "RFX Technical note RFX_SPIDER_TN_003", Task deliverable: T4.2/D1.2.1 Performance of SPIDER diagnostics – Diagnostic Calorimeter for SPIDER- Preliminary specifications and feasibility study, 26/05/2009.

[51] M. De Muri, G. Serianni, P. Veltri, "RFX Technical note RFX_SPIDER_TN_005", Task deliverable: T4.2/D1.2.3 Performance of SPIDER diagnostics – Diagnostic Calorimeter for SPIDER-Measurement of divergence, 26/05/2009.

[52] S. Dal Bello et al., "Technical Specification for the Supply of the Diagnostic Calorimeter, STRIKE, for the SPIDER Experiment", 29/10/2010.

[53] R.J. Diefendorf, "Continuous Carbon Fibre reinforced Carbon matrix composite", in Engineereing materials handbook: composites, ASM International (1988).

[54] A. Patterson, "The Scherrer Formula for X-Ray Particle Size Determination", Phys. Rev. 56 (10): (1939) 978.

[55] M. Brombin et al., "First Measurements of the multichannel far-infrared polarimeter on RFX-mod", Journal of Physics **227** (2010) 012031.

[56] K. Tate, C. Stackpole, "The Advanced Project Management Memory Jogger", 2006 by GOAL/QPC.

[57] A. Fiorentin, "Project Risk Management Procedure-Consorzio RFX" (2009), unpublished.

[58] Potential Failure Mode and Effects Analysis (FMEA), Reference Manual, 2001, www.aiag.org.

[59] C. Wagner, "Specification Risk Analysis: Avoiding product performance deviation through an FMEA-Based Method", Diploma Thesis (2007).

[60] M. Boldrin et al., "Potential failure mode and effects analysis for the ITER NB injector" Fusion Eng. Des. **84**, (2009) 466.

[61] A. Fiorentin, "Standard Quality Plan-Consorzio RFX", 2012.

[62] ISO 9000:2005, "Quality management system-Fundamentals and vocabulary".

[63] S. Dal Bello, M. Dalla Palma, M. De Muri, D. Fasolo, R. Pasqualotto, N. Pomaro, A. Rizzolo, M. Tollin, G.Serianni, "T3.3-P2_RFX_SPIDER_TN_137_r2_Annex_B STRIKE_Tech_Spec_20111115".

[64] M. Dalla Palma et al., "Final Report of F4E Contract No. F4E-2009-GRT-032-01 (PMS-H.CD) T3.23/D3", 2011 (unpublished).

[65] R. Pasqualotto, "Final Report of F4E Contract No. F4E-2009-GRT-032-01 (PMS-H.CD) T3.23/D3", 2011 (unpublished).

[66] G. Serianni et al., "Thermal and electrostatic simulations of the diagnostic calorimeter for the Source for Production of Ion of Deuterium Extracted from RF plasma beam", Rev. Sci. Instrum. **83**, 02B725 (2012).

[67] P. Franzen et al., "Performance of multi-aperture grid extraction system for an ITER-relevant RF-driven negative hydrogen ion source", Nucl. Fusion **47** (2007) S264.

[68] B. Ruf, "Preparation of modelling for miniSTRIKE tests at BATMAN", IPP report (2011).

[69] F. Rossetto, R. Rizzieri, “RFX_SXM_TN 55” (2007).

[70] L. Schiesko et al., “Magnetic field dependence of the plasma properties in a negative hydrogen ions source for fusion”, Plasma Phys. Control. Fusion **54** (2012) 105002.

[71] B. Ruf, private communication.

[72] IPP, private communication.

[73] H. S. Carslaw. J. C. Jaeger, “Conduction of Heat in Solids”, Oxford University Press, USA, 1986.

[74] ITER Materials Property Handbook.

[75] H. Greuner et al., “High heat flux facility GLADIS: Operational characteristics and results of W7-X pre-series target tests”, Journal of Nuclear Materials **367–370** (2007) 1444.

[76] M. Cavenago et al., “Development of a versatile multiaperture negative ion source”, Rev. Sci. In. **83**, (2012) 02A707.

[77] M. Cavenago et al., “Status of NIO1 construction”, AIP conf. Proc. **1390**, (2011) 640.

Appendix

System: STRIKE
Core Team: M.Dalla Palma, M.De Muri, D.Fasolo, R.Pasqualotto, A.Rizzolo, M.Tollin, G.Serianni

Potential Failure Mode and Effects Analysis
(Machinery FMEA)

Revision Date: 14/04/2011
last review by: M. De Muri, G

Item / Function	Potential Failure Mode	Potential Effect(s) of Failure	Severity	Potential Cause(s)/ Mechanism(s) of Failure	Occurrence	Current Machinery Controls Prevention	Current Machinery Controls Detection	Detection	R.P.N.	Recommended Action(s)	Responsability & Target Completion Date	Action Results: Actions Taken	New Sev	New Occ	New Det	New RPN
Assuring vacuum tightness	air leakage inside vessel	pressure out of range; impurity injection; presence of water vapour; increased probability of breakdown; freezing of coolant inside components; accelerated saturation of cryopanels; beam out of specifications	6	air leakage from feed-throughs	2	factory guarantee, frequent leakage tests	pressure measurements, RGA, spectroscopy	8	96	purchase of spare feedthrough						
			6	air leakage from observation windows	5	flange design verification, frequent leakage tests	pressure measurements, RGA, spectroscopy	8	240	purchase of spare parts						
Being UHV-compatible	component excessive outgassing	pressure out of range; impurity injection; presence of water vapour; increased probability of breakdown; freezing of coolant inside components; accelerated saturation of cryopanels; beam out of specifications	4	overheating-induced desorption of particles from tile surface	5	vacuum compatible materials; design avoiding air reservoirs; component cleaning specifications; outgassing tests at working temperature; reduction of exposure time	pressure measurements, RGA, spectroscopy	6	120							
			5	bad cleaning of tile surfaces	5	handling adopting UHV procedures; component cleaning specifications; outgassing tests at room temperature; outgassing tests at working temperature	pressure measurements, RGA, spectroscopy	7	175							
Maintaining system integrity	detachment of components	reduction of STRIKE diagnostic capability; short circuit to ground; damage to power supply; damage to cables; impairment of moving capability; dangling tile/kerb	3	disconnection of thermocouple cable	5	periodic check during ordinary maintenance; suitable design; suitable assembly	temperature measurement; periodic electrical continuity check; visual inspection by camera	7	105							
			6	disconnection of electrical cable	2	periodic check during ordinary maintenance; suitable design; suitable assembly	current measurement; periodic electrical continuity check; visual inspection by camera	7	84							
			3	disconnection of cable of electrostatic sensor	5	periodic check during ordinary maintenance; suitable design; suitable assembly	electrostatic sensor measurement; periodic electrical continuity check; visual inspection by camera	7	105							
			6	disconnection of cable of moving system	2	periodic check during ordinary maintenance; factory guarantee	no movement; periodic eletrical continuity check; visual inspection by camera	7	84							
			7	loosened screw	5	periodic check during ordinary maintenance; suitable design; suitable assembly	periodic electrical continuity/insulation check; periodical mechanical inspection	6	210							
	fall of components	reduction of STRIKE diagnostic capability; short circuit to ground; damage to power supply; damage to panel; damage to tiles; damage to cables; impairment of moving capability; damage to pumping systems; damage to observation windows; damage to dampers; damage to source	8	detachment of panel	2	periodic check during ordinary maintenance; suitable design; suitable assembly	visual inspection; electrical continuity/insulation check	7	112							
			7	broken tile	5	periodic check during ordinary maintenance; suitable design; suitable assembly	visual inspection by camera; periodical mechanical inspection	8	280							
			3	broken electrode of electrostatic sensor	5	periodic check during ordinary maintenance; suitable design; suitable assembly	visual inspection by camera; periodical mechanical inspection	7	105							
			3	loosened screw	2	periodic check during ordinary maintenance; suitable design; suitable assembly	periodical mechanical inspection; electrical continuity/insulation check	9	54							
			8	overheating of panel	5	infrared inspection; suitable design; reduction of exposure time	visual inspection by camera; infrared inspection; electrical continuity/insulation check	6	240							

diagnosis of beam performances	mechanical failure	reduction of STRIKE diagnostic capability; impairment of movement; damage to motor	6	obstructed linear bearings	2	periodic check during ordinary maintenance; suitable design; suitable assembly	encoder; visual inspection by camera; periodical mechanical inspection	7	84							
	tile misalignment	reduction of STRIKE diagnostic capability	4	non-planar panel and/or frame at construction	2	suitable design (tolerance); proper construction; suitable assembly;	acceptance criteria; alignment procedure; thermal pattern analysis	3	24							
			4	non-planar panel and/or frame due to thermal expansion	5	suitable design	thermal pattern analysis; frame temperature measurements	7	140							
			4	non-planar panel and/or frame due to mechanical stresses combined with thermal loads	5	suitable design; suitable construction	thermal pattern analysis; frame temperature measurements	8	160							
	panel misalignment	reduction of STRIKE diagnostic capability; interference with lines-of-sight of other diagnostics	4	misaligned supporting and positioning system at construction	2	suitable design; proper construction; suitable assembly; suitable installation	acceptance criteria; alignment procedure; thermal pattern analysis	3	24							
			4	misaligned supporting and positioning system due to thermal expansion	2	suitable design	thermal pattern analysis	7	56							
			4	misaligned supporting and positioning system due to mechanical stresses combined with thermal expansion	5	suitable design	thermal pattern analysis	8	160							
	insufficient space resolution	reduction of STRIKE diagnostic capability	4	use of thermal camera with insufficient space resolution	2	suitable choice of thermal cameras and lenses	data analysis with different zooms	3	24							
	erroneous thermal pattern	reduction of STRIKE diagnostic capability	4	insufficiently known surface emissivity	5	suitable choice of thermal cameras; avoid extreme exposure angles; use tiles with uniform surface	data analysis; comparison with thermocouples	5	100							
	damage to thermocouples	reduction of STRIKE diagnostic capability; thermal cameras can not be calibrated; local temperature measurement can not be performed	7	too high panel temperature	5	suitable design; temperature monitoring; reduction of exposure time	temperatue monitoring	6	210							
	bad thermal contact of thermocouples	reduction of STRIKE diagnostic capability; thermal cameras can not be calibrated; local temperature measurement can not be performed	6	loosening due to thermal cycles	5	suitable design; reduction of exposure time	comparison with thermal cameras	6	180							
	noisy signals	reduction of STRIKE diagnostic capability; local temperature measurement can not be performed; thermal cameras can not be calibrated; current measurements are disturbed	4	electromagnetic pick-up	5	suitable design (shielding, grounding), on-site verifications	data analysis	7	140							
	loss of insulation	reduction of STRIKE diagnostic capability	4	short-circuit between tiles	5	suitable design	off-line measurement of electrical insulation	7	140							
		reduction of STRIKE diagnostic capability	4	short-circuit between tiles and other items at the same voltage	5	suitable design	off-line measurement of electrical insulation; tile current measurement	7	140							
		reduction of STRIKE diagnostic capability; damage to power supply; damage to cabling	7	short-circuit between tile and grounded items	5	suitable design; protection of power supply	off-line measurement of electrical insulation; total current measurement	7	245							
		reduction of STRIKE diagnostic capability; damage to feed-through	7	short-circuit between feed-through pins	5	suitable design	off-line measurement of electrical insulation	7	245							
positioning system	movement is hindered	reduction of STRIKE diagnostic capability	7	motors out of order	5	periodic check during ordinary maintenance; suitable design; motor protections	encoder; visual inspection by camera; motor protections	6	210							
		damage to positioning system; reduction of STRIKE diagnostic capability	7	beam hitting positioning system	5	periodic check during ordinary maintenance; suitable design	encoder; visual inspection by camera; motor protections; infrared inspection	6	210							
		damage to positioning system; reduction of STRIKE diagnostic capability	7	non parallel guides at installation	2	periodic check during ordinary maintenance; suitable design; suitable assembly	encoder; motor protections	6	84							
		damage to positioning system; reduction of STRIKE diagnostic capability	7	non parallel guides due to thermal expansion	5	suitable design; measurement of trolley temperature	encoder; motor protections	7	245							
	motors out of order	reduction of STRIKE diagnostic capability	6	electrical failure	5	periodic check during ordinary maintenance; suitable design; motor protections	encoder; visual inspection by camera; motor protections; check at feedthrough	7	210							
			7	overheating due to beam	5	suitable design	encoder; visual inspection by camera; motor protections	5	175							

Participation to national and international conferences

- "Quinta conferenza annuale del Dipartimento Energia e Trasporti del CNR", Roma, Italy, 26-27 April 2010, with presentation of a poster titled "Neutral Beam Test Facility R&D in Progress: Diagnostic Calorimeter".
- AIV (XX Congresso Nazionale sulla Scienza e Tecnologia del vuoto), Padova, Italy, 17-19 maggio 2011; coordination of 5 posters concerning activities performed together with colleagues of Consorzio RFX; presentation of 2 posters titled: "STRIKE, the diagnostic calorimeter for SPIDER: design and dedicated diagnostics" and "Characterisation of the plume of an atmospheric plasma torch".
- ICIS (14th International Conference on Ion Sources), Giardini Naxos, Italy, 12-16 September 2011, with presentation of a poster titled "Design and specifications of the diagnostics for the instrumented calorimeter of SPIDER".
- SOFT (27th Symposium on Fusion Technology), Lièges, Belgium, 24-29 September 2012, with presentation of a poster titled "Characterisation, test and interpretative simulations of one-dimensional Carbon Fibre Composite prototype for SPIDER experiment".

Publications in international journals

- Andrea Rizzolo, Mauro Dalla Palma, Michela De Muri, Gianluigi Serianni, "Design and analyses of a onedimensional CFC calorimeter for SPIDER beam characterization", Fusion Eng. Des. 85 (2010) 2268-2273.
- M. Dalla Palma, M. De Muri, R. Pasqualotto, A. Rizzolo, G. Serianni, P. Veltri, "Numerical Assessment of the Diagnostic Capabilities of the Instrumented Calorimeter for SPIDER (STRIKE)", AIP Conf. Proc. 1390 (2011) 584-593.
- M. De Muri, M. Dalla Palma, D. Fasolo, R. Pasqualotto, N. Pomaro, A. Rizzolo, G. Serianni, M. Tollin, "Design and specifications of the diagnostics for the instrumented calorimeter of Source for the Production of Ions of Deuterium Extracted from Radio frequency plasma", Rev. Sci. Instrum. 83 (2012) 02B724,
- G. Serianni, M. Dalla Palma, M. De Muri, D. Fasolo, R. Pasqualotto, N. Pomaro, A. Rizzolo, M. Tollin, "Thermal and electrostatic simulations of the diagnostic calorimeter for the Source for Production of Ion of Deuterium Extracted from RF plasma beam", Rev. Sci. Instrum. 83 (2012) 02B725.

- R. Pasqualotto, G. Serianni, P. Sonato, M. Agostini, M. Brombin, G. Croci, M. Dalla Palma, M. De Muri, E. Gazza, G. Gorini, N. Pomaro, A. Rizzolo, M. Spolaore, B. Zaniol, “Diagnostics of the ITER neutral beam test facility”, Rev. Sci. Instrum. 83 (2012) 02B103.
- M. Cavenago, G. Serianni, T. Kulevoy, S. Petrenko, P. Agostinetti, V. Antoni, M. Bigi, D. Conventi, F. Fellin, A. Minarello, M. De Muri, R. Pasqualotto, M. Recchia, M. Rigato, M. Sattin, M. Barbisan, F. Rossetto, M. Valente and P. Veltri, “Construction of a Versatile Negative Ion Source and Related Developments”, accepted for publication in AIP Conf. Proc.
- - G. Serianni, M. De Muri, D. Fasolo, R. Pasqualotto, V. Cervaro, S. Dal Bello, M. Dalla Palma, L. Franchin, A. Rizzolo, M. Tollin, “Thermal Simulations of STRIKE tiles for the assessment of the CFC prototypes and of the configuration for SPIDER”, accepted for publication in AIP Conf. Proc.
- M. De Muri, V. Cervaro, S. Dal Bello, M. Dalla Palma, D. Fasolo, L. Franchin, R. Pasqualotto, N. Pomaro, A. Rizzolo, M. Tollin, G. Serianni, “Characterisation, test and interpretative simulations of one-dimensional Carbon Fibre Composite prototype for SPIDER experiment”, accepted for publication in Fusion Eng. Des.

Technical notes of Consorzio RFX

- - T3.23D4-RFX_SPIDER_TN_144_r0_STRIKE-procfollowup Documentation for the CfT and procurement follow-up.
- - T6.2-D7.1_RFX_SPIDER_TN_080_r0_graphite Diagnostic Calorimeter for SPIDER: Proposal of an alternative Design using graphite tiles.
- - T6_2-D7_2_RFX_SPIDER_TN_081_r0_orthogonal Diagnostic Calorimeter for SPIDER Assessment of the effect of radiation by comparing 60° and orthogonal exposure.
- - AppendixA_T3.23-D2.2_RFX_SPIDER_TN_095_r3_20101102_3 General Requirements and Interfaces for STRIKE.
- - AppendixB_T3.23-D2.1_RFX_SPIDER_TN_086_r1_20101102_2 Diagnostic Calorimeter for SPIDER: Requirements of data acquisition.
- -T6.2D8.2_RFX_SPIDER_TN_136_r1_nibs.
- -T3.23-D1.3_RFX_SPIDER_TN_138_r1_Overall System Description of STRIKE, the diagnostic calorimeter of SPIDER.
- -T6.2D8.3_RFX_SPIDER_TN_135_r1_trajectory comparison.
- - T3.3-P4.3-P3.5_RFX_SPIDER_TN_195_thermocouple-mock-up.
- -T3.3-P4.2_RFX_SPIDER_TN_194_articlesICIS.

- -T3.3-P4.1_RFX_SPIDER_TN_148_variation of acceleration voltage.
- -T3.3-P3.4_RFX_SPIDER_TN_171_OpticalThermalAnalysesCFCtiles.
- -T3.3-P3.2_RFX_SPIDER_TN_158_PreliminaryAnalysesCFC-A.
- -T3.3-P3.1_RFX_SPIDER_TN_145_Fibres&Voids.
- -T3.3-P3.3_RFX_SPIDER_TN_147_meetingIPP4STRIKE.
- -T3.3-P1_RFX_SPIDER_TN_150_MeetingIImonth.
- -T3.3-P2_RFX_SPIDER_TN_137_r2_Annex_B Technical Specifications for the supply of the diagnostic calorimeter, STRIKE, for the SPIDER Experiment.
- -T3.23-D1.4_RFX_SPIDER_TN_139_r0_STRIKE-FMEA.
- -T3.23-D1.1_RFX_SPIDER_TN_068_r0_Graphite laser test.